Magnetic Minerals in Soils and Paleosols as Recorders of Paleoclimate

A THESIS
SUBMITTED TO THE FACULTY OF THE GRADUATE SCHOOL
OF THE UNIVERSITY OF MINNESOTA
BY

Daniel P. Maxbauer

IN PARTIAL FULFILLMENT OF THE REQUIREMENTS
FOR THE DEGREE OF
DOCTOR OF PHILOSOPHY

Joshua M. Feinberg and David L. Fox

June, 2017

Acknowledgements

My experience in graduate school has been influenced by many people, but none more so than my two advisors, Josh Feinberg and David Fox (alphabetical order, of course). David and Josh have both been incredible mentors to me. The flexibility David gave me allowed me to pursue my own interests, even as they repeatedly changed during my first year, and that ultimately led me to pursue this research. I am extremely grateful for that academic freedom. The patience and support Josh offered to me, particularly early on as I began learning about rock magnetism was incredible. I am so grateful for all the discussions we have had about many of the topics discussed in this dissertation. I look forward to being friends and collaborators with them both for years to come.

Thank you to everyone at the Institute for Rock Magnetism, especially Mike Jackson, Peat Solheid, Subir Banerjee, and Dario Bilardello for providing support and guidance to me that made my research possible. My committee members - Bruce Moskowitz and Ed Nater - have helped to shape my research, and I'm grateful for their time and energy. Field work for the soils discussed in Chapter 6 wouldn't have been possible without help from Ed and his expertise. Thanks to Brandy Toner and Jake Bailey for their support and for serving on my preliminary exam committee. Sharon Kressler and Jen Petrie provide unending support to all graduate students, me included, and I thank them for all their help. There are many other many other collaborators who have influenced this work, and individual acknowledgment has been offered them at the end of the appropriate chapters of this dissertation.

This work was supported by the Richard C. Dennis Fellowship through the Earth Sciences Department and the Standwood Johnston and Doctoral Dissertation Fellowships through the University of Minnesota Graduate School. Research funding was provided by a GSA Student Grant, an SEPM Student Grant, and the Quaternary Paleoecology

program at UMN.

Thanks to all my friends and colleagues in the Fox Lab (David Birlenbach, Andrew Haveles, Wes Rutelonis, and Nikki Garrett), the IRM (Mark Bourne, Becky Strauss, Michele Stillinger, and Rudy Molinek), elsewhere in the department (Amanda Yourd, Amy Myrbo, and Ania Fayon), and the many others whom I haven't named here.

Finally, thank you to my family and friends for their support over the years. Their many well placed jokes about how I'm still in school never failed to remind me that I've never had a "real job". Thanks to Caity for never caring about that.

Daniel P. Maxbauer

March, 2017

Abstract

It is a fundamental challenge for geologists to create quantitative estimates of rainfall and temperature in past climates. Yet, records of past climates are integral for understanding the complexities of earth system dynamics. The research presented in this dissertation begins to establish a framework for reconstructing paleoclimates using the magnetic properties of fossilized soils. Magnetic minerals are ubiquitous in soils, and their composition, grain size, and concentration is often directly related to the ambient climatic conditions that were present during soil formation. Using rock magnetic methods, it is possible to sensitively characterize the magnetic mineral assemblages in natural materials - including soils and paleosols. The fundamentals of rock magnetism and many of the common methods used in rock magnetic applications are presented in chapter 2 and chapter 3, respectively. Chapter 4 reviews the physical, chemical, and biological factors that affect magnetic mineral assemblages in soils, the magnetic methods we use to characterize them, and the known relationships between magnetic minerals in soils and climate. A critical component to developing replicable tools for reconstructing paleoclimate is developing analytical and statistical tools that are accessible to the greater community. Chapter 5 introduces a new model, MAX UnMix, that was developed as an open-source, online tool for rock magnetic data processing that is designed to be user-friendly and accessible. Two case studies, on both fossil (Chapter 7) and modern (Chapter 6) soils, are presented and discuss many issues related to applying magnetic paleoprecipitation proxies in deep time. Chapter 7 discusses difficulties in disentangling the effects of pedogenesis, diagenesis, and recent surficial weathering in Paleocene-Eocene ($\sim$ 56-55 Ma) paleosols. Chapter 6 explores the relative influence of soil forming factors (vegetation vs. climate) on controlling the pedogenic formation of magnetic minerals in soils developing across the forest-to-prairie ecotone in NW Minnesota. The body of research presented in this dissertation provides many challenges to future workers, while at the same time highlighting that rock magnetism should be a useful tool for researchers interested in deep time paleoclimates moving forward.

Contents

List of Tables

List of Figures

Chapter 1

Introduction

Interactions between climate, life, tectonics, and the environment are complex and occur over different timescales, ranging from decadal variability in the climate system to tectonic changes that occur over millions of years. Effectively understanding the complexity amongst these disparate, yet interconnected systems is critically important for anticipating and preparing for the long-term future of our climate, environment, natural resources, and human societies. Changes in the modern earth system can often be directly observed. Yet, understanding what the earth system might look like in the future requires an understanding of how the earth system has changed and operated in the past. Luckily, the geologic record preserves a treasure trove of information about past environments (both marine and terrestrial) and the biotic communities that inhabited them. However, it remains a challenge to reconstruct the climates in which these environments and biotic communities existed - particularly for deep time ($>$ 2.5 Ma) terrestrial deposits that preserve many of the non-analog environments and climates we cannot study in modern systems (for example, greenhouse climates of the early Cenozoic $\sim$65-34 Ma).

In order to understand the complexities of the climate system in deep time, geologists need tools that allow us to look into the past and to reconstruct variables such as annual precipitation and temperature. The particular class of tools that allow geologists to do this are called paleoclimate proxies. Proxy methods can vary greatly, for instance models exist to reconstruct paleoclimate from the size and shape of fossil leaves (*Peppe et al.*, 2011; *Royer*, 2012) and from the isotopic composition of carbonate nodules that form

in soils (e.g., *Snell et al.*, 2012). A common characteristic amongst all paleoclimate proxies, regardless of how different the analytical approach may be, is that studies of modern systems have established a relationship between climate and some physical, biological, or chemical property that has the potential to be preserved in the sedimentary record. In turn, that relationship can be applied throughout the geologic record to reconstruct climate. The motivation behind the research presented in this dissertation was to improve our understanding of the relationships between magnetic minerals in soils with climate, and as a result to create more robust models for reconstructing paleoclimate in deep time.

For many decades, geologists have focused efforts on understanding terrestrial paleoclimates through investigating the physical and chemical properties of fossilized soils (paleosols), which are ubiquitous in the fossil record and form in direct connection with ambient climatic conditions. Quantitative geochemical proxy models are now widely applied to reconstruct mean annual precipitation (MAP) and mean annual temperature (MAT) from paleosols preserved in deep time (see review by *Sheldon and Tabor*, 2009). Similarly, in more recent loess-paleosol sequences (Quaternary and younger, < 2.5 Ma) the magnetic properties of paleosols have become a powerful tool to reconstruct ancient rainfall and temperature fluctuations (*Heller and Liu*, 1986; *Maher et al.*, 1994; *Porter et al.*, 2001; *Balsam et al.*, 2004). Yet, magnetic methods have rarely been applied to more ancient paleosols in pre-Quaternary systems and as a result, magnetic proxies that are appropriate for deep time applications are underdeveloped relative to geochemical methods.

This dissertation establishes the framework to begin using magnetic minerals (magnetite, maghemite, hematite, and goethite) preserved in pre-Quaternary paleosols as proxies for paleoprecipitation. This is no small task, and I am fortunate to be able to rely on decades of work by others that established environmental magnetism as a powerful tool in Quaternary environments, including a variety of lacustrine and marine systems (see reviews by *Thompson and Oldfield*, 1986; *Evans and Heller*, 2003; *Maher*, 2007, 2011; *Liu et al.*, 2012). There remain challenges to applying quantitative magnetic paleoclimate models in deep time, but this dissertation present compelling evidence that support a strong influence of climate on magnetic mineral assemblages in both modern and fossil soils. Looking to the future, there is enormous potential that has yet to

be reached for deep time applications of environmental magnetism. As always, there simply remains more work to be done.

1.1 Overview of Chapters

The chapters of this dissertation represent a collection of papers that address key issues regarding the development of more widely applicable magnetic-based paleoclimate proxies. The contents of each chapter are briefly outlined below.

- **Chapters 2** and **3** provide an overview of the fundamentals of rock and mineral magnetism as well as details regarding some of common methods. Much of these two chapters were orignally published as an appendix to *Maxbauer et al.* (2016a), but some modifications and additions have been made for this dissertation.

- **Chapter 4** presents a review (recently published in *Earth Science Reviews*, see *Maxbauer et al.*, 2016a) of many of the key aspects of this work including a review of magnetic minerals in soils (formation mechanisms and magnetic properties), current magnetic paleoprecipitation proxies, complications that arise when relating magnetic mineral assemblages in soils to climate and environment, and research themes that present challenges to the community moving forward.

- Building accurate and robust magnetic paleoclimate proxies hinges, in part, on replicability in the analytical approaches used to characterize magnetic mineral assemblages in soils and paleosols. In **Chapter 5** of this dissertation, I describe a new model, MAX UnMix, that allows users to unmix coercivity distributions from field-dependent magnetizations curves. Coercivity analysis of this type is critical in studying magnetic mineral assemblages where complex signals must be decomposed into their constituent parts. This work builds off of pre-existing models (*Kruiver et al.*, 2001; *Heslop et al.*, 2002; *Egli*, 2003) and attempts to strike a balance between complexity that improves model performance (e.g., *Egli*, 2003) and simplicity that encourages a diverse group of researchers to apply the model (e.g., *Kruiver et al.*, 2001). MAX UnMix functions as an online web-application (`www.irm.umn.edu/maxunmix`) that is designed to be accessible, user-friendly, and

intuitive. The contents of Chapter 5 were originally published in *Computers and Geosciences*, see *Maxbauer et al.* (2016c) for details.

- A study of modern soils from Minnesota is presented in **Chapter 6**. The goal of this study was to investigate the impact of vegetation on the magnetic properties of soils that develop under uniform climate. A soils transect across the forest-to-prairie transition in NW Minnesota allows us to compare the magnetic properties of prairie, transitional, and forest soils that have developed under uniform climates. The results presented in Chapter 6 highlight the importance of isolating specific populations of magnetic minerals out of the overall assemblage in order to properly interpret environmental and climatic processes. For instance, isolating the fine-grained, soil formed fraction of magnetic material in these MN soils shows a general consistency - which supports climate as a primary driver for pedogenic magnetic minerals found in soils. Supplemental material to Chapter 6 is included as an appendix to this dissertation and can be found in section A.

- In **Chapter 7**, I present results from a unique study where magnetic properties of paleosol layers were compared from exposures in outcrop to equivalent paleosols recently recovered as sediment cores from the Bighorn Basin, Wyoming. Results from this study of Paleocene-Eocene (∼56-55 Ma) sediments highlighted two critical concepts regarding magnetic mineral assemblages in paleosols. First, diagenetic and more recent surface weathering processes affect the preservation of magnetic minerals in ancient paleosols. Establishing novel and reproducible methods to fingerprint and correct for different types of alterations will be essential to developing robust magnetic paleoclimate models moving forward. Second, magnetic properties of paleosols in the Bighorn Basin compare favorably to geochemical records and it is likely that the geochemical and magnetic properties of paleosols record complementary information about paleoclimate. Integrated geochemical and magnetic methods are likely to be a key theme of future research. The contents of Chapter 7 were originally published in *Earth and Planetary Science Letters*, see *Maxbauer et al.* (2016b) for details. The supplement that was originally published with *Maxbauer et al.* (2016b) is included in this dissertation as an appendix, see section B.

Chapter 2

Fundamentals of mineral magnetism

The contents of this section were originally published as an appendix the a review article published in the journal Earth Science Reviews *under the title 'Magnetic mineral assemblages in soils and paleosols as the basis for paleoprecipitation proxies: A review of magnetic methods and challenges'. The main body of this paper is presented as Chapter 4 of this dissertation. See reference to Maxbauer et al. (2016a) for details. All published material is reproduced with permission of the coauthors. In some instances, additional material as been added to supplement the original, published work. Much of the additional material is summarized from Tauxe et al. (2014), who provide a more complete overview of the fundamentals discussed here.*

2.1 Origin of magnetism in natural materials

Magnetic fields arise in response to flow of electrical currents through conductive wire. A basic definition of a magnetic field (H) is given by Ampére's Law:

$$H = i/2\pi r \tag{2.1}$$

where i is an electrical current (units of Ampére, A) and r is the distance between the current and the induced magnetic field (units of meters, m). From equation 2.1 it follows

that the unit measure for H is Am^{-1}, and that the magnetitude of H scales with the strength of the current, i. We can expand the definition of a magnetic field by imaging a current that is flowing through a wire that is twisted into a loop, here the magnetic field produced is quantified as a magnetic moment, m, where:

$$m = ni\pi r^2 \tag{2.2}$$

and r now refers to the radius of the loop, i is again the electrical current, and n is the number of individual loops in a given set. Following this definition we derive units for m as Am^2.

The electrical current required to produce a magnetic moment in natural materials is provided by phenomena related to the motion and arrangement of electrons at the atomic level. In any atom, there is a small magnetic moment that arises from angular momentum created by electron motion. The magnetic moment that is created by this electron orbital angular momentum is defined as a Bohr magneton (m_b). Magnetic moments are also created at the atomic level as a results of unpaired electron spins within orbital shells surrounding an atomic nucleus. Each unpaired electron spin produces a magnetic moment of 1 m_b. In the case of iron (Fe), with an electron configuration of $1s^2 2s^2 2p^6 3s^2 3p^6 3d^6 4s^2$ (note that the 3d orbital has a capacity of 10 electrons), there are 4 unpaired spins - giving Fe a net magnetic moment of 4 m_b. In natural systems, iron exists as an ion of Fe^{3+} or Fe^{2+} where electrons have first been lost from the 4s and then 3d orbitals - resulting in a 5 m_b moment for Fe^{3+} and 4 m_b for Fe^{2+}. The arrangement of iron atoms, or other transitional metals with unpaired electron spins, in mineral crystal structures is what ultimately determines a material's magnetic properties (see section 4.3 for more details). In most cases, magnetic moments of natural materials are expressed as magnetization (M), where the magnetic moment is normalized to either volume (M with units of Am^{-1}) or mass (M with units of Am^2kg^{-1}).

2.2 Magnetic susceptibility

Natural samples can often contain a mixture of various mineral and organic constituents of various grain size and composition. When a material is placed in an applied magnetic field (H) it will produce an induced magnetization (M). The volume magnetic

susceptibility (κ) of that material is expressed as the induced magnetization divided by H:

$$\kappa = M/H \tag{2.3}$$

where M and H both have units of $\mathrm{Am^{-1}}$ and κ is dimensionless (*Evans and Heller*, 2003; *Tauxe et al.*, 2014). Mass normalized susceptibility (χ), which is predominantly used in soil and paleosol studies, is defined as the volume magnetic susceptibility divided by the density (ρ) of the material (*Thompson and Oldfield*, 1986):

$$\chi = \kappa/\rho \tag{2.4}$$

where χ has units of $\mathrm{m^3kg^{-1}}$. Reported values of χ are frequently measures of the low-field (< 800 $\mathrm{Am^{-1}}$) magnetic susceptibility (χ_{lf}). We note that susceptibility is defined using the applied magnetic field, H ($\mathrm{Am^{-1}}$) while the induced magnetic field (B, units of Tesla) can be derived using the relationship $B = \mu_o H$, where μ_o is the permeability of free space ($4\pi \times 10^{-7}$ $\mathrm{Hm^{-1}}$; *Stacey and Banerjee*, 1974). Most recent studies report magnetic properties with respect to B fields, and we will use B predominately through the remainder of this appendix and throughout the main body of the review.

2.3 Diamagnetism, paramagnetism, and ferromagnetism

Measured values of χ represent contributions of induced magnetizations from diamagnetic, paramagnetic, and various ferromagnetic minerals in a soil. The distinction between these mineral types is related to crystal structure and the interactions between unpaired electron spins in neighboring atoms (*Harrison and Feinberg*, 2009; *Tauxe et al.*, 2014). Diamagnetic minerals (e.g., quartz, carbonates) have very weak, negative induced magnetizations ($\chi \sim -8 \times 10^{-8}$ $\mathrm{m^3kg^{-1}}$). Paramagnetic minerals (e.g., ferromagnesian silicate minerals) produce a weak, positive magnetization that varies linearly with applied magnetic field strength. Both diamagnetic and paramagnetic minerals have no net magnetization in the absence of an applied field.

Ferromagnetic materials (e.g., pure iron) produce a permanent spontaneous magnetization in the absence of an applied field that arises due to a parallel coupling of magnetic moments produced by unpaired electron spins within a mineral's crystal lattice.

Perfect antiferromagnetic minerals should have an antiparallel arrangement of magnetic sub-lattices and no net magnetization in the absence of an applied field. However, due to defects in crystal structures and spin canting, so-called antiferromagnetic minerals (e.g., hematite and goethite) produce permanent magnetizations as well as weak positive induced magnetization ($\chi \sim 60 - 70 \times 10^{-8}$ m^3kg^{-1}; *Maher*, 2007). Ferrimagnetic minerals (e.g., magnetite and maghemite) have unequal antiparallel arrangements of electron spin moments and characteristically produce both strong permanent and induced magnetizations (e.g., χ of magnetite is $\sim 500 \times 10^{-6}$ m^3kg^{-1}; *Maher*, 2007).

Due to the order of magnitude difference in strength of the induced magnetizations between ferrimagnetic minerals and all other soil constituents (e.g., antiferromagnetic, paramagnetic, and diamagnetic minerals), χ is often viewed as a rough proxy for the abundance of ferrimagnetic minerals, when present, regardless of grain size and composition. However, in some clay rich soils paramagnetic susceptibility can be dominant (*Dearing et al.*, 1996b; *Yamazaki and Ioka*, 1997; *Jordanova and Jordanova*, 1999).

2.4 Magnetic grain size

The magnetic properties of iron oxide minerals in soils are highly dependent on the grain sizes of individual mineral particles. The smallest iron oxide nanoparticles (< 30 nm; all grain size boundaries discussed here are specific to magnetite; *Dunlop*, 1973; *Butler and Banerjee*, 1975) are superparamagnetic (SP). SP particles are uniformly magnetized, however they are unable to hold a permanent magnetization because thermal energy randomizes any magnetic alignment at room temperature in the absence of an applied field. As grain size increases ($30 - \sim$75 nm; *Dunlop*, 1973; *Butler and Banerjee*, 1975) magnetic particles have a stable, uniform magnetization and are referred to as stable single domain (SSD). These grains are capable of accurately recording the direction and strength of the Earth's magnetic field, and their presence is critical to paleomagnetic studies. For larger mineral particles (> 300 nm $- 100$ μm; *Worm and Markert*, 1987; *Heider et al.*, 1992), it becomes more energetically favorable for grains to form multiple zones of uniform magnetization separated by highly mobile domain walls, and mineral particles of this size are referred to as multidomain (MD). Notably, grains that fall in the grain size range between SSD and MD have variable magnetic behavior and are referred

to as pseudo-single domain (PSD). As will be highlighted below (and throughout the main portions of this review), the interpretation of a soil's magnetism is informed in large part by the distribution of magnetic domain states (SP, SSD, PSD, and MD) that are present.

2.5 Magnetic remanence and hysteresis

If a natural material is exposed to a weak magnetic field, then the measured magnetization relative to the field is expressed as the low field χ (discussed above). If the applied field is then reduced to zero, then the material's induced magnetization returns to zero (e.g., magnetization goes from t_1 back to t_0 in Figure 2.1A and 2.1B). If the applied field is large enough to "flip" the magnetic moments of some individual ferrimagnetic or antiferromagnetic SSD grains and/or unpin magnetic domain walls in MD mineral grains, then the specimen will retain a permanent magnetization parallel to the applied field when the field is removed. This permanent magnetization is referred to as magnetic remanence (M_r, see Figure 2.1; recall that SP grains do not retain remanence). M_r acquired in response to a direct field at room temperature is referred to as an isothermal remanent magnetization (IRM_{xmT}, where the subscript describes the strength of the applied field used to impart remanence in units of milliTesla). A specimen typically reaches saturation magnetization, where the magnetizations of its constituent grains are maximally aligned with the applied field (Figure 2.1A,B) in large applied fields (generally greater than or equal to the 1T available in most laboratories). These fields are strong enough to saturate 'soft' ferrimagnetic minerals, such as magnetite and maghemite, but larger fields are required to saturate 'hard' magnetic minerals like hematite and goethite (e.g., *Maher et al.*, 2004; *Rochette et al.*, 2005). When a sufficiently strong field is used to completely saturate a specimen's magnetization, the specimen will retain a saturation remanence when the field is removed (saturation isothermal remanent magnetization, $SIRM$ or saturation remanent magnetization M_{rs}; see Figure 2.1). Application of a field in the opposite direction will begin to reduce the magnetization of the sample from $SIRM$ towards saturation in the opposite direction.

The strength of the field required to reduce a saturated specimen's induced magnetization to zero is referred to as the bulk coercivity (B_c; Figure 2.1C). If a specimen's

remanence is monitored as successively larger, negative fields are momentarily applied, then we can determine the coercivity of remanence (B_{cr}; Figure 2.1C), which corresponds to the field that reduces the specimen's M_r from $SIRM$ to zero. By definition, B_{cr} is equal to or greater than B_c. At the scale of an individual, uniaxial SSD grain, coercivity is defined as the field required to irreversibly 'flip' the direction of magnetization. For a natural specimen, B_c can be thought of as the field required to reverse the magnetic moments of enough grains within a specimen such that half of the magnetization is aligned in the opposite direction of the saturating field. Coercivity for individual grains of ferrimagnetic and antiferromagnetic minerals varies greatly, and is influenced by mineralogy, shape, volume, and internal strain. The distribution of coercivity values present within an individual specimen is critical to several magnetic methods (e.g., coercivity unmixing and first order reversal curves) used to differentiate between various sub-populations of magnetic iron oxides (discussed in section 4.5).

A separate form of magnetic remanence, anhysteretic remanent magnetization (ARM), is used extensively in environmental magnetic studies of soils (e.g., *Geiss and Zanner*, 2007; *Geiss et al.*, 2008). In most rock magnetic laboratories, an ARM is imparted to a specimen using a magnetizer that is capable of simultaneously generating a small direct field ($\sim 8 - 16 \times 10^4$ Am^{-1}; referred to as H_{bias}, similar in magnitude to the Earth's magnetic field) as well as a much stronger alternating field (AF), whose peak strength, frequency, and attenuation rate are controlled by the user. As the alternating field oscillates back and forth, it forces the magnetization of magnetic grains within the specimen to align in both the positive and negative directions of the attenuating wave form according to their own individual coercivities. The small direct field acts to bias the alignment of the grains' magnetizations as the alternating field decays. If no direct field bias is used, and the peak alternating field strength is greater than the coercivity of all grains in the specimen, then half of the magnetization will be positive with the other half being negative, ultimately resulting in a net zero remanence (i.e., AF demagnetization; *Tauxe et al.*, 2014). ARM is commonly normalized by H_{bias}, in which case it is referred to as the ARM susceptibility (χ_{ARM}), with units of m^3kg^{-1}. ARM, χ_{ARM}, and the ratio of ARM (or χ_{ARM}) to IRM are excellent indicators of the presence of SSD grains in a sample (e.g., *Maher and Taylor*, 1988) due to the fact that MD grains generally have exceedingly low coercivities and are unable to retain any

significant ARM.

As a soil specimen is exposed to increasing fields its constituent magnetic minerals will eventually become saturated, where the magnetization of each grain has reached maximum alignment with the applied field. At field strengths higher than saturation, a specimen's magnetization will continue to increase linearly as magnetic moments in paramagnetic and purely antiferromagnetic minerals become progressively more aligned with the applied field. The slope of the linear increase is referred to as the high field susceptibility (χ_{hf}; see Figure 2.1D) and the difference between χ and χ_{hf} yields the contribution of ferrimagnetic minerals (regardless of grain size) to the susceptibility and is termed 'ferrimagnetic susceptibility' (χ_{ferri}; *Evans and Heller*, 2003).

2.6 Temperature dependence of magnetism

Ferromagnetism (including ferrimagnetism and antiferromagnetism discussed above) arises in natural materials as a result of interactions between neighboring iron atoms with the crystal structure of magnetic minerals. Both the induced and remanent magnetization of ferromagnetic materials are dependent in part on temperature. At high temperatures the crystal structure of magnetic minerals will expand, resulting in decreased interactions between the magnetic moments of neighboring iron atoms. It follows then that an increasing temperature will act to decrease the magnetization (both induced and remanent) of ferromagnetic materials up to a certain characteristic temperature, known as the Curie Temperature (T_C). The T_C is unique to the crystal structure of each magnetic mineral and represents the transition where thermal energy dissipates all the interaction between neighboring iron atoms, resulting in a change from ferromagnetism to paramagentism. For ferrimagnetic material (for example, magnetite and maghemite described in section 4.3) the critical transitions at high temperature are termed Curie Temperatures, although for the antiferromagnets (hematite and goethite, see section 4.3) these critical temperatures are termed Néel Temperatures (T_N). Low-temperatures also result in characteristic changes in the magnetism of ferromagnetic materials. In particular magnetite and hematite loose magnetization as a result of the Verway Transition (T_V) and the Morin Transition (T_M), respectively. These transitions are due to a reordering of crystal structures from cubic (above T_V) to monoclinic (below T_V) in

magnetite and in a loss of spin-canting below T_M in hematite. The details of these transitions are discussed in more detail in section 4.3 and some useful application of temperature dependent experiments in rock magnetism are discussed in the following chapter.

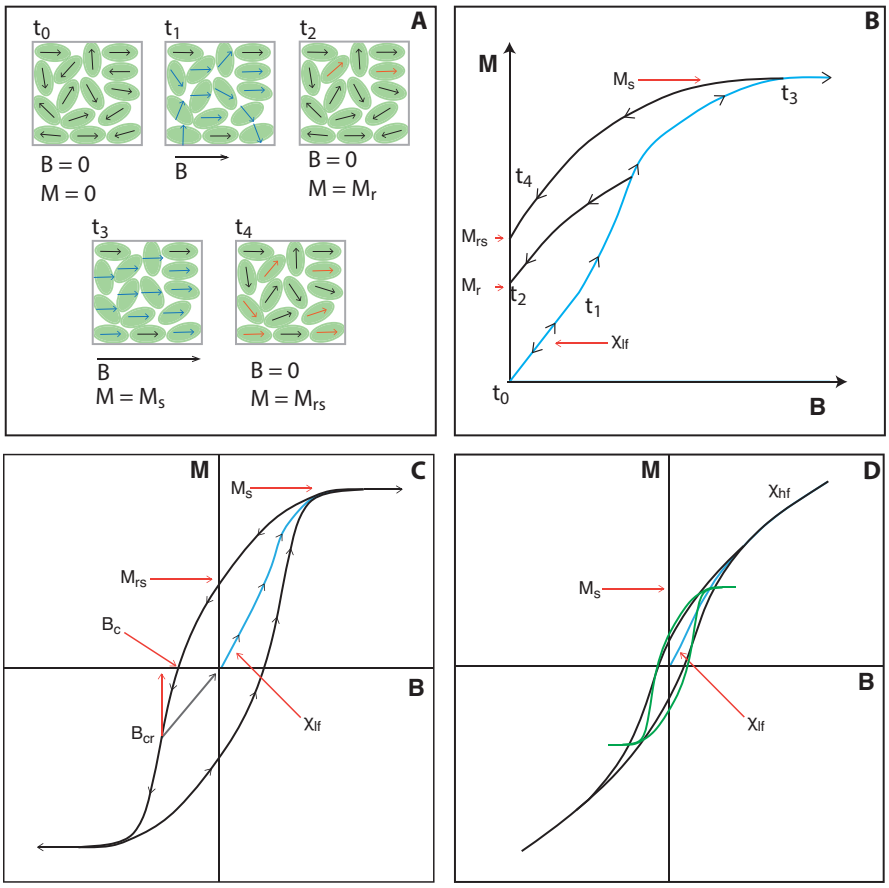

Figure 2.1

Magnetic hysteresis and coercivity. **A.** Schematic representation of the magnetic moments (arrows) of an ensemble of individual single domain grains (represented as green ovals). Paired with the magnetization curve in **B** it is possible to follow the effects of increasing the applied field to the magnetization.

(continued on next page)

Figure 2.1: *continued caption*

From t_0 to t_1 some of the individual magnetic moments begin to align with the magnetic field (indicated by blue arrows within grains at t_1), which results in a measurable low-field susceptibility (χ). If the applied field remains less than the coercivities of all individual grains, the magnetic moments for all particles will return to their original state at t0 when the field is removed. In the case that the applied field exceeds the coercivities of some individual grains, those magnetic moments will permanently change to be more in line with the field direction (orange arrows at t_2) and there will be a remanent magnetization (M_r) when the applied field is removed. Further increases in the magnetic field will continue to align the magnetic moment of individual grains until a maximum alignment is reached. The magnetization measured in the presence of this saturating field is the saturation magnetization (M_s). The magnetization measured in the absence of the field, after saturation, is the remanent saturation magnetization (M_{rs}) and is shown at t_4. **C.** The application of an increasing field in the opposite direction will eventually reduce the induced magnetization to zero, and the strength of this field is referred to as the bulk coercivity (B_c). A slightly larger field is required to reduce the remanent magnetization to zero (B_{cr}). B_{cr} is a measure of the direct field that must be applied to remagnetize individual particles in the ensemble such that the remanent magnetization is zero. The outline of the black curve is referred to as a major hysteresis loop. **D.** The hysteresis loop shown in C is an idealized loop where all measured particles are capable of retaining a remanence. The slope of the line above the loop closure in D is referred to as high field susceptibility (χ_{hf}) and represents the net induced contribution from paramagnetic and diamagnetic materials in a specimen (both of which respond linearly in applied magnetic fields). Typically this contribution is mathematically removed during data processing and a ferromagnetic hysteresis loop is obtained that is similar to that shown in C (green loop in D). Figures and captions adapted from *Tauxe et al.* (2014).

Chapter 3

Common methods in mineral magnetism

Much of the content in this section were originally published as an appendix the a review article published in the journal Earth Science Reviews *under the title 'Magnetic mineral assemblages in soils and paleosols as the basis for paleoprecipitation proxies: A review of magnetic methods and challenges'. The main body of this paper is presented as Chapter 4 of this dissertation. See reference to Maxbauer et al. (2016b) for details. All published material is reproduced with permission of the coauthors. In some instances, additional material as been added to supplement the original, published work.*

There are many ways in which the rock magnetic properties of natural materials can be manipulated and observed in order to characterize the concentration, composition, and magnetic grain size of magnetic mineral assemblages. Using instrumentation common in most paleomagnetic laboratories, it is possible to observe basic induced and remanent magnetizations such as magnetic susceptibility (discussed in section 2.2) and low-field remanences and hysteresis properties (discussed in section 2.5). Some other useful magnetic methods, particularly those that are important for this dissertation, are discussed in detail in chapter 4. These include the frequency dependence of susceptibility (χ_{fd}, see section 4.5.1), the 'hard' isothermal remanent magnetization ($HIRM$) typically used to characterize the concentration of antiferromagnets like hematite and/or geothite (see section 4.5.2), and techniques to unmix magnetization held by individual

magnetic mineral populations in a mixed magnetic mineral assemblage (see section 4.3). More detail on common methods not discussed in chapter 4 are provided below.

3.1 Demagnetization techniques

Magnetization (either natural or laboratory induced) in soils or sediments arises due to an alignment of magnetic moments held by individual mineral grains in a sample. In samples with a mixed magnetic mineral assemblage it is often useful to progressively remove (*demagnetize*) magnetization of a sample using one of three methods.

3.1.1 Direct current demagentization

As discussed above in section 2.5, application of a direct current (DC) magnetic field along the $+z$ axis of a sample will align the magnetic moments of magnetic mineral grains whose coercivities are less than the applied field strength, the result being that the material will acquire an IRM in the absence of a field. The IRM imparted on a sample, in theory, can be reversed by simply applying a DC field in the -z direction, where all grains whose coercivities where low enough to be affected by the DC field in the $+z$ direction will be reversed to align in the -z direction. In the case that a "saturating" field is used, in most instances a 1 or 1.5 T field, the measured remanence will be $\pm M_r$ or $\pm SIRM$. In practice, once a saturating field is applied to a sample and M_r or $SIRM$ can be measured, the $+M_r$ is removed progressively by applying a DC field that incrementally increases to a saturating field in the -z direction (for example, 0 to -1 T by 50 steps). The remanence measured during this progressive DC demagnetization is referred to as a backfield remanence curve. At some point during DC demagnetization, the measured remanence will be zero and the field strength required to demagnetize a sample from $SIRM$ to zero is referred to as the coercivity of remanence (B_{cr}, defined above in section 2.5). Subsequent work in this dissertation highlight the utility of decomposing backfield remanence curves to identify magentic mineral components in mixed mineral assemblages (see chapters 4, 5, 7, and 6).

3.1.2 Alternating field demagnetization

Alternating field (AF) demagnetization relies on the same concepts as DC demagnetization - namely that magnetic grains whose coercivities are lower than the applied field will align in the direction of the applied field. AF fields oscillate between positive and negative field strengths as a magnetic field decays from some peak field to zero. As the field decays, magnetic moments of individual grains will track with the oscillations of the AF until the field has decayed below that characteristic coercivity of an individual grain, at which point the grain moment will become locked in and will no longer be affected by progressively weaker fields. In a natural sample composed of mixed magnetic mineral assemblages with variable coercivities, AF demagnetization results in about half of the grain magnetic moments aligned along the $+z$ axis and half along the -z axis, consequently reducing the measured remanence to zero. AF demagnetization is used extensively in a variety of applications in rock and paleomagnetism and can be particularly useful for isolating magnetization of grains with specific coercivities.

3.1.3 Thermal demagnetization

Magnetization can also be removed from a sample by heating. At room temperature, grains that hold stable magnetization have relaxation times that are long enough that magnetization (both natural and laboratory induced) can be stable for millions of year or longer. This is due, in part, because the thermal energy at room temperature is much less than the anisotropy energy (which is controlled by grain volume, crystal structure, stress, and grain shape). As thermal energy increases at elevated temperatures relaxation times decrease to a point that magnetization is lost, or unblocked. The unblocking temperature of a given mineral can be informative of its composition - but is often below the Curie Temparature of the same mineral phase.

3.2 S-Ratio and L-Ratio

The *S-Ratio* is a common parameter that is used in environmental magnetism to quantify the proportion of hard and soft magnetic minerals in natural sediments (e.g., *Stober and Thompson*, 1979; *Bloemendal et al.*, 1992). The *S-Ratio* originally was expressed as

the ratio of an IRM acquired at some non-saturating backfield (often -300 mT or -100 mT) measured after the acquisition of an $SIRM$ (e.g., $-IRM_{-300mT}/SIRM$; *Stober and Thompson*, 1979). Values close to unity are interpreted to indicate that remanence within a specimen is held primarily by soft magnetic minerals. In most cases in which natural sediment or soil specimens are studied, there will be a measurable remanence in the backfield direction after the application of a small backfield (the blue arrow in Figure 3.1) because of the strong remanence held by even trace amounts of soft ferrimagnets. In the traditional treatment of the *S-Ratio*, IRM_{-300mT} will represent the contribution of soft minerals to the initially measured $SIRM$. However, in theory the true contribution of the soft minerals to $SIRM$ is one half the original $SIRM$ minus IRM_{-300mT}. This is highlighted by the special case that IRM_{-300mT} is zero (shown as red in Figure 3.1). If the original $SIRM$ is held equally by a soft and hard component, the application of a backfield will reduce the specimen's remanence to zero and a traditional *S-Ratio* will be zero. For these reasons, the *S-Ratio* is often calculated following the definition of *Bloemendal et al.* (1992):

$$S - Ratio = 0.5 \times (SIRM - IRM - 300mT)/SIRM \tag{3.1}$$

where the numerator now represents the true contribution from the soft mineral component to $SIRM$ (the compliment to $HIRM$). If calculated according to eq. 3.1, values for the *S-Ratio* between 1 and 0.5 would indicate greater than 50% remanence held by a soft component, values less than 0.5 would indicate greater than 50% remanence held by a hard component (green arrow in Figure 3.1), and a value of 0.5 would indicate remanence held equally by soft and hard minerals. We stress that magnetic based comparisons of relative contributions to remanence are not equivalent to mass or volume estimates of these minerals (see section 4.5.4). For example, a 0.5 *S-Ratio* (according to eq. 3.1) would indicate an order of magnitude difference between the mass/volume fractions of the hard antiferromagnets with respect to magnetite/maghemite in order for the bulk remanence held by these components to be equivalent(*Bloemendal et al.*, 1992).

Liu et al. (2007a) proposed the *L-Ratio* as a complimentary measure to aide in the interpretation of both the *S-Ratio* and $HIRM$. The *L-Ratio* is defined as the ratio of the resultant IRM_{1T} magnetization remaining after AF demagnetization at

two intermediate fields (e.g., 300 and 100 mT):

$$L - Ratio = IRM_{AF@300mT}/IRM_{AF@100mT} \tag{3.2}$$

where values close to 1 indicate higher B_{cr} values. For a given set of samples, if the *L-Ratio* remains relatively constant it can be taken that coercivity distributions are constant and that traditional interpretations of $HIRM$ and the *S-Ratio* are valid. In the case that the *L-Ratio* is variable for a set of samples, it is suggested to indicate that coercivity distributions are variable within individual specimens and that variations in the $HIRM$ and the *S-Ratio* are likely due to coercivity variations rather than relative differences in the contributions of these minerals to overall remanence.

3.3 Some useful high and low temperature measurements

Lowrie (1990) proposed orthogonal IRM acquisition followed by thermal demagnetization as a way to isolate a soft (∼120 mT), intermediate (∼400 mT), and hard (5 T) component within a specimen. Monitoring the remanence loss as temperature increases allows for identification of major slope changes indicating remanence lost at characteristic transition temperatures for ferromagnetic minerals (e.g. Curie temperature, T_C for ferrimagnets and Néel Temperature, T_N for antiferromagnets; see *Lowrie*, 1990; *Tauxe et al.*, 2014, for more details related to T_C and T_N). In the case that thermal demagnetization confirms that individual mineral components hold remanence only along one orthogonal axis (e.g., soft axis is held entirely by magnetite, intermediate only by hematite, and hard only by goethite), an absolute value for the remanence held by individual mineral components can be attained. However, because variability in coercivity can cause overlap between coercivity distributions of mineral phases (e.g., low coercivity hematite and hard maghemite) and the potential to induce mineral transformations at elevated temperature, care needs to be taken in order to assign a specific mineral phase to the remanence held along each axis.

Low temperature remanence cycling is a useful alternative to high temperature cycling because it avoids thermal alteration of mineral phases. Using a Magnetic Properties Measurement System (MPMS; Quantum Designs Inc., San Diego CA) it is possible to impart large direct current fields (∼5−7 T) and to observe induced magnetization

and remanence while temperature is cycled from room temperature (RT, ∼300 K) down to ∼10 K. A typical routine used to characterize magnetic mineralogy is a RT-$SIRM$ (shown in Figure 3.2; see *Lascu and Feinberg*, 2011). An initial IRM at some saturating field (∼2.5−7 T) is applied while the specimen is at room temperature. Following this treatment, remanence is monitored while the temperature is decreased to ∼10 K and subsequently increased back to 300 K. Hematite displays a large drop in remanence at the Morin transition (T_M, ∼260 K; see Figure 3.2) while magnetite loses remanence at the Verwey transition (T_V, ∼110 K; see Figure 3.2). Goethite is characterized by a factor of ∼2 increase in remanence on cooling (*Lascu and Feinberg*, 2011). We note that in many soils the Morin transition is suppressed due to defects and substitutions common to soil hematite; however it is possible to identify hematite by inspection of the first derivative of the RT-$SIRM$ curve where sharp deviations of the derivative curve at T_M are indicative of hematite (see *Lascu and Feinberg*, 2011; *Morón et al.*, 2013).

For magnetic mineral characterization, particularly for the identification of goethite and hematite within a specimen, RT-$SIRM$ is a particularly useful tool that ought to be applied in the study of soils. It is possible to quantify the remanence held by each mineral phase by conducting a series of RT-$SIRM$ experiments that are separated by sequential demagnetization experiments aimed to "remove" the magnetization of individual mineral phases. Demagnetization of the soft ferrimagnets can be achieved by AF demagnetization (either via traditional methods in a U-channel magnetometer or via the "oscillation" mode of a MPMS), while goethite can be demagnetized by heating of the sample to 400 K (above the T_N of goethite, but not sufficiently high to induce mineral transformations; see *Guyodo et al.*, 2006, for a detailed example).

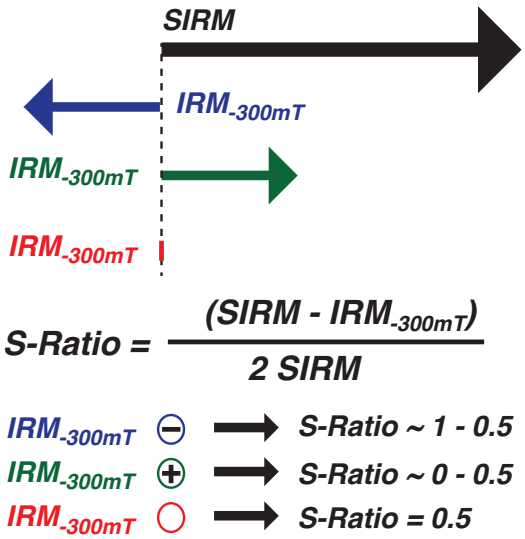

Figure 3.1: Schematic representation of the magnetizations and formula used to calculate the *S-Ratio*. If the *S-Ratio* is calculated according to the equation shown here (eq. 3.1 in text) then values between 1 and 0.5 indicate greater than 50% of the remanence is held by soft ferrimagnetic minerals. An *S-Ratio* of 0.5 is a special case such that exactly 50% of remanence is held by ferrimagnets and 50% is held by antiferromagnets. An *S-Ratio* of less than 0.5 indicates that antiferromagnets hold more than 50% of the remanence measurable in a specimen. See text for more details.

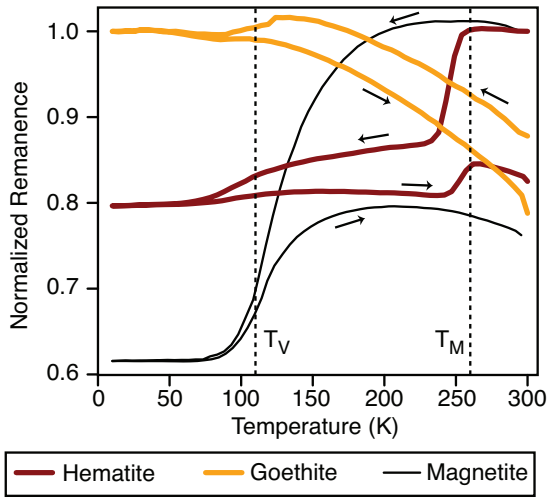

Figure 3.2: Room temperature (RT) $SIRM$ for synthetic specimen of magnetite, goethite (with trace magnetite), and hematite. Note the characteristic loss of remanence at the Verwey transition for magnetite (T_V; indicated with dashed line at 110 K) and the Morin transition for hematite (T_M; indicated with dashed line at 260 K). Goethite is characterized by an increase in remanence upon cooling. Note that the Verwey transition is apparent from this synthetic powder sample, indicating a trace amount of magnetite contamination in this specimen. All data displayed here is freely available from the Institute for Rock Magnetism online Rock Magnetic Bestiary (http://www.irm.umn.edu/bestiary2/). Remanence values for hematite and magnetite are normalized to initial $SIRM$ values measured at 300 K. Goethite values are normalized to the IRM value measured at 10 K.

Chapter 4

Magnetic mineral assemblages in soils and paleosols as the basis for paleoprecipitation proxies: A review of magnetic methods and challenges

The contents of this section were originally published in the journal Earth Science Reviews *under the title 'Magnetic mineral assemblages in soils and paleosols as the basis for paleoprecipitation proxies: A review of magnetic methods and challenges'. See reference to Maxbauer et al. (2016b) for details. This work is included below it its published form with permission of all authors.*

4.1 Synopsis

Magnetic iron oxide minerals, principally magnetite, maghemite, hematite, and goethite are formed in well-drained soils in response to a suite of physical, chemical, and biological factors. Despite a wide range of complexity in the pedogenic processes that

lead to magnetic mineral formation, dissolution, and transformation, there are well-documented empirical relationships between various magnetic mineral assemblages in soils with environmental and climatic conditions. Recently there has been an increase in the number of quantitative magnetic paleoprecipitation proxies that have been developed, and there is great potential for magnetic methods to be used in the geologic record to develop reconstructions of past climates. Magnetic paleoprecipitation proxies have been widely utilized in Quaternary or younger loess-paleosol systems; however, they have yet to be utilized in the pre-Quaternary fossil record. Future studies of magnetic mineralogy of soils and paleosols should aim to explore non-loessic modern soils and pre-Quaternary paleosols with more focus on understanding the interaction between magnetic mineral assemblages and soil moisture. Applications of existing and novel magnetic paleoprecipitation proxies in the fossil record should prove to be a valuable resource for paleoclimatologists.

4.2 Introduction

Magnetism in well-drained soil is controlled by the abundance, grain size, and chemical composition of various iron oxide and oxyhydroxide minerals (hereafter referred to simply as "oxides"). In soils, the most abundant (by volume) iron oxides are goethite ($\alpha-$FeOOH) and hematite ($\alpha-Fe_2O_3$), which are antiferromagnetic and produce weak permanent magnetizations. Magnetite (Fe_3O_4) and maghemite ($\gamma-Fe_2O_3$), both ferrimagnetic with strong magnetizations, are far less abundant in soils but tend to dominate bulk magnetic properties. Magnetic minerals form in soil in response to a suite of complex pedogenic processes that are sensitive to physical, chemical, and biological conditions. Despite these complexities, empirical relationships between soil iron oxides and climate have been observed for decades (e.g., *Kampf and Schwertmann*, 1983) and environmental magnetic studies of soils and sediments routinely make qualitative climatic interpretations (see reviews by *Maher*, 1998, 2007, 2011; *Liu et al.*, 2012).

Quantitative reconstructions of past environmental conditions, such as mean annual precipitation and temperature, are of fundamental interest to paleoclimatologists. For example, methods to reconstruct paleoprecipitation in pre-Quaternary terrestrial systems (>2.6 Ma) have been developed using leaf physiognomic approaches (*Peppe*

et al., 2011; *Royer*, 2012), bulk geochemical weathering indices of paleosols (*Sheldon et al.*, 2002; *Sheldon and Tabor*, 2009), the depth to the carbonate horizon of paleosols (*Retallack*, 2005), and the ecophysiology of mammalian fauna (e.g., *Eronen et al.*, 2010b,a). A growing number of studies have proposed methods to link magnetic minerals within a soil quantitatively to the mean annual precipitation (MAP) under which the soil developed (e.g., *Maher and Thompson*, 1995; *Balsam et al.*, 2011; *Geiss et al.*, 2008; *Orgeira et al.*, 2011; *Hyland et al.*, 2015). Historically this work has focused on magnetite/maghemite variations in loess-derived soils developed under a limited range of MAP ($\sim$200-1000 mm yr^{-1}), although some recent studies have expanded their scope to recognize quantitative relationships between precipitation rates and the abundance of hematite and goethite in soils that have experienced more rainfall (up to 3000 mm yr^{-1}; *Long et al.*, 2011; *Hyland et al.*, 2015).

Magnetic paleoprecipitation proxies have the potential to be broadly applicable to pre-Quaternary paleosols. However, current models have large uncertainties (*Heslop and Roberts*, 2013; *Maher and Possolo*, 2013) and it is clear from well-studied loess-paleosol sequences in China (*Maher and Thompson*, 1991; *Porter et al.*, 2001), New Zealand (*Ma et al.*, 2013), Alaska (*Begét et al.*, 1990), North America (*Geiss et al.*, 2004; *Geiss and Zanner*, 2006, 2007), and Russia (*Maher et al.*, 2002, 2003a) that relationships between iron oxide mineralogy and MAP can vary regionally. This variability highlights the need to re-evaluate our current understanding of the factors that control the abundance of iron oxides in soils, the magnetic methods we use to identify them, and the potential applicability of magnetic paleoprecipitation proxies to paleosols in the pre-Quaternary geological record.

In the first part of this review we provide an overview of the major iron oxide minerals found in soils (§4.3). This is followed by a discussion of the pedogenic processes that lead to the formation and transformation of magnetic iron oxides in soils (§4.4). We then discuss the relevant magnetic methods used to identify and quantify the abundance of magnetic minerals in soils (§4.5). The available magnetic paleoprecipitation proxies are reviewed in section five (§4.6). In section 6 (§4.7) we address natural mechanisms that complicate and limit the applicability of different magnetic paleoprecipitation proxies. Further, we explore the potential pathways for iron oxide mineral destruction or transformation due to diagenetic processes that occur during the transition from soil

to paleosols (§4.8). We conclude this review with a number of challenges and research themes that we hope will guide future research (§4.9).

We direct readers that are relatively new to the field of environmental magnetism to the appendix (*note:* the contents of the appendix to this paper has been repurposed for this dissertation as Chapters 2 and 3) where we include a brief primer on many common magnetic properties. This review draws from a broad body of previous published work. For further details on specific topics, readers are referred to the following resources: for a full review of iron oxide minerals see *Cornell and Schwertmann* (2003); for previous reviews on magnetism in soils see *Mullins* (1977) and *Maher* (1998); for more encompassing reviews of environmental magnetism in general see *Thompson and Oldfield* (1986), *Evans and Heller* (2003), *Maher* (2007), *Maher* (2011), and *Liu et al.* (2012).

4.3 Major Iron Oxides in Soil

We describe here the magnetic minerals that display correlation between mineral abundance and precipitation (i.e., goethite, hematite, magnetite, maghemite). In addition, we have included some related information about ferrihydrite because it is a common soil constituent and often is involved as a precursor phase in pedogenic processes that lead to the formation of the more stable magnetic iron oxides. Lepidocrite ($\gamma-$FeOOH) is a polymorph of goethite that is generally less abundant compared with other iron oxides, but is associated with goethite in some poorly drained redoximorphic soils (*Schwertmann*, 1988; *Till et al.*, 2014). Siderite ($FeCO_3$), greigite (Fe_3S_4), and pyrrhotite (Fe_7S_8 – $Fe_{11}S_{12}$) are other magnetic iron minerals that are sometimes found in poorly drained, water-logged soils (*Postma*, 1983; *Fassbinder and Stanjek*, 1994). The hydration state of these water-logged soils is often more related to drainage than to climate, and the production of these minerals is not necessarily related to precipitation in most cases.

4.3.1 Magnetite and Maghemite

Magnetite (Fe_3O_4) is a mixed Fe(II)/Fe(III) oxide with an inverse spinel crystal structure (see Figure 4.1). Ferric iron occupies all of the tetrahedral A−sites (yellow in Figure 4.1) while both Fe(III) and Fe(II) occupy octahedral B-sites (maroon in Figure 4.1).

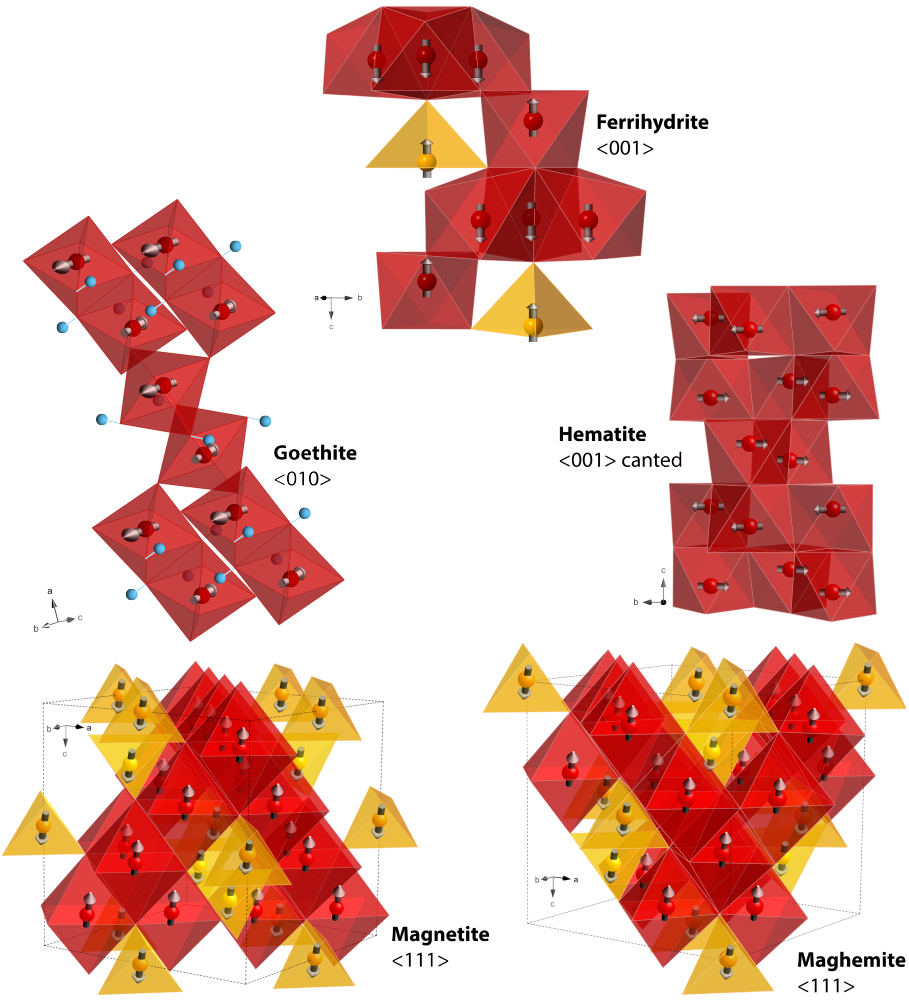

Figure 4.1

Crystal structure and magnetic moment alignments for common soil iron oxides and hydroxides. Orientations of the magnetic moments for individual iron atoms are shown with grey arrows. Octahedral sites are shown in maroon and tetrahedral sites are shown in yellow. Hydrogen is shown as blue in the crystal structure of goethite.

(continued on next page)

The spin moments of A−site and B−site iron atoms are aligned antiparallel along

Figure 4.1: *continued caption*

In each mineral structure the alignment of individual spin moments of iron atoms are aligned antiparallel along the indicated crystallographic axes. Except in the case of hematite, shown here with hexagonal crystal structure, where the spin alignment is nearly anti-parallel within the c-plane (above 260 K) however because of spin-canting of neighboring iron atoms there is a weak permanent magnetization that aligns along to the c-axis (*Stacey and Banerjee*, 1974; *Dunlop and Özdemir*, 2001, 2006). For goethite, spin alignments are antiparallel along the b-axis and weak parasitic and permanent remanence is due to defects and substitutions within the crystal structure that are not shown here (*Liu et al.*, 2006)(Liu et al., 2006). In magnetite imbalance in the antiparallel alignment along the crystallographic <111> axis is due to Fe(II), which occupies octahedral B-sites, and gives rise to magnetite's ferromagnetic properties (*Banerjee and Moskowitz*, 1985). Maghemite is composed entirely of Fe(III) and its ferrimagnetism is attributed to cation vacancies within the B sub-lattice. Crystal structure and spin alignment for ferrihydrite follows *Michel et al.* (2010). Note that the spin alignment for ferrihydrite shown here represents the transient ferrimagnetic ferrihydrite (also referred to as "hydromaghemite") phase that has been identified as a possible source of magnetic enhancement in soils. See section 4.6 for more discussion.

---

the crystallographic 111 axis (denoted <111> in Figure 4.1) and the imbalance caused by Fe(II) within the B sub−lattice gives rise to magnetites ferrimagnetism (*Banerjee and Moskowitz*, 1985). Maghemite ($\gamma-Fe_2O_3$) is a ferric oxide with similar cubic spinel crystal structure and ferrimagnetic properties to magnetite. The ferrimagnetism of maghemite is due to vacancies within octahedral B−sites that cause imbalance between the A and B sub−lattice alignment along the <111> axis (Figure 4.1).

Magnetite and maghemite are typically minor constituents (by volume or mass) of both bulk soils and the magnetic mineral fraction, but their ferrimagnetic properties tend to dominate many of the magnetic properties of soils (*Maher*, 1998). Magnetic susceptibility (χ; defined in § A.1) values for magnetite can be as high as ∼500 x10^{-6} m^3kg^{-1}, with slightly lower values for maghemite (*Maher*, 2007). Saturation magnetization (M_s; see § A.3) for magnetite is ∼92 Am^2kg^{-1} and ∼74 Am^2kg^{-1} for maghemite (*Pauthenet*, 1950; *Hunt et al.*, 1995; *Tauxe et al.*, 2014). For an assemblage of purely stable single domain (SSD) magnetite/maghemite grains with random orientations a saturation remanence (M_{rs}; see § A.3) would be half of M_s ($M_{rs}/M_s = 0.5$; *Day et al.*,

1977; *Parry*, 1982; *Dunlop*, 2002). This ratio decreases both as grain size increases into multi domain (MD) size classes and/or as grain size decreases and behavior begins to resemble that of superparamagnetic (SP) grains (see § A.2 for further discussion of magnetic grain size). Coercivity (B_c) and coercivity of remanence (B_{cr}) for magnetite and maghemite are generally low (typically 10's of mT; parameters defined in § A.3) with a maximum B_{cr} for magnetite of ∼300 mT (*Hunt et al.*, 1995), meaning that saturation properties of these minerals can be easily studied using instruments that are standard to most rock magnetic laboratories. Magnetite and maghemite are referred to as magnetically "soft" minerals because of their relatively low coercivities.

4.3.2 Hematite and Goethite

Hematite (α-Fe_2O_3) and goethite (α-FeOOH) are both so-called 'antiferromagnetic' minerals and are usually the most abundant and stable iron oxides present in the soil environment (*Cornell and Schwertmann*, 2003). Despite their nearly antiferromagnetic alignments both hematite and goethite produce weak permanent magnetizations (note that pure antiferromagnetism is characterized by a lack of permanent magnetization in the absence of an applied field). In hematite, weak permanent magnetization arises at temperatures above ∼260 K (temperature of the Morin transition in hematite) due to spin canting in neighboring iron atoms that have magnetic moments nearly antiparallel within the crystallographic c-plane (see Figure 4.1; *Stacey and Banerjee*, 1974; *Dunlop and Özdemir*, 2001, 2006). When temperature falls below the Morin transition (∼260 K) the spin alignment in pure hematite will become perfectly antiparallel along the c-axis and the weak permanent magnetization due to canting is lost (*Stacey and Banerjee*, 1974). In goethite, a weak permanent magnetization is due to parasitic remanence that arises as a result of defects and substitutions within the crystal structure (Figure 4.1; *Liu et al.*, 2006). In general, hematite and goethite are best characterized by their relatively weak magnetizations and remarkably high coercivities (see below).

The χ of hematite and goethite is similar, and roughly $2-3$ orders of magnitude weaker than ferrimagnetic minerals (Dekkers, 1989; Maher, 2007). The saturation magnetization and remanence (M_s and M_{rs}) of these minerals is less well-constrained, but typically reported values for M_s are ∼0.4 Am^2kg^{-1} for pure hematite and $\sim 0.05-0.30$ Am^2kg^{-1} for naturally occurring goethite (*Dekkers*, 1989; *Maher*, 2007; *Martin-Hernandez*

and García-Hernández, 2010; *Martin-Hernandez and Guerrero-Suárez*, 2012; *Özdemir and Dunlop*, 2014). The M_{rs}/M_s ratio in goethite and hematite is typically between 0.5 and 1 and is sensitive to variations in grain size and degree of saturation (for example, calculating the ratio for goethite, for which true saturation is often not possible to achieve, using magnetizations measured at 5 T vs. 9 T will likely yield variable results). Many previous studies report M_{rs}/M_s ratios that are largely incorrect, as they were calculated from non-saturated specimens (see *Rochette and Fillion*, 1989; *Özdemir and Dunlop*, 2014).

In contrast to the "soft" ferrimagnetic minerals, hematite and goethite are referred to as "hard" magnetic minerals due to their characteristically high B_{cr} (in general $>$ 300 mT) and the large fields required to saturate these minerals. *Maher et al.* (2004) reported non-saturation in a range of hematite samples above 2 T and in some samples as high as $\sim$4-5 T (achieving only $\sim$60-70% true M_{rs} value at 2 T; *Maher*, 2011). In goethite, and some fine-grained hematite, non-saturation has been reported in fields up to 57 T, as an extreme example (*Rochette et al.*, 2005). Goethite is almost never saturated in fields produced by most laboratory instruments ($1-3$ T) and some studies suggest that only 10-20% of the true M_{rs} is imparted by 2 T (e.g., *Rochette and Fillion*, 1989; *France and Oldfield*, 2000; *Maher et al.*, 2004; *Maher*, 2011).

The magnetic properties of hematite and goethite can vary greatly depending on grain size, defect density, and crystalline impurities such as aluminum substitutions (e.g., *Dekkers*, 1989; *Liu et al.*, 2004, 2006; *Roberts et al.*, 2006; *Özdemir and Dunlop*, 2014). Goethite, which is prone to Al-substitution (*Fitzpatrick*, 1988), has a characteristic decrease in B_{cr} and an increase in M_s with increasing Al% (*Liu et al.*, 2006; *Roberts et al.*, 2006). Further, increasing Al% in goethite acts to lower the Néel temperature (400 K for pure goethite, above this temperature goethite is unable to hold stable remanence) towards room temperature (*Liu et al.*, 2006; *Roberts et al.*, 2006). Aluminum substitution in hematite results in an increase in B_{cr} and a more variable effect on M_s with increasing Al% (*Liu et al.*, 2006; *Roberts et al.*, 2006). These complications become important when using magnetic measurements to estimate the abundance of hematite and goethite in natural sediments (see section 4.5.4).

4.3.3 Ferrihydrite

Ferrihydrite ($Fe_2O_3 \cdot 4H_2O$; Figure 1) is a poorly crystalline, metastable ferric iron oxide that is ubiquitous in many modern soils, particularly in young soils where weathering rates are high (*Childs*, 1992; *Schwertmann*, 1993; *Jambor and Dutrizac*, 1998; *Cornell and Schwertmann*, 2003). Ferrihydrite occurs in small, nanoscale (1−7 nm) particles that typically form coatings on silt and sand sized soil particles. The small particle size and poor crystallinity of ferrihydrite result in a high specific surface area (200−500 m^2g^{-1}) and a high residual structural charge, both of which act to make it highly reactive (*Childs*, 1992; *Jambor and Dutrizac*, 1998; *Cornell and Schwertmann*, 2003).

Ferrihydrite is a frequent precursor to the more thermodynamically stable iron oxides, such as goethite and hematite (see *Cornell and Schwertmann*, 2003). Despite its ubiquity, the magnetic properties of ferrihydrite are very poorly constrained. Further, the crystal structure of pure, synthetic ferrihydrite remains an active area of debate (e.g., *Michel et al.*, 2007; *Maillot et al.*, 2011; *Manceau*, 2012; *Peak and Regier*, 2012a,b). Natural ferrihydrites are commonly impure (i.e., have isomorphic substitution) and sorb silica, aluminum, and soil organic matter (*Cismasu et al.*, 2011, 2012, 2013). This results in a decrease in long-range crystallinity for natural ferrihydrites, as compared with synthetic samples, and causes spatially variable surface properties (e.g., *Eusterhues et al.*, 2008; *Cismasu et al.*, 2013). Accordingly, the crystal structure of natural ferrihydrite is even less well understood. Lab experiments that describe transformation pathways of iron oxides (discussed in more detail in section 4.4) often use synthetic samples of 2−line or 6−line ferrihydrite (where the latter exhibits slightly more long range order than the former) or isolated natural specimens. The heterogeneity of natural ferrihydrites likely is a cause of the variable magnetic properties of ferrihydrite and of the complexities of transformation pathways that occur in soils.

4.4 Formation of Iron Oxides in Soils

Iron oxide minerals occur in soils variously from pedogenic formation, input from eolian processes (i.e., wind-blown dust), formation by burning during forest and grassland fires, deposition from industrial pollution, or inheritance from the soil parent material. When using precipitation proxies that link soil iron oxides with climate processes, it is critical

that the iron oxides of interest are formed through pedogenic processes related to the soil moisture budget, and ultimately the long term input of rainfall to the soil. Here, we focus solely on the pedogenic processes known to produce iron oxide minerals in soils.

In oxic soils with a pH greater than 3, dissolution of ferrous iron-bearing primary minerals (e.g., pyroxene, olivine, biotite, fayalite) releases Fe^{2+} ions into the soil solution where rapid oxidation occurs, and poorly soluble Fe^{3+} ions rapidly undergo hydrolysis to precipitate ferrihydrite (*Schwertmann*, 1988; *Cornell and Schwertmann*, 2003). Ferrihydrite is unstable with respect to the more crystalline ferrimagnetic and antiferromagnetic minerals and, with time, will progressively transform into these more stable phases as soil conditions allow.

4.4.1 Iron oxide formation models describing magnetic enhancement

In many well-drained soils there is an observed increase in χ (and certain other magnetic properties such as anhysteretic and isothermal remanent magnetization, ARM and IRM respectively; for descriptions of these parameters see §A.3) between the upper A and/or B soil horizon compared to the unaltered parent material (e.g., Figure 4.2). This phenomenon is referred to as "magnetic enhancement" and has been a topic of interest for decades (e.g., *Le Borgne*, 1955, 1960; *Mullins*, 1977; *Dearing et al.*, 1996a; *Maher*, 1998; *Boyle et al.*, 2010; *Orgeira et al.*, 2011). Magnetic enhancement arises primarily from the presence of SP/SSD magnetite and/or maghemite. Below we discuss the two main pathways that are attributed to the pedogenic production of SP/SSD ferrimagnetic minerals in soils.

Redox oscillations and the fermentation mechanism

The first mechanism proposed to explain the magnetic enhancement of well drained, temperate soils involves a so called "fermentation" process in which redox oscillations during wet/dry cycles result in the production of very-fine grained magnetite (*Le Borgne*, 1955, 1960; *Mullins*, 1977; *Maher*, 1998; *Orgeira et al.*, 2011). During wet periods, where water saturation in a soil is prolonged enough to create anoxic conditions in soil pore spaces, reduction of Fe(III) in oxides (primarily ferrihydrite) or other soil minerals releases Fe^{2+} into solution. The resultant mixed Fe^{2+}/Fe^{3+} solution can then

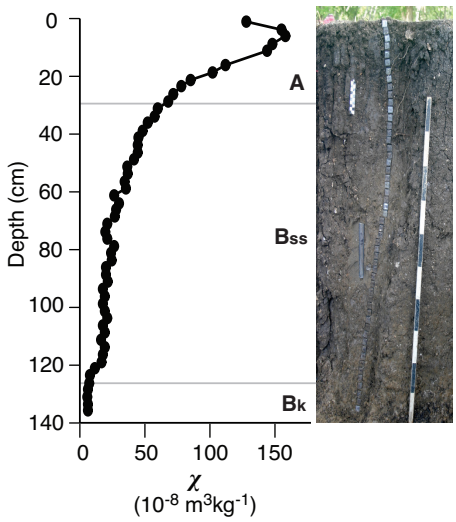

Figure 4.2: Example of a magnetically enhanced alluvial Vertisol from Buttermilk Creek, Texas (*Lindquist et al.*, 2011). Data at left is shown next to an image of the soil profile with sample cubes in place. The increase in magnetic susceptibility of the upper soil horizons relative to the lower horizons is common in many modern soils and is attributed in most cases to the pedogenic production of magnetite and/or maghemite. Magnetic unmixing methods have shown that "pedogenic" magnetite occurs in a variety of modern soils (see Figure 3). Horizons are denoted with grey lines and follow descriptions in (*Lindquist et al.*, 2011). ss denotes presence of slickensides, k denotes the presences of carbonate

precipitate nanocrystalline magnetite (in the SP/SSD size class) upon drying at near neutral pH (*Taylor et al.*, 1987; *Maher and Taylor*, 1988).

This process has been demonstrated to occur abiotically in laboratory settings (*Taylor et al.*, 1987; *Maher and Taylor*, 1988); however, under anoxic conditions the oxidation of organic matter is often coupled to the microbial reduction of Fe(III)-oxides in a process referred to as dissimilatory iron reduction (DIR; for reviews see *Lovley et al.*, 2004; *Lovley*, 2013). The DIR bacterium *Geobacter metallireducins* (formerly strain GS-15) was the first organism discovered that coupled degradation of organic matter (acetate) to the reduction of ferric iron leading to the extracellular precipitation of SP/SSD magnetite *Lovley et al.* (1987). This discovery was coincident with the experimental results of *Taylor et al.* (1987), which along with subsequent studies showed that biotic and abiotic precipitates of magnetite were both similar to natural SP/SSD magnetites (*Maher*

and Taylor, 1988; *Sparks et al.*, 1990). Despite a lack of direct observational evidence, it is now generally assumed that DIR bacteria play an integral role in the pedogenic production of magnetite during wet/dry cycles in well-drained temperate soils (e.g., *Maher et al.*, 2003a; *Guyodo et al.*, 2006; *Maher*, 2007).

Maghemite is commonly present in soils in combination with magnetite. The physical relationship between these two minerals is important to consider. Following the fermentation mechanism, maghemite is interpreted to have formed via the slow oxidation of magnetite (*van Velzen and Dekkers*, 1999; *Chen et al.*, 2005, see section 4.4.1 below for alternative model). The oxidation of magnetite occurs at the rims of individual grains and proceeds inward while oxidizing structural Fe^{2+} slowly diffuses out of the crystal structure. Oxidation of magnetite commonly results in partially oxidized magnetite grains that have a maghemitized rim and a magnetite core (*van Velzen and Dekkers*, 1999; *Chen et al.*, 2005; *Ge et al.*, 2014). Partial oxidation of magnetite may produce unusual, yet distinctive hysteresis behavior (e.g., *Ge et al.*, 2014) and may ultimately lead to the complete maghemitization of the original grain.

Ageing pathway of ferrihydrite to hematite

More recently, the slow transformation of ferrihydrite to hematite, during which an intermediate ferrimagnetic phase is produced, has been proposed as an alternative pathway that can lead to magnetic enhancement (*Barrón and Torrent*, 2002; *Barrón et al.*, 2003; *Torrent et al.*, 2006; *Liu et al.*, 2008). Initial experiments showed that phosphate 2-line ferrihydrite ages to hematite in a two-step process where an ordered ferrimagnetic phase, similar to maghemite, is produced as a metastable intermediary (*Barrón and Torrent*, 2002). Subsequent studies referred to the intermediate phase as hydromaghemite (*Barrón et al.*, 2003; *Torrent et al.*, 2006; *Liu et al.*, 2008; *Cabello et al.*, 2009) and ferrimagnetic ferrihydrite (*Michel et al.*, 2010, shown in Figure4.1). Extrapolation of laboratory conditions (transition occurs in the laboratory at $\sim$150 °C under ambient atmosphere) indicates that the timescale for a full transformation of ferrihydrite to hematite would be on the order of 10^5–10^6 years. This transformation is highly dependent on the presence of ligands in the soil to effectively block the direct transformation of ferrihydrite to more thermodynamically favored phases, such as hematite and goethite, at such elevated temperatures (*Liu et al.*, 2010).

Ferrihydrite is often categorized as one of two different types based on the number of distinctive X−ray diffraction peaks: 2−line and 6−line ferrihydrite. 2−line ferrihydrite is generally considered to represent a less crystalline form of ferrihydrite than 6−line. Ageing of 2−line ferrihydrite at ∼150 °C in open air results in the production of hematite with the characteristic magnetic intermediate phase being produced (*Barrón and Torrent*, 2002). However, ageing of 6−line ferrihydrite (∼175 °C) undergoes a direct transformation to hematite or goethite without a magnetic intermediate phase (*Barrón et al.*, 2003). Tetrahedrally coordinated iron is thought to be present in 2−line, but not 6−line, ferrihydrite and maghemite (see *Michel et al.*, 2007; *Janney et al.*, 2000), and this has been suggested as a reason why only 2−line ferrihydrite ages into a transient maghemite-like intermediary (*Barrón et al.*, 2003; *Liu et al.*, 2010, see Figure 4.1). However, recent work has reported the presence of tetrahedrally coordinated Fe(III) in 6−line ferrihydrite, which appears to have antiferromagnetic spin coupling between tetrahedral and octahedral sublattices (*Guyodo et al.*, 2012). The crystallographic complexities in ferrihydrite highlight the likelihood that transformations of iron oxides in soils are more complex than controlled laboratory experiments.

An important gap in this ageing model is that there is no pathway for the production of magnetite, which is a common pedogenic mineral that causes magnetic enhancement in modern soils. However, it does not appear to be necessary that these two pathways (fermentation and ageing) be exclusive. There is no necessity for anoxic conditions in the ferrihydrite ageing mechanism, so it may be the case that during prolonged dry seasons magnetic mineral production is associated primarily with ferrihydrite ageing while rainy season conditions favor a fermentation model.

4.4.2 Goethite and Hematite formation and distribution

Transformations of less crystalline iron oxides, like ferrihydrite, directly to goethite and hematite are common in soils and are dependent on the soil conditions. In general, goethite is favored in cool, moist soils that only rarely experience prolonged intervals of aridity. By contrast, hematite is more abundant in subtropical, Mediterranean, or tropical soils with frequent episodes of prolonged dryness (*Kampf and Schwertmann*, 1983; *Schwertmann*, 1988; *Cornell and Schwertmann*, 2003). Soils with near neutral pH and low organic content tend to favor hematite over goethite, and vice-versa (*Schwertmann*

and Murad, 1983; *Das et al.*, 2011).

Transformations between the more crystalline iron oxides are also possible, and likely occur in soils over a range of timescales. Goethite dehydroxylates to hematite when heated in ambient air in the laboratory and converts to magnetite when heating occurs in reductive conditions (*Till et al.*, 2015). Hematite can also form simply as the ultimate product of the slow oxidation of magnetite (first to maghemite and then to hematite) via structural rearrangements (*Cornell and Schwertmann*, 2003). Transformations between iron oxides in soils after burial and disconnection with prevailing climatic conditions may be a serious source of error in any proxy method relating iron oxide minerals with precipitation, and this is discussed in more detail below. However, despite complexities in the transformational pathways described in laboratory experiments, the predominance of goethite and/or hematite in modern soils in specific environmental conditions suggests that climate does play a profound role in the iron mineralogy of soils (e.g., *Kampf and Schwertmann*, 1983).

4.5 Characterizing iron oxide mineral assemblages

Below we discuss the environmental magnetic parameters that have been utilized in previous work to characterize magnetic mineral assemblages with the aim of determining emperical relationships with precipitation. Some additional environmental magnetic methods and parameters are described in the appendix (§A) and may be of interest to readers seeking further detail.

4.5.1 Frequency dependence of susceptibility

The frequency dependence of magnetic susceptibility (χ_{fd}) is a measure of the contribution of SP sized grains to the mass normalized magnetic susceptibility (χ, m^3kg^{-1}) of a specimen (*Dearing et al.*, 1996b). Nearly all SP grains can become dynamically aligned with an alternating magnetic field ($< \sim 1 \times 10^4$ Am^{-1}) of low frequency (e.g., 465 Hz). The relaxation time of SP grains (τ, defined as the time for the magnetization of an ensamble of grains to decay to 1/e of its original value following Néel's equation; see *Dunlop and Özdemir*, 2001) is typically much shorter than the period of the weak alternating magnetic field (AF) used during measurement of susceptibility, and thus the

magnetizations of these grains will contribute strongly to the measured magnetic susceptibility (χ_{465Hz}; *Thompson and Oldfield*, 1986; *Dearing et al.*, 1996b; *Maher*, 2007). However, at higher frequencies (e.g., 4650 Hz) the relaxation time of SP grains near the threshold for SP/SSD behavior is longer than the period of the AF. Accordingly, these grains are unable to fully align with the AF and their magnetization is out-of-phase with the alternating field. At such high frequencies these grains are no longer able to contribute as much to the measured magnetic susceptibility (χ_{4650Hz}). Thus, specimens enriched in SP grains will display an inverse relationship between susceptibility and AF frequency. It is important to note that SSD and MD grains do not fully track the alternating current at either low or high frequency, and so their contribution to χ remains constant at variable frequency (*Dearing et al.*, 1996b). Although we note, as an aside, that MD grains tend to show a variable χ response to the amplitude of the AF (*Jackson et al.*, 1998).

It is conventional to report χ_{fd} as a percentage, where:

$$\chi_{fd} = [(\chi_{465Hz}\chi_{4650Hz})/\chi_{465Hz}] \times 100 \tag{4.1}$$

Diamagnetic, paramagnetic, and non-saturated high-coercivity ferromagnetic minerals contribute equally to susceptibility regardless of frequency. Accordingly, the contribution of paramagnetic and diamagnetic minerals is removed from numerator, but not the denominator, when χ_{fd} is calculated according to Equation 4.1. It is more appropriate to calculate the frequency dependence of susceptibility using the ferrimagnetic susceptibility (χ_{ferri}; defined in §A.3) in the denominator (e.g., $\chi_{fd} = [(\chi_{465Hz}\chi_{4650Hz})/(\chi_{465Hz} - \chi_{ferri})] \times 100$) so that the contribution of paramagnetic and diamagnetic minerals is removed in all cases. This is rarely done in practice and in many cases would only have a minimal impact on calculated values due to the low χ_{lf} values associated with diamagnetic and paramagnetic material. Although, we wish to emphasize the importance using χ_{ferri} in clay rich soils, where the contribution of paramagnetic minerals to susceptibility may be dominant (*Dearing et al.*, 1996b; *Yamazaki and Ioka*, 1997; *Jordanova and Jordanova*, 1999).

The low and high frequency values of 465 Hz and 4650 Hz are not specific to the calculation of frequency dependence of magnetic susceptibility; nor is the specific form of Equation 4.1, for example some researchers simply report the difference between the

low and high frequency values, rather than normalize it (*Thompson and Oldfield*, 1986). These frequencies simply represent the factory settings included on the most commonly used commercial susceptibility meter in environmental magnetism labs around the world (the Bartington 2). However, regardless of the exact frequency values used, it is important to include instrument details, such as the frequency and amplitude of magnetic field, in published studies so that future workers may be able to reproduce the measurements.

In general, χ_{fd} percentages greater than ∼6% indicate a considerable abundance of SP ferrimagnetic particles, while maximum observed values of ∼15% indicate a specimen whose susceptibility is dominated by SP ferrimagnets (*Dearing et al.*, 1996b). Studies of modern soils and loessic paleosols routinely use χ_{fd} as an indicator of SP ferrimagnets; however, this method cannot by itself distinguish the composition of the magnetic minerals in the specimen (e.g., magnetite vs. maghemite). However, magnetic paleoprecipitation proxies routinely use χ, χ_{fd}, and the susceptibility of ARM (χ_{ARM}; see §A.3) as indirect measures of ferrimagnetic mineral abundance.

4.5.2 HIRM

The remanence held by "hard" magnetic minerals (goethite and hematite) within sediments has been estimated by the "hard" IRM, or $HIRM$ for decades (*Robinson*, 1986). $HIRM$ is typically defined as half of the difference in saturation and non-saturation IRM (e.g., $HIRM = 0.5 * SIRM + IRM_{-300mT}$; *Robinson*, 1986), where a backfield IRM (typically on the order of $\sim 100-300$ mT) is applied following saturation in the opposite direction. The origination of $HIRM$ was based on the longstanding observation that above ∼300 mT isothermal remanence is held primarily by hematite and/or goethite (*Collinson*, 1968). Increasing values of $HIRM$ are interpreted to represent greater contributions of hard antiferromagnetic minerals to remanence.

Care needs to be taken in interpretations of soil $HIRM$ for a number of reasons. First, $HIRM$ is a remanence parameter, which means zero representation is given to SP grains and grains whose remanence state is a non-uniformly magnetized configuration will be underrepresented (e.g., pseudo-single domain, PSD, and multi-domain, MD, grains; see §A.2). Second, $HIRM$ is often calculated using 'saturating' fields of ∼1 T, which is too low to be a true saturating field for antiferromagnetic minerals (see section

4.3.2 above). Finally, an implicit assumption in $HIRM$ is that all antiferromagnetic minerals acquire only minimal remanence in fields < 300 mT, while the ferrimagnetic minerals stop acquiring additional remanence in fields > 300 mT (or some other intermediate field of choice). However, maghemite and partially oxidized magnetite can continue to acquire remanence in fields > 300 mT (*Liu et al.*, 2002) and nanometer-scale or aluminous hematite can have widely variable B_c (*Liu et al.*, 2007a; *Özdemir and Dunlop*, 2014). For these reasons, we stress that $HIRM$ values be evaluated with some caution and that additional parameters be used to aid in the interpretation of $HIRM$ data (e.g., *Liu et al.*, 2002, see the appendix (§A.4) for more detail).

4.5.3 Unmixing magnetic mineral mineral components

Natural sediments represent a complex assemblage of magnetic minerals that vary in composition and magnetic grain size due to environmental or geological processes that promote iron oxide formation, dissolution, or transformation. In order to investigate these processes, it is often necessary to magnetically "unmix" sediments in order to identify the relative contributions from various individual magnetic mineral components (*Robertson and France*, 1994; *Stockhausen*, 1998; *Kruiver et al.*, 2001; *Heslop et al.*, 2002; *Egli*, 2003, 2004a,b; *Heslop et al.*, 2004; *Geiss and Zanner*, 2006; *Heslop and Dillon*, 2007; *Heslop*, 2015).

In the simplest sense, the intensity of remanence (IRM or ARM) is a reflection of remanence carried by SSD and MD grains. For example, take the following expressions for IRM and ARM (*Geiss and Zanner*, 2006):

$$IRM = IRM_{SSD} + IRM_{MD} = M_s \alpha_{ISD} f_{SSD} + M_s \alpha_{IMD} (1 - f_{SSD}) \tag{4.2}$$

$$ARM = ARM_{SSD} + ARM_{MD} = M_s \alpha_{ASD} f_{SSD} + M_s \alpha_{AMD} (1 - f_{SSD}) \tag{4.3}$$

where IRM_{SSD}, IRM_{MD} and their ARM equivalents are the SSD and MD components of IRM or ARM, M_s is the saturation magnetization described in §A.3, f_{SSD} is the volumetric fraction of SSD particles (ranging from $0-1$), and the α terms describe the acquisition efficiency of SSD and MD domain grains for IRM (α_{ISD} and α_{IMD}) and ARM (α_{ASD} and α_{AMD}). The α terms are generally unknown but can be approximated

based on theoretical and empirical arguments. Setting (eq.4.2) equal to (eq. 4.3) yields a solvable expression for f_{SSD} that can be thought of as representing the "pedogenic" component of remanence (f_{ped}), because SSD magnetic minerals are often associated as byproducts of pedogenic processes (section 4.4; *Geiss and Zanner*, 2006).

In many instances it is desirable to isolate the relative magnetic contribution of individual magnetic mineral phases (e.g., magnetite, hematite, etc.) within a specimen at a finer detail than simply SSD versus MD grains. *Robertson and France* (1994) proposed that because the shape of an IRM acquisition curve for a monomineralic specimen often resembles a cumulative log-Gaussian (CLG) function it may be possible to approximate a specimen's IRM acquisition curve given three parameters: the mean coercivity (B_h), a dispersion parameter (D_p, equivalent to one standard deviation in log space), and the inferred saturation IRM (M_r; see Figure 4.3). If there is more than one magnetic mineral phase contributing to the measured IRM acquisition, *Robertson and France* (1994) suggested that each magnetic component could be represented by individual CLG functions where the parameters (B_h, D_p, and M_r) would be informative about their respective mineral phase.

If it assumed that any interaction between magnetic mineral grains is negligible, then a simple linear combination of these component CLG function would create a modeled IRM acquisition curve that could be compared against observations (*Robertson and France*, 1994). Subsequent work built on these concepts and began to use log-Gaussian probability density functions to model coercivity spectra (the absolute value of the first derivative of a magnetization curve, e.g., IRM or ARM acquisition or demagnetization curves and backfield curves; see Figure 4.3 *Stockhausen*, 1998; *Kruiver et al.*, 2001; *Heslop et al.*, 2002). Coercivity distributions represent the individual coercivities of all particles contained within a specimen. Models that approximate coercivity distributions for a natural specimen by linear combinations of component distributions assume that individual magnetic components represent a specific subset of magnetic minerals that are similar in composition, degree of crystallinity, grain size, grain shape, and concentration of defects (*Egli*, 2003).

Despite the wide use of log-Gaussian functions in modeling natural coercivity spectra, it was noted by *Robertson and France* (1994) and confirmed by subsequent studies (e.g., *Egli*, 2004a; *Heslop et al.*, 2004) that many populations of magnetic mineral

grains produce coercivity distributions that deviate from pure log-Gaussian behavior. The distribution of coercivities within a magnetic mineral assemblage can diverge from normality for a number of reasons, including: grain size distribution, grain elongation, thermal relaxation, and the initial magnetization state after demagnetization or saturation (see *Egli*, 2004a; *Heslop et al.*, 2004). Importantly, it appears that non-Gaussian behavior is to be expected in natural samples. In order to more accurately account for these deviations, *Egli* (2003) describes an adaption to the generalized Gaussian function (skewed generalized Gaussian, SGG) that incorporates both skewness and kurtosis. Many natural samples display left-skewed tails (particularly at low fields) that may require two log-Gaussian distributions to fit appropriately (*Egli*, 2004a; *Heslop et al.*, 2004). In contrast, the SGG model of *Egli* (2003) allows for a single component to fit a skewed distribution. For this reason we suggest that methods incorporating skewness be favored over earlier work (*Egli*, 2003; *Heslop et al.*, 2004; *Heslop*, 2015).

Unmixing methods have been applied to a wide range of natural materials, including soils (*Egli*, 2004a; *Geiss et al.*, 2008; *Lindquist et al.*, 2011). Importantly, the main parameters describing the distributions of individual magnetic components (B_h and D_p) are remarkably consistent for soils regardless of the unmixing methods used (see Figure 4.3; *Egli*, 2004b; *Geiss et al.*, 2008). In general, unmixing approaches are used in order to differentiate between various types of soft ferrimagnetic magnetite because field strengths achievable in most laboratories are sufficient to saturate the magnetization of these minerals (usually saturated in fields below ∼300 mT). However, recent work has attempted to use the unmixing methods developed by *Kruiver et al.* (2001) to quantify the abundance of antiferromagnetic minerals in marine sediment cores (*Abrajevitch et al.*, 2009) and soils (*Hyland et al.*, 2015).

4.5.4 Determination of goethite and hematite concentrations

In order to effectively relate precipitation to the abundance of hematite and goethite within a soil it is critical that estimates of mineral abundances are accurate. Due to the large fields required to saturate both goethite and hematite, and their relatively weak magnetizations, it is common to estimate their absolute abundances using non-magnetic methods. The most commonly used techniques are X-Ray diffraction (XRD), diffuse reflectance spectroscopy (DRS; *Balsam et al.*, 2004; *Torrent et al.*, 2007; *Zhang et al.*,

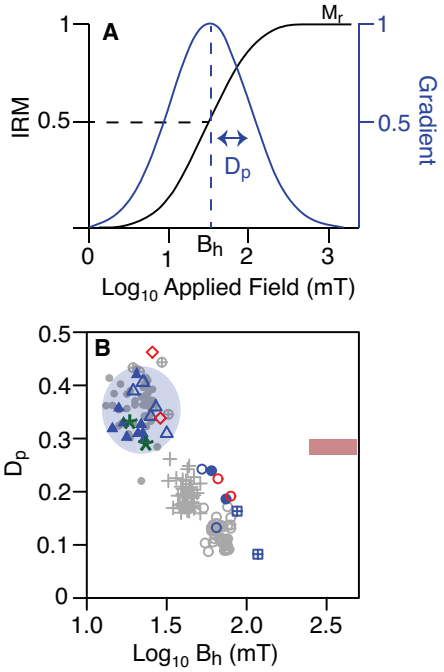

Figure 4.3: **A.** Schematic representation of an IRM acquisition curve (in black) and its first derivative, commonly referred to as a coercivity distribution (in blue). The coercivity distribution can be described by its median coercivity (B_h) and the distribution width (dispersion parameter, D_p). Representation is a simplification of Figure 1 from *Kruiver et al.* (2001) and assumes a log Gaussian probability distribution approximates the coercivity distribution. Note that both the IRM and gradient data are normalized to their respective maximum values. **B.** A biplot of D_p and $\log_{10}$ (B_h) for isolated magnetic components from a mixture of natural sediments. Data taken from *Egli* (2004b), *Geiss and Zanner* (2006), and *Lindquist et al.* (2011). Blue shaded oval highlights the ranges of Dp and Bh observed for pedogenic magnetite in soils. Blue symbols = soils, grey symbols = lake sediments, red symbols = loess, green asterisks = dissimilatory iron reducing (DIR) bacteria produced magnetite (extracellular magnetite). Open triangles = detrital + pedogenic magnetite, closed triangles = pedogenic magnetite, open circles = biogenic hard component, open diamonds = eolian dust, + = biogenic soft magnetite, closed circles = detrital + extracellular magnetite. Red rectangle corresponds to the "hematite" component used by *Abrajevitch et al.* (2009). All magnetic component descriptions follow *Egli* (2004b).

2007; *Lyons et al.*, 2014; *Hu et al.*, 2015), or Mössbauer spectroscopy (e.g., *Carter-Stiglitz et al.*, 2006). Often these methods are more costly in comparison with magnetic

approaches and are only sufficiently sensitive when the iron oxide minerals within a specimen are concentrated using chemical treatments (*Liu et al.*, 2002). Magnetic determinations of hematite and goethite abundance would be advantageous because of their lower analytical costs, their greater sensitivity to iron oxides in low volume abundances, and for their potential to more quickly analyze a greater number of samples. However, despite the increasingly frequent use of magnetic methods (e.g., *Sangode et al.*, 2008; *Abrajevitch et al.*, 2009; *Hao et al.*, 2009; *Morón et al.*, 2013; *Hyland et al.*, 2015) there is no straightforward protocol for accurately estimating the abundance of goethite or hematite by mass or volume from rock magnetic measurements (*Hao et al.*, 2009).

One recent approach estimates the contribution of individual antiferromagnetic minerals to remanence by unmixing high field IRM acquisition curves (e.g., *Abrajevitch et al.*, 2009; *Hyland et al.*, 2015). This approach requires a priori knowledge of what magnetic minerals are present in a set of specimens (which, for example, can be achieved by the heating experiments described in the appendix, §A.5) or an assumption that each of the magnetic components chosen to fit an IRM acquisition curve represents a different magnetic mineral. The M_{rs} value of each magnetic component in theory represents the M_{rs} held by an individual magnetic mineral (*Kruiver et al.*, 2001). In order to convert these values into estimates of mass or volume, it is necessary to normalize the M_{rs} derived from unmixing with a M_{rs} value for a pure standard of hematite or goethite (e.g., *Abrajevitch et al.*, 2009; *Morón et al.*, 2013). There is considerable variability in the M_{rs} values for pure hematite and naturally occurring goethite (Figure 4.4) due to grain size, crystal defects, substitutions, and the field strength used to achieve saturation (*Dekkers*, 1989; *Liu et al.*, 2006; *Özdemir and Dunlop*, 2014). This is particularly true for goethite because of the extreme difficulty in achieving saturation (e.g., *Rochette et al.*, 2005). We stress that care needs to be taken when magnetic measurements are converted into absolute estimates of mineral abundances by mass or volume.

4.6 Magnetic proxies for precipitation

In the mid 1980's researchers first began to recognize that variations in magnetic susceptibility of loess-paleosol sequences on the Chinese Loess Plateau (CLP) correlated well with marine δ^{18}O records of benthic foraminifera (*Heller and Liu*, 1986). This

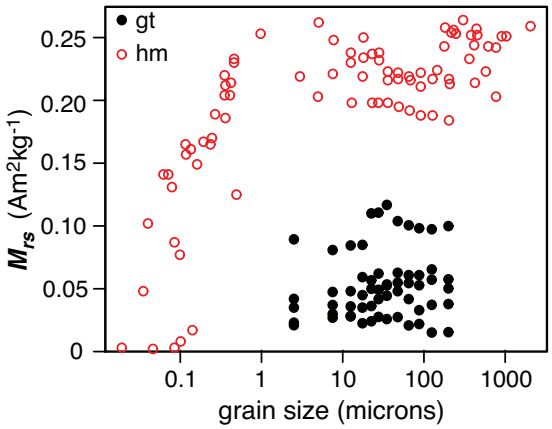

Figure 4.4: Saturation remanence (M_{rs}) values reported in the literature for hematite (hm, shown in red) and goethite (gt, shown in black) shown with respect to grain size. Literature values displayed for hematite come from the compilation in *Özdemir and Dunlop* (2014) and for goethite are shown from *Dekkers* (1989). For goethite data, grain size ranges are reported in *Dekkers* (1989) and we plot data here according to the midpoint of each size class. Note that the M_{rs} values shown here are not necessarily true saturation values due to the large field required to saturate these minerals. The M_{rs} values for goethite were all acquired in a 15 T field (*Dekkers*, 1989). Field strengths corresponding to the reported values of M_{rs} in hematite vary.

discovery sparked interest in using magnetic variations within loessic paleosol sequences to reconstruct climatic changes in central China. Early work aimed to elucidate the relative importance of various processes that might contribute to the observed magnetic variability. The two processes that received the most attention were aeolian dust flux, whose variability was controlled by regional monsoonal climate patterns, and pedogenic processes that intensified with increasing rainfall and temperature (e.g., *Kukla et al.*, 1988; *Maher and Thompson*, 1991, 1992). Since these early studies there has been a tremendous amount of work on loess records in China (see recent review by *Liu et al.*, 2007b) and elsewhere (Alaska, Russia, and Argentina) to explore the relationships between iron oxide mineralogy and climate. Here we focus only on the work that has documented correlation between precipitation and pedogenic magnetic minerals.

4.6.1 Relationships between magnetic enhancement and precipitation in loessic soils

After establishing that χ variations in CLP soils and paleosols were driven by the pedogenic production of SP/SSD magnetite (*Maher and Thompson*, 1991, 1992), quantitative estimates of the relationships between χ and mean annual precipitation (MAP; typically defined as a 30 year average of nearby or interpolated meteorological data) began to arise. *Maher et al.* (1994) introduced the concept of pedogenic susceptibility (χ_{ped}), which is an absolute measure of the difference in χ between a soil's B horizon and its underlying C horizon ($\chi_{ped} = \chi_B - \chi_c$; note that the C horizon is assumed to be equivalent to the parent material). The B horizon is used instead of the A horizon, which in most soils is more magnetically enhanced than the B horizon, in order to avoid the effects of contamination in modern soils and because the A horizon is rarely preserved in paleosols (*Maher et al.*, 1994).

In a preliminary set of modern soils from the CLP (37 soils from 9 locations), χ_{ped} showed strong positive, log-linear correlation with MAP ($R^2 = 0.95$; Figure 4.5) and was used to reconstruct precipitation records back some ∼125 ka (*Maher et al.*, 1994). Correlations between χ and mean annual temperature were also noted (*Maher et al.*, 1994; *Jiamao et al.*, 1996), although far more attention has been given to relationships with precipitation. Subsequent studies (e.g., *Liu et al.*, 1995; *Jiamao et al.*, 1996) observed similar empirical relationships between χ and climate on the CLP and recognized the potential for quantitative estimates of paleoprecipitation from magnetic mineral assemblages preserved within paleosols. The calibration of χ_{ped} with MAP was expanded to include loessic soils from across the Northern Hemisphere (*Maher and Thompson*, 1995), additional CLP soils (*Porter et al.*, 2001), as well as loessic soils in Russia (*Maher et al.*, 2002, 2003a).

However, the addition of more soils from diverse environmental settings introduced considerable scatter to the initial relationship ($n = 115$, $R^2 = 0.52$; see Figure 4.5). More recent work on loessic soils in the U.S. Great Plains shows only weak positive correlation between χ_{ped} and MAP ($R^2 = 0.25$, $n = 72$; *Geiss and Zanner*, 2007, Figure 4.5). A compilation of all available χ_{ped} data for loessic soils displays a similarly weak ($R^2 = 0.24$), but still significant ($p < 0.001$) positive correlation (see Figure 4.5). Despite the statistical significance of these correlations, the relatively low R^2 values that result

from combining regional datasets suggest that global χ_{ped} models are poor predictors of MAP.

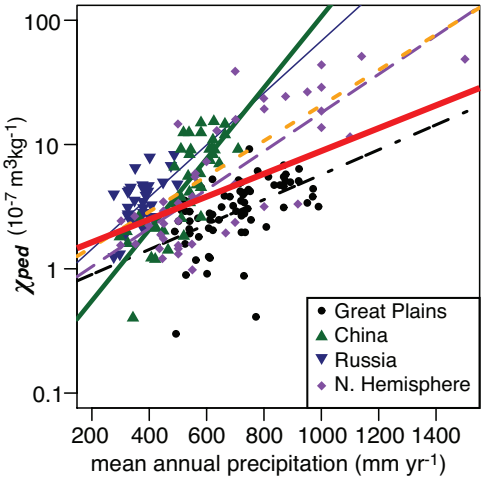

Figure 4.5: Pedogenic susceptibility (χ_{ped}) versus mean annual precipitation. Great Plains data from *Geiss et al.* (2008) and *Geiss and Zanner* (2007), data for China are from *Porter et al.* (2001) and *Maher et al.* (1994), data from Russia from *Maher et al.* (2002) and *Alekseev et al.* (2003), and Northern Hemisphere data compiled in *Maher and Thompson* (1995). All lines represent simple linear regression models. All models were statistically significant ($p < 0.05$). Thin blue line = Russia ($R^2 = 0.35$), double dashed black line = Great Plains ($R^2 = 0.25$), thick green line = China ($R^2 = 0.61$), coarse-dashed purple line = N. Hemisphere ($R^2 = 0.60$), fine-dashed orange line = Russia, China, and N. Hemisphere data combined ($R^2 = 0.52$), thick solid red line = all data ($R^2 = 0.24$).

Additional complications in the interpretation of soil magnetic mineral assemblages were revealed during investigations of loess-paleosol sequences in Alaska ((*Begét et al.*, 1990) and Argentina (*Orgeira et al.*, 1998, 2003), which showed magnetic depletions in paleosols (in contrast to magnetic enhancement). In these settings the role of aeolian dust flux and wind strength was interpreted to outweigh the efficiency of pedogenic enhancement (*Lagroix and Banerjee*, 2002, 2004). Thus, it is important to note that no single model of soil magnetism can explain the magnetic mineral assemblage of all soils. Rather, the variability of local processes (e.g., wind speed, mean annual precipitation and temperature) can lead to different controlling mechanisms for the formation of magnetic minerals in soils, and great care needs to be taken during the interpretation

of soil magnetism records.

The χ_{ped} parameter defined by *Maher et al.* (1994) is an example of an absolute magnetic enhancement parameter that aims to quantify the concentration of pedogenic magnetite and/or maghemite. *Geiss and Zanner* (2007) argue that simple ratios between magnetically enhanced soil horizons relative to their parent materials provide a more direct measure of pedogenic ferrimagnetic mineral production (e.g., χ_{enh}/χ_{parent}). Variations in the physical and chemical properties of the parent material can have a large influence on absolute enhancement parameters (see section 4.7.1). For example, some geologic materials are enriched in iron (e.g., basalts), and thus, the absolute value of pedogenic enhancement for soils developed on these materials may be different than that of soils developed on less iron-rich materials (e.g., limestone). By using relative parameters, such as those proposed by *Geiss and Zanner* (2007), the influence of parent material is normalized. For the U.S. Great Plains, mean annual precipitation rates of loessic soils show stronger correlations with relative enhancement parameters (*Geiss and Zanner*, 2007; *Geiss et al.*, 2008) than with absolute enhancement parameters like χ_{ped}. It is important to note, however, that despite these improved correlations with relative enhancement parameters, there are still regional differences in the relationships between precipitation and magnetic enhancement (*Geiss and Zanner*, 2007). Thus, a precipitation transform function calibrated using data from loessic soils in Russia is not able to accurately reproduce precipitation rates in the U.S. Great Plains. Extraneous variables such as the floral and faunal soil ecology or parent material (amongst others) are likely contributing to the observed regional variation in modern systems. The inability to sufficiently control for these variables in the fossil record poses a serious problem for the application of these methods to ancient systems.

In an effort to directly quantify magnetic enhancement and remove the influence of parent material altogether, *Geiss et al.* (2008) proposed the ratio of χ_{ARM}/IRM as a direct estimate of pedogenic (SSD) magnetite. For the loessic Great Plains soils, this ratio shows strong positive correlation with MAP ($R^2 = 0.70$; Figure 4.6), although data from other areas again highlight regional differences (*Geiss et al.*, 2008). Coercivity unmixing of modern soils has shown that the pedogenic magnetite component appears to be relatively consistent across different continents and environmental conditions (*Egli*, 2004b; *Geiss and Zanner*, 2006; *Geiss et al.*, 2008). Typically, pedogenic

magnetite/maghemite assemblages in modern soils have a B_h of ∼20 mT and a D_p of ∼0.3 ($\log_{10}$ scale; see shaded blue area in Figure 3; *Egli*, 2004b; *Geiss et al.*, 2008). Using coercivity unmixing to directly characterize the abundance of pedogenic magnetite in an individual specimen, rather than comparing an enhanced specimen to an unaltered parent material has major advantages over traditional approaches. If future work is able to describe pedogenic magnetite in more modern soils, across a range of soil types and climates, it may become possible to identify additional empirical relationships that exist solely between pedogenic magnetite and MAP or soil moisture. Ultimately, such approaches would render magnetic characterization of the parent material unnecessary (*Geiss et al.*, 2008) but may prove challenging to develop.

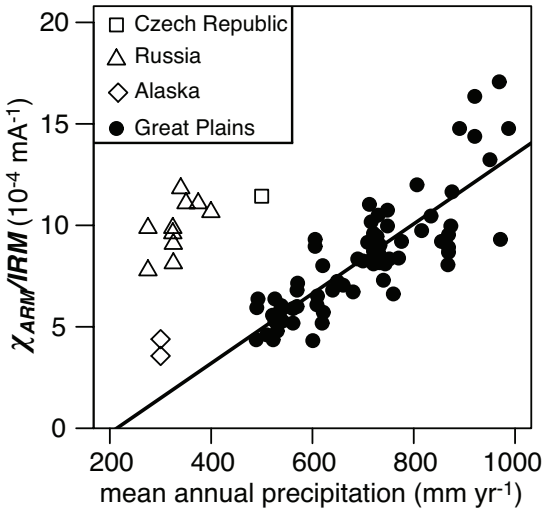

Figure 4.6: Correlation between MAP and χ_{ARM}/IRM for an assemblage of modern loessic soils. Simple linear regression through the Great Plains data has an $R^2 = 0.70$ (data from *Geiss et al.*, 2008). However, data from other locations highlight that regional variation exists in this relationship, which inhibits the predictive power of this relationship in ancient systems. Czech Republic data from *Oches and Banerjee* (1996), Russian data from *Alekseev et al.* (2003), and Alaska data from *Sharpe* (1996).

A complicating factor in the relationship between MAP and magnetic enhancement in loessic soils is variation in soil moisture, which ultimately controls the chemical reactions that form or dissolve magnetic minerals in soil, that is not captured by changes in

MAP (e.g., *Porter et al.*, 2001; *Orgeira et al.*, 2011). For example, in two systems receiving equivalent MAP but with different temperatures and vegetation there is likely to be variation in soil moisture that will drive changes in the magnetic mineralogy. *Orgeira et al.* (2011) describe the *magnetic enhancement proxy* (MEP), which is a quantitative model based on physical principles that describes magnetic mineral production (magnetite and maghemite) with respect to soil moisture. The MEP model relates the soil moisture ratio (W), defined as the ratio of MAP to potential evapotranspiration (PET), with ferrimagnetic mineral production (p). The MEP model assumes that magnetite forms according to the fermentation mechanism (described in section 4.4.1) where wet-dry cycles in soils are critical in maintaining the balance of ferrimagnetic mineral production and dissolution (see *Orgeira et al.*, 2011, for details). Their model can more accurately describe variations in magnetic enhancement observed in loessic, and some non-loessic, soils from various geographical regions, which suggests that regional variations in the MAP magnetic enhancement correlations may be due more to deviations in soil moisture with respect to MAP than to variable regional processes that form magnetic minerals (*Orgeira et al.*, 2011).

The MEP model successfully reproduces magnetic enhancements in many modern environments, although one of its limitations is that it relies on parameters that are difficult to extend to the past and that inhibit its use as a paleoenvironmental tool. The difficulty in applying the MEP model to ancient systems underscores the fact that many of our existing environmental magnetic tools for understanding past climate are based on overly simple variables that do not take into account natural processes that are known to influence the magnetic properties of modern soils. Future work should aim to develop new methods that incorporate aspects of the MEP, like the focus given to soil moisture, while remaining simple enough to allow for application to fossil systems.

All of the magnetic methods discussed to this point have been calibrated using modern soils, where magnetic enhancement is controlled by the pedogenic production of magnetite and/ maghemite. MAP ranges for these calibrations are generally limited to temperate conditions between ~200 1000 mm yr^{-1}. Rates of pedogenesis are likely to be too slow to generate magnetic enhancement in climates where the MAP is less than 200 mm yr^{-1}. Conversely, in humid climates where MAP exceeds ~1000 mm yr^{-1}, it is observed that positive correlations between MAP and magnetic enhancement

parameters either flatten (e.g., *Maher and Thompson*, 1995) or become negative (e.g., *Balsam et al.*, 2011; *Long et al.*, 2011). This non-linear response is attributed to the increased dissolution of iron oxides and leaching that persists in water-saturated soils with only limited dry periods *Maher* (2011). The calibration range for magnetic paleoprecipitation proxies poses an important problem in the fossil record where MAP exceeded ∼1000 mm yr^{-1}. This problem is not unique to magnetic methods and also limits geochemically-based paleoprecipitation proxies for paleosols.

4.6.2 Relationships between precipitation and abundances of goethite and hematite

Goethite and hematite are more abundant (by volume and mass) in modern soils than magnetite and maghemite, and are also thought to be more stable and resistant to reductive dissolution. Further, as mentioned in section 4.4.2, there is a well-documented, general relationship between goethite and hematite and climate, where hematite is generally thought to occur in warmer drier conditions, while goethite is thought to occur in cooler wetter environments (*Kampf and Schwertmann*, 1983). There have been a number of recent studies that have proposed precipitation proxies that include, either directly or indirectly, information about the abundance of goethite and hematite (*Balsam et al.*, 2004; *Torrent et al.*, 2007, 2010a,b; *Long et al.*, 2011; *Liu et al.*, 2013; *Hyland et al.*, 2015).

Qualitative interpretations of paleoprecipitation changes are often inferred using variable abundances of goethite with respect to hematite. For example, *Balsam et al.* (2004) used DRS-based estimates of goethite and hematite abundances to study climatic variations on the CLP dating back some 2.6 Ma. *Sangode and Bloemendal* (2004) used goethite-to-hematite ratios, estimated using $IRM_{4-3T}/IRM_{1-0.5T}$ (where remanence acquired between fields of between 4 and 3 T is attributed to goethite and between 1 and 0.5 T is attributed to hematite), to reconstruct the soil hydration state of Pliocene-Pleistocene paleosols of the Siwalik Group from the Himalaya, India. Later studies from modern soils in Spain highlighted the relationship between hematite (derived from DRS) and χ_{fd} and suggested that precipitation reconstructions should be based on proxies such as the hematite−to−χ_{fd} ratio or a ratio of hematite to goethite (*Torrent et al.*, 2007, 2010a,b).

A promising study of 10 modern soils in China spanning ∼300−1000 mm yr^{-1} MAP shows a strong, positive correlation with $\chi_{fd}/HIRM$ of the A/B horizons ($R^2 = 0.92$; *Liu et al.*, 2013). In theory, this relationship represents the partitioning of iron between hard magnetic phases such as goethite and hematite (as represented by $HIRM$) and SP ferrimagnets (represented by χ_{fd}) during pedogenesis. Higher values correspond to a greater iron allocation to magnetite and/or maghemite as MAP increases up to ∼1000 mm yr^{-1}. The $\chi_{fd}/HIRM$ ratio is calculated as the slope of a bivariate plot of χ_{fd} versus $HIRM$ (where the "background" values for each parameter are subtracted from the data) for the entire B horizon, which removes the need to construct an enhancement ratio or to select an "enhanced" sample from the B horizon alone (*Liu et al.*, 2013).

Other recent studies have presented encouraging new magnetic paleoprecipitation proxies that relate MAP to the ratio of goethite-to-hematite (Gt/Hm) in modern soils distributed globally (*Hyland et al.*, 2015) and for a climosequence in South China (*Long et al.*, 2011). Methods relating Gt/Hm to MAP are particularly desirable because this ratio appears to be sensitive to a wide range of MAP (200 − 3000 mm yr^{-1}; *Hyland et al.*, 2015) and goethite and hematite are likely to be stable iron oxide minerals over geologically relevant timescales. *Hyland et al.* (2015) report Gt/Hm ratios for the B horizon of 70 modern soils that have a remarkably strong correlation with MAP ($R^2 = 0.96$; Figure 4.7). *Long et al.* (2011) also report a strong correlation between the ratio of hematite-to-goethite and MAP within soil B horizons ($R^2 = 0.64$; Layer II in *Long et al.*, 2011, taken as equivalent to B horizon; Figure 4.7). These new correlations demonstrate the great potential that Gt/Hm based magnetic paleoprecipitation proxies may hold for application in the fossil record.

Although Gt/Hm paleoprecipitation proxies hold considerable potential for advancing paleoclimate studies, we note a number of problems inherent in the analytical approach taken by *Hyland et al.* (2015). *Hyland et al.* (2015) assign mineral abundances to goethite and hematite using remanence unmixing methods developed by *Kruiver et al.* (2001). This approach is problematic for two reasons. First, minor amounts of cation substitution (usually Al) into goethite or hematite can dramatically alter the coercivities of these minerals *Liu et al.* (2006); *Roberts et al.* (2006), and thus, the magnetic components identified using these proxies may not in fact accurately represent the true concentrations of goethite and hematite present in a specimen. Second, the

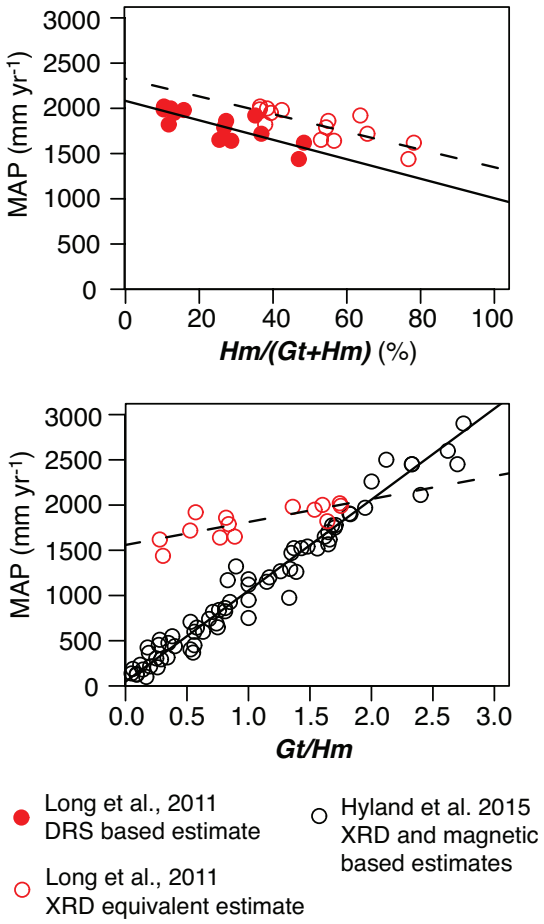

Figure 4.7: Correlations between goethite and hematite abundances in modern soils with MAP. **A.)** Data shown in closed red symbols are from *Long et al.* (2011) from modern soils in South China and are derived using a DRS-based calibration between hematite and goethite weight percent and redness (see *Long et al.*, 2011, for details). Open red symbols are corrected using the relationship described by *Long et al.* (2011) between DRS and XRD based estimates (see Figure 2 in *Long et al.*, 2011). **B.)** Black open circles show data from *Hyland et al.* (2015) for 70 modern soils with a global distribution. Methods used to derive data are a mixture of magnetic and XRD based approaches. The XRD-equivalent estimates from *Long et al.* (2011) have been transformed to the Gt/Hm ratio for comparison purposes. Note that only Layer II data is shown (approximated as B horizon).

proxies are only sensitive to a fraction of the goethite present in a specimen. Unusually high fields (as much as $>$ 57 T; *Rochette et al.*, 2005) are required to fully saturate

goethite, whereas most paleomagnetic labs are only able to generate impulse fields of ∼5 T. Thus, the highest coercivity fractions of goethite are unlikely to be included in Gt/Hm paleoprecipitation estimates or the calibrations that underlie the method. Further, soils frequently contain significant concentrations of goethite and hematite in superparamagnetic grain sizes (*Maher*, 1998; *Guyodo et al.*, 2006; *Till et al.*, 2015). By definition, these grains are unable to retain remanence and would be invisible to existing Gt/Hm paleoprecipitation proxies. The calibration presented by *Hyland et al.* (2015) contains data from the literature derived mostly from XRD-based ratios, but also from magnetism-based ratios. The authors report equivalence (a nearly 1:1 relationship) between these non-magnetic and magnetic methods for 5 modern soils; however, methods based on the coercivity distributions of magnetic remanence are not sensitive to the entire magnetic mineral assemblage in a soil, and hence, should not show equivalence with Gt/Hm estimates derived from X-ray diffraction (e.g., *Hao et al.*, 2009).

A final concern regarding these methods is the poor correlation that the two data sets show when combined (Figure 4.7). The data from *Long et al.* (2011) are derived from DRS based goethite and hematite abundances. Previous work has shown that DRS methods do not agree well with magnetic-based approaches to quantify antiferromagnetic abundance (*Hao et al.*, 2009). However, even after correcting the DRS estimates to be equivalent to XRD based estimates (using a relationship provided in *Long et al.*, 2011, see their Figure 2), there is still a dramatic disagreement in calibrations. The calibration of *Hyland et al.* (2015) is far more sensitive to variation in MAP and will produce vastly different estimates of MAP than the *Long et al.* (2011) model for the same abundances of goethite and hematite, which should be cause for concern. Some of these discrepancies may be due to local or regional-scale processes that complicate this relationship as observed in calibrations for magnetic enhancement in loessic soils (e.g., *Geiss et al.*, 2008; *Maher and Thompson*, 1995) or to variations in soil moisture that are not related to precipitation (e.g., *Orgeira et al.*, 2011). However, the scale of differences between the existing Gt/Hm paleoprecipitation proxies is much greater than the regional differences observed with magnetic proxies based on pedogenic enhancement of magnetite and maghemite. We highlight these variations as examples of complications that can arise when non-uniform methods are used for estimates of goethite and hematite abundances.

4.6.3 Recognizing error in magnetic paleoprecipitation proxies

The goal of developing suitable magnetic paleoprecipitation proxies is ultimately to use these methods to make quantitative estimates of MAP in the geologic past. It is critical that any proxy-based estimation of MAP is reported with a realistic uncertainty. Recent discussions in the literature about how best to calculate uncertainties for magnetic paleoprecipitation proxies for loessic soils show that susceptibility-based paleoprecipitation estimates have large uncertainties (e.g., *Heslop and Roberts*, 2013; *Maher and Possolo*, 2013). The uncertainties in recent Gt/Hm paleoproxies have yet to be critically evaluated (e.g., *Long et al.*, 2011; *Liu et al.*, 2013; *Hyland et al.*, 2015). Considering the ambiguities associated with estimating the abundance of these minerals using magnetic methods, and the complexities in the pedogenic formation of these minerals, a responsible appraisal of the uncertainty in these methods should be a theme for future research.

4.7 Physical, chemical, and biological complications

4.7.1 Physical

Three physical factors play an important role in soil formation (*Jenny*, 1941) and may confound relationships between precipitation and iron oxide mineralogy: (1) duration of pedogenesis, (2) parent material, and (3) topography/soil drainage.

An important assumption for magnetic paleoprecipitation proxies is that soils reach a quasi-equilibrium state with respect to ferrimagnetic and/or antiferromagnetic mineral production (*Thompson and Maher*, 1995; *Orgeira et al.*, 2011). In other words, we assume that the relative abundance of iron oxide minerals does not change after some equilibrium state has been reached within a soil, regardless of the duration of pedogenesis. For instance, alternating redox oscillations under wet/dry cycles promotes both the precipitation of new magnetite as well as the dissolution of preexisting magnetite or maghemite. If these paleoprecipitation proxies are to be useful in reconstructing environmental conditions on timescales of centuries, then the competition between precipitation and dissolution must reach steady state equilibrium on timescales of decades to centuries.

The influence of time on the magnetic properties of soils remains poorly constrained. Studies of soil chronosequences in northern California have shown that the duration of pedogenesis has a strong correlation with soil magnetism and that soils younger than ∼40 ka display only minimal magnetic enhancement (*Fine et al.*, 1989; *Singer et al.*, 1992). This is supported by Holocene soils in the Wind River Range, Wyoming (*Quinton et al.*, 2011) and the Chinese Loess Plateau (*Vidic et al.*, 2004). However, others have argued that such soils have not yet attained equilibrium and that soil age is not the primary control on a soil's magnetic properties (e.g., *Maher et al.*, 2003b). This line of reasoning is supported by observations of significant magnetic enhancement in loessic soils in the Great Plains that formed since the retreat of the last glaciation (∼15 ka; *Geiss et al.*, 2004; *Geiss and Zanner*, 2007). Observations of soils and paleosols within the Chinese Loess Plateau also support this interpretation (compare *Vidic et al.*, 2004; *Maher and Hu*, 2006). A study of alluvial vertisols in Texas documented magnetic enhancement that developed over the course of centuries (Figure 4.2; *Lindquist et al.*, 2011). However, recent observations of magnetism in alluvial soils developed on differently aged river terraces along the Delaware River Valley suggest that time does influence magnetic mineralogy in this system (*Stinchcomb and Peppe*, 2014).

These observations do not exclude the effects of time on the development of magnetic enhancement within soils, but rather suggest that the rate of magnetic enhancement in any given region is a reflection of several interconnected environmental conditions, including MAP, temperature, seasonality of precipitation, parent material, topography, and time. Thus, soils in each landscape will require their own characteristic time to equilibrate their magnetic mineral assemblages. Such regionally variable rates of magnetic enhancement are a concern for researchers aiming to reconstruct precipitation rates from paleosols whose pedogenic equilibration rates are unknown.

The iron content of a soil's parent material is likely to be a major control on the amount of iron that is supplied to the soil solution during weathering reactions and pedogenesis. Studies using a large dataset of χ and χ_{fd} measurements in topsoil (upper 15 cm) across England and Wales have suggested that parent material is the primary control of bulk χ_{fd} in the soils of this region (*Dearing et al.*, 1996a; *Blundell et al.*, 2009; *Boyle et al.*, 2010). This is consistent with soils from across Austria where parent material is important in determining the amount of ferrimagnetic mineral production via

pedogenesis (*Hanesch and Scholger*, 2005). However, (*Orgeira et al.*, 2011) argue that the wt% iron that is present within soils in ferrimagnetic minerals is so small (generally <0.1 wt%) in comparison to total iron content (∼2−5 wt%) that it is unlikely that a supply of iron is a limiting factor in their formation, at least in loess derived soils (see also *Maher*, 1998). Instead, it is more likely that ferrimagnetic mineral formation is more closely linked to environmental factors like soil moisture (*Maher*, 1998; *Orgeira et al.*, 2011). Although, total iron content may be more important for magnetic minerals that occur in greater abundance (hematite and goethite) and future work should continue to treat parent material as a potential complication in magnetic paleopreciptiation proxies.

Topography and soil drainage are two factors that might have considerable control on soil moisture, and ultimately the formation and transformation of magnetic minerals. Topography and drainage, as well as duration of pedogenesis, were factors identified as secondary controls on χ_{fd} in the dataset of English topsoil (*Blundell et al.*, 2009; *Boyle et al.*, 2010). Well-drained soils have higher χ_{fd}, while more poorly drained (or 'gleyed') soils have characteristically low χ_{fd} (*Dearing et al.*, 1996a; *Blundell et al.*, 2009; *Lu et al.*, 2012). This is consistent with nearly all other studies to our knowledge that document magnetic enhancement. In fine-grained (clay rich) soil sequences, χ increases as you proceed downhill (*de Jong et al.*, 1998); this pattern is reversed in soil with grain sizes dominated by coarser sands (higher χ at hilltops; *de Jong et al.*, 2000; *Blundell et al.*, 2009). Given these patterns, it is advisable that calibrations linking magnetic mineral assemblages to climate variables be based exclusively on soils that are well-drained and located within uniform topography. In turn, application of these proxy calibrations must be applied in the fossil record only when independent evidence exists to support similar conditions of drainage and topography at the time of soil formation.

4.7.2 Chemical

The chemical conditions in a soil environment influence the abiotic and biotic processes that initiate the precipitation, dissolution, and transformation of various iron oxide mineral phases. These factors include soil pH, isomorphic substitutions and ion adsorption, abundance of soil organic matter, and the concentration of molecular oxygen.

The combination of pH and oxygenation of pore spaces and fluids within a soil are two main controls on the solubility of ferrous and ferric iron. Ferric iron (Fe^{3+}) is only

soluble in acidic soils (pH $< \sim$3). In near neutral pH ranges, common in most soils, Fe^{3+} ions in solution will rapidly undergo hydrolysis to form poorly crystalline ferric iron hydroxides and ferrihydrite if the soil conditions are oxic (*Colombo et al.*, 2013). In contrast to ferric iron, ferrous iron (Fe^{2+}) is much more soluble in soils with near neutral pH. However, if the soil solution at these pH levels is also oxygenated the Fe^{2+} ions will rapidly oxidize to Fe^{3+} and initiate mineral precipitation.

Isomorphic substitution is common in natural iron oxides. The most common ion that substitutes into Fe(III)-oxides is Al^{3+} because of its abundance in the soil environment, its similar valence state to Fe^{3+}, and its tendency towards octahedral site occupancy (*Cornell and Schwertmann*, 2003; *Essington*, 2004). Aluminum for iron substitution generally does not cause changes in structural charge, indicating that the reactivity of various iron oxides is likely to be dominated by surface area and structural vacancies (*Essington*, 2004). However, aluminum substitution does impact the magnetic properties of iron oxides, particularly goethite and hematite as discussed above (*Murad*, 1988, see section 4.3). Importantly, pedogenic magnetite and maghemite are often substitution free, indicating direct in-situ formation rather than transformation from other commonly substituted iron oxides (*Maher and Taylor*, 1988).

Organic matter inhibits the formation of more crystalline iron oxide phases. Soils with high organic matter content tend to have more abundant iron-organic complexes and ferrihydrites. These soils require longer durations to attain equilibrium between ambient climate conditions and stable oxide phases, and are likely not as useful for magnetic paleoprecipitation proxies. For example, Histosols (wetland soils) have the highest average soil organic matter content of any soil order, and consistently display low χ (*Dearing et al.*, 1996a; *Blundell et al.*, 2009; *Lu et al.*, 2012). These low χ values are likely due to a combination of reductive dissolution of preexisting stable iron oxide phases, the inhibition of ferrihydrite transformation to more stable phases by soil organic matter, and simply dilution due to the abundance of non-magnetic organic material.

4.7.3 Biological

Microbes play an integral role in the redox cycling of iron across a diverse range of natural settings, including soils (*Colombo et al.*, 2013). Similar to abiotic reactions, biological processes are sensitive to soil conditions such as pH and dissolved oxygen

content. Therefore, in a broad sense, physio-chemical soil conditions are the overriding control on both biotic and abiotic processes that control iron oxide mineral speciation.

As previously noted, dissimilatory iron reducing bacteria (DIRB) couple the oxidation of organic matter with the reduction of ferrous oxide minerals for metabolic energy gain (see reviews by *Lovley et al.*, 2004; *Lovley*, 2013). DIRBs include those in the well-studied genera *Geobacter* and *Geothrix* among others (*Lovley*, 2013, provides a complete list of DIRBs). DIRB contribute to both to the dissolution of ferrous iron oxide minerals when soils become anoxic and also to the production of extracellular magnetite (see section 4.4.1). However, DIRBs are typically anaerobic and occupy localized water-logged zones within a soil. As we have noted, water-logged soils that are anoxic for prolonged periods of time should be avoided in magnetic paleoprecipitation proxy calibrations.

If DIRBs are the primary drivers for the production of pedogenic magnetite in well-drained soils, which are largely oxic for long periods of time, then it follows that there must be a way for these bacteria to tolerate or avoid oxic conditions. DIRBs survive oxic conditions using a combination of at least four mechanisms. First, DIRBs preferentially occupy anoxic microenvironments, such as pore spaces within soil aggregates where anoxic conditions are more stable (*Ranjard and Richaume*, 2001; *Hansel et al.*, 2008). Second, in some species of DIRBs we observe metabolic flexibility in the presence of oxygen (i.e., switching from anaerobic metabolism to aerobic; *Methé et al.*, 2003; *Lin et al.*, 2004; *Núñez et al.*, 2006). Third, some DIRBs go dormant in unfavorable conditions by lowering their metabolism and energy requirements (*Holmes et al.*, 2009; *Lin et al.*, 2009; *Mouser et al.*, 2009; *Marozava et al.*, 2014). And lastly, DIRBs have been shown to secrete enzymes with a high redox potential so that their reducing potential is maintained even in microoxic conditions (*Mehta-Kolte and Bond*, 2012).

The rate and extent of DIRB dissolution in soils is likely to be governed by the amount of soil organic matter, humic substances within the soil (which act as electron shuttles during dissimilatory iron reduction; *Nevin and Lovley*, 2000; *Weiss et al.*, 2004), and the degree of crystallinity and composition of ferrous iron oxide minerals within the soil (*Bonneville et al.*, 2004; *Roden*, 2006). Predictably, high soil organic matter, high concentrations of humic acids, high reactive surface area, and low crystallinity are all associated with more rapid rates of mineral dissolution (e.g., *Emerson and Weiss*, 2004;

Dubinsky et al., 2010). The reduction of structural ferric iron releases Fe^{2+} ions into the soil solution (*Cornell and Schwertmann*, 2003) and over time scales of many hours the accumulation of Fe^{2+} in solution appears to limit the rates of DIRB dissolution (*Roden*, 2006).

Of importance for understanding the magnetic enhancement observed in many soils is the biotic precipitation of iron oxides, principally magnetite. Biological mineralization processes can produce magnetite intracellularly (e.g., magnetotactic bacteria) or extracellularly as has been discussed with respect to DIR bacteria (*Frankel and Blakemore*, 1991). The most well-known example of biologically synthesized magnetite is that of magnetotactic bacteria (see reviews by *Blakemore*, 1982; *Moskowitz*, 1995; *Bazylinski et al.*, 2013). Magnetotactic bacteria synthesize SSD grains of magnetite (termed magnetosomes) that are encased in a protein membrane and often are aligned in chains along a common crystallographic axis (*Baumgartner et al.*, 2013). The principle function of the magnetosomes are for navigation and orientation in a process referred to as magnetotaxis.

Magnetotactic bacteria are common in oxic-anoxic transition zones in stratified water columns or surface sediments in both freshwater and marine environments (*Bazylinski et al.*, 2013). *Fassbinder et al.* (1990) discovered magnetotactic bacteria in a waterlogged soil in Germany and others have noted biogenic greigite in gley soils (*Stanjek et al.*, 1994); however to our knowledge there has been no other report of magnetotactic bacteria in soils. Further, the amount of bacterial cells recovered by *Fassbinder et al.* (1990) was insufficient to have been a significant cause of magnetic enhancement (*Maher*, 1998). The well-developed euhedral crystals produced by magnetotactic bacteria are easily distinguishable from pedogenic magnetite using scanning electron microscopy images and by magnetic measurements (*Moskowitz et al.*, 1993; *Moskowitz*, 1995). Given that inputs of magnetite into a soil by magnetotactic bacteria should be detectable by electron microscopy and by rock magnetic measurements, the rarity of magnetosomes in soils suggests that magnetotactic bacteria are not a significant source of magnetite in most soils.

4.8 Diagenetic concerns

There is still much to learn about the influence of post-burial diagenetic processes that occur during the transition from an active soil into a paleosol. In this review, diagenesis refers to post-burial processes excluding metamorphism.

Compaction is one of the most fundamental processes that occur to soils upon burial. Compaction in paleosols is a function of burial overburden and soil solidity (the density ratio between the soil and the solid parent material), and therefore varies between different soil orders (*Sheldon and Retallack*, 2001; *Sheldon and Tabor*, 2009). Paleosol compaction alone is not likely to influence the iron oxide mineral phases, although the extent of soil compaction will decrease the porosity and permeability, which in turn controls the exposure of magnetic minerals to potentially altering groundwater solutions.

Yet burial depths are important to the magnetic mineral assemblages in paleosols. Investigations of a sequence of Miocene to Holocene paleosols showed that increasing burial depths (range from $0 - 5$ km) were associated with an increase in hematite and goethite abundance and a decrease in the SP/SSD fraction of magnetite and maghemite (*Sangode et al.*, 2008). If the observed differences in the paleosols are due to diagenetic processes driven by overburden pressure, rather than to changing environmental conditions between the Miocene to Holocene, then these diagenetic processes may be a significant source of uncertainty when using magnetism to study paleosols from deep time. Alternatively, the observed variation in magnetic mineral assemblages with depth may reflect processes that are simply related to burial time. Disentangling a paleosol's primary recording of the environmental conditions in which it equilibrated from the distorting effects of diagenesis remains a difficult challenge to the paleoclimate community.

Gleying (prolonged reduction under water-logged conditions) of previously well-drained soils upon burial can occur in paleosols that subside below the water table, and can create anoxic conditions in paleosol pore spaces (*Retallack*, 1991). Post-burial gleying often causes dissolution of ferric iron oxides and may decrease the preservation of magnetic minerals in paleosols. Typically, post-burial gleying results in fine iron oxide coatings on ped surfaces, in particular coatings that span microfractures through pedogenic structures (*Nordt et al.*, 2011). Iron oxides precipitated in root casts, usually surrounding a grey interior core, are common evidence of surface gleying (*PiPujol*

and Buurman, 1997; *Kraus and Hasiotis*, 2006). If significant post-burial gleying has occurred, then it is likely that this will disturb the original assemblage of pedogenic magnetic minerals. For practical purposes, large root trace zones or other prominent redoximorphic features should be avoided when sampling paleosols for magnetic analyses.

The dehydration of goethite and recrystallization to hematite has been proposed as one mechanism for the post-burial reddening of many terrestrial red beds and paleosols (*Retallack*, 1991). Post-burial dehydration reactions should impact iron oxide minerals pervasively within a paleosol, given the timescales over which these processes occur (*Kraus and Hasiotis*, 2006). The presence of goethite and hematite mixtures in paleosols, as well as their complex color assemblages, has been used as evidence of the minimal role played by diagenetic transformations of iron oxides in paleosols from the Bighorn Basin, Wyoming (*Kraus and Hasiotis*, 2006). However, recent recovery of sediment cores by the Bighorn Basin Coring Project shows that oxidative weathering fronts penetrate nearly 30 meters below the Earth's surface (*Clyde et al.*, 2013). This recent observation suggests that oxidative surficial weathering significantly alters the magnetic mineral assemblage of paleosols exposed as outcrops. However, the extent of this process has yet to be quantified in detail.

Several studies have documented that diagenetic processes can create secondary chemical remagnetizations in terrestrial sandstone and carbonate deposits within orogenic belts (e.g., *McCabe and Elmore*, 1989; *Banerjee et al.*, 1997; *Katz et al.*, 2000; *Cox et al.*, 2005; *Tohver et al.*, 2008). Possible mechanisms for chemical remagnetization include the dissolution and remobilization of Fe^{2+} by thermal maturation of organic matter (*Banerjee et al.*, 1997), and the release of Fe^{2+} during the illitization of Fe-rich smectite clay minerals (*McCabe and Elmore*, 1989; *Woods et al.*, 2002; *Cox et al.*, 2005). Both of these processes are associated with the authigenic production of magnetite. Paleomagnetic studies of the Chinese Loess Plateau have explored remagnetization in loessic deposits (e.g., *Lovlie et al.*, 2011). However, to our knowledge these mechanisms have not been considered in the context of paleosol diagenesis, particularly with respect to magnetic minerals produced during pedogenesis. These processes are likely only relevant for paleosols that have subsided to burial depths of at least $2 - 3$ km (the depth associated with illitization of smectites; *Woods et al.*, 2002; *Cox et al.*,

2005).

Diagenesis may also be microbially mediated. Microbes, particularly Archaea, can exist in some of the most extreme environments on Earth. This holds true for the subsurface, including buried paleosols (e.g., *Khomutova et al.*, 2014). Dormant microbial communities have been recovered in buried paleosols of age $1 - 4$ Ma (*Brockman et al.*, 1992) and portions of these communities can be re-animated with the onset of favorable conditions (*Demkina et al.*, 2008). A more extreme example of subsurface microbial life is the recovery of very fine grained magnetite associated with gas and oil deposits ∼6.7 km below the Earth's surface that are attributed to Fe(III)-reducing bacteria (*Gold*, 1992).

The generally accepted threshold temperature for the upper limit of microbial life is ∼120 °C (*Colwell*, 2001). Thermophillic Fe(III)-reducing bacteria have been recovered from ∼2.1 km below the surface in the Cretaceous sediments of the Piceance Basin of western Colorado (*Liu*, 1997). The presence of Fe(III)-reducing bacteria in subsurface deposits may aid in the degradation of organic matter and the addition of Fe^{2+} into groundwater. This microbial activity has the potential to alter the primary magnetic mineralogy of paleosols because magnetite is an associated byproduct of Fe(III)-reduction via DIRB. While it is probable that microbes contribute to the post-burial destruction or addition of ferrimagnetic minerals in some systems, the magnitude of this contribution remains unknown.

Post-burial gleying of originally well-drained soils has been invoked to explain low χ ($\sim 5-20 \times 10^{-8}$ m^3kg^{-1}) in Precambrian and early Paleozoic paleosols, as compared to temperate modern soils whose χ values tend to be higher ($\sim 500 \times 10^{-8}$ m^3kg^{-1}) (*Maher*, 1998; *Retallack et al.*, 2003). Similarly low χ values ($2-20 \times 10^{-8}$ m^3kg^{-1}) have been documented in the Pennsylvanian Roca Shale (*Rankey and Farr*, 1997) as well as loessite-paleosol sequences in the Permian Maroon Formation (*Soreghan et al.*, 1997; *Cogoini et al.*, 2001; *Soreghan et al.*, 2002; *Tramp et al.*, 2004) and the upper-Paleozoic lower Cutler beds of Utah (*Cogoini et al.*, 2001). Despite the low values of χ in many of these paleosols, many of these studies have concluded that the magnetic minerals preserved within these soils are pedogenic (e.g., *Rankey and Farr*, 1997; *Cogoini et al.*, 2001; *Tramp et al.*, 2004). Further, the observed enhancement ratio of susceptibility in paleosols to loessite for the loessite-paleosol sequences in the Maroon Formation

(*Cogoini et al.*, 2001; *Tramp et al.*, 2004) are comparable to the χ enhancement in modern loessic soils of the U.S. Great Plains (*Geiss et al.*, 2008). Comparable measures of magnetic enhancement between modern soils and paleosols alone should not be taken to indicate that similar climatic regimes were present during soil formation. However, observable magnetic enhancement in ancient paleosols does provide a positive outlook for rock magnetic studies by suggesting that primary magnetic enhancement signals are preserved to some extent in even the oldest paleosols.

4.9 Challenges for future work

Despite the interrelated complications associated with the physical, chemical, and biological evolution of soils and paleosols there is considerable promise that quantitative magnetic methods can be developed to better interpret records of magnetic mineral assemblages preserved in paleosols. Future work should target two key themes:

1. The community needs to quantify more precisely the relationships between the formation of iron oxide minerals in modern soils and ambient environmental parameters such as precipitation, temperature, and seasonality across a range of environments. We encourage studies that explore more broadly how these environmental parameters act to control soil moisture, which is the ultimate driver for magnetic mineral production, as well as other parameters such as duration of pedogenesis. Much of the existing work has focused on loess-derived soils, which while informative, represent only a small fraction of possible soil orders. Future work ought to expand and build upon existing methods to determine how applicable magnetic paleoprecipitation proxies might be in different soil orders and from more variable geographical locations.

2. The rock magnetic community needs to develop clear and easily followed experimental protocols for determining the mass or volume abundances of individual iron oxide minerals within soils. Such methods will be essential for properly calibrating paleoproxy tools based on hematite and goethite abundance, as well as for determining the fraction of pedogenic magnetite/maghemite that has been preserved within a paleosol. In order for methods to be widely applicable it will be necessary that future researchers be able to directly replicate the methods of previous studies to ensure that parameters used in proxies are uniformly measured and calculated.

4.10 Acknowledgements

The authors wish to thank Brandy Toner and Jake Bailey for discussion that helped to shape early versions of this work. Subir Banerjee, Christoph Geiss, and David Heslop contributed thoughtful comments that greatly improved this review. DPM acknowledges funding provided by the Richard C. Dennis Fellowship through the UMN Department of Earth Sciences and the UMN Stanwood Johnston Fellowship. This is IRM contribution 1510.

Chapter 5

MAX UnMix: A web application for unmixing magnetic coercivity distributions

The contents of this section were originally published in the journal Computers and Geosciences *under the title 'MAX UnMix: A web application for unmixing magnetic coercivity distributions'. See reference to Maxbauer et al., 2016b for details. This work is included below it its published form with permission of all authors.*

5.1 Synopsis

It is common in the fields of rock and environmental magnetism to unmix magnetic mineral components using statistical methods that decompose various types of magnetization curves (e.g., acquisition, demagnetization, or backfield). A number of programs have been developed over the past decade that are frequently used by the rock magnetic community, however many of these programs are either outdated or have obstacles inhibiting their usability. MAX UnMix is a web application (available online at `http://www.irm.umn.edu/maxunmix`), built using the `shiny` package for `R` studio, that can be used for unmixing coercivity distributions derived from magnetization curves. Here, we describe in detail the statistical model underpinning the MAX UnMix web

application and discuss the programs functionality. MAX UnMix is an improvement over previous unmixing programs in that it is designed to be user friendly, runs as an independent website, and is platform independent.

5.2 Introduction

Magnetic minerals are ubiquitous in a variety of natural systems. Progress in the fields of environmental and rock magnetism has increasingly led to an ability to quantify the abundance, grain size, and chemical composition of various magnetic minerals, which has been critical in enhancing our understanding of an array of natural and anthropogenic processes (see recent reviews by *Maher*, 2011; *Liu et al.*, 2012; *Hatfield*, 2014; *Maxbauer et al.*, 2016a). In particular, there are a variety of methods available that allow for the statistical unmixing of measured magnetization curves (*Robertson and France*, 1994; *Stockhausen*, 1998; *Kruiver et al.*, 2001; *Heslop et al.*, 2002; *Egli*, 2003; *Heslop and Dillon*, 2007; *Heslop*, 2015, provides an excellent review). These methods are widely applied in the literature and have helped to advance our understanding of the processes which govern magnetic mineral formation, transformation, and deposition.

Robertson and France (1994) made the seminal observation that the shape of isothermal remanent magnetization (IRM) acquisition curves for an assemblage of grains of a single magnetic mineral could be approximated by a cumulative log-Gaussian function given three parameters: the mean coercivity of an individual grain population (B_h), the component saturation magnetic remanence (M_r), and the dispersion parameter (DP; given by one standard deviation in log space). For a given field value of B, the IRM of an individual component is given by (*Robertson and France*, 1994):

$$IRM(B) = \frac{M_r}{DP(2\pi)^{(1/2)}} \int_{-\infty}^{\infty} \exp\left[\frac{(log(B) - log(B_h))^2}{2DP^2}\right] dlog(B) \qquad (5.1)$$

In the case that a specimen is composed of multiple magnetic mineral components, the individual *IRM* aquisition functions (given by eq. 1) for each component can be added linearly to approximate the measured data (*Robertson and France*, 1994; *Kruiver et al.*, 2001). *Kruiver et al.* (2001) popularized the use of a gradient acquisition plot (GAP) to assist in curve fitting. Subsequent studies refer to the GAP as the coercivity distribution (or spectra; e.g., *Heslop et al.*, 2002; *Egli*, 2003; *Heslop et al.*, 2004), which is

the absolute value of the first derivative of the magnetic acquisition dataset (*Egli*, 2003). Coercivity distributions can be modeled in a similar way to *IRM* acquisition curves by approximation of a probability density function using the same three parameters (*Kruiver et al.*, 2001; *Heslop et al.*, 2002):

$$f(B) = \sum_{i=1}^{n} M_{ri} k(B; B_{hi}; DP_i) \tag{5.2}$$

where n is the number of magnetic mineral components within a specimen and k corresponds to a log-normal probability density function. From eq. 2, it is possible to calculate a function that represents the continuous realization of the discrete measured data. Various statistical procedures are used to determine the goodness of fit for a particular model compared to the measured data using either statistical tests (F-test and t-test; *Kruiver et al.*, 2001) or automated iterative approaches (Expectation Algorithm; *Heslop et al.*, 2002). These models are accessible for readers to use through downloads of an excel workbook (IRM-CLG; *Kruiver et al.*, 2001) and a Fortran90 executable program (IRM UnMix, available for PCs; *Heslop et al.*, 2002). Fitting is achieved through either manual entry (*Kruiver et al.*, 2001) or through automated optimization (*Heslop et al.*, 2002).

The functions described by eq. 1 and eq. 2 operate under the assumption that coercivities of a given magnetic mineral grain population can be closely approximated by a log-normal distribution (*Robertson and France*, 1994; *Kruiver et al.*, 2001; *Heslop et al.*, 2002; *Egli*, 2003). However, it is well known that many natural samples contain magnetic mineral components whose coercivities are not log-normal (*Egli*, 2003, 2004a; *Heslop et al.*, 2004). To account for non-normality, *Egli* (2003) introduced the skew generalized Gaussian (SGG) function:

$$SGG(x, \mu, \sigma, q, p) = \frac{1}{2^{(1+1/p)}\sigma\rho(1+1/p)} \frac{|qe^{qx*} + q^{-1}e^{x*/q}|}{e^{qx*} + e^{x*/q}} \exp\left[-\frac{1}{2} \left| ln\left(\frac{e^{qx*} + e^{x*/q}}{2} \right) \right|^p \right] \tag{5.3}$$

where x is equivalent to B in eqs. 1 and 2, μ is the equivalent of B_h, σ is equivalent to DP, q is related to skewness, and p is related to kurtosis (*Egli*, 2003). The variable $x*$ arises from a substitution of x with $x*$, where $x* = g(x, q)$ (see *Egli*, 2003, for

details). A Gaussian distribution is equivalent to the SGG when $q = 1$ and $p = 2$ (decreasing q from 1 to 0 creates left skewed distributions, changing the sign creates right skewed distributions; decreasing p increases peakedness and increasing p enhances squaredness *Egli*, 2003). The SGG function has major advantages over simple Gaussian distributions because it can better account for non-normal behavior that is common in natural samples. Deviations from normality can necessitate the need for additional normal or log-normal components within a model to achieve a satisfactory fit, whereas a single skew-component may prove sufficient (see *Egli*, 2003; *Heslop*, 2015). The MAG-MIX method of *Egli* (2003) is available as a set of Mathematica notebooks (CODICA, for deriving coercivity distributions and GECA, for analyzing coercivity distributions) that include graphical user interfaces to assist in data processing. MAG-MIX has been used to analyze the coercivity spectra from a wide range of natural samples and details of those results can be found in *Egli* (2004b,a,c).

The methods provided by *Kruiver et al.* (2001), *Heslop et al.* (2002), and *Egli* (2003) have proven to be an excellent basis for more detailed interpretation of the magnetic mineralogy of sediments and other geologic samples. However, despite the certain advances presented by *Egli* (2003), which continues to be utilized by researchers (e.g., *Lascu and Plank*, 2013; *Li et al.*, 2013; *Ludwig et al.*, 2013; *Liu et al.*, 2014), many studies continue to utilize older methods from *Kruiver et al.* (2001) (recent examples include *Font et al.*, 2012; *Yamazaki and Ikehara*, 2012; *Ao et al.*, 2013; *Hu et al.*, 2013; *Abrajevitch et al.*, 2015) and *Heslop et al.* (2002) (e.g., *Roberts et al.*, 2012; *Channell and Hodell*, 2013; *Weil et al.*, 2014; *Dorfman et al.*, 2015). This may be in response to difficulties in applying the SGG method, or in response to the software being available only for Mathematica users (which requires expensive licensure). Here, we present a new program, MAX UnMix, that was designed in the statistical computing language `R` (which is open source and available for MAC, PC, and Linux; *R-Core-Team*, 2015) and built using `shiny` for `R` studio (*Chang et al.*, 2015). The application functions as a web application (available online at `http://www.irm.umn.edu/maxunmix`) where users interact with the model via a graphical user interface. Supporting information, including instructional videos and a user manual, are available on the MAX UnMix webpage. Below, we describe the statistical model underpinning MAX UnMix and provide a number of examples to highlights aspects of the model's performance.

5.3 Model Description

The observed coercivity distribution, C, of a measured set of magnetization data (M; may be acquisition, demagnetization, or backfield curves) is defined as the absolute value of the first derivative of the raw data:

$$C = \left| \frac{dM}{dlog(B)} \right| \tag{5.4}$$

where M and B are the respective magnetization and field values for a given dataset. Note we define C in eq. 4 using the $log(B)$ scaling, however various field scalings can be used by simple substitution (e.g., *Egli*, 2003). MAX UnMix utilizes the `predict()` function to calculate C on either a log_{10} or linear scale, depending on user selection. In line with previous methods, we recommend fitting magnetization curves with a minimum of 25 data points, although generally it is advantageous to have more if possible (*Kruiver et al.*, 2001).

It is often necessary to remove measurement noise within datasets by either application of a spline function (*Heslop et al.*, 2002) or more sophisticated filtering (e.g., the CODICA program described by *Egli*, 2003). In MAX UnMix, a simple monotonic spline function, `smooth.spline()`, allows the user to determine the appropriate level of smoothing. The smoothing factor, sf, can be varied between 0 and 1, where $sf = 0$ is equivalent to no smoothing and $sf = 1$ is the maximum degree of smoothing for a given dataset. Spline fitting prevents large influences of measurement noise, however over smoothing of data can result in spurious features (typically at low and high-fields; see *Heslop et al.*, 2002; *Heslop*, 2015) and careful observation of this balance should be monitored by users. To avoid complications resulting from smoothing users have the option to perform smoothing on either raw magnetization data ("Magnetization smoother", C derived from smoothed magnetization data) or raw coercivity data ("Coercivity smoother", C is smoothed directly from raw coercivity data), these choices work variously well at low and high fields and users can determine which method is optimal for a given dataset. As a general rule, the effects of measurement noise are best reduced by maximizing the degree of smoothing imposed on a data set, while taking special care to avoid 'over-smoothing', which can create artifacts.

When a suitable C has been determined from the measured data, the aim is to determine a model function that approximates C for a given set of field values, B.

Within the MAX UnMix framework this is achieved using a skew-normal distribution from the `fGarch` package in `R` (*Wuertz and Chalabi*, 2015). The `dsnorm()` function within the package creates skew-normal probability density functions that we use within our model in the following form:

$$C_m(B) = \sum_{i=1}^{n} p_i w(B; B_{hi}; DP_i; S_i) \tag{5.5}$$

where p_i is a proportion factor that describes the height of the distribution for each component (p_i can range from 0 to 1, normalized such that a value of 1 is equivalent to the maximum of C), $w()$ is the skew-normal probability density function, S_i is a parameter describing skewness (for S_i less than 1 distributions skew left, and vice versa), and C_m represents the modeled approximation of C. In the special case that $S = 1$, $w()$ is equivalent to the normal probability function, $k()$, utilized by previous studies (eq. 2; *Kruiver et al.*, 2001; *Heslop et al.*, 2002). Skew-left distributions ($S < 1$) are the result of thermal effects and interactions between magnetic particles in a grain population (*Heslop et al.*, 2004) and have been shown to be common in natural populations (*Egli*, 2004b,a). Skew-right distributions ($S > 1$) are less well understood on a physical basis and may indicate mixed mineralogy within a single skew-right component (*Heslop et al.*, 2004). Accordingly, care should be taken when interpreting results for components with S values much greater than 1. Note that our skew-normal function does not incorporate kurtosis (which is included in the *SGG* function of *Egli* (2003)), however nearly all natural samples are successfully fit when $p = 2$ meaning that kurtosis is not a feature common to natural magnetic mineral components (see *Egli*, 2004b).

The user determines an initial set of values for B_{hi}, DP_i, p_i, and S_i to set the initial model parameters, P_{in}. Determining initial inputs is a subjective process achieved through an interactive user interface where values are selected with slider bar inputs. We emphasize that initial component fits should be constructed with care and consideration for known parameters of magnetic mineral components. Initial starting components can be saved within a user-session so that a number of datasets may be analyzed from a consistent and objective starting point. Optimization of P_{in} is achieved using the `optim()` function, which iteratively determines the ideal values of P_{in} to minimize the residual sum squared (RSS) between C and C_m. Results for an optimized set of parameters P_{opt} are returned along with the minimized RSS value. In order to determine the

number of magnetic mineral components to be used in the model, there is functionality built in to the web application to perform an F-test for models with variable numbers of components. We suggest that additional information and data regarding the likely components in a sample be used to aid in determining the proper number of components to use in model fitting, as statistical significance is not an absolute measure of the quality of a model. Many common components in natural samples have been described by *Egli* (2004b,a,c) and a table summarizing many of those components is provided on the 'Fitting' page of MAX UnMix for reference.

In addition to determining the optimal number of magnetic mineral components within a specimen, it is often of interest to calculate the relative contribution of each component to the total measured magnetization. Here, both the observed and extrapolated contribution (OC and EC, respectively) of each model component are determined as the integrated area under individual component distributions relative to the area under C_m for the observed set of field values B (OC) or an extended set of field values such that all components are saturated (EC). In the case of full saturation, OC will equal EC exactly. Previous methods (e.g., *Kruiver et al.*, 2001; *Heslop et al.*, 2002) extrapolate magnetic contributions of unsaturated components and so EC will be the most comparable parameter to other methods. It is important to note that our calculation of OC and EC is independent of the user defined p_i, the parameter controlling distribution amplitude, meaning that values of p_i need not equal to 1 during model fitting.

A resampling routine is used to assign uncertainty for the optimized model parameters and resultant C_m (method similar to that of *Egli*, 2003). For a user-defined number of resampling events, j, the model calculates a newly optimized C_m and set of parameters P_{opt} based on a Monte-Carlo style resampling of all input parameters (P_{in} and C). For P_{in}, random sampling assumes a normally distributed error of 2%. Each iteration recalculates C from a random subset of M based on a proportion set by the user (0.95 as default, can range from 0.8 - 1.0). Mean values and standard deviations for the resultant set of P_{opt} and $C_{m(opt)}$ are returned and available for download. An approximate 95% confidence interval (2.5 and 97.5 percentiles) is used to display uncertainty in component and model distributions in the final output plot. The final set of results provides users with a robust sense of uncertainty and model quality.

5.4 Example Datasets and Model Comparison

In order to evaluate the performance of the MAX UnMix model we analyzed data from three natural samples using the MAX UnMix model described here, the CODICA and GECA programs provided by *Egli* (2003), IRM UnMix (*Heslop et al.*, 2002), and the IRM-CLG method of *Kruiver et al.* (2001). For each sample, we compare the B_h and DP values for each model component (see Figures 5.1, 5.2, and 5.3). These model parameters are common amongst all four methods and are often used as diagnostic indicators in assigning magnetic mineralogy to model components (e.g., *Egli*, 2004b,a,c; *Lindquist et al.*, 2011; *Bourne et al.*, 2015, other parameters from each model are reported in Table 5.1). The analyzed samples ranged from lake sediments (G010 and Birch-05; *Egli*, 2003; *Lascu and Plank*, 2013, respectively) to an Eocene paleosol B-horizon (PCB-01-TRB-050). Magnetization data for each specimen varied from ARM demagnetization (G010; *Egli*, 2003), IRM demagnetization (Birch-05; *Lascu and Plank*, 2013), and backfield remanence data (PCB-01-TRB-050).

Evaluation of the G010 ARM demagnetization sample data set from *Egli* (2003) reveals a broad consistency of results across methods (see Figure 5.1). MAX UnMix modeling results in a three component model with a primary low coercivity component (component 1) with a B_h of 1.37 ($\pm$ 0.02) log_{10} units (23.4 mT) and a DP of 0.32 ($\pm$ 0.01). The intermediate component 2 is characterized by a B_h of 1.88 ($\pm$0.01) log_{10} units (75.9 mT) and a DP of 0.14 ($\pm$ 0.01). A final high coercivity component 3 has a B_h of 2.24 ($\pm$0.05) log_{10} units (75.9 mT) and a DP of 0.24 ($\pm$ 0.04). The original analysis of G010 (anoxic lake sediment) presented by *Egli* (2003) reported three primary components that are closely replicated here. The low coercivity component (component 1) was identified as detrital magnetite and could also be identified from fluvial sediments elsewhere in the lake catchment (see *Egli*, 2003, for details). Component 2 and 3 are nearly identical to the biogenic magnetite and oxidized magnetite (or hematite) components reported by *Egli* (2003).

The resultant B_h and DP values for both GECA and IRM-CLG are within $\pm$ 10% of the values resulting from MAX UnMix and suggest that comparable results are obtainable across methods despite certain differences in the statistical models (see also *Spassov et al.*, 2003). However, the IRM UnMix software was unable to produce a satisfactory fit

to the G010 dataset using it's automated fitting routine (*Heslop et al.*, 2002). A major advantage of having an automated fitting routine is that objectivity can be maintained and results can be easily replicated by different users. Despite these advantages, there are certain cases, including G010, where it becomes beneficial to have a higher degree of user control (which is possible in IRM UnMix, but not in a user friendly way). In contrast, the IRM-CLG model is entirely subjective to user control and includes no optimization or error analysis. Results for the IRM-CLG method show good correlation for G010 (and in other examples described below), but these results are in part due to the difficulty in remaining objective while model fitting. MAX UnMix, in a similar way to the MAG-MIX software from *Egli* (2003), allows for subjectivity in determination of an initial model fit, but retains objectivity by performing automated optimization and error analysis in order to produce a final model.

Decomposition of the Birch-05 IRM demagnetization data from *Lascu and Plank* (2013) using MAX UnMix reveal two primary magnetic components (Figure 5.2A). The low coercivity component (component 1) is characterized by a B_h of 1.19 ($\pm$ 0.02) log_{10} units (15.5 mT) and a DP of 0.38 ($\pm$ 0.01; see Figure 5.2A). Component 2 has a B_h of 1.58 ($\pm$ 0.01) log_{10} units (38 mT) and a DP of 0.27 ($\pm$ 0.01; see Figure 5.2A). *Lascu and Plank* (2013) reported results of coercivity unmixing using the CODICA and GECA programs of *Egli* (2003) for a sequence of lake sediments (including Birch-05) and identified detrital soft (B_h 10 - 30 mT, DP 0.3 - 0.5) and biogenic soft (B_h 30 - 50 mT, DP 0.15 - 0.32) components that are entirely consistent with component 1 and 2, respectively.

Reanalysis of the Birch-05 data using CODICA and GECA (*Egli*, 2003) as well as IRM-UnMIx (*Heslop et al.*, 2002) and IRM-CLG (*Kruiver et al.*, 2001) produces results that are mostly consistent for B_h and DP (see Figure 5.2B). In general, data across methods is within $\pm$ 10% of the results obtained from Max UnMix. There is more variability in the results for DP compared with the consistency observed in B_h (Figure 5.2). The variability in DP is primarily related to a relatively high degree of skewness in both model components ($S_1 = 0.72$ and $S_2 = 0.71$) which is accounted for in slightly different ways in Max UnMix compared with the SGG function (eq. 3) of *Egli* (2003), or in the case of the other methods is not incorporated.

Remanence is held by two primary components in PCB-01-TRB-050. The high-coercivity component (component 1) is characterized by B_h of 2.66 ($\pm$ 0.02) log_{10} units ($\sim$ 457 mT) and a DP of 0.34 ($\pm$ 0.01; see Figure 5.3). The low coercivity component (component 2) has a B_h of 1.51 ($\pm$ 0.01) log_{10} units ($\sim$ 32 mT) and a DP of 0.51 ($\pm$ 0.01). These components are interpreted to represent partially oxidized pedogenic magnetite (component 2) and fine grained hematite (component 1).

Similar to the results for Birch-05, increased skewness also increases variability in results obtained from various methods for component 2 in specimen PCB-01-TRA-050 (Figure 5.3B) where skewness is also considerable ($S_2 = 0.68$). In contrast, the model parameters for component 1 in PCB-01-TRB-050 is only slightly skewed ($S_1 = 1.09$) and the B_h and DP for component 1 are highly consistent across methods. This variability is important to recognize, particularly when comparing results from studies where unmixing analyses were conducted using different methods and highlights the need for consistent methodology to be utilized moving forward if possible.

Results from TRB-050 highlight that care should be taken when interpreting results for dispersion and skewness. Model fits for TRB-050 show component 1 is slightly skew-right and component 2 has DP values that are in excess of 0.5 in all models (see Table 5.1). In general, values of DP far exceeding 0.5 should be interpreted with caution, as it can infer that a magnetic mineral component is both "hard" and "soft". For skewness, as previously mentioned, skew-right distributions ($S > 1$) are poorly understood and should be avoided in fitting if possible. Component 1 is interpreted is be primarily pigmentary hematite, although it is possible that more minor contributions from goethite may be responsible for the skew-right behavior. Component 2 is interpreted as partially oxidized pedogenic magnetite likely represents a mixture of magnetite and partially (or fully) oxidized magnetite/maghemite, which increases the range of coercivities (and thus DP) within a single component. In the case that $DP > 0.5$ and $S > 1$, it may be an indicator for mixed mineralogy within a single component (*Heslop et al.*, 2004) and physical interpretations such as those reported here should accompany results of this type.

Comparison of EC calculated by MAX UnMix to the contribution calculated by other methods is mostly consistent for components in both TRB-050 and G010 (generally within $\pm$ 8 %). The variability in EC for Birch-05 is more considerable ($\pm$ 14%)

and is particularly poor when comparing results from MAX UnMix and GECA to those of IRM-UnMix and IRM-CLG (see Table 5.1. The potential for variability in estimated contribution to remanence for model components highlights the need for transparency and consistency in methodology for quantifying component remanence using coercivity unmixing methods.

5.5 Conclusions

MAX UnMix is a new method for the statistical unmixing of magnetization data. The program functions as a web application (available online at `http://www.irm.umn.edu/maxunmix`) and was written in `R` studio using the package `shiny` (both open source and available for Mac, PC, and Linux). Model results are comparable to existing methods that are frequently used within the environmental and rock magnetic community. In contrast to older methods, MAX UnMix provides users a friendly interface that is available online (with the code accessible via open source, platform independent software). Moving forward, future work should to aim to utilize coercivity unmixing methods that are consistent and account for skewness of component distributions as increased skewness has a considerable impact on affecting other model parameters. Given the accessibility and user-friendly nature of MAX UnMix it should serve as a useful resource for future work.

5.6 Acknowledgments

We thank members of the Institute for Rock Magnetism for comments that helped to improve early versions of this program. Mark Dekkers, Ramon Egli, and Christoph Geiss provided thoughtful reviews that greatly improved this work. DPM acknowledges funding from the Stanwood Johnston and Doctoral Dissertation Fellowships from the University of Minnesota. This is IRM contribution 1606.

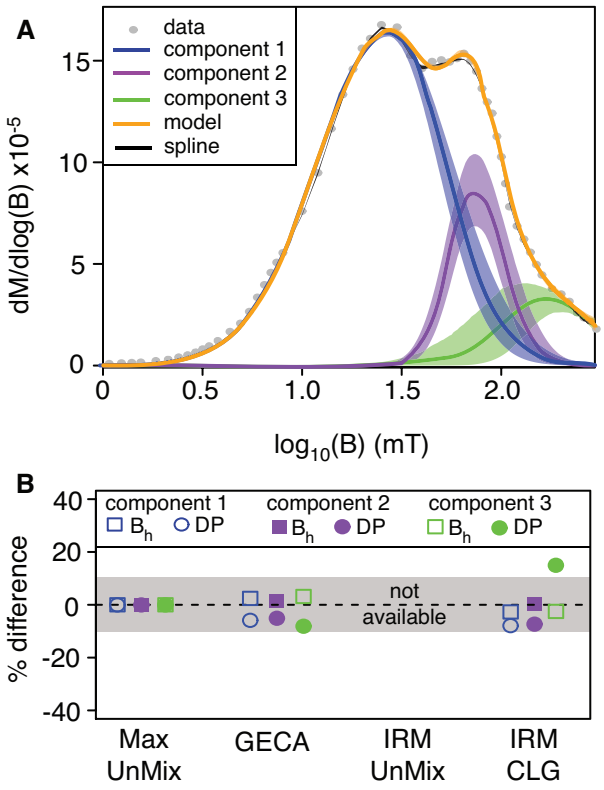

Figure 5.1: **A.** Model fit example for sample G010 (anoxic lake sediments) from Egli (2003). Coercivity distribution (data shown in grey circles, spline fit partially visible as black line) derived from *ARM* demagnetization data. Shaded area represents error envelopes of 95% confidence intervals. In the cases where no shading is present (e.g., spline fit and model fit) it is because 95% confidence intervals are thinner than line. **B.** Comparison of B_h and DP parameters for individual model components across methods. Percentage difference calculated relative to results for Max UnMix. Shaded region represents plus or minus 10%. GECA program from Egli (2003), IRM UnMix from Heslop et al. (2002), and IRM CLG from Kruiver et al. (2001). Note that the IRM UnMix program in this case was unable to produce a satisfactory fit comparable to other models.

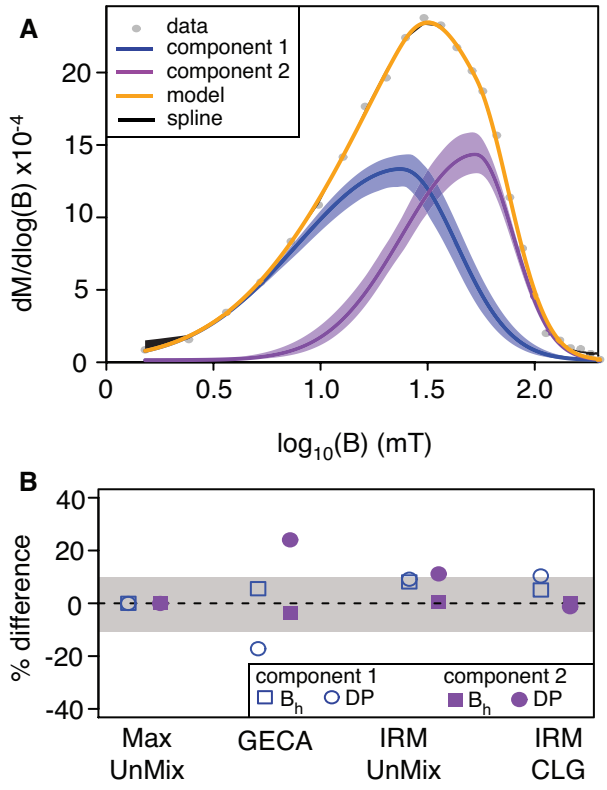

Figure 5.2: **A.** Model fit example for sample Birch-05 (lake sediment) from Lascu and Plank (2013). Coercivity distribution (data shown in grey circles, spline fit partically visible as black line) derived from IRM demagnetization measurements. Shaded area represents error envelopes of 95% confidence intervals. In the cases where no shading is present, confidence intervals are thinner than line. **B.** Comparison of B_h and DP parameters for individual model components across methods. Percentage difference calculated relative to results for MAX UnMix. Shaded region represents plus or minus 10%. GECA program from Egli (2003), IRM UnMix from Heslop et al. (2002), and IRM CLG from Kruiver et al. (2001).

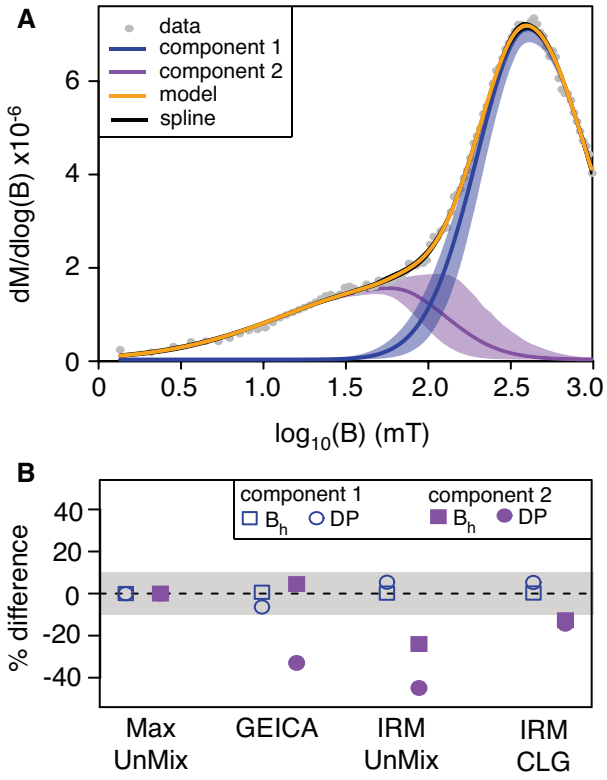

Figure 5.3: **A.** Model fit example for sample PCB-01-TRB-050 (paleosol B horizon). Coercivity distribution (data shown in grey circles, spline fit partically visible as black line) derived from backfield remanence data up to 1T. Shaded area represents error envelopes of 95% confidence intervals. In the cases where no shading is present, confidence intervals are thinner than line. **B.** Comparison of B_h and DP parameters for individual model components across methods. Percentage difference calculated relative to results for MAX UnMix. Shaded region represents plus or minus 10%. GECA program from Egli (2003), IRM UnMix from Heslop et al. (2002), and IRM CLG from Kruiver et al. (2001).

Table 5.1: Results of model fitting for three specimen using variable unmixing methods: MAX UnMix (described here), GECA (Egli, 2003), IRM-UnMix (Heslop et al., 2002), and IRM-CLG (Kruiver et al., 2001). Note that all parameters (B_h, DP, S, OC, and EC) are labeled according to the nomenclature in MAX UnMix with the exception of q, which refers to kurtosis in the SGG function of Egli (2003). Specimen G010 (ARM demagnetization) and Birch-05 (IRM demagnetization) are lake sediments from Egli (2003) and Lascu and Plank (2013), respectively. Specimen TRA-050 (backfield remanence data up to 1T) is an Eocene paleosol B-horizon.

Specimen	**Method**	**Component 1**						**Component 2**						**Component 3**					
		Bh	***Dp***	***S***	***q***	***OC***	***EC***	***Bh***	***Dp***	***S***	***q***	***OC***	***EC***	***Bh***	***Dp***	***S***	***q***	***OC***	***EC***
G010	Max UnMix	1.37	0.32	0.87	-	0.72	0.73	1.88	0.14	1.09	-	0.18	0.18	2.24	0.24	1.10	-	0.10	0.09
	GECA	1.34	0.34	0.60	2.10	-	0.66	1.85	0.15	1.00	2	-	0.24	2.17	0.25	0.95	2.00	-	0.11
	IRM-UnMix	-	-	-	-	-	-	-	-	-	-	-	-	-	-	-	-	-	-
	IRM-CLG	1.41	0.35	-	-	-	0.78	1.88	0.15	-	-	-	0.15	2.30	0.20	-	-	-	0.07
Birch-05	Max UnMix	1.19	0.38	0.72	-	0.57	0.57	1.58	0.27	0.71	-	0.43	0.43	-	-	-	-	-	-
	GECA	1.12	0.44	0.44	2.10	-	0.52	1.64	0.20	1.00	2.00	-	0.48	-	-	-	-	-	-
	IRM-UnMix	1.09	0.34	-	-	-	0.43	1.58	0.24	-	-	-	0.57	-	-	-	-	-	-
	IRM-CLG	1.13	0.34	-	-	-	0.43	1.58	0.27	-	-	-	0.57	-	-	-	-	-	-
TRB-050	Max UnMix	2.66	0.34	1.09	-	0.73	0.76	1.51	0.51	0.64	-	0.27	0.24	-	-	-	-	-	-
	GECA	2.64	0.36	-0.75	1.79	-	0.80	1.44	0.67	0.45	2.19	-	0.20	-	-	-	-	-	-
	IRM-UnMix	2.65	0.32	-	-	-	0.64	1.87	0.73	-	-	-	0.36	-	-	-	-	-	-
	IRM-CLG	2.65	0.32	-	-	-	0.71	1.70	0.58	-	-	-	0.29	-	-	-	-	-	-

Chapter 6

Pedogenic magnetite is conservative in different soil types developed under uniform climate

6.1 Synopsis

Non-detrital magnetic minerals occur in soil as a result of a complex set of processes that are controlled by soil forming factors during pedogenesis. Interpretations of paleoclimate and paleoenvironment based on magnetic mineral assemblages in paleosols are complicated by the difficulty of distinguishing magnetic mineral populations that are controlled by climate and soil moisture from populations that are more sensitive to other processes. Here, we present evidence that grain-size specific magnetic properties, such as the frequency dependence of susceptibility and the ratio of anhysteretic to isothermal remanent magnetization, are insensitive to changing vegetation in soils developing under uniform climate, topography, and on similar parent material along the forest-prairie ecotone in NW Minnesota. Quantitative unmixing of coercivity spectra and first-order reversal curve diagrams across the transect support an easily identifiable fraction of fine-grained pedogenic magnetite that is highly consistent regardless of vegetation. In contrast, detrital magnetite is more abundant in prairie soils compared with forest soils indicating a partitioning in the preservation and/or deposition of detrital magnetite in

soils developing under variable vegetation. This work highlights the need for careful identification of magnetic mineral populations in soils and sediments prior to making climatic and environmental interpretations.

6.2 Introduction

Magnetic properties of soils are an important archive of the climatic and environmental conditions present during soil formation (*Maher et al.*, 1994; *Maher and Thompson*, 1995; *Maher*, 1998, 2007; *Geiss and Zanner*, 2007; *Geiss et al.*, 2008; *Balsam et al.*, 2011; *Orgeira et al.*, 2011; *Long et al.*, 2011; *Liu et al.*, 2012; *Maxbauer et al.*, 2016a). Fine grained superparamagnetic (SP) and stable single domain (SSD) magnetite are produced by microbially mediated redox processes associated with wet and dry cycling in well-drained soils (*Maher*, 1998; *Orgeira et al.*, 2011). Soil formed magnetite is often exposed to oxic conditions that promote partial maghemitization during dry periods (*van Velzen and Dekkers*, 1999; *Chen et al.*, 2005). This population of SP/SSD magnetite and partially-oxidized magnetite, referred to together as pedogenic magnetite, is integrated into the pre-existing population of detrital magnetic minerals, often of coarser grain sizes, that are derived from physical weathering of parent material and/or deposited by eolian processes. Mixtures of both pedogenic and detrital magnetic minerals are subjected to a range of pedogenic processes that vary in response to soil forming factors (climate, vegetation, topography, time, and parent material (*Jenny*, 1941)) and act to produce, transform, or destroy magnetic minerals (*Liu et al.*, 2012). As a result, researchers interested in interpreting the ambient climate conditions during soil formation are challenged to disentangle mixed magnetic mineral assemblages in order to relate magnetic properties of soils with climate (*Liu et al.*, 2012; *Hatfield*, 2014; *Heslop*, 2015; *Maxbauer et al.*, 2016a).

Most studies focus on interpreting soil sequences where climate varies in order to determine empirical relationships between soil magnetic properties and mean annual precipitation (MAP) or mean annual temperature (MAT) (*Maher et al.*, 1994; *Maher and Thompson*, 1995; *Porter et al.*, 2001; *Geiss et al.*, 2008; *Long et al.*, 2011; *Hyland et al.*, 2015). Magnetic paleoclimate proxies have proven to be powerful tools for reconstructing climate variability, particularly on the Chinese Loess Plateau (*Liu et al.*,

2012). However, regional differences and large uncertainties associated with magnetic proxies currently limit their applicability in other systems and in deep-time (*Maher and Possolo*, 2013; *Heslop and Roberts*, 2013; *Maxbauer et al.*, 2016a). Targeted studies investigating the influence of other soil factors have improved our understanding into how the duration of soil development (*Stinchcomb and Peppe*, 2014; *Maher and Hu*, 2006; *Vidic et al.*, 2004; *Fine et al.*, 1989), parent material (*Hanesch and Scholger*, 2005; *Blundell et al.*, 2009; *Boyle et al.*, 2010), and topography (*de Jong et al.*, 1998, 2000) impact magnetic mineralogy of soils. Yet, details of how soil processes that vary relative to vegetation cover can deferentially impact pedogenic and detrital magnetic minerals are not well constrained.

Here, we investigate magnetic properties of soils forming across the forest-to-prairie transition in NW Minnesota to evaluate the influence of changing vegetation and soil type on populations of detrital and pedogenic magnetic minerals (Figures 6.1, A.1, A.2, and A.3). Soils along the study transect have been developing on Des Moine Lobe glacial till capped by a thin layer of loess since the retreat of the last glacial (*Severson and Arneman*, 1973; *Lusardi et al.*, 2011). Climate across the transect is highly uniform (MAT = 4.6 °C, MAP = 650 mm yr^{-1}; data from the PRISM Climate Group, Oregon State University, `http://prism.oregonstate.edu`, 9 March 2016; Fig. A.4) and all soils were sampled from stable uplands on relatively subtle topography (see Figure 6.1) that has been mostly undisturbed (see Figures A.1, A.2, A.3 and discussion below). Vegetation differences along the transect are controlled by episodic burning, which acts to reestablish prairie post-burning (*Severson and Arneman*, 1973; *Clark*, 1990). We expect that if pedogenic production of magnetic minerals is controlled by climate that we will observe consistency in magnetic properties that isolate only the pedogenic population of magnetic minerals. In contrast, variability in magnetic properties can be taken as an indication that soil processes governed by vegetation changes are controlling magnetic mineral formation and/or dissolution.

6.3 Methods

Soil samples were collected from a combination of freshly dug soil pits, slide-hammer cores, and augered samples. Augered samples were collected from the inside of soil clods

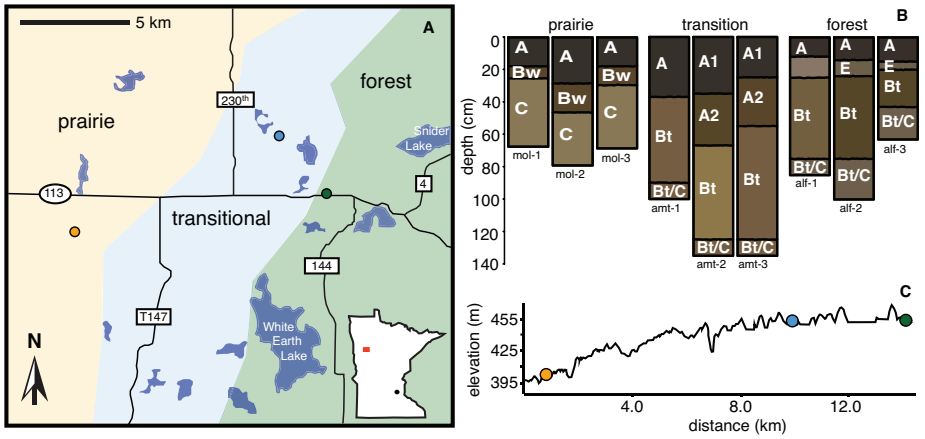

Figure 6.1: Site details and soil profiles. (**A**) Map of soil sampling localities within Minnesota (inset shown in bottom left of panel A, sampling locality is highlighted by the orange square, the black dot indicates Twin Cities area). Sampling localities within forest (dark green), prairie (orange), and transitional (blue) zones indicated with colored symbols. (**B**) Soil profiles and horizon designations for A, E, B, and C horizons. Labels below profiles correspond to specimen labels included in the Supplemental File. (**C**) Elevation profile for sampling sites along transect.

to avoid contamination. Soil color for wet samples was recorded using a Munsell color chart. All samples were dried, lightly crushed to homogenize, and seived to remove soil particles larger than 5 mm. Specimens for magnetic measurements were prepared by packing soil samples into diamagnetic plastic cubes and securing with a non-magnetic potassium silicate adhesive. Magnetic measurements were conducted at the Institute for Rock Magnetism at the University of Minnesota. All specimens in this study (n = 98) were evaluated for magnetic susceptibility (χ, m^3kg^{-1}), frequency dependence of susceptibility (χ_{fd}, %), isothermal remanent magnetization (IRM, Am^2kg^{-1}), anhysteretic remanent magnetization (ARM, Am^2kg^{-1}), and hysteresis properties. Magnetic susceptibility was measured at low (465 Hz, low frequency susceptibility is reported as χ) and high (4650 Hz) frequencies using a Magnon variable frequency susceptibility meter in an alternating current (AC) field of 300 Am^{-1}. χ_{fd} was calculated as a percentage, where $\chi_{fd} = (\chi_{465} - \chi_{4650})/\chi_{465} \times 100$. IRM was imparted using three pulses of a 100 mT direct current (DC) field in a pulse magnetizer and ARM was imparted in a peak alternating field (AF) of 100 mT in the presence of a weak DC bias field of 50 μT. Both IRM and ARM were measured using a 2G Enterprises 760-R SQUID magnetometer

within a shielded room with a background field of less than 100 nT. The susceptibility of ARM (χ_{ARM}, mA^{-1}) is calculated by dividing ARM by the bias field. Enhanced and background samples were determined by threshold criteria for χ_{fd} and χ_{ARM}/IRM, where specimen with χ_{fd} >2% and $\chi_{ARM}/IRM > 4.5 \times 10^{-4}$ mA^{-1} were categorized as enhanced and all other specimen were determined to be background.

Hystersis loops and backfield remanence curves were measured using a Princeton Measurements Corporation Micromag vibrating sample magnetometer (VSM) at room temperature in fields up to 1 T. Saturation magnetization (M_s, Am^2kg^{-1}) and coercivity (B_c, mT) are determined from hysteresis loops, while saturation remanent magnetization (M_{rs}, Am^2kg^{-1}) and coercivity of remanence (B_{cr}, mT) are calculated from backfield curves (*Tauxe et al.*, 2014). Coercivity spectra were derived for all specimens as the absolute value of the first derivate of backfield curves. Coercivity unmixing was performed using MAX UnMix (*Maxbauer et al.*, 2016c), a new program for coercivity unmixing based on previous work (*Kruiver et al.*, 2001; *Heslop et al.*, 2004; *Egli*, 2003) (available online at `www.irm.umn.edu/maxunmix`).

A subset of samples, both background and enhanced, were analyzed using more sophisticated measurements in order to better constrain grain size distributions and magnetic mineralogy. An initial room temperature (300 K) remanence (RT-$SIRM$) imparted using a 5 T DC field (followed by 2.5 T pulse along same axis to minimize recoil within system) was measured during cooling to 20 K and warming back to room temperature using a Quantum Design Magnetic Properties Measurement System (MPMS). Field cooled (FC) and zero-field cooled (ZFC) remanence (2.5 T) was measured on cooling from 300 K to 20 K. RT-$SIRM$ and FC-ZFC curves reveal remanence loss at diagnostic transitions, for example the Verwey transition for magnetite. To characterize magnetic grain size distributions, first order reversal curve (FORC) diagrams were measured using a Micromag-VSM. All FORC diagrams were processes using FORCinel v3.0 and smoothed using the simple smooth functionality with a smoothing factor of 5 (*Harrison and Feinberg*, 2009). Decomposition of FORC diagrams was performed using FORCem (*Lascu et al.*, 2015). FORCem unmixes FORC data using a principle component approach that allows for quantification of end member contributions to magnetization. The graphical output from the PCA analysis is provided in Figure A.11.

6.4 Results

Magnetic susceptibility (χ, Fig. 6.2a) and saturation magnetization (M_s, Fig. 6.2b) show similar trends with depth in soil profiles. χ ranged between 4×10^{-7} and 15×10^{-7} Am^2kg^{-1}. M_s ranges from 3.8×10^{-2} to 22.6×10^{-2} Am^2kg^{-1}. Both χ and M_s are significantly greater in the enhanced prairie specimens compared with enhanced specimens in the forest and transitional soils ($p < 0.001$ for unpaired t-tests and Wilcoxon Signed Rank tests; see Methods and Fig. 6.2 for enhancement criteria). Frequency dependence of susceptibility (χ_{fd}, Fig. 6.2d) and the ratio of the susceptibility of anhysteretic remanent magnetization to isothermal remanent magnetization (χ_{ARM}/IRM, Fig. 6.2e) show similar trends with depth that are mostly consistent between profiles ($p > 0.05$ for all unpaired t-tests and Wilcoxon Signed Rank tests). χ_{fd} and χ_{ARM}/IRM are both increased in the upper soil horizons for all profiles and display trends consistent with a classical magnetically enhanced soil profile (*Maher*, 1998; *Orgeira et al.*, 2011; *Maxbauer et al.*, 2016a). Coercivity (B_c, Fig. 6.2c) ranges primarily from ~4-15 mT and shows remains fairly consistent with depth in profiles. The mean B_c of enhanced forest specimen (8.5 ± 0.37 mT, reported error is one standard deviation) is significantly greater than both prairie and transitional enhanced specimen (5.9 ± 0.43 mT and 5.9 ± 1.44 mT, respectively; $p < 0.001$ for all t-tests and Wilcoxon Signed Rank tests). In contrast, coercivity of remanence (B_{cr}, Fig. 6.2f) is consistent for enhanced specimen across the transect (all p-values > 0.05 for t-tests and Wilcoxon Signed Rank tests) with enhanced values ranging from 32.8 - 58.5 mT. Results for all parameters are available in Supplementary Fig. A.5.

Unmixing coercivity distributions derived from backfield remanence curves resulted in a three component model fit for all specimens. Each component is described by its characteristic median coercive field (B_h) and dispersion parameter (DP; one standard deviation in $\log_{10}$ space) (*Maxbauer et al.*, 2016c). Example fit results are shown in Fig. 6.3. Component parameters were consistent across the transect and did not show systematic variations with changes in vegetation and soil type. A high coercivity component (HCC, component 1) is characterized by a B_h of 1.97 ± 0.02 $\log_{10}$ mT (93.7 mT) and a DP of 0.29 ± 0.02. Mean B_h for an intermediate covercivity component (ICC, component 2) is 1.38 ± 0.03 $\log_{10}$ mT (24.0 mT) with a DP of 0.35 ± 0.02. Lastly, a

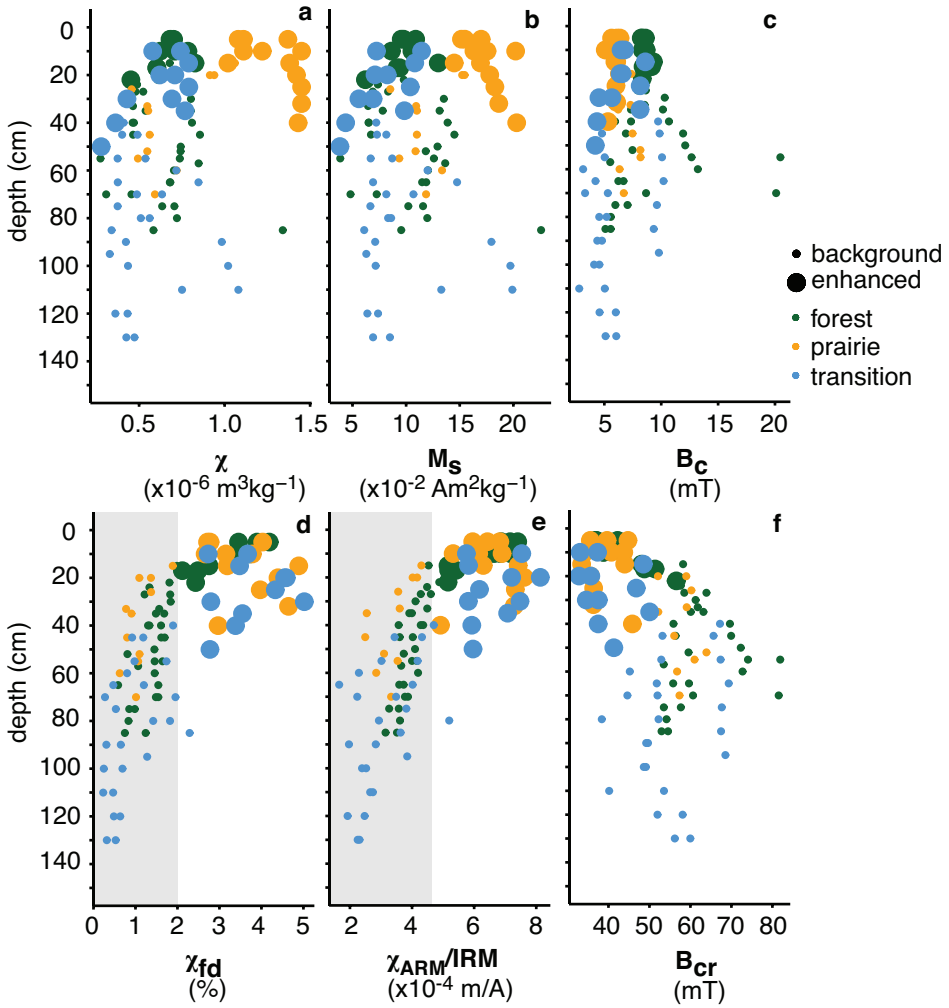

Figure 6.2: Magnetic properties with depth for soil transect. Data reported here for magnetic susceptibility (**a**), saturation magnetization (**b**), coercivity (**c**), frequency dependence of susceptibility (**d**) Background and enhanced specimen in all cases are determined by criteria highlighted by shaded boxes in panels **d** and **e**, where enhanced specimen where greater than thresholds for χ_{fd} and χ_{ARM}/IRM in both cases.

low-coercivity component (LCC, component 3) has mean B_h of 0.53 ± 0.10 $\log_{10}$ mT (3.4 mT) and a DP of 0.44 ± 0.09. Skewness for the HCC, ICC, LCC, is 0.86 ± 0.04, 0.089 ± 0.04, and 1.04 ± 0.14 respectively (note that skewness of 1 is equivalent to a normal distribution *Maxbauer et al.* (2016c)).

First-order reversal curves for background and enhanced specimen from each profile record contributions from three distinct end members (Fig. 6.5). The strong isolated contributions along the central ridge observed in the first end member (EM-1) is diagnostic of non-interacting SSD magnetite (*Lascu et al.*, 2015; *Roberts et al.*, 2014) and the spread about the horizontal axis observed in the second end member (EM-2) is characteristic of MD magnetite (*Roberts et al.*, 2014) (Fig 6.5). The observed FORC distribution for the third end member (EM-3) is consistent with a mixture of interacting SP and SSD grains of magnetite (*Roberts et al.*, 2014) (Fig. 6.5). Contributions of EM-1 and EM-2 to overall magnetization are variable, but mostly consistent between studied background specimens (Fig. 6.5). There is a clear distinction between enhanced specimen and background specimen driven by an increase in contribution of EM-3, and within enhanced specimen forest and transitional specimen are generally more enriched in EM-3 compared with prairie specimen (Fig. 6.5). We interpret EM-1 and EM-2 to represent detrital magnetite that is inherited from parent material, while EM-3 is interpreted as pedogenic magnetite.

Temperature dependent experiments (described in Methods) indicate that magnetite, and partially oxidized magnetite are the dominant magnetic mineral for all studied samples (see Supplementary Figs. A.6 and A.7). Contributions of so-called 'antiferromagnetic' minerals such as goethite and hematite are minimal. However, goethite appears to be present in enhanced forest specimen (Fig. reffig:fczfc) and iron concretions were observed during sampling in parent materials of forest soils. The presence of goethite in forest soils may be important to distinguishing variable soil processes across this soil transect and we discuss this in more detail below.

6.5 Discussion and Conclusions

This work represents, to our knowledge, the most rigorous evaluation of the effects of changing vegetation on magnetic mineral production in soils that developed under

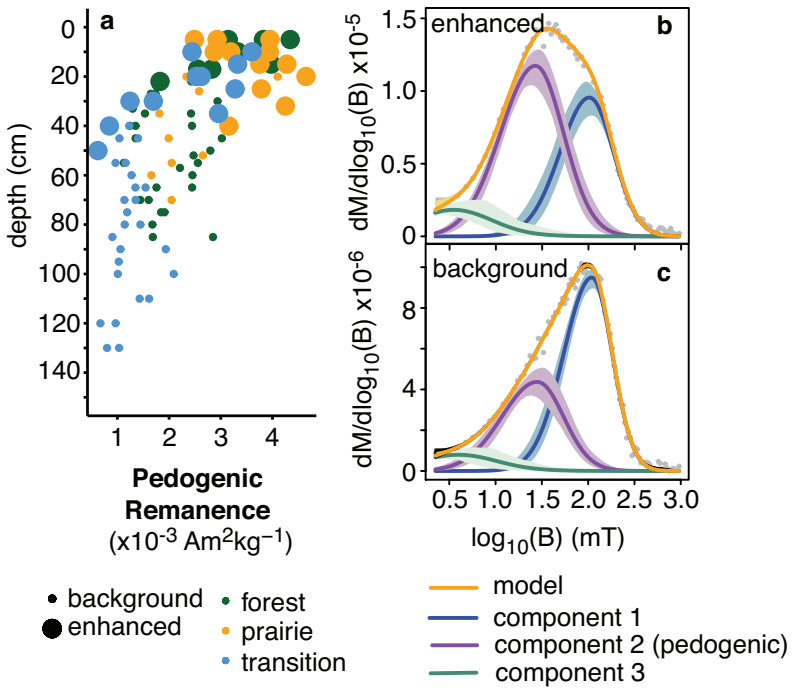

Figure 6.3: Results of coercivity analysis showing pedogenic remanence (**a**) and an example fit for enhanced (**b**, M-2-01) and background (**c**, M-2-09) specimen. Pedogenic remanence is calculated based on the proportion of remanence at 1 T (M_r) held by component 2 within the mixing model (*Maxbauer et al.*, 2016c). Parameters describing component 2 are highly consistent with observations of pedogenic magnetite from previous work (*Egli*, 2004b; *Geiss et al.*, 2008; *Maxbauer et al.*, 2016a).

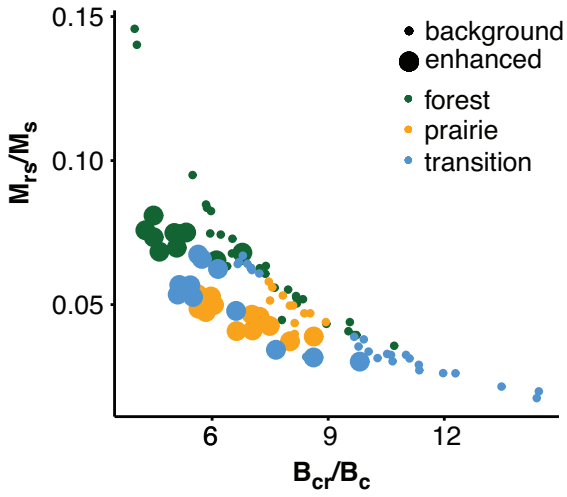

Figure 6.4: Day Plot of magnetic hysteresis properties. Background and enhanced specimen determined by criteria highlighted in Fig. 6.2d,e. Clear trends can be observed for background and enhanced specimen from all study sites and strong differentiation is observed between the enhanced forest and prairie data.

uniform climate. The observed consistency in χ_{fd} and χ_{ARM}/IRM in topsoils across the study transect suggest that biomediated redox processes (*Orgeira et al.*, 2011) leading to the production of SP/SSD magnetites in soils are mostly independent of the influence of variable soil type and vegetation. Further, the median coercivity and dispersion reported for the ICC from coercivity analyses agrees well with previous studies that have isolated pedogenic magnetites from soils ranging across the globe (*Egli*, 2004b; *Geiss et al.*, 2008; *Maxbauer et al.*, 2016a) and we interpret the ICC reported here to be pedogenic magnetite. Pedogenic magnetite contributes ~45% of M_r for enhanced forest and prairie specimens and shows a decreasing pattern with depth similar to trends observed in χ_{fd} and χ_{ARM}/IRM (Fig. 6.3a). There is also clear consistency in EM-3 from FORCem analysis (Fig 6.5) that strengthens the idea that pedogenically produced SP/SSD magnetite consistently dominates the magnetization of enhanced soil horizons across the transect. Together, our data set supports a pedogenic population of magnetite that is formed in soils independent of changing vegetation and that is comparable to pedogenic magnetite populations recovered in soils developing under variable conditions throughout the world.

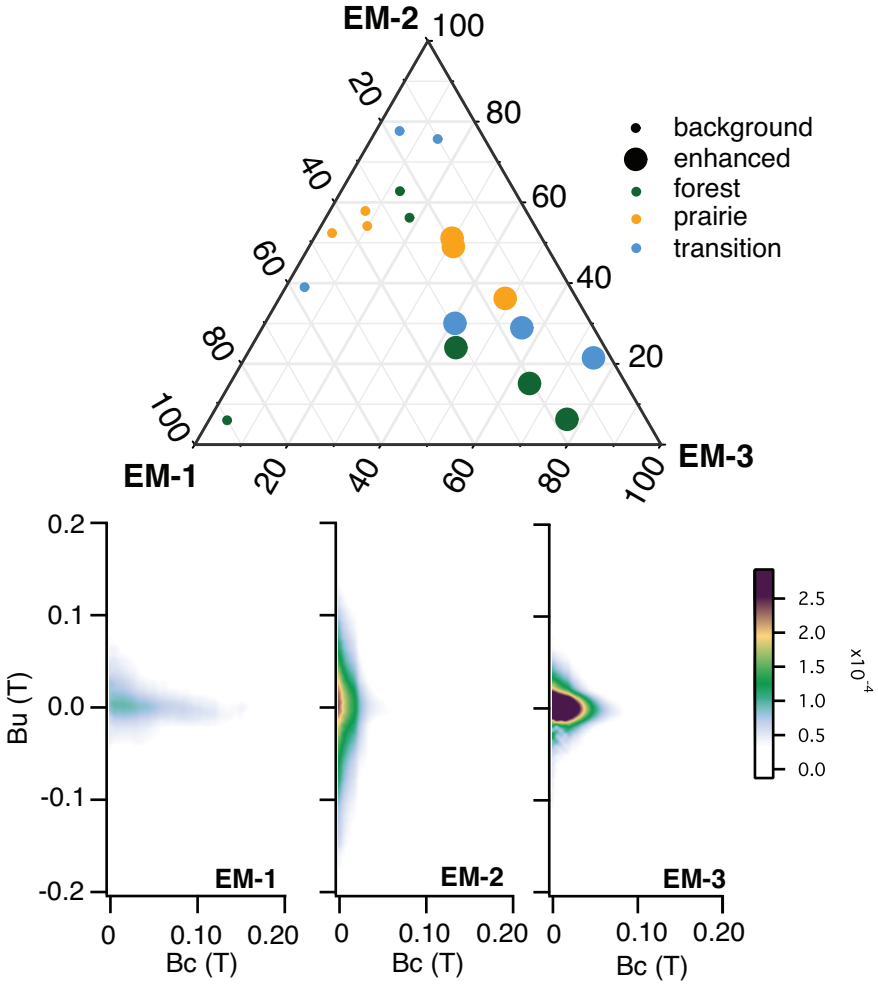

Figure 6.5: Ternary diagram and end member first-order reversal curve diagram results from FORCem analysis (*Lascu et al.*, 2015). EM-1 is interpreted to represent detrial single domain magnetite inherited parent material. Coarser, detrital magnetite in the multi-domain state is represented by EM-2. Pedogenic magnetite, a mixture of SP and SSD magnetite is represented by EM-3. All enhnaced specimen are enriched in pedogenic EM-3, however prairie soils have higher contributions from detrital EM-1 and EM-2. Examples of individual FORC diagrams are provided in Figs. A.8, A.9, and A.10. The color scale applied to all FORC diagrams.

Climatic interpretations based on magnetic mineralogy of paleosols are supported by the fundamental assumption that ambient climate conditions are the principal control on the production of fine-grained, SP/SSD magnetite in upper soil horizons. In order to test the predictive power of recent paleoprecipitation proxies based on pedogenic magnetite in Great Plains loessic soils (*Geiss et al.*, 2008) we reconstructed precipitation for each sampling zone based on the χ_{ARM}/IRM of the enhanced horizons (Fig. A.12). Estimates for mean annual precipitation (MAP) are within ∼8% of the observed value (Fig A.12) and have good agreement between sampling zones. These results suggest that pedogenic production of magnetite in soils is consistent enough with respect to changing vegetation that climatic inferences can still be made based on magnetic mineral assemblages. However, despite the general consistency in grain-size dependent properties across the transect, important differences observed in the induced magnetization and coercivity of enhanced topsoils may complicate climatic interpretations (Fig. 6.2a,b). For example, pedogenic susceptibility (χ_{ped}, equivalent to the $\chi_{enhanced} - \chi_{background}$), which is used as a climatic indicator (*Maher et al.*, 1994; *Maher and Thompson*, 1995), is much greater in prairie soils ($57.5 \pm 26.5 \times 10^{-8}$ m^3kg^{-1} compared to forest and transitional soils ($8.43 \pm 10.2 \times 10^{-8}$ and $11.5 \pm 27.9 \times 10^{-8}$ m^3kg^{-1}, respectively) and overall variability for χ_{ped} between individual profiles is extremely high. Significant increases in χ and M_s indicate that the overall concentration of magnetic material in prairie topsoils is elevated relative to forest and transitional soils. Elevated induced magnetization is associate with decreased B_c in enhanced prairie specimen relative to forests (Fig. 6.2c). These differences suggest variable soil processes act across the study transect and complicate climatic interpretations made from parameters such as χ, χ_{ped}, and M_s.

Increased χ and induced magnetization in prairie soils indicates an overall increase in the concentration of magnetic material in prairie soils compared to forest and transitional soils. Remanent magnetization properties across the transect are more conservative (Fig. 6.2 and S2), especially for the grain-size sensitive remanent property $\chi ARM/IRM$ as discussed above. End member contributions from FORCem unmixing (Fig. 6.5) suggest that this increase in concentration of magnetic material in prairie soils is due to a relative enrichment in prairie soils (or, alternatively, depletion in forests and transitional soils) of detrital MD magnetite (EM-2, see Fig. 6.5). An important difference between unmixing FORC diagrams and coercivity distributions is that the latter

only considers remanent magnetization, and so grains with stronger induced magnetizations will be underrepresented relative to grains with strong remanence. The increased contributions of detrital end members to the induced magnetization is clear from the FORCem analysis and helps to explain the lower coercivity and stronger induced magnetization observed in prairie soils.

It is important the constrain the soil processes that lead to the relative enrichment of detrital magnetite in prairie soils, which may be the result of either a loss of magnetite from forest soils or additional inputs into prairie soils. A possible pathway for the production of magnetite in prairie soils may be burning, which is known to produce fine grained magnetite in top soil and is a key factor in determing the boundary of the forest-to-prairie transition in this region. However, if burning is the primary process responsible for the increased induced magnetization in prairie soils we would expect the elevated magnetization to be restricted to the uppermost 5-10 cm of soil. Yet, we observe elevated induced magnetization down to 40 cm depth in prairie soils (Fig. 6.2a,b). Magnetite formed during burning is often fine-grained and resembles the type of magnetite formed during pedogenesis. Increased magnetizations in prairie soils is driven by contributions from components with coarser magnetic grain sizes, for example EM-2 in the FORCem analysis is similar to MD magnetite (Fig. 6.5) that would be unlikely to have originated from processes related to burning. Finally, although early work highlighted burning as a process that can produce magnetites in top soils, more recent work has shown that it is not likely to be a primary driver for magnetic enhancement (*Quinton et al.*, 2011). We suggest that instead of additional magnetite being produced in prairie soils, the enrichment of detrital magnetite in prairie soils is a results of selective removal of detrital magnetite in forest soils. Dissolution of magnetite is facilitated by increasingly acidic soil conditions (*Cornell and Schwertmann*, 2003; *Maher et al.*, 2003a). Measurements of pH on soil horizons from this study are in agreement with previous work (*Severson and Arneman*, 1973) and show that forest soil, particularly top soil, is more acidic compared to prairie and transitional soils Table 6.1. Goethite is favored in soils with lower pH (*Cornell and Schwertmann*, 2003; *Maher et al.*, 2003a) and is detectable only in enhanced forest top soil where conditions are most acidic (forest A horizons pH = 6.85). We suggest that detrital magnetite in forest soils is removed, possible in favor of goethite, via dissolution and reprecipitation of iron into other phases.

An equilibrium balance between magnetic mineral formation and dissolution with respect to soil conditions is essential for a stable populations of magnetic minerals to develop in soils in response to long term climatic and environmental conditions. Here, we present evidence that supports two important conclusions regarding mixed assemblages of magnetic minerals in soils. First, contributions from detrital magnetic minerals to the overall magnetization of soil samples complicate signals from pedogenic minerals. Detrital magnetic minerals are not likely to be formed in soil, are subject to dissolution processes, and so are very unlikely to be in equilibrium with climatic conditions. As a result, climatic interpretations based on bulk magnetic properties of soils without removal of detrital signals are likely to be poorly constrained and uncertain. Second, the SP/SSD population of magnetite in enhanced soil horizons across the study transect is highly consistent, is easily identifiable using a range of targeted magnetic parameters and techniques, and indicates that the processes controlling pedogenic production of magnetite is independent of vegetation cover. Dissolution processes effecting detrital magnetic minerals are also likely to impact pedogenically produced magnetites. However, based on the consistency reported here in pedogenic populations for magnetites across the transect, it is apparent that equilibrium conditions are reached between formation and dissolution processes with respect to the ambient climatic conditions.

Table 6.1: Average pH for soil horizons across study transect. Standard deviations are reported in parentheticals. All horizons match those displayed in Fig. 6.1.

Horizon	**Prairie**	**Transitional**	**Forest**
A	7.74 (0.25)	7.85 (0.23)	6.85 (0.31)
A2	-	8.07 (0.05)	-
Bw	7.87 (0.16)	-	-
E	-	-	7.03 (0.27)
Bt	-	7.94 (0.22)	7.03 (0.27)
BtC	-	-	7.15 (0.20)
C	8.01 (0.22)	7.67 (0.39)	-

Chapter 7

Magnetic minerals as recorders of weathering, diagenesis, and paleoclimate: a core-outcrop comparison of Paleocene-Eocene paleosols in the Bighorn Basin, WY, U.S.A.

The contents of this section were originally published in the journal Earth and Planetary Science Letters *under the title 'Magnetic minerals as recorders of weathering, diagenesis, and paleoclimate: a core-outcrop comparison of Paleocene-Eocene paleosols in the Bighorn Basin, WY, U.S.A.'. See reference to Maxbauer et al. (2016b) for details. This work is included below it its published form with permission of all authors.*

7.1 Synopsis

Magnetic minerals in paleosols hold important clues to the environmental conditions in which the original soil formed. However, efforts to quantify parameters such as mean

annual precipitation (MAP) using magnetic properties are still in their infancy. Here, we test the idea that diagenetic processes and surficial weathering affect the magnetic minerals preserved in paleosols, particularly in pre-Quaternary systems that have received far less attention compared to more recent soils and paleosols. We evaluate the magnetic properties of non-loessic paleosols across the Paleocene-Eocene Thermal Maximum (a short-term global warming episode that occurred at 55.5 Ma) in the Bighorn Basin, WY. We compare data from nine paleosol layers sampled from outcrop, each of which has been exposed to surficial weathering, to the equivalent paleosols sampled from drill core, all of which are preserved below a pervasive surficial weathering front and are presumed to be unweathered. Comparisons reveal an increase in magnetization in outcrops compared with core equivalents, which is principally driven by secondary hematite production. Authigenic hematite production in outcrops presents a complication for goethite-hematite based paleoprecipitation proxies where estimates will be biased toward drier climate regimes. The occurrence of low coercivity minerals is more consistent between core and outcrop. However, we propose an alteration process for pedogenic magnetite that is observed in both core and outcrop, where pedogenic magnetite becomes progressively oxidized leading to higher mean coercivities and broader coercivity distributions compared to modern pedogenic magnetite. This combination of diagenetic processes and surface weathering influences the magnetic properties of paleosols. Despite these changes, magnetic enhancement ratios from B-horizons correlate with independent MAP estimates from geochemical proxies, which suggests that paleoprecipitation information is preserved. Future work should continue to address these complications by developing useful protocols that isolate the magnetic properties that are most resistant to alteration and remain strong indicators of MAP and climate.

7.2 Introduction

The magnetic properties of soils and paleosols are often used to make environmental and climatic interpretations throughout the geologic record (see reviews by *Maher*, 1998; *Maxbauer et al.*, 2016a). This is possible largely because magnetic minerals such as goethite (FeOOH), hematite ($\alpha-Fe_2O_3$), magnetite (Fe_3O_4), and maghemite ($\gamma-Fe_2O_3$) form through a combination of processes that are often critically dependent

on soil moisture (*Maxbauer et al.*, 2016a, and references therein). Many studies have established empirical, quantitative relationships between pedogenic iron oxide minerals and the mean annual precipitation (MAP) under which the soil formed (e.g., *Maher and Thompson*, 1995; *Geiss et al.*, 2008; *Long et al.*, 2011; *Hyland et al.*, 2015). These quantitative methods, along with earlier more qualitative interpretations, hold enormous potential for understanding environmental variability in the deep past. Two recent studies have highlighted the potential for methods based on the ratio of goethite-to-hematite (G/H; *Hyland et al.*, 2015) and direct estimates of pedogenically produced magnetite (*Geiss et al.*, 2008). The G/H method presented by *Hyland et al.* (2015) was calibrated using modern soils that formed over a wide range of MAP values (200 - 3000 mm yr^{-1}). In contrast, the calibrations of *Geiss et al.* (2008) are similar to other pedogenic magnetic susceptibility based proxies (e.g., *Maher and Thompson*, 1995) in that they only range up to ∼1000 mm yr^{-1}. However, *Geiss et al.* (2008) offered calibrations between MAP and magnetic enhancement ratios (M_B/M_C, where M is the mean value of a generic magnetic property for the B and C soil horizons) or direct measures of pedogenic magnetite (e.g., ratio of anhysteretic to isothermal remanence) that may prove useful in expanding methods developed on loessic soils into other soil types and climatic regimes.

Most paleosol studies are based on observations from Quaternary or younger loess-paleosol sequences (e.g., *Geiss et al.*, 2008; *Maher and Thompson*, 1995; *Maher et al.*, 2003a) so little is known about the magnetic properties of more ancient paleosols as paleoclimatic indicators. The few studies that examine this topic report low magnetic susceptibility (χ) in ancient paleosols compared to modern soils (*Rankey and Farr*, 1997; *Cogoini et al.*, 2001; *Retallack et al.*, 2003; *Tramp et al.*, 2004). However, in some ancient systems there is evidence for preservation of pedogenic magnetic mineral assemblages that may be useful for reconstructing past environmental conditions (*Rankey and Farr*, 1997; *Cogoini et al.*, 2001; *Tramp et al.*, 2004; *Morón et al.*, 2013; *Hyland et al.*, 2015). Despite these exciting suggestions, there remains a general lack of information regarding the role of diagenesis and weathering in altering the original magnetic mineral assemblages in ancient paleosols, which limits our ability to interpret environmental conditions from ancient paleosol sequences with confidence. We must learn more about the diagenetic changes that affect soil magnetic mineral assemblages throughout their

transformation into paleosols, throughout the subsequent burial history and exposure to chemically variable groundwater, and throughout their weathering history (for a recent review on magnetic mineral diagenesis, see *Roberts*, 2015).

Here, we examine these processes in paleosols preserved at the Polecat Bench locality in the Bighorn Basin, Wyoming (Figure 7.1). The Bighorn Basin Coring Project (BBCP; *Clyde et al.*, 2013) recovered nearly 900 meters of sediment core from three localities in the Bighorn Basin, including Polecat Bench. Core scan images (Figure 7.2A) clearly indicate that oxidative weathering has altered sediment color to depths of up to 25 meters below the ground surface (*Clyde et al.*, 2013). This observation calls into question whether magnetic mineral assemblages in paleosol outcrops reflect the original pedogenic assemblage and the environmental conditions in which they formed. This question has important implications for applying most magnetic-based paleoprecipitation proxies to ancient systems since they assume that the magnetic minerals preserved in paleosols are pedogenic and are not significantly altered by subsequent diagenesis and late-stage weathering.

The presence of the same paleosols in both BBCP cores and nearby outcrops presents an opportunity to test whether surficial weathering of outcrops significantly affects magnetic mineral preservation. We present magnetic data from nine marker bed paleosols, which were sampled from both core and outcrop (Figure 7.3). All paleosols occur well below the oxidative weathering front in the sediment core and we assume that these sediments are largely unweathered compared to equivalent outcrop exposures (see Figure 7.2). Both core and outcrop paleosols have likely been subjected to various long-term diagenetic processes (for example, interaction with fluids and elevated temperatures post-burial and before exposure of the basin). We compare magnetic properties of the Bighorn Basin paleosols to those of some modern soils to evaluate the effects that diagenesis can have on magnetic mineral preservation, independent from weathering.

Our record spans the Paleocene-Eocene Thermal Maximum (PETM, 55.5 Ma), which was a rapid global warming event driven by a massive release of isotopically light carbon into the mixed atmosphere/ocean system (see review by *McInerney and Wing*, 2011). In the Bighorn Basin, the PETM was associated with a transient precipitation decrease that has been well documented in qualitative and quantitative paleoflora records (*Wing et al.*, 2005) and from paleosol geochemistry and morphology (*Kraus and*

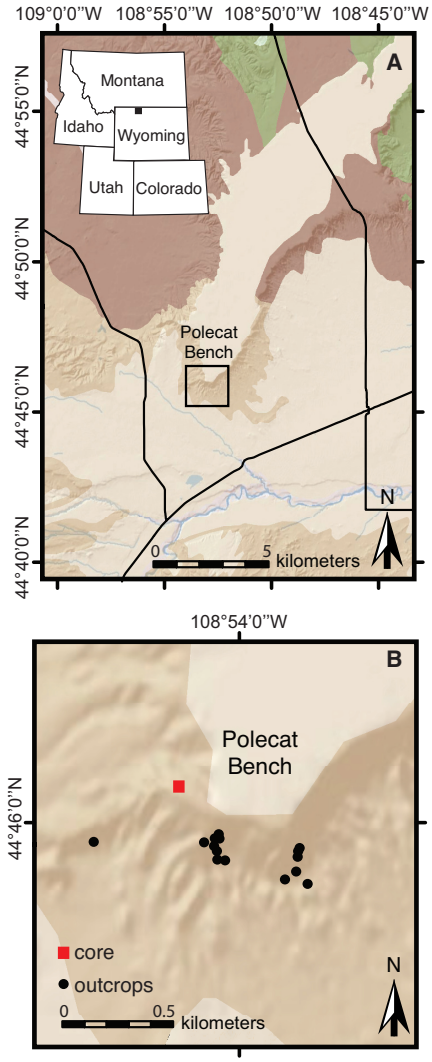

Figure 7.1: Maps of the study site at Polecat Bench in the Bighorn Basin, WY. **A.** Map of the northern Bighorn Basin. The highlighted and labeled box indicates the study area at Polecat Bench. The location of the study site in Wyoming is indicated in the inset of panel A. **B.** Polecat Bench locality with sampling locations indicated for outcrop paleosols (black circles) and coring location (red square). Color guide: darkest brown = Paleocene Fort Union Formation, dark tan = Paleocene-Eocene Willwood Formation, light tan = Quaternary gravels, and green = Cretaceous units.

Riggins, 2007; *Adams et al.*, 2011; *Kraus et al.*, 2015). We compare our rock magnetic record to a recent study of MAP estimates derived from geochemical weathering indices (*Kraus et al.*, 2015) to evaluate whether magnetic mineral assemblages in these paleosols record paleoprecipitation changes during the PETM.

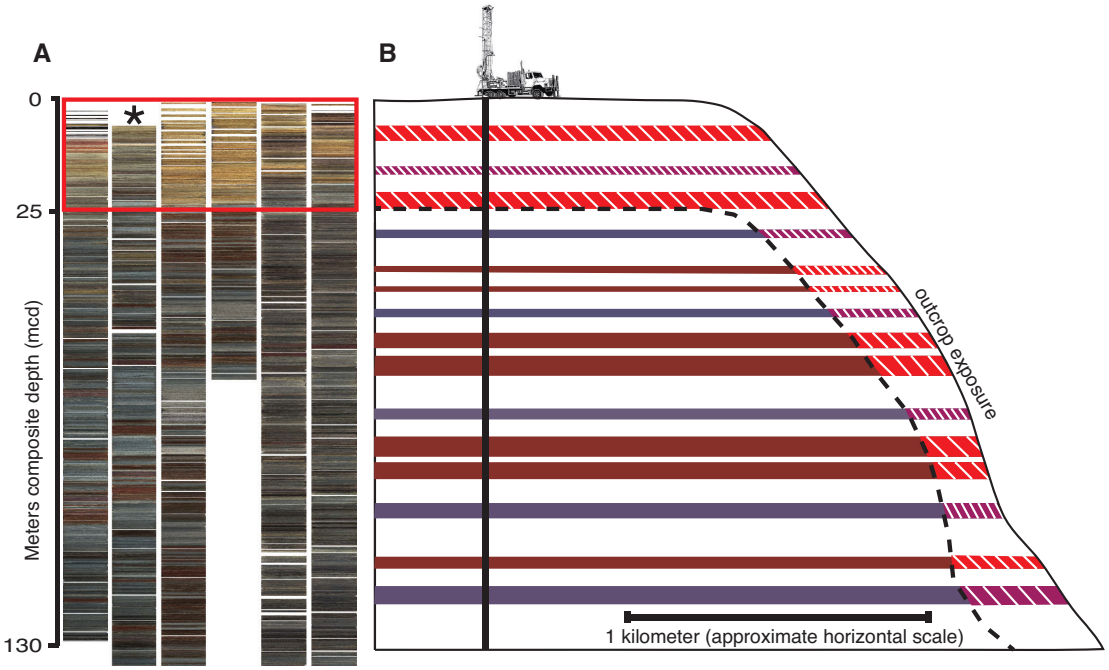

Figure 7.2: **A.** Line scan images from sediment cores recovered by the Bighorn Basin Coring Project (BBCP; Clyde et al., 2013). The approximate thickness of the weathering zone in sediment cores, as determined by color changes, is highlighted by the red box around the upper 25 meters of core. The asterisk in the red box highlights the Polecat Bench sediment core that is the focus of this study. **B.** Schematic illustration of how the weathering front (indicated with brighter, hashed colors) has affected outcrop exposures. Colored horizons indicate laterally continuous paleosols that are preserved in both core and outcrop. The drilling rig and black vertical line approximates a core location. Paleosols in the sediment core below the weathered zone are presumably relatively unweathered compared to their laterally equivalent exposure in outcrop.

7.3 Geological Setting

The Bighorn Basin in northwestern Wyoming is a NW-to-SE trending intermontane basin that formed in response to local subsidence and regional uplift during the Laramide orogeny throughout late Cretaceous to Paleogene time (Figure 7.1; *Gingerich*, 2001). Paleocene and Eocene sediments of the Willwood Formation are well exposed at the Polecat Bench locality in the northern reaches of the basin (*Gingerich*, 2001; *Kraus*, 2001). These sediments have been the focus of extensive research due to interest in biotic and climatic changes associated with the PETM (*Clyde et al.*, 2013; *Bowen et al.*, 2015).

Paleosols within the Willwood Formation, including the marker bed paleosols studied here, have all been described extensively by previous workers (*Kraus*, 2001; *Kraus and Hasiotis*, 2006; *Kraus and Riggins*, 2007; *Smith et al.*, 2008; *Kraus et al.*, 2013, 2015). At Polecat Bench, paleosols are sorted into two general categories based on their B-horizon color. Red paleosols are characterized by a main red mudstone to silty mudstone B-horizon that is sometimes overlain by a grey or yellow-brown A horizon. Calcium carbonate nodules, slickensides, and grey mottles with red or purple rims are common in red paleosols and have been interpreted to represent generally well-drained and oxidizing conditions (*Kraus and Hasiotis*, 2006). In contrast, the purple paleosols are characterized by a purple mudstone B-horizon with abundant yellow-brown mottling and nodules, a lack of calcium carbonate nodules, abundant grey mottles with red rims, and slickensides (*Kraus and Hasiotis*, 2006).

Red paleosols are associated with generally dry climatic conditions where seasonal wetting and drying drove nucleation and growth of calcium carbonate nodules as well as the shrink-swell slickenside structures (*Kraus and Hasiotis*, 2006). Purple paleosols are interpreted to represent more poorly drained conditions likely reflecting increased moisture and precipitation (*Kraus and Hasiotis*, 2006; *Kraus and Riggins*, 2007). These qualitative interpretations of paleosol color and climatic conditions are reinforced by a semi-quantitative morphology index (*Adams et al.*, 2011) and quantitative geochemical weathering indices (*Kraus and Riggins*, 2007; *Kraus et al.*, 2013, 2015) that produce similar reconstructions for paleoprecipitation within the Bighorn Basin.

7.4 Methods

7.4.1 Sampling

All outcrop marker bed profiles were identified within the stratigraphic framework of *Gingerich* (2001) (also used by *Abdul Aziz et al.*, 2008). Previous work has established correlations between the *Gingerich* (2001) outcrop section and the sediment cores recovered by the BBCP (see *Bowen et al.*, 2015). We utilized these correlations and confirmed all relationships using line scan images prior to sampling of core sediments (see Figure 7.3). Depth below the surface for the Polecat Bench core studied here (core 2B) was converted to meters composite depth (mcd) following *Bowen et al.* (2015) using standards determined by the BBCP science team. All outcrop profiles were projected onto the mcd scale using either the top or base of paleosol B-horizons to anchor correlations.

In an effort to collect the freshest outcrop samples possible, and thus to mimic the sampling routine normally used in outcrop settings, the uppermost 0.5 to 1 m of rock was removed before paleosol samples were collected in the field. For each marker bed, samples were taken at 5 cm intervals through B-horizons and at 10 cm intervals through C (parent material) and A-horizons (when present). In order to assess the reproducibility of magnetic properties in individual paleosols, we collected additional profiles (with the number of profiles collected in parentheses) for four marker beds at lateral distances ranging from ∼10's of meters to nearly a kilometer from the original profile (see Figure 7.1): Purple-Red Mudstone (3), Red Mudstone (2), Purple-2 (3), and Top Red A (3). All designations for the studied paleosols and their stratigraphic order are indicated in Figure 7.3. This approach allows us to quantify magnetic variability in soils that were originally developed in subtly different settings across a landscape. These additional lateral profiles were sampled at 10 cm intervals through all horizons. Notably, no additional detail was derived from the 5 cm sampling resolution in the original profiles compared with the 10 cm sampling resolution in the additional profiles, which suggests that 10 cm resolution is sufficient to capture the important magnetic variability in these paleosols. Samples from correlative paleosols in the core were acquired at roughly 10 cm intervals, with occasional minor adjustments to accomodate the availability of sediment core remaining after previous sampling.

Sample preparation and magnetic measurements were performed at the Institute

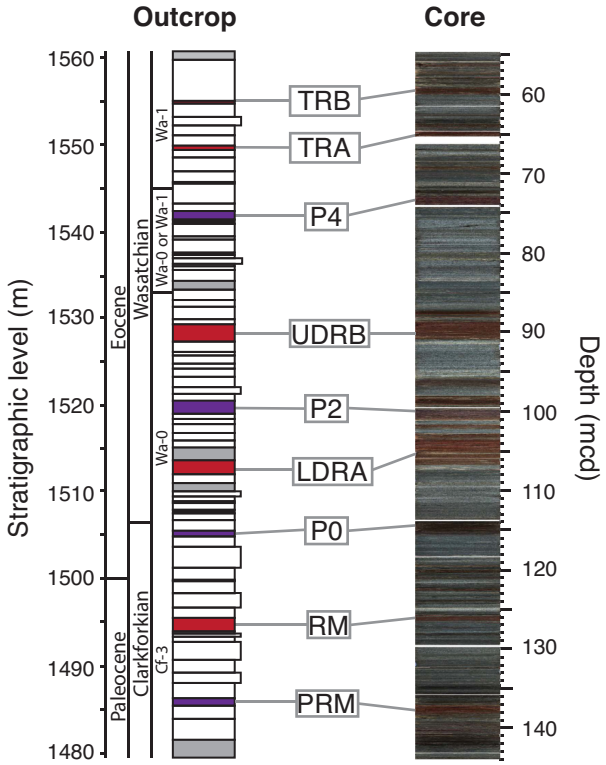

Figure 7.3: Correlations between outcrop stratigraphy (following Gingerich, 2001) and core stratigraphy. All correlations follow those of Bowen et al. (2015) and were independently confirmed from line scan images and during core sampling for this study. Marker paleosols in outcrop stratigraphy are denoted with red and purple. Marker bed abbreviations are as follows: TRB = Top Red B, TRA = Top Red A, P4 = Purple 4, UDRB = Upper Double Red B, P2 = Purple 2, LDRA = Lower Double Red A, P0 = Purple 0, RM = Red Mudstone, and PRM = Purple Red Mudstone.

for Rock Magnetism, University of Minnesota. Core and outcrop samples were placed into diamagnetic plastic cubes and were secured using a non-magnetic potassium silicate adhesive. Samples were neither crushed nor homogenized in order to avoid altering the natural grain size distribution of the paleosols, which can significantly impact grain size dependent magnetic properties (for example, anhysteretic remanent magnetization). However, multiple individual mudstone pieces were included in each cube and highly mottled and/or depleted rhizosphere zones were avoided during sampling. Each specimen underwent all of the magnetic measurements described below unless otherwise indicated. All B-horizon mean values come from individual paleosol profiles and are a mean of all B-horizon specimens measured for a particular profile and measurement. Comparisons between core and outcrop are between core profiles and individual outcrop profiles, even where an individual paleosol layer was collected from multiple outcrop profiles.

7.4.2 Magnetic Susceptibility

In-phase magnetic susceptibility (χ) was measured on all specimens (n = 376 outcrop, n = 169 core) at low (465 Hz) and high frequency (4650 Hz) using a Magnon variable frequency susceptibility meter in an alternating current (AC) field of 300 Am^{-1}. Reported values for individual specimens represent the mean of 4 replicate low frequency measurements. The frequency dependence of χ is commonly used in environmental magnetic studies of soils and paleosols as an indicator of the presence of ultrafine grained magnetite/maghemite that is close to the grain size threshold of stable single domain (SSD) and superparamagnetic (SP) magnetite (*Dearing et al.*, 1996b). Frequency dependence of susceptibilty ($\chi_{fd}\%$) was calculated, where $\chi_{fd}\% = [(\chi_{465Hz} - \chi_{4650Hz})/\chi_{465Hz}] \times 100\%$.

7.4.3 IRM and ARM

An isothermal remanent magnetization (IRM) and an anhysteretic remanent magnetization (ARM) were imparted to all specimens (n = 376 outcrop, n = 169 core). For each specimen, ARM was imparted in a peak alternating field (AF) of 100 mT in the presence of a weak direct current (DC) bias field of 50 μT. The ARM susceptibility

(χ_{ARM}), was calculated by dividing the measured ARM by the bias field. $IRMs$ were imparted using three pulses of a 100 mT direct current field in a pulse magnetizer. IRM and ARM remanences were measured immediately using a 2G Enterprises 760-R SQUID magnetometer within a shielded room with a background field of less than 100 nT.

7.4.4 Hysteresis Properties

Hysteresis loops and backfield remanence curves were measured on a subset of samples from each paleosol profile (n = 170 outcrop, n = 70 core) using a Princeton Measurements Corporation Micromag vibrating sample magnetometer (VSM) at room temperature in fields up to 1 Tesla. Saturation magnetization (M_s), saturation remanent magnetization (M_{rs}; equivalent to saturation IRM, or $SIRM$), coercivity (B_c), and coercivity of remanence (B_{cr}) are all derived from hysteresis and backfield measurements (see overview in *Maxbauer et al.*, 2016a). The remanence held by magnetic minerals between 100 mT and 1 T is referred to as the "hard" IRM, or $HIRM$, where $HIRM = 0.5 \times (SIRM + IRM_{-100mT})$.

7.4.5 Coercivity Unmixing

For all B-horizon specimens where backfield curves were collected, we calculated coercivity distributions using the absolute value of the first derivative of backfield remanence. In order to identify the individual components that contribute to remanence at various field strengths up to 1 T we used a curve-fitting program developed in the `R` programming language (available on-line at `http://www.irm.umn.edu/maxunmix`), which is based on similar methods to those of *Kruiver et al.* (2001), *Heslop et al.* (2002), and *Egli* (2003). Our method uses skew-normal distributions that can be described with a mean coercivity (B_h), a dispersion parameter (DP, equivalent to one standard deviation in log-space), and a skewness factor (S). Modeled distributions for each component can be added linearly to approximate the measured coercivity distribution (on a coercivity versus log-field diagram). The total contribution of each component to the $SIRM$ is calculated as the integrated area under each model component divided by the total integrated area underneath the coercivity distribution across the range of field

values covered by the magnetization data (i.e., there is no extrapolation for unsaturated backfield curves).

Initial optimization of user-defined fitting was automated to minimize the residual sum squared (RSS) between the measured and modeled coercivity distributions. Error in the model is accounted for by a Monte Carlo style resampling routine. For each iteration, the program randomly drops 5% of the original magnetization data prior to deriving coercivity distributions. The resampled coercivity distributions are then fitted using the initial optimized fits (achieved using the entire magnetization dataset), which are resampled assuming a 2% error in their initial value. Optimization is again automated for each resampled coercivity distribution and the reported models for coercivity distributions and individual components are the mean of 100 resamples with error envelopes representing the 2.5 and 97.5 percentiles (95% confidence interval).

7.4.6 Temperature dependent measurements

Temperature dependent measurements were conducted on a small subset of specimens in order to more definitively identify magnetic minerals within the studied paleosols. Room temperature saturation IRM (RT-$SIRM$) was measured using a Quantum Design Magnetic Properties Measurement Systems (MPMS). Specimens were first given an IRM of 5 T at room temperature (300 K; followed by a smaller IRM of 2.5 T along the same axis to minimize recoil within the MPMS system). Remanence was then measured during cooling to 20 K and subsequent warming back to room temperature. RT-$SIRM$ curves reveal remanence loss at diagnostic transition temperatures (e.g., the Verwey and Morin transitions for magnetite and hematite, respectively). However, the Morin transition of hematite is often suppressed in natural soils and sediments due to defects and aluminum substitution (e.g., *Maher et al.*, 2004). In order to confirm the presence of hematite, we measured backfield remanence curves with saturating fields of 1.5 T at 25 °C (298 K) and 130 °C (403 K). The high temperature backfield curve was measured above the Néel temperature of goethite (125 °C) and all high-field remanence in this experiment is attributed to hematite.

7.5 Results

7.5.1 Magnetic Susceptibility, ARM, and IRM

Bulk χ within core and outcrop paleosol profiles range from 5×10^{-8} to 25×10^{-8} m^3kg^{-1}, which is consistent with values reported for ancient paleosols (Figure 7.4A and Figure B.1; *Rankey and Farr*, 1997; *Cogoini et al.*, 2001; *Retallack et al.*, 2003; *Tramp et al.*, 2004; *Morón et al.*, 2013). Frequency dependence of susceptibility for the paleosols studied here was low ($< 2\%$) and inconsistent, which suggests either the absence of ferrimagnetic minerals in the SP state in these soils prior to fossilization, or their poor preservation. ARM (Figure 7.4C and Figure B.2) and IRM (Figure 7.4E and Figure B.3) both have similar trends within and amongst paleosol profiles in core and outcrop. ARM ranges from 3×10^{-6} to 30×10^{-6} Am^2kg^{-1} and IRM values are between 1×10^{-4} and 15×10^{-4} Am^2kg^{-1} (Figure B.2 and B.3, respectively). Vertical profiles of χ, ARM, and IRM variations within paleosols generally do not have systematic magnetic parameter increases within the upper B-horizon, as is commonly observed in modern soils (see Figures B.1-B.3; *Maher*, 1998; *Geiss et al.*, 2008; *Lindquist et al.*, 2011). We note that the A-horizon for these paleosols has been mostly stripped off, which likely contributes, in part, to the lack of an enhanced magnetic signature. In nearly all instances, ARM and IRM values for B-horizons are greater than the underlying C-horizons upon which the soil developed (Figures B.1-B.3). Notably, the χ, ARM, and IRM data are not offset systematically between core and outcrop for equivalent paleosol B-horizons (Figure 7.4A, C, and E; $p > 0.25$ for all paired t-tests and Wilcoxon Signed-Rank Tests, which supports no difference between core and outcrop records).

7.5.2 Hysteresis Properties

Example hysteresis loops and backfield curves for both low and high coercivity end member specimens are shown in Figure 7.5. All hysteresis loops are wasp-waisted to varying extents, which indicates mixed magnetic mineral assemblages (*Roberts et al.*, 1995; *Tauxe et al.*, 1996). Mean B-horizon B_c varies between 10 and 160 mT with B_{cr} values ranging from 80 to 500 mT. Both B_c and B_{cr} are considerably higher in paleosol B-horizons compared with underlying C-horizons (Figures B.6 and B.7). Similar to the patterns observed for the χ, ARM, and IRM data, despite variations amongst various

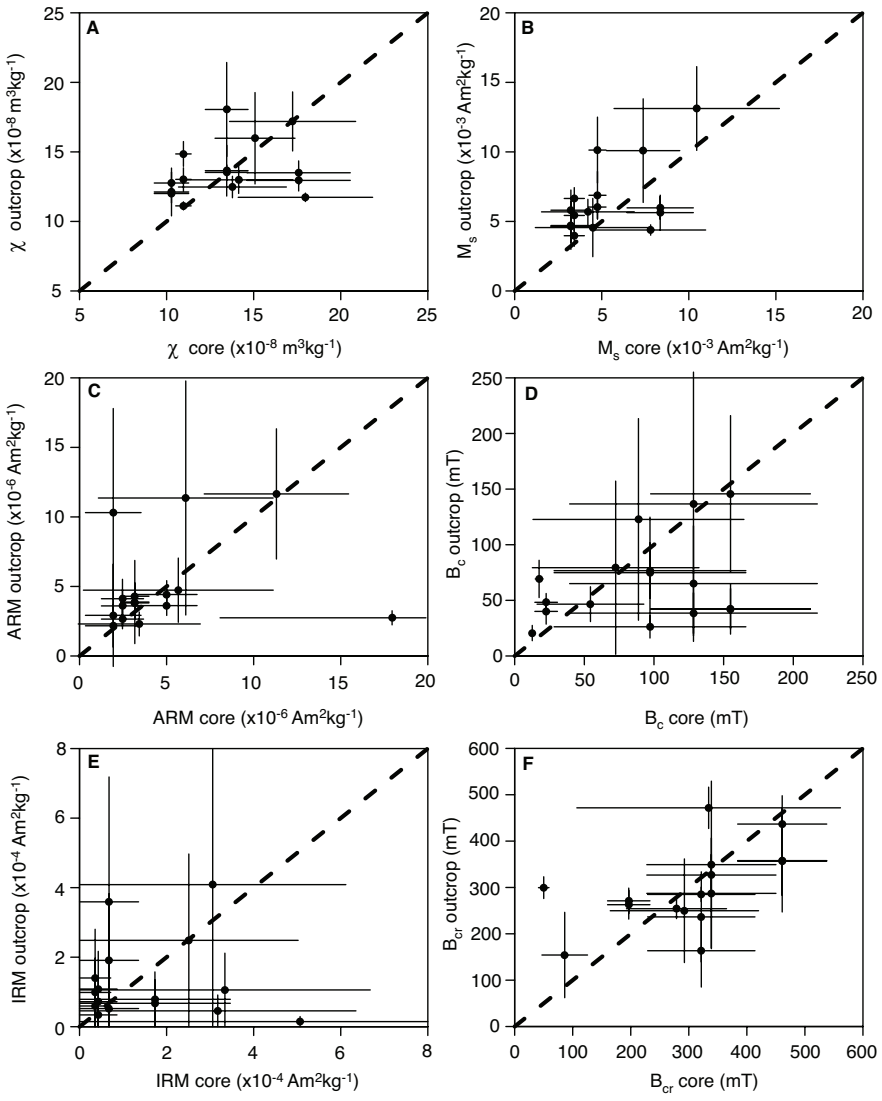

Figure 7.4: Comparison of magnetic parameters for equivalent B-horizons preserved in core and outcrop. The data are expected to fall on 1-to-1 lines (dashed lines in all plots) if there is no difference between core and outcrop data. All data points represent mean B-horizon values with error bars at $\pm$ 1 standard deviation. For all parameters there is high variability, but no significant difference between outcrop and core values (all p-values > 0.25 for a paired t-test and Wilcoxon Signed-Rank Test).

outcrop and core profiles (Figures B.6 and B.7) for equivalent paleosol layers, there is no consistent difference in bulk B_c or B_{cr} between core and outcrop (Figure 7.4D and 7.4F; $p > 0.3$ for all paired t-tests and Wilcoxon Signed-Rank Tests). By contrast, M_r and $HIRM$ for B-horizons sampled from core sediments are consistently lower than those observed in equivalent outcrop B-horizons (Figure 7.6; $p < 0.05$ for all paired t-tests and Wilcoxon Signed-Rank Tests, which indicate that outcrop values are significantly greater than core values). On average mean B-horizon M_r increases by 23% in outcrops and $HIRM$ increases by 41% in equivalent outcrop profiles. B-horizon values of M_s within both cores and outcrop profiles range between 4×10^{-3} and 12×10^{-3} Am^2kg^{-1}. Although there is mostly a similar trend of increased M_s in outcrops relative to core equivalents, this effect is not as consistent as M_r and $HIRM$ observations (compare Figure 7.4B with Figure 7.6C and 7.6D).

7.5.3 Coercivity Unmixing

Analysis of coercivity distributions of B-horizon samples revealed that the remanent magnetization is principally held by two components (e.g., Figure 7.7A). The low-coercivity component (LCC) is characterized by average B_h values between 1.3 and 2.1 ($20 - 126$ mT) and DP between 0.3 and 0.8 (Figure 7.7B). The average B_h and DP observed for the LCC in both core and outcrop paleosols are generally higher than values typically reported in the literature for pedogenic magnetite (green squares in Figure 7.7B; *Egli*, 2004b; *Geiss et al.*, 2008; *Lindquist et al.*, 2011). The degree of skewness for the LCC is pronounced ($0.46 - 0.76$; upper and lower quartiles; note that $S = 1$ is equivalent a normal distribution; see Table B.5), with a consistent low-field tail observed. There is generally no consistent deviation between the LCC preserved in the core compared to the LCC preserved in equivalent outcrops (consistent B_h and contribution to remanence, all p-values ≥ 0.05).

The HCC in both core and outcrops is characterized by B_h values between 2.4 and 3.0 ($251 - 1000$ mT) with DP consistently between 0.2 and 0.7 (Figure 7.7B). Skewness in the HCC is less pronounced, with a median value for S of 1.01 (0.96, 1.04; upper and lower quartiles). The remanence held by the HCC is consistently higher in outcrops ($\sim$46% increase in outcrop relative to core) and has a consistent pattern with observations made from $HIRM$ and M_r values. The observed B_p and DP of

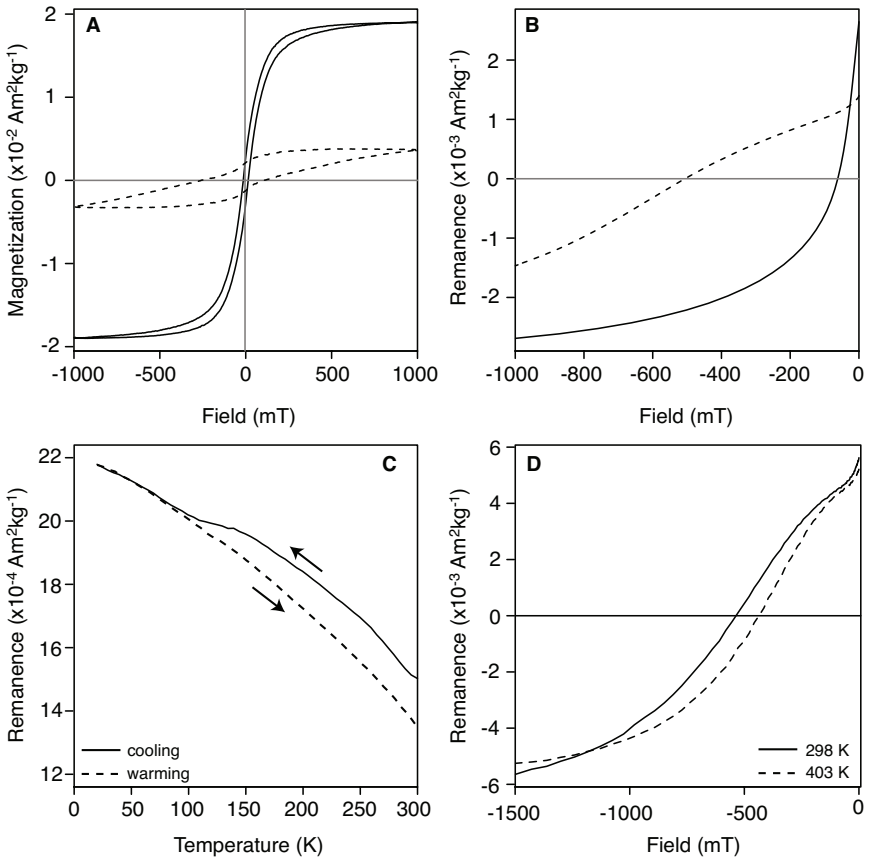

Figure 7.5: **A-B.**Example hysteresis loops (A) and backfield demagnetization curves (B). The solid line is from specimen PCB-01-LDRA-070 and represents a relatively low-coercivity but strongly magnetic end member (common in the large red paleosols LDRA and UDRB). The wasp-waistedness of this loop is likely due to a mixed magnetic assemblage of 'hard' and 'soft' magnetic minerals. The dashed line for specimen P2-155 represents an example of a more weakly magnetic, but higher-coercivity specimen more commonly observed in purple paleosols. **C.** A room-temperature *SIRM* for specimen PCB-03-PRM-100 undergoes a loss of magnetization across the Verwey transition of magnetite (110 K for pure magnetite) and an overall remanence increase on cooling that indicates likely contributions from goethite (*Maher et al.*, 2004). **D.** Backfield curves measured on specimen PCB-01-UDRB-145 at room temperature (solid line) and at 403 K (130 °C; dashed line), above the Néel temperature of goethite. The high temperature backfield curve still carries a majority of the room temperature remanence, which suggests that hematite and not goethite is the primary high field remanence carrier in these specimen.

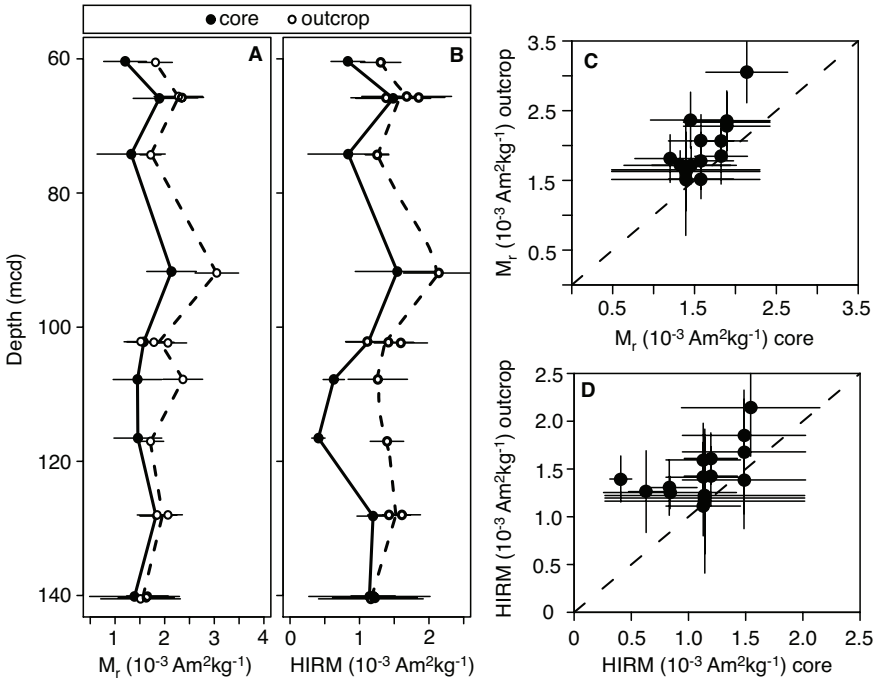

Figure 7.6: **A-B.** Mean B-horizon remanent magnetization (M_r, A) and 'hard' isothermal remanent magnetization ($HIRM$, B) for equivalent paleosol layers in the core (closed symbols, solid line) and outcrop (open symbols, dashed line). **C-D.** Cross plots of M_r (C) and $HIRM$ (D) highlight the observed increase in both magnetic parameters within outcrops compared with the equivalent paleosol preserved in the core. All error bars are $\pm$ 1 standard deviation. For both $HIRM$ and M_r, there is a significant ($p < 0.05$; for both paired t-test and paired Wilcoxon Signed-Rank Test) increase observed in outcrops relative to the equivalent core.

the *HCC* reported here are consistent with work from a previous study that identified high-coercivity components with similar B_h and DP as hematite (*Hyland et al.*, 2015, note that they used non-skewed normal distributions).

7.5.4 Temperature Dependent Measurements

RT-$SIRM$ undergoes a characteristic decrease just prior to 110 K, which is diagnostic of the Verwey transition of magnetite (or partially oxidized magnetite), and a nearly 2-fold increase in remanence on cooling, which indicates contribution from goethite and/or fine-grained hematite (Figure 7.5C; *Maher et al.*, 2004). Previous work has shown that both hematite and goethite are present in Bighorn Basin paleosols based on XRD data (note that magnetite is too scarce volumetrically to be detected by XRD; *Kraus and Hasiotis*, 2006). The Morin transition is absent from the RT-$SIRM$ measured in this study (similar to some modern red soils; *Maher et al.*, 2004). However, the presence of hematite as the dominant high-field remanence carrier is inferred by comparison of backfield demagnetization curves measured at room temperature (25 °C; 298 K) and at 130 °C (403 K). The majority of high-field remanence (> 100 mT) in specimen PCB-01-UDRB-145 remains when backfield remanence is monitored above the Néel temperature of goethite (125 °C; above which goethite carries no remanence), which indicates that hematite is the dominant 'so-called' antiferromagnetic phase in these paleosols (Figure 7.5D).

7.6 Discussion

Our results comprise arguably the most complete magnetic dataset for an ancient (pre-Quaternary) non-loessic paleosol sequence. Furthermore, detailed correlations between core and outcrop, for the first time, allow direct comparison of the magnetic properties of weathered and unweathered sections of the same paleosols. Our dataset allows us to directly address two fundamental assumptions that must be made when applying magnetic paleoprecipitation proxies to ancient paleosols: (1) surficial weathering of outcrops does not impact magnetic mineral preservation, and (2) magnetic minerals retain information about paleoprecipitation. We address these two assumptions below.

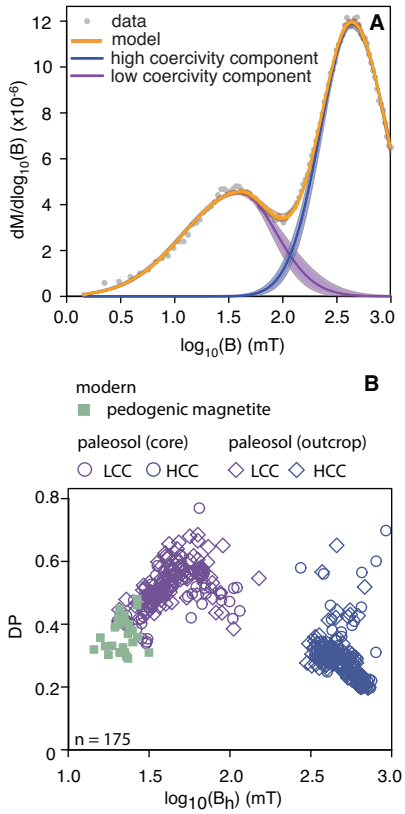

Figure 7.7: **A.** Example of backfield coercivity spectra (data shown in grey symbols) with the modeled best fit (orange). Data were fitted using a two-component model with a high (blue) and low (purple) coercivity component. Shaded envelopes for component distributions and model indicate an approximate 95% confidence interval. Data shown are from core specimen UDRB-100. **B.** Cross plot of the dispersion parameter (DP) and mean coercivity (B_h). Examples of modern pedogenic magnetite (green squares) are displayed with data from *Egli* (2004b), *Geiss and Zanner* (2006), *Lindquist et al.* (2011), and *Bourne et al.* (2015). Note that *Bourne et al.* (2015) presented data recovered from a speleothem, but were interpreted to represent partially oxidized pedogenic magnetite. Data for B-horizon specimen from core and outcrop are shown in purple (low-coercivity component; LCC) and blue (high-coercivity component; HCC).

7.6.1 Magnetic mineral resistance to surficial weathering

The observed increase in M_r, $HIRM$, and the remanence held by the HCC all indicate that there is a consistent remanence increase for high coercivity minerals in outcrop paleosols relative to their core equivalents (Figure 7.6). Notably, this increase is not observed in $HIRM$ if calculated using a backfield of 300 mT instead of 100 mT. This indicates that the principal increase in remanence is acquired in magnetic fields of 100 − 300 mT. Remanence acquired at these field strengths is most likely held by either partially oxidized magnetite/maghemite or by low-coercivity, ultrafine-grained hematite (*Liu et al.*, 2002, 2007a; *Özdemir and Dunlop*, 2014). We propose that the increase in both M_r and $HIRM$ that is observed in outcrops is due to formation of ultrafine (25 − 100 nm) pigmentary hematite within outcrops that formed via oxidation associated with surficial weathering.

Similar to observed color changes in the upper 25 meters of sediment cores recovered by the BBCP, visual inspection suggests that the outcrop paleosols have a more intense red coloration. Comparison of the semi-quantitative redness index (a$*$; calculated from reflectance spectral data; *Abdul Aziz et al.*, 2008; *Bowen et al.*, 2015) for outcrop marker bed paleosols compared with their core counterparts indicates a consistent and significant redness increase within outcrops (Figure 7.8; $p < 0.003$ for both paired t-test and Wilcoxon Signed-Rank Test). Fine-grained hematite acts as a red pigment in a variety of sedimentary settings (*Chen et al.*, 2010). Furthermore, the magnetic properties of ultrafine pigmentary hematite are consistent with the observed variations noted here between core and outcrop paleosols. Grain sizes associated with pigmentary hematite in paleosols on the Chinese Loess Plateau are roughly 50 − 100 nm (*Chen et al.*, 2010), which corresponds roughly to B_c values on the order of 10 − 200 mT (*Özdemir and Dunlop*, 2014). This suggests that ultrafine grained hematite, if present, would acquire M_r beginning at low fields (100 mT) and could be the primary source of the anomalously high M_r and $HIRM$ in outcrops.

Pigmentary hematite formation within outcrops could result from either transformation of low-coercivity magnetite/maghemite, alteration of pre-existing clay minerals, or dehydration of goethite to hematite. Transformation of low-coercivity ferrimagnets into ultrafine hematite would likely be associated with a paired decrease in χ, ARM, and IRM values for outcrops. This is not consistent with our data (Figure 7.4), where

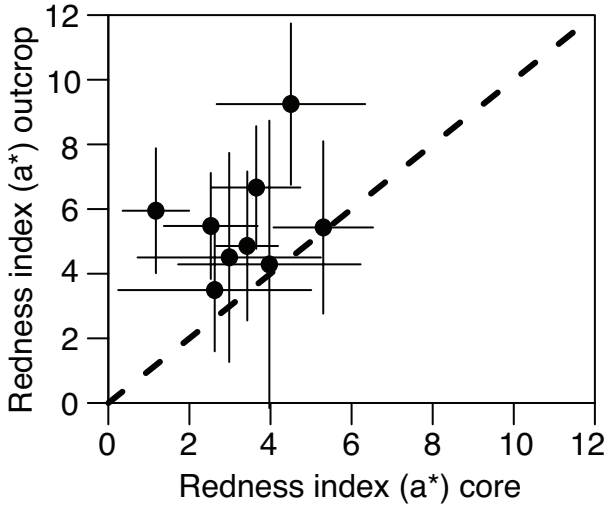

Figure 7.8: Redness Index (a∗) data from paleosol B-horizons at Polecat Bench. The dashed line indicates the 1:1 relationship. Note that in each paleosol, the mean a∗ value of the outcrop is higher than the equivalent paleosol layer sampled from core. Redness data for the core are from Bowen et al. (2015) and are from Abdul Aziz et al. (2008) for the outcrop.

despite deterioration of the low-coercivity minerals, their contribution to remanence is not significantly different between core and outcrop (e.g., remanence held by the LCC, $p \geq 0.38$ for paired t-test and paired Wilcoxon Signed-Rank Test). Alteration of iron-bearing clay minerals is associated with pigmentary hematite formation within paleosols on the Chinese Loess Plateau (*Chen et al.*, 2010) and remains a possibility in the Bighorn Basin sequence, where clay minerals are abundant within B horizons (∼30 weight %; *Kraus et al.*, 2015).

Dehydration of goethite to hematite is a proposed mechanism for the post-burial reddening of red beds and paleosols (*Retallack*, 1991). Previous work mostly discounted this mechanism for paleosols in the Bighorn Basin on the basis that the effect should be pervasive and would erase the complex color assemblages that preserve pedogenic mottling in these deposits (*Kraus and Hasiotis*, 2006). Dehydration of fine-grained goethite in these paleosols into hematite would be consistent with observed increases in M_r, $HIRM$, and increased remanence held by HCC in outcrops. Secondary hematite formation in this system may also explain the strong normal polarity overprint that has been observed in paleomagnetic studies from the Bighorn Basin (e.g., *Clyde et al.*, 2007).

However, we cannot make a definitive conclusion about the dehydration mechanism because our saturating fields (1 T) were far too low to efficiently magnetize goethite within these sediments (*Rochette et al.*, 2005). The production of secondary hematite as a weathering product in outcrop paleosols, regardless of the exact geochemical pathway, challenges the assumption that magnetic minerals within paleosols, and outcrops of sedimentary rocks in general, remain unaffected by surface weathering.

7.6.2 Relationships between magnetic minerals and precipitation

Whether pedogenic magnetic mineral assemblages are preserved in ancient paleosols remains a fundamental question when applying magnetic paleopreciptiation proxies to ancient systems. As discussed above, it appears that surficial weathering of outcrops results in authigenic pigmentary hematite formation. The presence of non-pedogenic hematite in outcrop paleosols has considerable implications for the application of G/H proxies (*Hyland et al.*, 2015; *Long et al.*, 2011). Additional hematite will act to decrease the G/H ratio and cause MAP estimates to be biased to lower values. Authigenic hematite formed via surficial weathering may help to explain G/H based MAP estimates that are drier than other geochemical and paleobotanical methods (*Hyland et al.*, 2015; *Hyland and Sheldon*, 2016). Accordingly, we suggest that G/H MAP estimates be viewed as minimum constraints.

Parameters that remain unaffected by weathering (e.g., χ, ARM, IRM) are generally controlled by low coercivity ferrimagnetic minerals (magnetite and maghemite). However, these parameters have considerable variability and lack characteristics of a magnetically enhanced profile similar to modern soils (*Maher*, 1998; *Geiss and Zanner*, 2006; *Geiss et al.*, 2008; *Lindquist et al.*, 2011). This suggests that diagenetic processes, independent of weathering, have altered the low coercivity ferrimagnetic mineral population. However, relative enhancement ratios (as used in modern calibrations with MAP; *Geiss et al.*, 2008) for the Polecat Bench section are comparable with those of some modern soils and appear to correlate with independent MAP estimates from the CALMAG geochemical weathering index (Figure 7.9 and Table 7.1; *Geiss et al.*, 2008; *Kraus et al.*, 2015). Correlations between MAP and enhancement ratios are generally higher for the core sediments compared with outcrop correlations, which may suggest

that more variability is introduced via surficial weathering to outcrops that are not observed in core sediments (Table 7.1). However, significant ($p < 0.05$) and moderately strong ($R^2 \geq 0.46$; Table 7.1) correlations still exist in the outcrop section, which suggest that despite small influences from surficial weathering qualitative climatic information will still be preserved by the magnetic mineral assemblage.

Table 7.1: Correlation of magnetic parameters with mean annual precipitation (MAP) and B-horizon thickness.[a.]

Parameter	**Core**		**Outcrop**	
	MAP	*Thickness*	*MAP*	*Thickness*
χ_B/χ_C	***0.79 (0.0014)***	0.02 (0.72)	***0.64 (0.0002)***	0.21 (0.08)
IRM_B/IRM_C	***0.79 (0.0014)***	0.04 (0.60)	***0.46 (0.0040)***	***0.30 (0.03)***
ARM_B/ARM_C	***0.55 (0.0227)***	0.05 (0.57)	***0.46 (0.0037)***	***0.30 (0.03)***
χ_{ARM}/IRM	0.03 (0.68)	0.23 (0.19)	0.12 (0.20)	0.07 (0.31)
$HIRM$	0.08 (0.46)	0.03 (0.65)	0.001 (0.90)	0.05 (0.41)

[a.] Mean B-horizon values are used for each indicated magnetic parameter. MAP data are derived from the geochemical weathering index CALMAG and come from Kraus et al. (2015). R^2 values are reported with p-values in parentheses. Significant correlations are highlighted with bold and italics.

Using empirical transfer functions to produce quantitative MAP estimates from the enhancement ratios shown in Figure 7.9 requires the assumption that the ratio has remained unchanged throughout the geologic history of a paleosol (from burial of the original soil to exposure as outcrop or recovery from core). Magnetic enhancement in modern soils is principally driven by pedogenic production of SSD and SP magnetite/maghemite in the upper soil horizons (*Maher*, 1998; *Geiss et al.*, 2008; *Orgeira et al.*, 2011). Coercivity spectra (from ARM and IRM experiments) from many modern soils have identified a low-coercivity component that is often referred to as pedogenic magnetite (Figure 7.7B; *Egli*, 2004b; *Geiss et al.*, 2008; *Lindquist et al.*, 2011). Recovery of a similar low-coercivity component within ancient paleosols would increase confidence

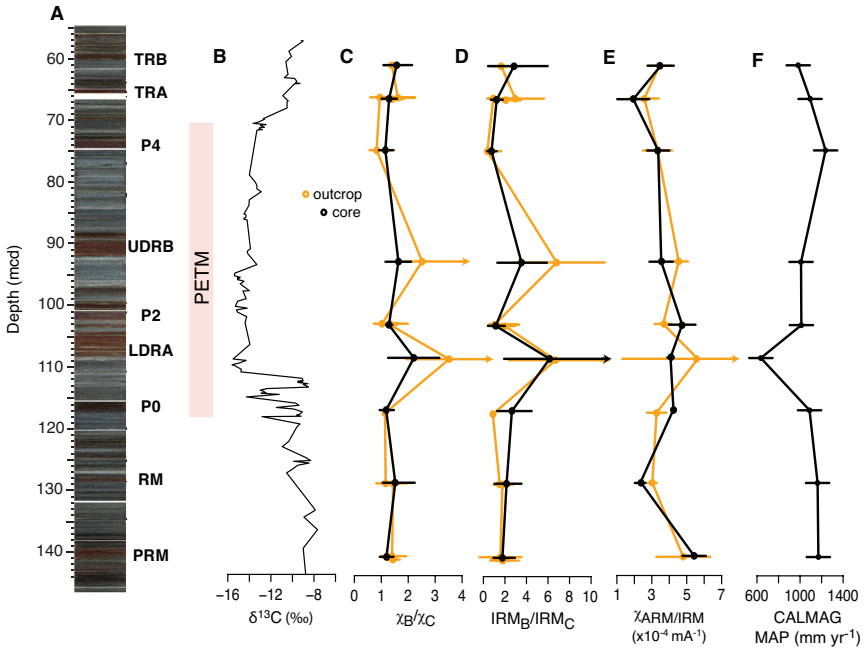

Figure 7.9: Mean B-horizon magnetic enhancement parameters for marker bed paleosols at Polecat Bench. **A.** Line-scan image of core stratigraphy and location of marker paleosols in the core. **B.** Carbon isotopic composition of pedogenic carbonates is shown to highlight the onset, main body, and recovery of the PETM (data from Bowen et al., 2015). **C-D.** B-horizon enhancement ratios for magnetic susceptibility (χ, C) and isothermal remanent magnetization (IRM, D). For each magnetic parameter the mean B-horizon value was normalized to the mean value of the C-horizon. B-horizon means for enhancement ratios were calculated using "enhanced" specimen, indicated in bold in Tables S1 and S3, similar to the approach taken by Geiss et al. (2008). Error bars approximate the 95% confidence interval and were calculated as the 2.5 and 97.5 percentiles of a Monte Carlo style resampling using B and C horizon means and standard deviations assuming a normal distribution. **E.** B-horizon mean ratio of susceptibility of anhysteretic remanent magnetization to IRM (χ_{ARM}/IRM). **F.** CALMAG mean annual precipitation (MAP) data are from Kraus et al. (2015) and represent independent estimates of MAP derived from the bulk geochemistry of the same marker bed paleosols (both core and outcrop). Note that in cases where arrows are on the ends of error bars the error bars were reduced to avoid overlap with adjacent panels.

in the assumption that observable magnetic enhancement in paleosols is driven by similar processes as in modern soils.

The LCC recovered from analysis of B horizons in the Bighorn Basin paleosols suggests either a lack of pedogenic magnetite in these soils or alteration of pedogenic magnetite via diagenesis and weathering (Figure 7.7B). Assuming that magnetite was produced in the original soils during pedogenesis, it is feasible that diagenetic processes increased B_p (via partial or complete maghemitization; e.g., *van Velzen and Dekkers*, 1999; *Chen et al.*, 2005) and DP (by increasing the range of coercivities within the original population of grains) of the pedogenic magnetite component. Notably, the average LCC of Bighorn Basin paleosols has this trend for pedogenic magnetite (Figure 7.7B) and, therefore, we suggest that the LCC represents partially oxidized pedogenic magnetite.

Magnetic paleoprecipitation proxies based on properties such as χ, ARM, and IRM (likely to be dominated by pedogenic magnetite/maghemite) in empirical relationships with MAP are likely to be compromised by the progressive oxidation of pedogenic magnetite during weathering and diagenesis. For example, the χ_{ARM}/IRM ratio is used as a direct indicator for pedogenic magnetite in the methods of *Geiss et al.* (2008); our data indicate no correlation between independent estimates of MAP and χ_{ARM}/IRM (Table 7.1; Figure 7.9E). Enhancement ratios may provide a means to normalize the effects of magnetic mineral oxidation, principally under the assumption that any magnetic minerals present in the parent material experience similar processes. It is encouraging that the magnetic enhancement ratios preserved in the studied Bighorn Basin paleosols are of a similar magnitude to those of modern soils (*Geiss et al.*, 2008). We urge caution in assuming that a similar degree of enhancement in a particular magnetic property suggests equivalence between modern and fossil soils. However, the good agreement between magnetic enhancement ratios and geochemical proxies highlights that magnetic minerals do record at least qualitative information about paleoclimate in the geologic record.

7.7 Conclusions

Our core-to-outcrop comparison of the magnetic properties of paleosols preserved in the Paleocene-Eocene Willwood Formation of the Bighorn Basin allows us to address two fundamental questions related to the application of magnetic paleoprecipitation proxies in ancient systems. First, we evaluated the effects of surficial weathering on the magnetic minerals preserved in outcrops. Outcrop samples have a consistent and significant increase of $\sim 23\%$ in M_r and $\sim 41\%$ for $HIRM$ compared with equivalent core samples (Figure 7.6). This increase is interpreted to be caused by secondary pigmentary hematite ($\sim 25 - 100$ nm) production in outcrops and is supported by similar increases in redness index (a$*$) within outcrops compared to the studied core (Figure 7.8). The increase in magnetic remanence within outcrops complicates application of magnetic paleoprecipitation proxies that use the proportion of total remanence held by hematite and goethite to estimate magnetic mineral abundance ratios (*Long et al.*, 2011; *Hyland et al.*, 2015). It may be possible with future work to address this complication by more detailed unmixing analysis to differentiate primary pedogenic hematite from the secondary authigenic hematite that forms in subaerial weathering regimes. In this way it may be possible to remove, or at least account for, this non-pedogenic magnetic mineral phase when applying methods based on high-field magnetic properties (e.g., *Long et al.*, 2011; *Hyland et al.*, 2015). At minimum, the observed increase in $HIRM$ and M_r increases the uncertainty in applying these methods and the associated error in MAP estimates derived from them. Attempts to address this uncertainty should be included in future work based on these methods.

Second, we evaluated the possibility that magnetic minerals in ancient paleosols record changes in paleoprecipitation across the PETM. Magnetic enhancement ratios of parameters such as χ and IRM correlate with independent MAP estimates from geochemical proxies (Figure 7.9, Table 7.1; *Kraus et al.*, 2015). However, applications of magnetic enhancement proxies are complicated by the fact that the pedogenic magnetite recovered from the Bighorn Basin appears to have been altered during diagenesis (in both core and outcrop), which results in higher mean coercivities and broader coercivity distributions. Additionally, current magnetic precipitation proxies have large uncertainties (*Heslop and Roberts*, 2013; *Maher and Possolo*, 2013) even when applied in

systems where pedogenic magnetite is not altered by diagenesis. So, while the magnetic mineral assemblage preserves qualitative information about paleoprecipitation, quantitative estimates from empirically derived transfer functions may prove difficult to defend if pedogenic magnetite commonly undergoes alteration during diagenesis.

Our analysis presents some challenging obstacles for quantitative application of soil magnetism to paleoclimate problems in deep time. However, environmental magnetic information is still preserved in these ancient paleosols (e.g., magnetic enhancement ratios, Figure 7.9), which suggests their continued promise for magnetic assessment of ancient MAP. In future studies, degradation of pedogenic magnetite should be possible to identify based on comparison of coercivity components to magnetites observed in modern soils as done here. Unfortunately, there is currently no obvious way to identify the presence of non-pedogenic, authigenic hematite in outcrops where comparison to equivalent core sediments is not possible. More detailed studies on pre-Quaternary paleosol sequences combined with expanded studies on modern soils could provide solutions to these complications and allow soil magnetism to become an important tool for reconstructing past climates.

7.8 Acknowledgements

We thank P. Gingerich and H. Abels for providing guidance and expertise during fieldwork, U. Röhl and the Marum staff for logistical support in core sampling, J. Munson for field assistance, and P. Solheid and M. Jackson for providing helpful assistance and discussions. Comments from A. Roberts and an anonymous reviewer helped to improve this manuscript. Funding to DPM for this work was provided by a GSA student research grant, the H.E. Wright Paleoecology Fellowship, the Richard C. Dennis Fellowship, and the Stanwood Johnston Fellowship through the University of Minnesota. The Bighorn Basin Coring Project was funded through NSF grant EAR-0958821. This is IRM contribution 1607.

Chapter 8

Concluding Remarks

The work presented in this dissertation establishes a robust framework for future work to continue developing rock magnetic tools that will be useful for reconstructing deep time terrestrial paleoclimate. Yet, many issues still remain in confidently reconstructing paleoclimate directly from the rock magnetic properties of ancient paleosols. Many of these challenges are inherent in the reconstruction of ancient climate, and are not likely to be solved easily or by any single analytical approach. As the paleoproxy community has recognized this, there is growing momentum towards interdisciplinary studies that pursue multi-proxy methods (geochemical, isotopic, biological, sedimentological), and these types of studies will likely become the standard moving forward. This dissertation highlights that at minimum, the rock magnetic properties of paleosols should become an integral part of multi-proxy studies. Looking optimistically into the future, there is good potential that additional work will establish magnetic mineral assemblages as a leading tool for geologists interested in the reconstruction of past climates of any age.

8.1 Themes for future work

There are many minor issues to address in the development and application of rock magnetism as tool for deep time paleoclimate reconstruction - and many of these have been highlighted in the preceding chapters of this dissertation and will not be repeated here. However, there are two overarching themes that deserve recognition here.

First, improving the methods for quantifying and identifying various magnetic mineral phases within mixed mineralogical assemblages is absolutely essential. The work presented in Chapter 5 begins to address these concerns by creating a tool that should lead to more standardized data analysis by researchers in the community. Using tools like MAX UnMix to isolate the magnetic signals from individual populations of magnetic minerals requires a solid fundamental understanding of mineral magnetism - especially if these types of tools will be used to determine the absolute abundances of these minerals. Considerable progress in this regards is being made through the development of more complex rock magnetic methods (e.g., *Harrison and Feinberg*, 2009; *Lascu et al.*, 2015) that can allow for sensitive differentiation of magnetic mineral populations. However, detailed analysis of known end member mineral phases (both synthetically produced and natural populations extracted from various media) will be crucial to ground truth interpretations made when decomposing magnetic signals from natural samples (including paleosols) with mixed mineral assemblages.

Second, future research on ancient paleosols that range in age, soil type, and depositional system will be critical to determining the trends in preservation of magnetic minerals. Work in Chapter 7 highlights that pedogenically produced magnetic minerals in the Bighorn Basin of Wyoming may be impacted by diagenetic processes that occur post-burial. If diagenetic processes are the rule, and not the exception, in deep time paleosol systems - this posses considerable obstacles to directly reconstructing paleoclimate from rock magnetic records in these systems. However, it is important to remember that magnetic properties of these same soils record much of the same information that bulk geochemical properties do. Moving forward, integrated magnetic and geochemical methods may provide the most robust models for reconstructing paleoclimates in deep time, while minimizing the potential effects of post-burial processes.

References

Abdul Aziz, H., F. J. Hilgen, G. M. van Luijk, A. Sluijs, M. J. Kraus, J. M. Pares, and P. D. Gingerich (2008), Astronomical climate control on paleosol stacking patterns in the upper Paleocene–lower Eocene Willwood Formation, Bighorn Basin, Wyoming, *Geology*, *36*, 531, doi:10.1130/G24734A.1.

Abrajevitch, A., R. Van der Voo, and D. K. Rea (2009), Variations in relative abundances of goethite and hematite in Bengal Fan sediments: Climatic vs. diagenetic signals, *Marine Geology*, *267*(3-4), 191–206, doi:10.1016/j.margeo.2009.10.010.

Abrajevitch, A., E. Font, F. Florindo, and A. P. Roberts (2015), Asteroid impact vs. Deccan eruptions: the origin of low magnetic susceptibility beds below the Cretaceous – Paleogene boundary revisited, *Earth and Planetary Science Letters*, *430*, 209–223, doi:doi:10.1016/j.epsl.2015.08.022.

Adams, J. S., M. J. Kraus, and S. L. Wing (2011), Evaluating the use of weathering indices for determining mean annual precipitation in the ancient stratigraphic record, *Palaeogeography, Palaeoclimatology, Palaeoecology*, *309*, 358–366, doi:10.1016/j.palaeo.2011.07.004.

Alekseev, A. O., T. V. Alekseeva, and B. A. Maher (2003), Magnetic properties and mineralogy of iron compounds in steppe soils, *Eurasian Soil Science*, *36*(1), 59–70.

Ao, H., M. J. Dekkers, Z. An, G. Xiao, Y. Li, H. Zhao, X. Qiang, C. Hong, Q. Chang, and D. Wu (2013), Magnetostratigraphic evidence of a mid-Pliocene onset of the Nihewan Formation – implications for early fauna and hominid occupation in the Nihewan Basin, North China, *Quaternary Science Reviews*, *59*, 30–42, doi:doi:10.1016/j.quascirev.2012.10.025.

Balsam, W., J. Ji, and J. Chen (2004), Climatic interpretation of the Luochuan and Lingtai loess sections, China, based on changing iron oxide mineralogy and magnetic susceptibility, *Earth and Planetary Science Letters*, *223*(3-4), 335–348, doi:10.1016/j.epsl.2004.04.023.

Balsam, W. L., B. B. Ellwood, J. Ji, E. R. Williams, X. Long, and A. El Hassani (2011), Magnetic susceptibility as a proxy for rainfall: Worldwide data from tropical and temperate climate, *Quaternary Science Reviews*, *30*(19-20), 2732–2744, doi:10.1016/j.quascirev.2011.06.002.

Banerjee, S., R. D. Elmore, and M. H. Engel (1997), Chemical remagnetization and burial diagenesis: Testing the hypothesis in the Pennsylvanian Belden Formation, Colorado, *Journal of Geophysical Research*, *102*(B11), 24,825, doi:10.1029/97JB01893.

Banerjee, S. K., and B. M. Moskowitz (1985), Ferrimagnetic properties of magnetite, in *Magnetite biomineralization and magnetoreception in organisms*, edited by J. L. Kirschvink, D. S. Jones, and B. J. MacFadden, pp. 17–41, Springer.

Barrón, V., and J. Torrent (2002), Evidence for a simple pathway to maghemite in Earth and Mars soils, *Geochimica et Cosmochimica Acta*, *66*(15), 2801–2806.

Barrón, V., J. Torrent, and E. de Grave (2003), Hydromaghemite, an intermediate in teh hydrothermal transformatoin of 2-line ferrihydrite into hematite, *American Mineralogist*, *88*, 1679–1688.

Baumgartner, J., G. Morin, N. Menguy, T. Perez Gonzalez, M. Widdrat, J. Cosmidis, and D. Faivre (2013), Magnetotactic bacteria form magnetite from a phosphate-rich ferric hydroxide via nanometric ferric (oxyhydr)oxide intermediates., *Proceedings of the National Academy of Sciences of the United States of America*, *110*(37), 14,883–8, doi:10.1073/pnas.1307119110.

Bazylinski, D. A., C. T. Lefevre, and D. Schuler (2013), Magnetotactic Bacteria, in *The Prokaryotes - Prokaryotic Physiology and Biochemistry*, edited by E. Rosenberg, E. F. DeLong, S. Lory, E. Stackebrandt, and F. Thompson, pp. 453–494, Springer Berlin Heidelberg, Berlin, Heidelberg, doi:10.1007/978-3-642-30141-4.

Begét, J. E., D. B. Stone, and D. B. Hawkins (1990), Paleoclimatic forcing of magnetic susceptibility variations in Alaskan loess during the late Quaternary, *Geology*, *18*, 40–43, doi:10.1130/0091-7613(1990)018⟨0040.

Blakemore, R. P. (1982), Magnetotactic bacteria, *Annual Review of Microbiology*, *36*, 217–238.

Bloemendal, J., J. King, F. Hall, and S.-J. Doh (1992), Rock magnetism of late neogene and pleistocene deep-sea sediments: Relationship to sediment source, diagenetic processes, and sediment lithology, *Journal of Geophysical Research: Solid Earth*, *97*(B4), 4361–4375.

Blundell, A., J. Dearing, J. Boyle, and J. Hannam (2009), Controlling factors for the spatial variability of soil magnetic susceptibility across England and Wales, *Earth-Science Reviews*, *95*(3-4), 158–188, doi:10.1016/j.earscirev.2009.05.001.

Bonneville, S., P. Vancappellen, and T. Behrends (2004), Microbial reduction of iron(III) oxyhydroxides: effects of mineral solubility and availability, *Chemical Geology*, *212*(3-4), 255–268, doi:10.1016/j.chemgeo.2004.08.015.

Bourne, M. D., J. M. Feinberg, B. E. Strauss, B. Hardt, H. Cheng, H. D. Rowe, G. Springer, and R. L. Edwards (2015), Long-term changes in precipitation recorded by magnetic minerals in speleothems, *Geology*, *43*, 595–598, doi:10.1130/G36695.1.

Bowen, G. J., B. J. Maibauer, M. J. Kraus, U. Röhl, T. Westerhold, A. Steimke, P. D. Gingerich, S. L. Wing, and W. C. Clyde (2015), Two massive, rapid releases of carbon during the onset of the palaeocene-eocene thermal maximum, *Nature Geoscience*, *8*, 44–47.

Boyle, J. F., J. a. Dearing, a. Blundell, and J. a. Hannam (2010), Testing competing hypotheses for soil magnetic susceptibility using a new chemical kinetic model, *Geology*, *38*(12), 1059–1062, doi:10.1130/G31514.1.

Brockman, F. J., T. L. Kieft, J. K. Fredrickson, B. N. Bjornstad, S.-m. W. Li, W. Spangenburg, and P. E. Long (1992), Microbiology of vadose zone paleosols in South-Central Washington State Hanford Site, *Microbial Ecology*, *23*, 279–301.

Butler, R., and S. K. Banerjee (1975), Theoretical singe-domain grain size range in magneitte and titanomagnetite., *Journal of Geophysical Research*, *80*, 4049–4058.

Cabello, E., M. Morales, C. Serna, V. Barrón, and J. Torrent (2009), Magnetic enhancement during the crystallization of ferrihydrite at 25 and 50 °C, *Clays and Clay Minerals*, *57*, 46–53, doi:10.1346/CCMN.2009.0570105.

Carter-Stiglitz, B., S. K. Banerjee, A. Gourlan, and E. Oches (2006), A multi-proxy study of Argentina loess: Marine oxygen isotope stage 4 and 5 environmental record from pedogenic hematite, *Palaeogeography, Palaeoclimatology, Palaeoecology*, *239*(1-2), 45–62, doi:10.1016/j.palaeo.2006.01.008.

Chang, W., J. Cheng, J. Allaire, Y. Xie, and J. McPherson (2015), *shiny: Web Application Framework for R*, r package version 0.12.2.

Channell, J. E. T., and D. A. Hodell (2013), Magnetic signatures of Heinrich-like detrital layers in the Quaternary of the North Atlantic, *Earth and Planetary Science Letters*, *370*, 260–270, doi:10.1016/j.epsl.2013.03.034.

Chen, T., H. Xu, Q. Xie, J. Chen, J. Ji, and H. Lu (2005), Characteristics and genesis of maghemite in Chinese loess and paleosols: Mechanism for magnetic susceptibility enhancement in paleosols, *Earth and Planetary Science Letters*, *240*(3-4), 790–802, doi:10.1016/j.epsl.2005.09.026.

Chen, T., Q. Xie, H. Xu, J. Chen, J. Ji, H. Lu, and W. Balsam (2010), Characteristics and formation mechanism of pedogenic hematite in Quaternary Chinese loess and paleosols, *Catena*, *81*, 217–225, doi:10.1016/j.catena.2010.04.001.

Childs, C. W. (1992), Ferrihydrite: A review of structure, properties and occurrence in relation to soils, *Geochimica et Cosmochimica Acta*, *155*, 441–448.

Cismasu, a. C., F. M. Michel, a. P. Tcaciuc, T. Tyliszczak, and G. E. Brown, Jr (2011), Composition and structural aspects of naturally occurring ferrihydrite, *Comptes Rendus Geoscience*, *343*(2-3), 210–218, doi:10.1016/j.crte.2010.11.001.

Cismasu, a. C., F. M. Michel, J. F. Stebbins, C. Levard, and G. E. Brown (2012), Properties of impurity-bearing ferrihydrite I. Effects of Al content and precipitation

rate on the structure of 2-line ferrihydrite, *Geochimica et Cosmochimica Acta*, *92*, 275–291, doi:10.1016/j.gca.2012.06.010.

Cismasu, a. C., C. Levard, F. M. Michel, and G. E. Brown (2013), Properties of impurity-bearing ferrihydrite II: Insights into the surface structure and composition of pure, Al- and Si-bearing ferrihydrite from Zn(II) sorption experiments and Zn K-edge X-ray absorption spectroscopy, *Geochimica et Cosmochimica Acta*, *119*, 46–60, doi:10.1016/j.gca.2013.05.040.

Clark, J. S. (1990), Fire and climate change during the last 750 years in northwestern minnesota, *Ecological Monographs*, *60*, 135–159.

Clyde, W. C., W. Hamzi, J. A. Finarelli, S. L. Wing, D. Schankler, and A. Chew (2007), Basin-wide magnetostratigraphic framework for the Bighorn Basin, Wyoming, *Bulletin of the Geological Society of America*, *119*, 848–859, doi:10.1130/B26104.1.

Clyde, W. C., P. D. Gingerich, S. L. Wing, U. Röhl, T. Westerhold, G. Bowen, K. Johnson, A. A. Baczynski, A. Diefendorf, F. McInerney, D. Schnurrenberger, A. Noren, and K. Brady (2013), Bighorn Basin Coring Project (BBCP): a continental perspective on early Paleogene hyperthermals, *Scientific Drilling*, *16*, 21–31, doi:10.5194/sd-16-21-2013.

Cogoini, M., R. D. Elmore, G. S. Soreghan, and M. T. Lewchuk (2001), Contrasting rock-magnetic characteristics of two Upper Paleozoic loessite-paleosol profiles, *Physics and Chemistry of the Earth, Part A: Solid Earth and Geodesy*, *26*, 905–910.

Collinson, D. W. (1968), An estimate of teh haematite content of sediments by magnetic analysis, *Earth and Planetary Science Letters*, *4*, 417–421.

Colombo, C., G. Palumbo, J.-Z. He, R. Pinton, and S. Cesco (2013), Review on iron availability in soil: interaction of Fe minerals, plants, and microbes, *Journal of Soils and Sediments*, *14*(3), 538–548, doi:10.1007/s11368-013-0814-z.

Colwell, F. (2001), Constraints on the distribution of microorganisms in subsurface environments, in *Subsurface Microgeobiology and Biogeochemistry*, edited by J. Fredrickson and M. Fletcher, Wiley-Liss, Inc.

Cornell, R., and U. Schwertmann (2003), *The Iron Oxides: Structures, Properties, Reactions, Occurences, and Uses*, 2nd ed., 664 pp., Wiley-VCH.

Cox, E., R. D. Elmore, and M. Evans (2005), Paleomagnetism of Devonian red beds in the Appalachian Plateau and Valley and Ridge provinces, *Journal of Geophysical Research*, *110*, B08,102, doi:10.1029/2005JB003640.

Das, S., M. J. Hendry, and J. Essilfie-Dughan (2011), Transformation of two-line ferrihydrite to goethite and hematite as a function of pH and temperature., *Environmental science & technology*, *45*(1), 268–75, doi:10.1021/es101903y.

Day, R., M. Fuller, and V. A. Schmidt (1977), Hysteresis properties of titanomagnetites: grain-size and compositional dependence, *Physics of the Earth and Planetary Interiors*, *13*, 260–267.

de Jong, E., P. Nestor, and D. Pennock (1998), The use of magnetic susceptibility to measure long-term soil redistribution, *Catena*, *32*(1), 23–35, doi:10.1016/S0341-8162(97)00051-9.

de Jong, E., D. Pennock, and P. Nestor (2000), Magnetic susceptibility of soils in different slope positions in Saskatchewan, Canada, *Catena*, *40*(3), 291–305, doi:10.1016/S0341-8162(00)00080-1.

Dearing, J. A., K. L. Hay, S. M. J. Baban, A. S. Huddleston, E. M. H. Wellington, and P. J. Loveland (1996a), Magnetic susceptibility of soil: an evaluation of conflicting theories using a national data set, *Geophysical Journal International*, *127*(3), 728–734, doi:10.1111/j.1365-246X.1996.tb04051.x.

Dearing, J. A., R. J. L. Dann, K. Hay, J. A. Lees, P. J. Loveland, B. A. Maher, K. O. Grady, S. Survey, and B. Mk (1996b), Frequency-dependent susceptibility measurements of environmental materials, *Geophysical Journal International*, *124*, 228–240.

Dekkers, M. J. (1989), Magnetic Properties of Natural Goethite-II. TRM Behaviour During Thermal and Alternating Field Demagnetization and Low-Temperature Treatment, *Geophysical Journal International*, *97*(2), 341–355, doi:10.1111/j.1365-246X.1989.tb00505.x.

Demkina, T. S., T. E. Khomutova, N. N. Kashirskaya, E. V. Demkina, I. V. Stretovich, G. I. El-Registan, and V. a. Demkin (2008), Age and activation of microbial communities in soils under burial mounds and in recent surface soils of steppe zone, *Eurasian Soil Science*, *41*(13), 1439–1447, doi:10.1134/S1064229308130139.

Dorfman, J. M., J. S. Stoner, M. S. Finkenbinder, M. B. Abbott, C. Xuan, and G. Stonge (2015), A 37,000-year environmental magnetic record of aeolian dust deposition from Burial Lake, Arctic Alaska, *Quaternary Science Reviews*, *128*, 81–97, doi:10.1016/j.quascirev.2015.08.018.

Dubinsky, E. a., W. L. Silver, and M. K. Firestone (2010), Tropical forest soil microbial communities couple iron and carbon biogeochemistry., *Ecology*, *91*(9), 2604–12.

Dunlop, D. J. (1973), Superparamagnetic and single-domain threshold sizes in magnetite, *Journal of Geophysical Research*, *78*, 459–471.

Dunlop, D. J. (2002), Theory and application of the Day plot (M_{rs}/M_s versus H_{cr}/H_c) 2. Application to data for rocks, sediments, and soils, *Journal of Geophysical Research B: Solid Earth*, *107*, 1–15.

Dunlop, D. J., and O. Özdemir (2001), *Rock Magnetism: Fundamentals and Frontiers v3*, Cambridge University Press.

Dunlop, D. J., and O. Özdemir (2006), Magnetic memory and coupling between spincanted and defect magnetism in hematite, *Journal of Geophysical Research*, *111*, B12S03.

Egli, R. (2003), Analysis of the field dependence of remanent magnetization curves, *Journal of Geophysical Research*, *108*, 2081, doi:10.1029/2002JB002023.

Egli, R. (2004a), Characterization of individual rock magnetic components by analysis of remanence curves. 2. Fundamental properties of coercivity distributions, *Physics and Chemistry of the Earth*, *29*, 851–867, doi:10.1016/j.pce.2004.04.001.

Egli, R. (2004b), Characterization of individual rock magnetic components by analysis of remanence curves. 1. Unmixing natural sediments, *Studia Geophysica et Geodaetica*, *48*, 391–446, doi:10.1023/B:SGEG.0000020839.45304.6d.

Egli, R. (2004c), Characterization of individual rock magnetic components by analysis of remanence curves. 3. Bacterial magnetite and natural processes in lakes, *Physics and Chemistry of the Earth*, *29*, 869–884, doi:10.1016/j.pce.2004.03.010.

Emerson, D., and J. V. Weiss (2004), Bacterial iron oxidation in circumneutral freshwater habitats: findings from the field and the laboratory, *Geomicrobiology Journal*, *21*, 405–414.

Eronen, J., K. Puolamäki, and L. Liu (2010a), Precipitation and large herbivorous mammals I: estimates from present-day communities, *Evolutionary Ecology Research*, *12*, 217–233.

Eronen, J. T., K. Puolamäki, L. Liu, K. Lintulaakso, J. Damuth, C. Janis, and M. Fortelius (2010b), Precipitation and large herbivorous mammals II: Application to fossil data, *Evolutionary Ecology Research*, *12*, 235–248.

Essington, M. (2004), *Soil and Water Chemistry: An Integrative Approach*, CRC Press, Boca Raton, FL.

Eusterhues, K., F. E. Wagner, W. Häusler, M. Hanzlik, H. Knicker, K. U. Totsche, I. Kögel-Knabner, and U. Schwertmann (2008), Characterization of ferrihydrite-soil organic matter coprecipitates by X-ray diffraction and Mössbauer spectroscopy., *Environmental science & technology*, *42*(21), 7891–7.

Evans, M. E., and F. Heller (2003), *Environmental Magnetism: Principles and Applications of Enviromagnetics*, 299 pp., Elsevier Science (USA), San Diego, CA.

Fassbinder, J. W. E., and H. Stanjek (1994), Magnetic properties of biogenic soil greigite ($Fe_3 S_4$), *Geophysical Research Letters*, *21*(22), 2349–2352, doi:10.1029/94GL02506.

Fassbinder, J. W. E., H. Stanjek, and H. Vali (1990), Occurrence of magnetic bacteria in soil, *Nature*, *343*, 161–162.

Fine, P., M. J. Singer, R. L. A. Ven, K. Verosub, and R. J. Southard (1989), Role of pedogenesis in distribution of magnetic susceptibility in two California chronosequences, *Geoderma*, *44*(2249), 287–306.

Fitzpatrick, R. (1988), Iron compounds as indicators of pedogenic processes: examples from the Southern Hemisphere, in *Iron in Soils and Clay Minerals*, edited by J. Stucki, B. Goodman, and U. Schwertmann, D. Rediel Publishing Company, The Netherlands.

Font, E., A. E. Rapalini, R. N. Tomezzoli, R. I. F. Trindade, and E. Tohver (2012), Episodic Remagnetizations related to tectonic events and their consequences for the South America Polar Wander Path, *Geological Society, London, Special Publications*, *371*, 55–87, doi:10.1144/SP371.7.

France, D. E., and F. Oldfield (2000), Identifying goethite and hematite from rock magnetic measurements of soils and sediments, *Journal of Geophysical Research*, *105*, 2781–2795.

Frankel, R., and R. P. Blakemore (1991), *Iron Biominerals*, Plenum Press, New York.

Ge, K., W. Williams, Q. Liu, and Y. Yu (2014), Effects of the core-shell structure on the magentic properties of partially oxidized magentite grains: Experimental and micromagnetic investigations, *Geochemistry, Geophysics, Geosystems*, *15*, 2021–2038, doi:10.1002/2014GC005265.

Geiss, C. E., and C. W. Zanner (2006), How abundant is pedogenic magnetite? Abundance and grain size estimates for loessic soils based on rock magnetic analyses, *Journal of Geophysical Research*, *111*(B12), B12S21, doi:10.1029/2006JB004564.

Geiss, C. E., and C. W. Zanner (2007), Sediment magnetic signature of climate in modern loessic soils from the Great Plains, *Quaternary International*, *162-163*, 97–110, doi:10.1016/j.quaint.2006.10.035.

Geiss, C. E., C. W. Zanner, S. K. Banerjee, and M. Joanna (2004), Signature of magnetic enhancement in a loessic soil in Nebraska, United States of America, *Earth and Planetary Science Letters*, *228*(3-4), 355–367, doi:10.1016/j.epsl.2004.10.011.

Geiss, C. E., R. Egli, and C. W. Zanner (2008), Direct estimates of pedogenic magnetite as a tool to reconstruct past climates from buried soils, *Journal of Geophysical Research*, *113*(B11), B11,102, doi:10.1029/2008JB005669.

Gingerich, P. D. (2001), Biostratigraphy of the continental Paleocene-Eocene boundary interval on Polecat Bench in the northern Bighorn Basin, *University of Michigan Papers on Paleontology*, *33*(37-67).

Gold, T. (1992), The deep, hot biosphere., *Proceedings of the National Academy of Sciences of the United States of America*, *89*(13), 6045–9.

Guyodo, Y., T. M. LaPara, A. J. Anschutz, R. L. Penn, S. K. Banerjee, C. E. Geiss, and W. Zanner (2006), Rock magnetic, chemical and bacterial community analysis of a modern soil from Nebraska, *Earth and Planetary Science Letters*, *251*(1-2), 168–178, doi:10.1016/j.epsl.2006.09.005.

Guyodo, Y., P. Sainctavit, M.-A. Arrio, C. Carvallo, R. Lee Penn, J. J. Erbs, B. S. Forsberg, G. Morin, F. Maillot, F. Lagroix, et al. (2012), X-ray magnetic circular dichroïsm provides strong evidence for tetrahedral iron in ferrihydrite, *Geochemistry, Geophysics, Geosystems*, *13*(6).

Hanesch, M., and R. Scholger (2005), The influence of soil type on the magnetic susceptibility measured throughout soil profiles, *Geophysical Journal International*, *161*(1), 50–56, doi:10.1111/j.1365-246X.2005.02577.x.

Hansel, C. M., S. Fendorf, P. M. Jardine, and C. a. Francis (2008), Changes in bacterial and archaeal community structure and functional diversity along a geochemically variable soil profile., *Applied and environmental microbiology*, *74*(5), 1620–33, doi: 10.1128/AEM.01787-07.

Hao, Q., F. Oldfield, J. Bloemendal, J. Torrent, and Z. Guo (2009), The record of changing hematite and goethite accumulation over the past 22 Myr on the Chinese Loess Plateau from magnetic measurements and diffuse reflectance spectroscopy, *Journal of Geophysical Research: Solid Earth*, *114*(12), 1–18, doi:10.1029/2009JB006604.

Harrison, R. J., and J. M. Feinberg (2009), Mineral magnetism: Providing new insights into geoscience processes, *Elements*, *5*, 209–215, doi:10.2113/gselements.5.4.209.

Hatfield, R. G. (2014), Particle size-specific magnetic measurements as a tool for enhancing our understanding of the bulk magnetic properties of sediments, *Minerals*, *4*, 758–787, doi:10.3390/min4040758.

Heider, F., D. J. Dunlop, and H. C. Soffel (1992), Low-temperature and alternating field demagnetization of saturation remanence and thermoremanence in magnetite grains (0.037 μm to 5 mm), *Journal of Geophysical Research*, *97*, 9371–9381.

Heller, F., and T.-s. Liu (1986), Palaeoclimate and sedimentary history from magnetic susceptibility of loess in China, *Geophysical Research Letters*, *13*, 1169–1172.

Heslop, D. (2015), Numerical strategies for magnetic mineral unmixing, *Earth-Science Reviews*, *150*, 256–284, doi:10.1016/j.earscirev.2015.07.007.

Heslop, D., and M. Dillon (2007), Unmixing magnetic remanence curves without a priori knowledge, *Geophysical Journal International*, *170*, 556–566, doi:10.1111/j.1365-246X.2007.03432.x.

Heslop, D., and A. P. Roberts (2013), Calculating uncertainties on predictions of palaeoprecipitation from the magnetic properties of soils, *Global and Planetary Change*, *110*, 379–385, doi:10.1016/j.gloplacha.2012.11.013.

Heslop, D., M. J. Dekkers, P. P. Kruiver, and I. H. M. van Oorschot (2002), Analysis of isothermal remanent magnetization acquisition curves using the expectation-maximization algorithm, *Geophysical Journal International*, *148*, 58–64.

Heslop, D., G. McIntosh, and M. J. Dekkers (2004), Using time- and temperature-dependent Preisach models to investigate the limitations of modelling isothermal remanent magnetization acquisition curves with cumulative log Gaussian functions, *Geophysical Journal International*, *157*, 55–63, doi:10.1111/j.1365-246X.2004.02155.x.

Holmes, D. E., R. a. O'Neil, M. a. Chavan, L. a. N'Guessan, H. a. Vrionis, L. a. Perpetua, M. J. Larrahondo, R. DiDonato, A. Liu, and D. R. Lovley (2009), Transcriptome of *Geobacter uraniireducens* growing in uranium-contaminated subsurface sediments., *The ISME journal*, *3*(2), 216–30, doi:10.1038/ismej.2008.89.

Hu, P., Q. Liu, J. Torrent, V. Barrón, and C. Jin (2013), Characterizing and quantifying iron oxides in Chinese loess/paleosols: implications for pedogenesis, *Earth and Planetary Science Letters*, *369-370*, 271–283, doi:10.1016/j.epsl.2013.03.033.

Hu, P., Q. Liu, D. Heslop, A. P. Roberts, and C. Jin (2015), Soil moisture balance and magnetic enhancement in loess–paleosol sequences from the Tibetan Plateau and Chinese Loess Plateau, *Earth and Planetary Science Letters*, *409*, 120–132, doi: 10.1016/j.epsl.2014.10.035.

Hunt, C. P., S. K. Banerjee, J. Han, P. a. Solheid, E. Oches, W. Sun, and T. Liu (1995), Rock-magnetic proxies of climate change in the loess-palaeosol sequences of the western Loess Plateau of China, *Geophysical Journal International*, *123*(1), 232–244, doi:10.1111/j.1365-246X.1995.tb06672.x.

Hyland, E., N. D. Sheldon, R. Van der Voo, C. Badgley, and A. Abrajevitch (2015), A new paleoprecipitation proxy based on soil magnetic properties: Implications for expanding paleoclimate reconstructions, *Geology*, pp. 1–9, doi:10.1130/B31207.1.

Hyland, E. G., and N. D. Sheldon (2016), Examining the spatial consistency of paleosol proxies: Implications for palaeoclimatic and palaeoenvironmental reconstructions in terrestrial sedimentary basins, *Sedimentology*, *63*, 959–971.

Jackson, M., B. M. Moskowitz, J. Rosenbaum, and C. Kissel (1998), Field-dependence of ac susceptibility in titanomagnetites, *Earth and Planetary Science Letters*, *157*, 129–139.

Jambor, J. L., and J. E. Dutrizac (1998), Occurrence and constitution of natural and synthetic ferrihydrite, a widespread iron oxyhydroxide., *Chemical reviews*, *98*(7), 2549–2586.

Janney, D., J. Cowley, and P. Buseck (2000), Structure of synthetic 2-line ferrihydrite by electron nanodiffraction, *American Mineralogist*, *85*, 1180–1187.

Jenny, H. (1941), *Factors of Soil Formation*, McGraw-Hill, New York.

Jiamao, H., L. Houyuan, W. Naiqin, and G. Zhengtang (1996), The magnetic susceptibility of modern soils in China and its use for paleoclimate reconstruction, *Studia Geophysica et Geodætica*, *40*(3), 262–275, doi:10.1007/BF02300742.

Jordanova, D., and N. Jordanova (1999), Magnetic characteristics of different soil types from bulgaria, *Studia Geophysica et Geodaetica*, *43*, 303–318.

Kampf, N., and U. Schwertmann (1983), Goethite and hematite in a climosequence in southern brazil and their application in classification of kaolinitic soils, *Geoderma*, *29*, 27–39.

Katz, B., R. Douglas, M. Cogoini, M. H. Engel, and S. Ferry (2000), Associations between burial diagenesis of smectite, chemical remagnetization, and magnetite authigenesis in the Vocontian trough, SE France, *105*, 851–868, doi:10.1029/1999JB900309.

Khomutova, T. E., T. S. Demkina, and V. a. Demkin (2014), The state of microbial communities in buried paleosols in relation to prevailing climates in steppes of the Lower Volga region, *Quaternary International*, *324*, 115–123, doi:10.1016/j.quaint.2014.01.039.

Kraus, M. J. (2001), Sedimentology and depositional setting of the Willwood Formation in the Bighorn and Clarks Fork Basins, *University of Michigan Papers on Paleontology*, *33*, 15–28.

Kraus, M. J., and S. T. Hasiotis (2006), Significance of different modes of rhizolith preservation to interpreting paleoenvironmental and paleohydrologic settings: examples from Paleogene paleosols, Bighorn Basin, Wyoming, U.S.A., *Journal of Sedimentary Research*, *76*, 633–646, doi:10.2110/jsr.2006.052.

Kraus, M. J., and S. Riggins (2007), Transient drying during the Paleocene–Eocene Thermal Maximum (PETM): Analysis of paleosols in the bighorn basin , Wyoming, *Palaeogeography, Palaeoclimatology, Palaeoecology*, *245*, 444–461, doi:10.1016/j.palaeo.2006.09.011.

Kraus, M. J., F. A. McInerney, S. L. Wing, R. Secord, A. A. Baczynski, and J. I. Bloch (2013), Paleohydrologic response to continental warming during the Paleocene–Eocene Thermal Maximum, Bighorn Basin, Wyoming, *Palaeogeography, Palaeoclimatology, Palaeoecology*, *370*, 196–208, doi:10.1016/j.palaeo.2012.12.008.

Kraus, M. J., D. T. Woody, J. J. Smith, and V. Dukic (2015), Alluvial response to the paleocene-eocene thermal maximum climatic event, polecat bench, wyoming (u.s.a.), *Palaeogeography, Palaeoclimatology, Palaeoecology*, *435*, 177–192.

Kruiver, P. P., M. J. Dekkers, and D. Heslop (2001), Quantification of magnetic coercivity components by the analysis of acquisition curves of isothermal remanent magnetisation, *Earth and Planetary Science Letters*, *189*, 269–276.

Kukla, G., F. Heller, L. X. Ming, X. T. Chun, L. T. Sheng, and A. Z. Sheng (1988), Pleistocene cliamtes in china dated by magnetic susceptibility, *Geology*, *16*, 811–814.

Lagroix, F., and S. K. Banerjee (2002), Paleowind directions from the magnetic fabric of loess profiles in central alaska, *Earth and Planetary Science Letters*, *195*, 99–112.

Lagroix, F., and S. K. Banerjee (2004), The regional and temporal significance of primary aeolian magnetic fabrics preserved in alaskan loess, *Earth and Planetary Science Letters*, *225*, 379–395.

Lascu, I., and J. M. Feinberg (2011), Speleothem magnetism, *Quaternary Science Reviews*, *30*(23-24), 3306–3320, doi:10.1016/j.quascirev.2011.08.004.

Lascu, I., and C. Plank (2013), A new dimension to sediment magnetism: charting the spatial variability of magnetic properties across lake basins, *Global and Planetary Change*, *110*, 340–349, doi:10.1016/j.gloplacha.2013.03.013.

Lascu, I., R. J. Harrison, Y. Li, J. R. Muraszko, J. E. T. Channell, A. M. Piotrowski, and D. A. Hodell (2015), Magnetic unmixing of first-order reversal curve diagrams using principle component analysis, *Geochemistry, Geophysics, and Geosystems*, *16*, 2900–2915, doi:10.1002/2015GC005909.

Le Borgne, E. (1955), Susceptibilité magnétiques anormale du sol superficiel, *Annals of Geophysics*, *11*, 399–419.

Le Borgne, E. (1960), Influence du feu sur les proprience magnétiques du sol et sur celles du schist et du granite, *Annals of Geophysics*, *16*, 159–195.

Li, S., C. Deng, H. Yao, S. Huang, C. Liu, H. He, Y. Pan, and R. Zhu (2013), Magnetostratigraphy of the Dali Basin in Yunnan and implications for late Neogene rotation of the southeast margin of the Tibetan Plateau, *Journal of Geophysical Research: Solid Earth*, *118*, 791–807, doi:10.1002/jgrb.50129.

Lin, B., H. V. Westerhoff, and W. F. M. Röling (2009), How Geobacteraceae may dominate subsurface biodegradation: physiology of *Geobacter metallireducens* in slow-growth habitat-simulating retentostats., *Environmental microbiology*, *11*(9), 2425–33, doi:10.1111/j.1462-2920.2009.01971.x.

Lin, W. C., M. V. Coppi, and D. R. Lovley (2004), *Geobacter sulfurreducens* can grow with oxygen as a terminal electron acceptor, *Applied and Environmental Microbiology*, *70*, 2525, doi:10.1128/AEM.70.4.2525.

Lindquist, A. K., J. M. Feinberg, and M. R. Waters (2011), Rock magnetic properties of a soil developed on an alluvial deposit at Buttermilk Creek, Texas, USA, *Geochemistry, Geophysics, Geosystems*, *12*, Q12Z36, doi:10.1029/2011GC003848.

Liu, P., Z. Wu, C. Deng, H. Tong, H. Qin, S. Li, B. Yuan, and R. Zhu (2014), Magnetostratigraphic dating of the Shanshenmiaozui mammalian fauna in the Nihewan Basin, North China, *Quaternary International*, *400*, 202–211, doi:doi:10.1016/j.quaint.2014.09.024.

Liu, Q., S. Banerjee, and M. J. Jackson (2002), A new method in mineral magnetism for the separation of weak antiferromagnetic signal from a strong ferrimagnetic background, *Geophysical Research Letters*, *29*(12), 1–4, doi:10.1029/2002GL014699.

Liu, Q., J. Torrent, Y. Yu, and C. Deng (2004), Mechanism of the parasitic remanence of aluminous goethite [α-(Fe, Al)OOH], *Journal of Geophysical Research B: Solid Earth*, *109*(12), 1–8, doi:10.1029/2004JB003352.

Liu, Q., Y. Yu, J. Torrent, A. P. Roberts, Y. Pan, and R. Zhu (2006), Characteristic low-temperature magnetic properties of aluminous goethite [α-(Fe, Al)OOH] explained, *Journal of Geophysical Research: Solid Earth*, *111*(12), 1–12, doi:10.1029/2006JB004560.

Liu, Q., A. P. Roberts, J. Torrent, C. S. Horng, and J. C. Larrasoaña (2007a), What do the HIRM and S-ratio really measure in environmental magnetism?, *Geochemistry, Geophysics, Geosystems*, *8*(9), doi:10.1029/2007GC001717.

Liu, Q., C. Deng, J. Torrent, and R. Zhu (2007b), Review of recent developments in mineral magnetism of the Chinese loess, *Quaternary Science Reviews*, *26*(3-4), 368–385, doi:10.1016/j.quascirev.2006.08.004.

Liu, Q., V. Barrón, J. Torrent, S. G. Eeckhout, and C. Deng (2008), Magnetism of intermediate hydromaghemite in the transformation of 2-line ferrihydrite into hematite and its paleoenvironmental implications, *Journal of Geophysical Research*, *113*(B1), B01,103, doi:10.1029/2007JB005207.

Liu, Q., P. Hu, J. Torrent, V. Barrón, X. Zhao, Z. Jiang, and Y. Su (2010), Environmental magnetic study of a Xeralf chronosequence in northwestern Spain: Indications for pedogenesis, *Palaeogeography, Palaeoclimatology, Palaeoecology*, *293*(1-2), 144–156, doi:10.1016/j.palaeo.2010.05.008.

Liu, Q., A. P. Roberts, J. C. Larrasoaña, S. K. Banerjee, Y. Guyodo, L. Tauxe, and F. Oldfield (2012), Environmental magnetism: principles and applications, *Review of Geophysics*, *50*, RG4002, doi:10.1029/2012RG000393.1.INTRODUCTION.

Liu, S. V. (1997), Thermophilic Fe(III)-reducing bacteria from the deep subsurface: the evolutionary implications, *Science*, *277*(5329), 1106–1109, doi:10.1126/science.277.5329.1106.

Liu, X., T. Rolph, J. Bloemendal, J. Shaw, and T. Liu (1995), Quantitative estimates of palaeoprecipitation at Xifeng, in the Loess Plateau of China, *Palaeogeography, Palaeoclimatology, Palaeoecology*, *113*(2-4), 243–248, doi:10.1016/0031-0182(95)00053-O.

Liu, Z., Q. Liu, J. Torrent, V. Barrón, and P. Hu (2013), Testing the magnetic proxy χFD/HIRM for quantifying paleoprecipitation in modern soil profiles from Shaanxi Province, China, *Global and Planetary Change*, *110*, 368–378, doi:10.1016/j.gloplacha.2013.04.013.

Long, X., J. Ji, and W. Balsam (2011), Rainfall-dependent transformations of iron oxides in a tropical saprolite transect of Hainan Island, South China: Spectral and magnetic measurements, *Journal of Geophysical Research*, *116*(F3), F03,015, doi:10.1029/2010JF001712.

Lovley, D. (2013), Dissimilatory Fe(III)- and Mn(IV)-Reducing Prokaryotes, in *The Prokaryotes - Prokaryotic Physiology and Biochemistry*, edited by E. Rosenberg, E. F. DeLong, S. Lory, E. Stackebrandt, and F. Thompson, Iii, pp. 287–308, Springer Berlin Heidelberg, Berlin, Heidelberg, doi:10.1007/978-3-642-30141-4.

Lovley, D. R., J. F. Stolz, G. L. Nord, and E. J. Phillips (1987), Anaerobic production of magnetite by a dissimilatory iron-reducing microorganism, *Nature*, *330*, 252–254.

Lovley, D. R., D. E. Holmes, and K. P. Nevin (2004), *Dissimilatory Fe(III) and Mn(IV) reduction.*, vol. 49, 219–86 pp., doi:10.1016/S0065-2911(04)49005-5.

Lovlie, R., R. Wang, and X. Wang (2011), In situ remagnetization experiments of loess on the chinese loess plateau: evidence for localized post-depositional remanent magnetization, *Geochemistry, Geophysics, Geosystems*, *12*, 1–18.

Lowrie, W. (1990), Identification of ferromagnetic minerals in a rock by coercivity and unblocking temperature properties, *Geophysical Research Letters*, *17*(2), 159–162.

Lu, S.-G., L. Zhu, and J.-Y. Yu (2012), Mineral magnetic properties of Chinese paddy soils and its pedogenic implications, *Catena*, *93*, 9–17, doi:10.1016/j.catena.2012.01.002.

Ludwig, P., R. Egli, S. Bishop, V. Chernenko, T. Frederichs, G. Rugel, S. Merchel, and M. Orgeira (2013), Characterization of primary and secondary magnetite in marine sediment by combining chemical and magnetic unmixing techniques, *Global and Planetary Change*, *110*, 321–339, doi:10.1016/j.gloplacha.2013.08.018.

Lusardi, B. A., C. E. Jennings, and K. L. Harris (2011), Provenance of des moines lobe till records ice-stream catchment evolution during laurentide deglaciation, *Boreas*, *40*, 585–597.

Lyons, R., S. Tooth, and G. a. T. Duller (2014), Late Quaternary climatic changes revealed by luminescence dating, mineral magnetism and diffuse reflectance spectroscopy of river terrace palaeosols: A new form of geoproxy data for the southern African interior, *Quaternary Science Reviews*, *95*, 43–59, doi:10.1016/j.quascirev.2014.04.021.

Ma, M., X. Liu, B. J. Pillans, S. Hu, B. Lu, and H. Liu (2013), Magnetic properties of Dashing Rocks loess at Timaru, South Island, New Zealand, *Geophysical Journal International*, *195*(1), 75–85, doi:10.1093/gji/ggt206.

Maher, B. (2011), The magnetic properties of Quaternary aeolian dusts and sediments, and their palaeoclimatic significance, *Aeolian Research*, *3*, 87–144, doi: 10.1016/j.aeolia.2011.01.005.

Maher, B., and a. Possolo (2013), Statistical models for use of palaeosol magnetic properties as proxies of palaeorainfall, *Global and Planetary Change*, *111*, 280–287, doi: 10.1016/j.gloplacha.2013.09.017.

Maher, B., R. Thompson, and L. Zhou (1994), Spatial and temporal reconstructions of changes in the Asian palaeomonsoon: A new mineral magnetic approach, *Earth and Planetary Science Letters*, *125*(1-4), 461–471, doi:10.1016/0012-821X(94)90232-1.

Maher, B., a. Alekseev, and T. Alekseeva (2002), Variation of soil magnetism across the Russian steppe: its significance for use of soil magnetism as a palaeorainfall proxy, *Quaternary Science Reviews*, *21*(14-15), 1571–1576, doi:10.1016/S0277-3791(02) 00022-7.

Maher, B., a. Alekseev, and T. Alekseeva (2003a), Magnetic mineralogy of soils across the Russian Steppe: climatic dependence of pedogenic magnetite formation, *Palaeogeography, Palaeoclimatology, Palaeoecology*, *201*(3-4), 321–341, doi: 10.1016/S0031-0182(03)00618-7.

Maher, B. a. (1998), Magnetic properties of modern soils and Quaternary loessic paleosols: paleoclimatic implications, *Palaeogeography, Palaeoclimatology, Palaeoecology*, *137*(1-2), 25–54, doi:10.1016/S0031-0182(97)00103-X.

Maher, B. a. (2007), Environmental magnetism and climate change, *Contemporary Physics*, *48*(5), 247–274, doi:10.1080/00107510801889726.

Maher, B. a., and M. Hu (2006), A high-resolution record of Holocene rainfall variations from the western Chinese Loess Plateau: antiphase behaviour of the African/Indian and East Asian summer monsoons, *The Holocene*, *16*(3), 309–319, doi:10.1191/0959683606hl929rp.

Maher, B. A., and R. M. Taylor (1988), Formation of ultrafine-grained magnetite in soils, *Nature*, *336*, 368–370.

Maher, B. A., and R. Thompson (1991), Geology Mineral magnetic record of the Chinese loess and paleosols Mineral magnetic record of the Chinese loess and paleosols, *Geology*, *19*, 3–6, doi:10.1130/0091-7613(1991)019⟨0003.

Maher, B. A., and R. Thompson (1992), Paleoclimatic Significance Chinese of the Mineral Magnetic Loess and Paleosols Record of the, *Quaternary Research*, *37*, 155–170.

Maher, B. A., and R. Thompson (1995), Paleorainfall reconstructions from pedogenic magnetic susceptibility variations in the Chinese Loess and Paleosols, *Quaternary International*, *44*, 383–391.

Maher, B. a., H. MengYu, H. M. Roberts, and A. G. Wintle (2003b), Holocene loess accumulation and soil development at the western edge of the Chinese Loess Plateau: implications for magnetic proxies of palaeorainfall, *Quaternary Science Reviews*, *22*(5-7), 445–451, doi:10.1016/S0277-3791(02)00188-9.

Maher, B. a., V. V. Karloukovski, and T. J. Mutch (2004), High-field remanence properties of synthetic and natural submicrometre haematites and goethites: Significance for environmental contexts, *Earth and Planetary Science Letters*, *226*(3-4), 491–505, doi:10.1016/j.epsl.2004.05.042.

Maillot, F., G. Morin, Y. Wang, D. Bonnin, P. Ildefonse, C. Chaneac, and G. Calas (2011), New insight into the structure of nanocrystalline ferrihydrite: EXAFS evidence for tetrahedrally coordinated iron(III), *Geochimica et Cosmochimica Acta*, *75*(10), 2708–2720, doi:10.1016/j.gca.2011.03.011.

Manceau, A. (2012), Comment on "direct observation of tetrahedrally coordinated Fe(III) in ferrihydrite"., *Environmental Science & Technology*, *46*, 6882–6884, doi:10.1021/es303084e.

Marozava, S., W. F. M. Röling, J. Seifert, R. Küffner, M. von Bergen, and R. U. Meckenstock (2014), Physiology of Geobacter metallireducens under excess and

limitation of electron donors. Part II. Mimicking environmental conditions during cultivation in retentostats., *Systematic and applied microbiology*, pp. 1–9, doi: 10.1016/j.syapm.2014.02.005.

Martin-Hernandez, F., and M. M. García-Hernández (2010), Magnetic properties and anisotropy constant of goethite single crystals at saturating high fields, *Geophysical Journal International*, *181*(2), 756–761, doi:10.1111/j.1365-246X.2010.04566.x.

Martin-Hernandez, F., and S. Guerrero-Suárez (2012), Magnetic anisotropy of hematite natural crystals: High field experiments, *International Journal of Earth Sciences*, *101*(3), 637–647, doi:10.1007/s00531-011-0665-z.

Maxbauer, D. P., J. M. Feinberg, and D. L. Fox (2016a), Magnetic mineral assemblages in soils and paleosols as the basis for paleoprecipitation proxies: A review of magnetic methods and challenges, *Earth Science Reviews*, *155*, 28–48, doi:10.1016/j.earscirev.2016.01.014.

Maxbauer, D. P., J. M. Feinberg, D. L. Fox, and W. C. Clyde (2016b), Magneti minerals as recorders of weathering, diagenesis, and paleoclimate: A core-outcrop comparison of paleocene-eocene paleosols in the bighorn basin, wy, usa, *Earth and Planetary Science Letters*, *452*, 15–26.

Maxbauer, D. P., J. M. Feinberg, and D. L. Fox (2016c), Max unmix: A web application for unmixing magnetic coercivity distributions, *Computers and Geosciences*, *95*, 140–145.

McCabe, C., and R. Elmore (1989), The occurrence and origin of Late Paleozoic remagnetization in the sedimentary rocks of North America, *Reviews of Geophysics*, *27*, 471–494.

McInerney, F. A., and S. L. Wing (2011), The Paleocene-Eocene Thermal Maximum: A Perturbation of Carbon Cycle, Climate, and Biosphere with Implications for the Future, *Annual Review Earth and Plantary Sciences*, *39*, 489–516, doi: 10.1146/annurev-earth-040610-133431.

Mehta-Kolte, M. G., and D. R. Bond (2012), *Geothrix fermentans* secretes two different redox-active compounds to utilize electron acceptors across a wide range of redox

potentials., *Applied and environmental microbiology*, *78*(19), 6987–95, doi:10.1128/AEM.01460-12.

Methé, B. a., K. E. Nelson, J. a. Eisen, I. T. Paulsen, W. Nelson, J. F. Heidelberg, D. Wu, M. Wu, N. Ward, M. J. Beanan, R. J. Dodson, R. Madupu, L. M. Brinkac, S. C. Daugherty, R. T. DeBoy, a. S. Durkin, M. Gwinn, J. F. Kolonay, S. a. Sullivan, D. H. Haft, J. Selengut, T. M. Davidsen, N. Zafar, O. White, B. Tran, C. Romero, H. a. Forberger, J. Weidman, H. Khouri, T. V. Feldblyum, T. R. Utterback, S. E. Van Aken, D. R. Lovley, and C. M. Fraser (2003), Genome of Geobacter sulfurreducens: metal reduction in subsurface environments., *Science (New York, N.Y.)*, *302*(5652), 1967–9, doi:10.1126/science.1088727.

Michel, F. M., L. Ehm, S. M. Antao, P. L. Lee, P. J. Chupas, G. Liu, D. R. Strongin, M. a. a. Schoonen, B. L. Phillips, and J. B. Parise (2007), The structure of ferrihydrite, a nanocrystalline material., *Science (New York, N.Y.)*, *316*(5832), 1726–9, doi:10.1126/science.1142525.

Michel, F. M., V. Barrón, J. Torrent, M. P. Morales, C. J. Serna, J.-F. Boily, Q. Liu, A. Ambrosini, a. C. Cismasu, and G. E. Brown (2010), Ordered ferrimagnetic form of ferrihydrite reveals links among structure, composition, and magnetism., *Proceedings of the National Academy of Sciences of the United States of America*, *107*(7), 2787–92, doi:10.1073/pnas.0910170107.

Morón, S., D. L. Fox, J. M. Feinberg, C. Jaramillo, G. Bayona, C. Montes, and J. I. Bloch (2013), Climate change during the Early Paleogene in the Bogotá Basin (Colombia) inferred from paleosol carbon isotope stratigraphy, major oxides, and environmental magnetism, *Palaeogeography, Palaeoclimatology, Palaeoecology*, *388*, 115–127, doi:10.1016/j.palaeo.2013.08.010.

Moskowitz, B. M. (1995), Biomineralization of magnetic minerals, *Review of Geophysics*, pp. 123–128.

Moskowitz, B. M., R. Frankel, and D. A. Bazylinski (1993), Rock magnetic criteria for the detection of biogenic magnetite, *Earth and Planetary Science Letters*, *120*, 283–300.

Mouser, P. J., D. E. Holmes, L. a. Perpetua, R. DiDonato, B. Postier, A. Liu, and D. R. Lovley (2009), Quantifying expression of Geobacter spp. oxidative stress genes in pure culture and during in situ uranium bioremediation., *The ISME journal*, *3*(4), 454–65, doi:10.1038/ismej.2008.126.

Mullins, C. E. (1977), Magnetic Susceptibility of the Soil and Its Significance in Soil Science - a Review, *Journal of Soil Science*, *28*(2), 223–246, doi:10.1111/j.1365-2389.1977.tb02232.x.

Murad, E. (1988), Properties and behavior of iron oxides as determined by Mossbauer spectroscopy, in *Iron in Soils and Clay Minerals*, edited by J. W. Stucki, B. Goodman, and U. Schwertmann, D. Rediel Publishing Company, The Netherlands.

Nevin, K. P., and D. R. Lovley (2000), Lack of Production of Electron-Shuttling Compounds or Solubilization of Fe (III) during Reduction of Insoluble Fe (III) Oxide by Geobacter metallireducens, *Applied and environmental microbiology*, pp. 2248–2251, doi:10.1128/AEM.66.5.2248-2251.2000.Updated.

Nordt, L. C., S. I. Dworkin, and S. C. Atchley (2011), Ecosystem response to soil biogeochemical behavior during the Late Cretaceous and early Paleocene within the western interior of North America, *Geological Society of America Bulletin*, *123*(9-10), 1745–1762, doi:10.1130/B30365.1.

Núñez, C., A. Esteve-nú nez, C. Giometti, S. Tollaksen, T. Khare, W. Lin, D. R. Lovley, and B. A. Methé (2006), DNA Microarray and Proteomic Analyses of the RpoS Regulon in Geobacter sulfurreducens, *Journal of bacteriology*, *188*, 2792, doi:10.1128/JB.188.8.2792.

Oches, E., and S. Banerjee (1996), Rock-magnetic proxies of climate change from loess-paleosol sediments of the Czech Republic, *Studia geophysica et geodaetica*, *40*(3), 287–300.

Orgeira, M., A. Walther, R. Tófalo, C. Vásquez, T. Berquó, C. Favier Dobois, and H. Bohnel (2003), Environmental magnetism in fluvial and loessic Holocene sediments and paleosols from the Chacopampean plain (Argentina), *Journal of South American Earth Sciences*, *16*, 259–274, doi:10.1016/S0895-9811(03)00067-1.

Orgeira, M. J., A. Walther, C. A. Vasquez, D. Tommaso, S. Alonso, G. Sherwood, H. Yuguan, and J. Vilas (1998), Mineral magnetic record of paleoclimate variation in loess and paleosol from the Buenos Aires formation (Buenos Aires , Argentina), *Journal of South American Earth Sciences*, *11*, 561–570.

Orgeira, M. J., R. Egli, and R. H. Compagnucci (2011), A Quantitative Model of Magnetic Enhancement in Loessic Soils, in *The Earth's Magnetic Interior*, edited by E. Petrovský, D. Ivers, T. Harinarayana, and E. Herrero-Bervera, pp. 361–397, Springer Netherlands, Dordrecht, doi:10.1007/978-94-007-0323-0.

Özdemir, O., and D. J. Dunlop (2014), Hysteresis and coercivity of hematite, *Journal of Geophysical Research : Solid Earth*, pp. 2582–2594, doi:10.1002/2013JB010739.

Parry, L. G. (1982), Magnetization of immobilized particle dispersions with two distinct particle sizes, *Physics of the Earth and Planetary Interiors*, *28*, 230–241.

Pauthenet, R. (1950), Variation thermique de l'aimantation spontaneé des ferrites de nickel, cobalt, fer et manganese, *Comptes Rendus de l'Académie des Sciences Series B*, *230*, 1842–1844.

Peak, D., and T. Regier (2012a), Direct observation of tetrahedrally coordinated Fe(III) in ferrihydrite., *Environmental science & technology*, *46*(6), 3163–8, doi:10.1021/es203816x.

Peak, D., and T. Z. Regier (2012b), Response to Comment on "Direct Observation of Tetrahedrally Coordinated Fe(III) in Ferrihydrite", *Environmental Science & Technology*, *46*(12), 6885–6887, doi:10.1021/es302143n.

Peppe, D. J., D. L. Royer, B. Cariglino, S. Y. Oliver, S. Newman, E. Leight, G. Enikolopov, M. Fernandez-Burgos, F. Herrera, J. M. Adams, E. Correa, E. D. Currano, J. M. Erickson, L. F. Hinojosa, J. W. Hoganson, A. Iglesias, C. a. Jaramillo, K. R. Johnson, G. J. Jordan, N. J. B. Kraft, E. C. Lovelock, C. H. Lusk, U. Niinemets, J. Peñuelas, G. Rapson, S. L. Wing, and I. J. Wright (2011), Sensitivity of leaf size and shape to climate: Global patterns and paleoclimatic applications, *New Phytologist*, *190*(3), 724–739, doi:10.1111/j.1469-8137.2010.03615.x.

PiPujol, M., and P. Buurman (1997), Dynamics of iron and calcium carbonate redistribution and palaeohydrology in middle Eocene alluvial paleosols of the southeast Ebro Basin margin (Catalonia, northeast Spain), *Palaeogeography, Palaeoclimatology, Palaeoecology*, *134*(1-4), 87–107, doi:10.1016/S0031-0182(97)00076-X.

Porter, S. C., B. Hallet, X. Wu, and Z. An (2001), Dependence of near-surface magnetic susceptibility on dust accumulation rate and precipitation on the Chinese Loess Plateau, *Quaternary Research*, *55*(3), 271–283, doi:10.1006/qres.2001.2224.

Postma, D. (1983), Pyrite and siderite oxidation in swamp sediments, *Journal of Soil Science*, *34*, 163–182.

Quinton, E. E., D. E. Dahms, and C. E. Geiss (2011), Magnetic analyses of soils from the Wind River Range, Wyoming, constrain rates and pathways of magnetic enhancement for soils from semiarid climates, *Geochemistry, Geophysics, Geosystems*, *12*(7), doi: 10.1029/2011GC003728.

R-Core-Team (2015), *R: A language and environment for statistical computing*, R Foundation for Statistical Computing, Vienna, Austria.

Ranjard, L., and A. Richaume (2001), Quantitative and qualitative microscale distribution of bacteria in soil., *Research in microbiology*, *152*(8), 707–16.

Rankey, E. C., and M. R. Farr (1997), Preserved pedogenic mineral magnetic signature, pedogenesis, and paleoclimate change: Pennsylvanian Roca Shale (Virgilian, Asselian), central Kansas, USA, *Sedimentary Geology*, *114*, 11–32.

Retallack, G. J. (1991), Untangling the effects of burial alteration and ancient soil formation, *Annual Review Earth and Plantary Sciences*, *19*, 183–206.

Retallack, G. J. (2005), Pedogenic carbonate proxies for amount and seasonality of precipitation in paleosols, *Geology*, *33*, 333–336, doi:10.1130/G21263.1.

Retallack, G. J., N. D. Sheldon, M. Cogoini, and R. Elmore (2003), Magnetic susceptibility of early Paleozoic and Precambrian paleosols, *Palaeogeography, Palaeoclimatology, Palaeoecology*, *198*(3-4), 373–380, doi:10.1016/S0031-0182(03)00479-6.

Roberts, A. P. (2015), Magnetic mineral diagenesis, *Earth Science Reviews*, *151*, 1–47.

Roberts, A. P., Y. Cui, and K. L. Verosub (1995), Wasp-waisted hysteresis loops: mineral magnetic characteristics and discrimination of components in mixed magnetic systems, *Journal of Geophysical Research: Solid Earth*, *100*, 17,909–17,924, doi:10.1029/95JB00672.

Roberts, A. P., Q. Liu, C. J. Rowan, L. Chang, C. Carvallo, J. Torrent, and C. S. Horng (2006), Characterization of hematite (α-Fe2O3), goethite (α-FeOOH), greigite (Fe3S4), and pyrrhotite (Fe7S8) using first-order reversal curve diagrams, *Journal of Geophysical Research: Solid Earth*, *111*(12), 1–16, doi:10.1029/2006JB004715.

Roberts, A. P., L. Chang, D. Heslop, F. Florindo, and J. C. Larrasoaa (2012), Searching for single domain magnetite in the "pseudo-single- domain" sedimentary haystack: implications of biogenic magnetite preservation for sediment magnetism and relative paleointensity determinations, *Journal of Geophysical Research: Solid Earth*, *117*, 1–26, doi:10.1029/2012JB009412.

Roberts, A. P., D. Heslop, X. Zhao, and C. R. Pike (2014), Understanding fine magnetic particle systems through use of first-order reversal curve diagrams, *Reviews of Geophysics*, *52*, 557–602, doi:10.1002/2014RG000462.

Robertson, D. J., and D. E. France (1994), Discrimination of remanence-carrying minerals in mixtures, using isothermal remanent magnetisation acquisition curves, *Physics of the Earth and Planetary Interiors*, *82*, 223–234.

Robinson, S. G. (1986), The late pleistocene palaeoclimatic record of north atlantic deep-sea sediments revealed by magnetic mineral measurements, *Physics of the Earth and Planetary Interiors*, *42*, 22–47.

Rochette, P., and G. Fillion (1989), Field and temperature behavior of remanence in synthetic goethite: Paleomagnetic implications, *Geophysical Research Letters*, *16*(8), 851, doi:10.1029/GL016i008p00851.

Rochette, P., P. E. Mathé, L. Esteban, H. Rakoto, J. L. Bouchez, Q. Liu, and J. Torrent (2005), Non-saturation of the defect moment of goethite and fine-grained hematite up to 57 Teslas, *Geophysical Research Letters*, *32*(22), 1–4, doi:10.1029/2005GL024196.

Roden, E. E. (2006), Geochemical and microbiological controls on dissimilatory iron reduction, *Comptes Rendus Geoscience*, *338*(6-7), 456–467, doi:10.1016/j.crte.2006.04.009.

Royer, D. L. (2012), Climate reconstruction from leaf size and shape: New developments and challenges, in *Reconstructing Earth's Deep-time Climate – The State of the Art in 2012*, vol. 18, edited by L. C. Ivany and B. T. Huber, pp. 195–212, The Paleontological Society Papers.

Sangode, S., V. Kumaravel, J. Bloemendal, and R. Kumar (2008), Effect of burial and compaction on soil magnetic properties: Results from soil-paleosol sequences in the Himalayan Foreland, India, *Palaeogeography, Palaeoclimatology, Palaeoecology*, *267*, 235–244, doi:10.1016/j.palaeo.2008.06.020.

Sangode, S. J., and J. Bloemendal (2004), Pedogenic transformation of magnetic minerals in Pliocene-Pleistocene palaeosols of the Siwalik Group, NW Himalaya, India, *Palaeogeography, Palaeoclimatology, Palaeoecology*, *212*(1-2), 95–118, doi:10.1016/j.palaeo.2004.05.019.

Schwertmann, U. (1988), Occurrence and Formation of Iron Oxides in Various Pedoenvironments, in *Iron in Soils and Clay Minerals*, edited by J. Stucki, B. Goodman, and U. Schwertmann, pp. 267–308, Springer Netherlands.

Schwertmann, U. (1993), Relations Between Iron Oxides, Soil Color, and Soil Formation, in *Soil Color*, edited by J. Bigham and E. Ciolkosz, pp. 51–69.

Schwertmann, U., and E. Murad (1983), Effect of pH on the formation of goethite and hematite from ferrihydrite, *Clays and Clay Minerals*, *31*(4), 277–284.

Severson, R. C., and H. F. Arneman (1973), Soil characteristics of teh forest-prairie ecotone in northwestern minnesota, *Soil Science Society of America*, *37*, 593–599.

Sharpe, J. L. (1996), Environmental archeology in central alaska: A magneto-stratigraphic correlation of tanana valley archeological sites with global climatic change.

Sheldon, N. D., and G. J. Retallack (2001), Equation for compaction of paleosols due to burial, *Geology*, *29*, 247–250, doi:10.1130/0091-7613(2001)029⟨0247.

Sheldon, N. D., and N. J. Tabor (2009), Quantitative paleoenvironmental and paleoclimatic reconstruction using paleosols, *Earth-Science Reviews*, *95*, 1–52, doi: 10.1016/j.earscirev.2009.03.004.

Sheldon, N. D., G. J. Retallack, and S. Tanaka (2002), Geochemical climofunctions from North American soils and application to paleosols across the Eocene Oligocene boundary in Oregon, *The Journal of Geology*, *110*, 687–696.

Singer, M., P. Fine, K. Verosub, and O. Chadwick (1992), Time dependence of magnetic susceptibility of soil chronosequences on the California coast, *Quaternary Research*, *37*(3), 323–332, doi:10.1016/0033-5894(92)90070-Y.

Smith, J. J., S. T. Hasiotis, M. J. Kraus, and D. T. Woody (2008), Relationship of floodplain ichnocoenoses to paleopedology, paleohydrology, and paleoclimate in the Willwood Formation, Wyoming, During the Paleocene-Eocene Thermal Maximum, *Palaios*, *23*, 683–699, doi:10.2110/palo.2007.p07-080r.

Snell, K. E., B. L. Thrasher, J. M. Eiler, P. L. Koch, L. C. Sloan, and N. J. Tabor (2012), Hot summers in the Bighorn Basin during the early Paleogene, *Geology*, *41*, 55–58, doi:10.1130/G33567.1.

Soreghan, G. S., R. D. Elmore, B. Katz, M. Cogoini, and S. Banerjee (1997), Pedogenically enhanced magnetic susceptibility variations preserved in Paleozoic loessite, *Geology*, *25*, 1003–1006, doi:10.1130/0091-7613(1997)025⟨1003.

Soreghan, G. S. L., R. D. Elmore, and M. T. Lewchuk (2002), Sedimentologic-magnetic record of western Pangean climate in upper Paleozoic loessite (lower Cutler beds , Utah), *Geological Society of America Bulletin*, *114*, 1019–1035, doi: 10.1130/0016-7606(2002)114⟨1019.

Sparks, N., S. Mann, D. Bazylinski, D. R. Lovley, H. Jannasch, and R. Frankel (1990), Structure and morphology of magnetite anaerobically-produced by a marine magnetotactic bacterium and a dissimilatory iron-reducing bacterium, *Earth and Planetary Science Letters*, *98*, 14–22.

Spassov, S., F. Heller, R. Kretzschmar, M. Evans, L. Yue, and D. Nourgaliev (2003), Detrital and pedogenic magnetic mineral phases in the loess/palaeosol sequence at lingtai (central chinese loess plateau), *Physics of the Earth and Planetary Interiors*, *140*, 255 – 275, doi:http://dx.doi.org/10.1016/j.pepi.2003.09.003.

Stacey, F. D., and S. K. Banerjee (1974), *Developments in Solid Earth Geophysics, 5: The Physical Principles of Rock Magnetism*, Elsevier Scientific Publishing Company, New York.

Stanjek, H., J. W. E. Fassbinder, H. Vali, H. Wagele, and W. Graf (1994), Evidence of Biogenic Greigite (Ferrimagnetic Fe3s4) in Soil, *European Journal of Soil Science*, *45*(2), 97–103.

Stinchcomb, G. E., and D. J. Peppe (2014), The influence of time on the magnetic properties of late Quaternary periglacial and alluvial surface and buried soils along the Delaware River , USA, *Frontiers in Earth Science*, doi:10.3389/feart.2014.00017.

Stober, J. C., and R. Thompson (1979), An investigation into the source of magnetic minerals in some finnish lake sediments, *Earth and Planetary Science Letters*, *45*, 464–474.

Stockhausen, H. (1998), Some new aspects for the modelling of isothermal remanent magnetization acquisition curves by cumulative log Gaussian functions, *Geophysical Research Letters*, *25*, 2217–2220.

Tauxe, L., T. A. T. Mullender, and T. Pick (1996), Potbellies, wasp-waists, and superparamagnetism in magnetic hysteresis, *Journal of Geophysical Research: Solid Earth*, *101*, 571–583, doi:10.1029/95JB03041.

Tauxe, L., S. K. Banerjee, R. Butler, and R. van der Voo (2014), *Essentials of Paleomagnetism*, 3rd web ed., University of California Press.

Taylor, R. M., B. A. Maher, and P. Self (1987), Magnetite in soils: I. The synthesis of single-domain and superparamagnetic magnetite, *Clay Minerals*, *22*, 411–422.

Thompson, R., and B. A. Maher (1995), Age models, sediment fluxes and paleoclimatic

reconstructions for the Chinese loess and palaeosol sequences, *Geophysical Journal International*, *123*, 611–622.

Thompson, R., and F. Oldfield (1986), *Environmental Magnetism*, Springer.

Till, J. L., Y. Guyodo, F. Lagroix, G. Ona-Nguema, and J. Brest (2014), Magnetic comparison of abiogenic and biogenic alteration products of lepidocrocite, *Earth and Planetary Science Letters*, *395*, 149–158, doi:10.1016/j.epsl.2014.03.051.

Till, J. L., Y. Guyodo, F. Lagroix, and G. Morin (2015), Goethite as a potential source of magnetic nanoparticles in sediments, (1), 75–78, doi:10.1130/G36186.1.

Tohver, E., A. Weil, J. Solum, and C. Hall (2008), Direct dating of carbonate remagnetization by 40Ar/39Ar analysis of the smectite–illite transformation, *Earth and Planetary Science Letters*, *274*, 524–530, doi:10.1016/j.epsl.2008.08.002.

Torrent, J., V. Barrón, and Q. Liu (2006), Magnetic enhancement is linked to and precedes hematite formation in aerobic soil, *Geophysical Research Letters*, *33*(2), L02,401, doi:10.1029/2005GL024818.

Torrent, J., Q.-S. Liu, J. Bloemendal, and V. Barron (2007), Magnetic enhancement and iron oxides in the upper Luochuan loess–paleosol sequence, Chinese Loess Plateau, *71*(5), doi:10.2136/sssaj2006.0328.

Torrent, J., Q. S. Liu, and V. Barrón (2010a), Magnetic susceptibility changes in relation to pedogenesis in a Xeralf chronosequence in northwestern Spain, *European Journal of Soil Science*, *61*(2), 161–173, doi:10.1111/j.1365-2389.2009.01216.x.

Torrent, J., Q. Liu, and V. Barrón (2010b), Magnetic minerals in Calcic Luvisols (Chromic) developed in a warm Mediterranean region of Spain: Origin and paleoenvironmental significance, *Geoderma*, *154*(3-4), 465–472, doi:10.1016/j.geoderma.2008.06.020.

Tramp, K. L., G. L. Soreghan, and R. D. Elmore (2004), Paleoclimatic inferences from paleopedology and magnetism of the Permian Maroon Formation loessite, Colorado, USA, *Geological Society of America Bulletin*, *116*, 671, doi:10.1130/B25354.1.

van Velzen, A. J., and M. J. Dekkers (1999), Low-temperature oxidation of magnetite in loess-paleosol sequences: a correction of rock magnetic parameters, *Studia geophysica et geodaetica*, *43*, 357–375.

Vidic, N. J., M. J. Singer, and K. L. Verosub (2004), Duration dependence of magnetic susceptibility enhancement in the Chinese loess–palaeosols of the past 620 ky, *Palaeogeography, Palaeoclimatology, Palaeoecology*, *211*(3-4), 271–288, doi: 10.1016/j.palaeo.2004.05.012.

Weil, A. B., A. Yonkee, and J. Kendall (2014), Towards a better understanding of the influence of basement heterogeneities and lithospheric coupling on foreland deformation: A structural and paleomagnetic study of Laramide deformation in the Southern Bighorn Arch, Wyoming, *Bulletin of the Geological Society of America*, *126*, 415–437, doi:10.1130/B30872.1.

Weiss, J. V., D. Emerson, and J. P. Megonigal (2004), Geochemical control of microbial Fe(III) reduction potential in wetlands: comparison of the rhizosphere to non-rhizosphere soil., *FEMS microbiology ecology*, *48*(1), 89–100, doi:10.1016/j.femsec.2003.12.014.

Wing, S. L., G. J. Harrington, F. A. Smith, J. I. Bloch, D. M. Boyer, and K. H. Freeman (2005), Transient floral change and rapid global warming at the Paleocene-Eocene boundary, *Science*, *310*, 993–996, doi:10.1126/science.1116913.

Woods, S. D., R. D. Elmore, and M. H. Engel (2002), Paleomagnetic dating of the smectite-to-illite conversion : Testing the hypothesis in Jurassic sedimentary rocks , Skye, Scotland, *Journal of Geophysical Research*, *107*.

Worm, H. U., and H. Markert (1987), The preparation of disperesed titanomagnetite particles by glass-ceramic method., *Physics of the Earth and Planetary Interiors*, *46*, 263–269.

Wuertz, D., and Y. Chalabi (2015), Package 'fgarch': Rmetrics – autoregressive conditional heteroskedastic modelling., *R Package version 3010.82. https://cran.r-project.org/web/packages/fGarch/fGarch.pdf*.

Yamazaki, T., and M. Ikehara (2012), Origin of magnetic mineral concentration variation in the Southern Ocean, *Paleoceanography*, *27*, PA2206, doi:10.1029/2011PA002271.

Yamazaki, T., and N. Ioka (1997), Environmental rock magnetism of pelagic clay: implications for asian eolian input to the north pacific since the pliocene, *Paleoceanography*, *12*, 111–124.

Zhang, Y. G., J. Ji, W. L. Balsam, L. Liu, and J. Chen (2007), High resolution hematite and goethite records from ODP 1143, South China Sea: Co-evolution of monsoonal precipitation and El Ni??o over the past 600,000??years, *Earth and Planetary Science Letters*, *264*(1-2), 136–150, doi:10.1016/j.epsl.2007.09.022.

Appendix A

Supplement to Chapter 6

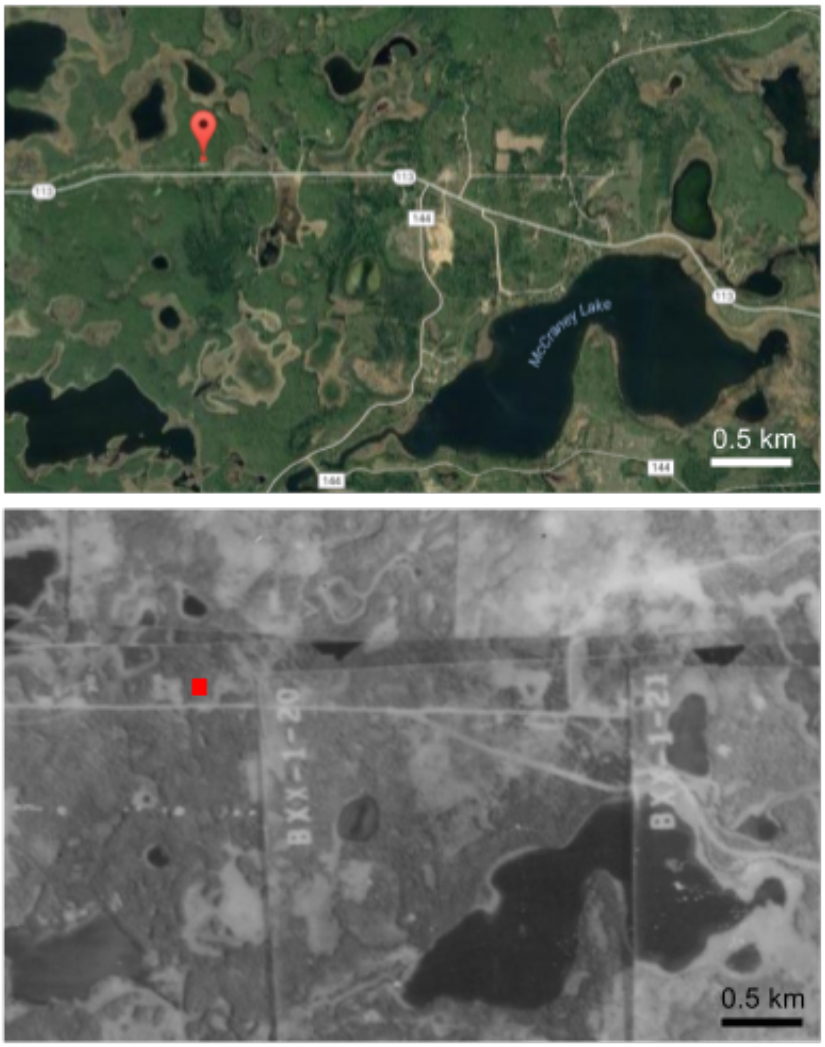

Figure A.1: Aerial imagery comparing the sampling location for forest soils. Top image is from Google Earth and can be compared to aerial photographs from 1939. Historical imagery is from the John R. Borchert Map Library, University of Minnesota using aerial photographs for Mahnomen County, Minnesota. Sampling location in both images highlighted with a red marker. The Borchert library collections are available at `http://geo.lib.umn.edu/aerial_photos/indexes/mahnomen.html#1939`

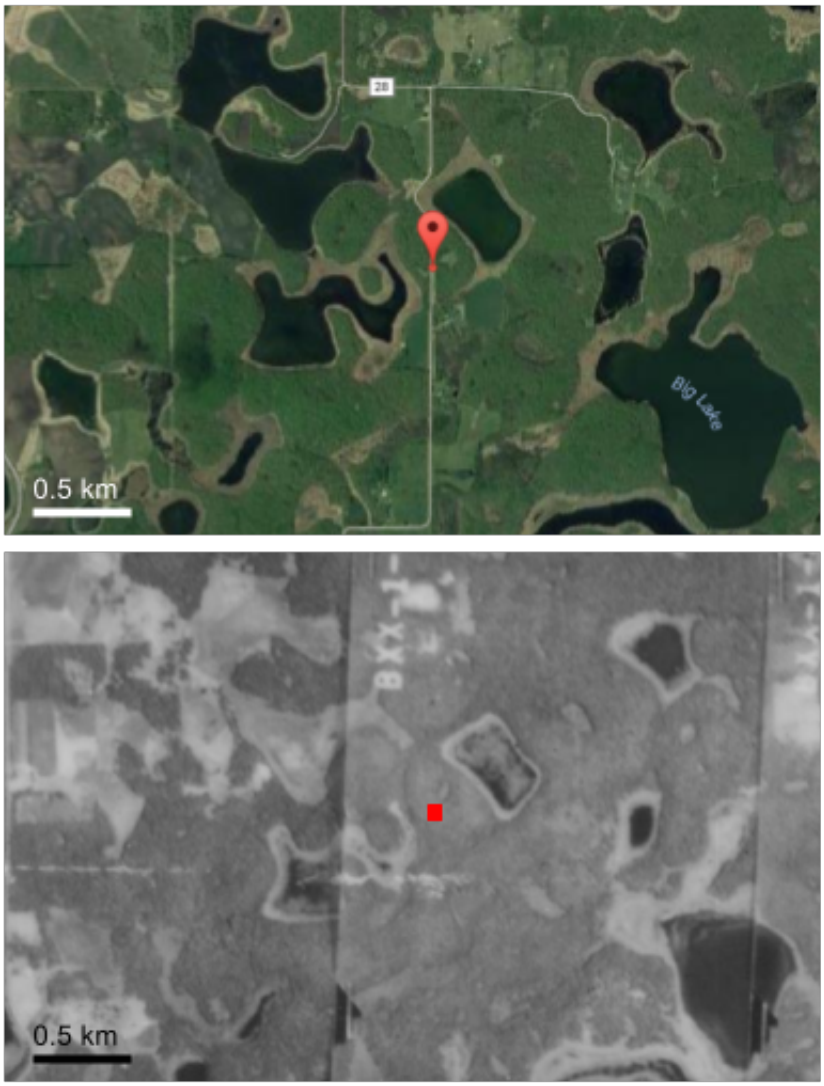

Figure A.2: Aerial imagery comparing the sampling location for transitional soils. Top image is from Google Earth and can be compared to aerial photographs from 1939. Historical imagery is from the John R. Borchert Map Library, University of Minnesota using aerial photographs for Mahnomen County, Minnesota. Sampling location in both images highlighted with a red marker. The Borchert library collections are available at `http://geo.lib.umn.edu/aerial_photos/indexes/mahnomen.html#1939`

Figure A.3: Aerial imagery comparing the sampling location for prairie soils. Top image is from Google Earth and can be compared to aerial photographs from 1939. Historical imagery is from the John R. Borchert Map Library, University of Minnesota using aerial photographs for Mahnomen County, Minnesota. Sampling location in both images highlighted with a red marker. The Borchert library collections are available at `http://geo.lib.umn.edu/aerial_photos/indexes/mahnomen.html#1939`

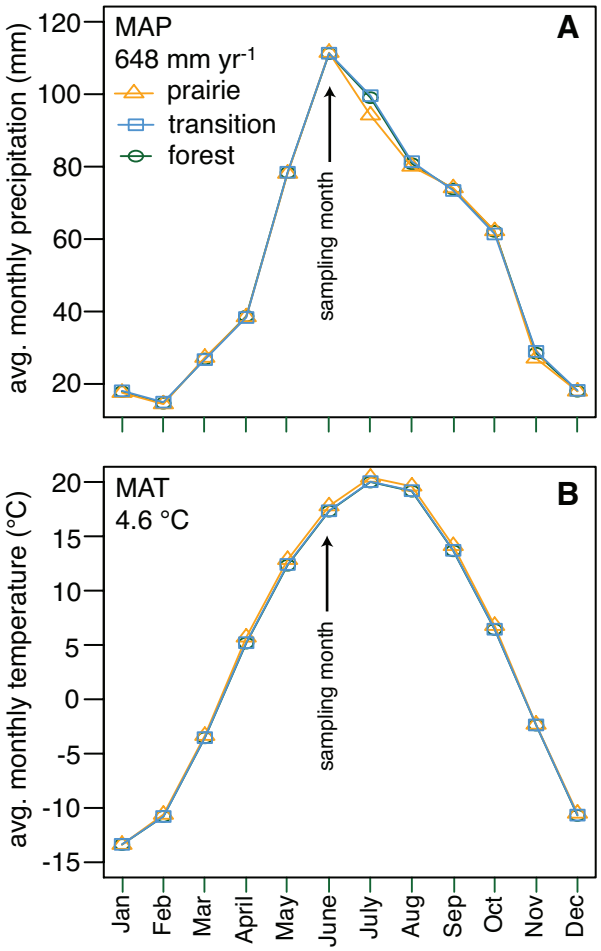

Figure A.4: Average 30-year normal (1981-2010) monthly precipitation (**A**) and temperature (**B**) normals for each sampling locality. Annual precipitation and temperature averages are reported in the upper left of each panel. The sampling month (June) is indicated with arrows in each plot. Data from the PRISM Climate Group, Oregon State University, http://prism.oregonstate.edu, created 9 March 2016.

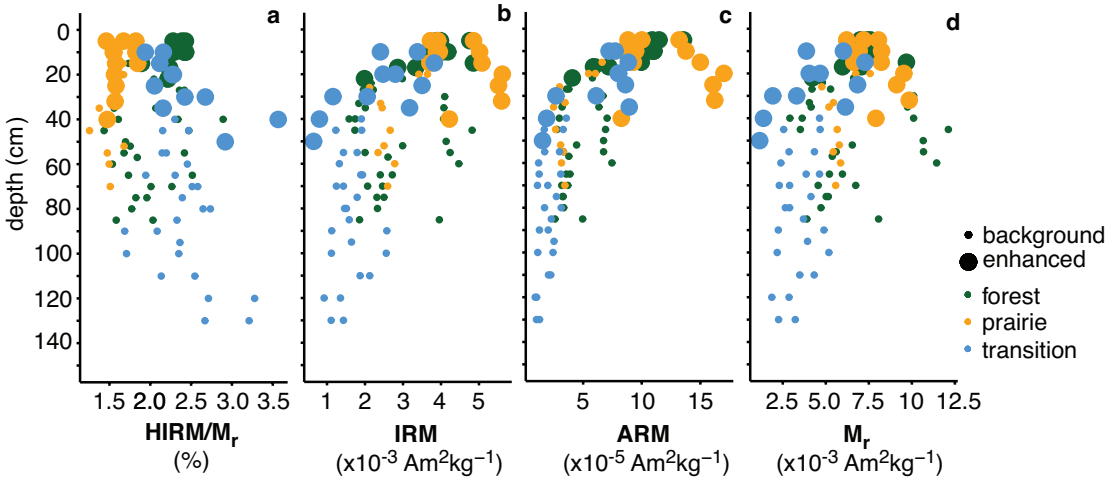

Figure A.5: Magnetic properties with depth for soil transect. Data reported here for hard isothermal remanent magnetization ($HIRM$, calculated with 300 mT intermediate field) relative to saturation remanences (M_r) (a), isothermal remanent magnetization (IRM) (b), anhysteretic remanent magnetization (ARM) (c), and M_r (d). Background and enhanced specimen in all cases are determined by criteria highlighted by shaded boxes in Figure 5.2d,e in the main body for this article.

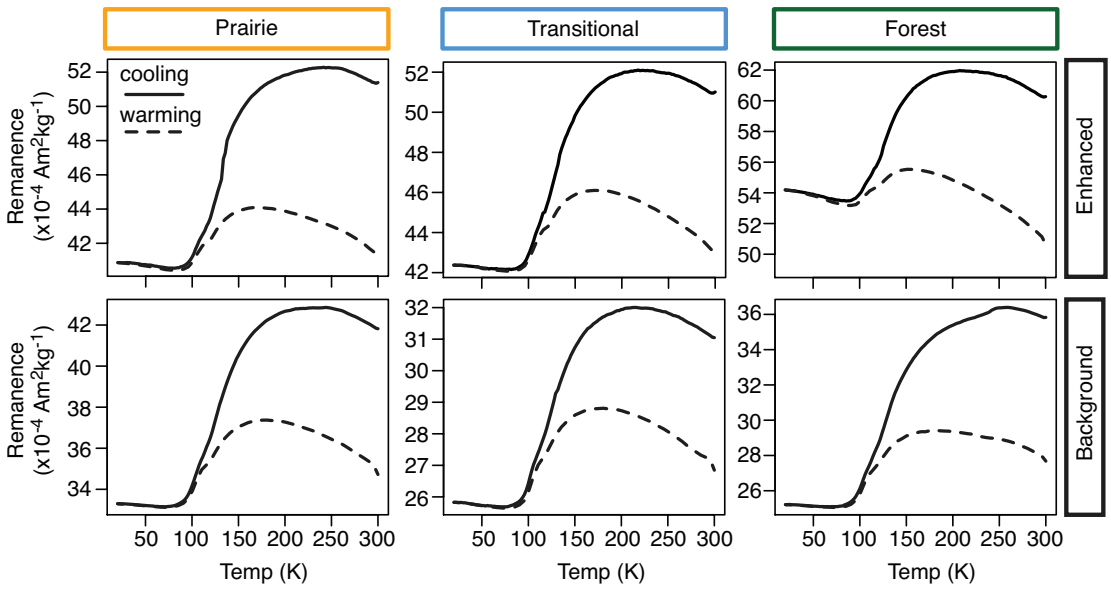

Figure A.6: Room-temperature saturation isothermal remanent magnetization (RT-SIRM) curves for enhanced and background specimen from prairie, transitional, and forest sampling localities. All samples display a broad loss of Magnetization just prior to the Verwey transition of magnetite (110 K for pure, stoichiometric magnetite) indicating magnetic mineralogy dominated by magnetite and partially oxidized magnetite. The increase in magnetization with cooling observed in the forest enhanced specimen is indicative of contributions from goethite (*Maher et al.*, 2004).

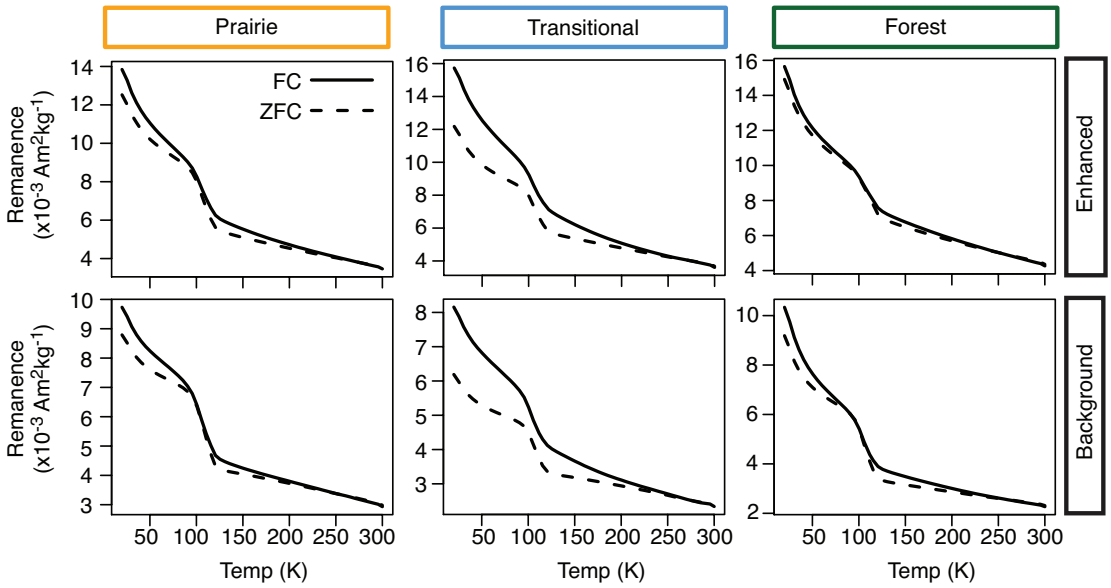

Figure A.7: Field cooled (FC) and zero field cooled (ZFC) remanence (2.5 T) for enhanced and background specimen from each sampling locality. FC remanence that is greater than ZFC remanence is indicative of single domain magnetite dominating the remanence held by these specimens. The Verwey transition of magnetite is clearly observed in all specimen confirming that magnetite is the primary magnetic carrier in this system.

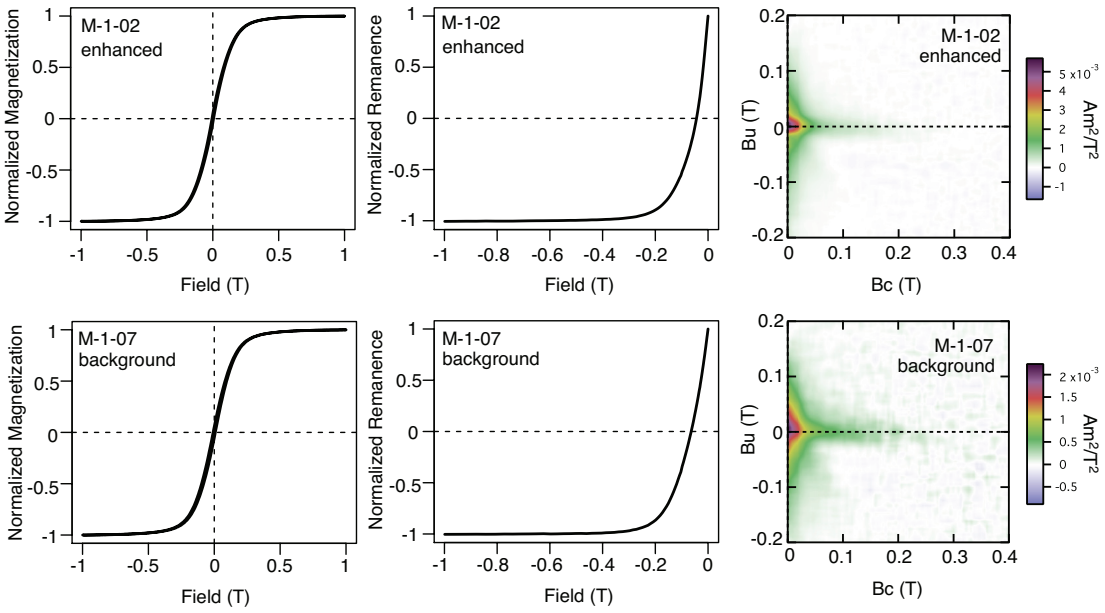

Figure A.8: Hysteresis loops (left column), backfield remanence curves (middle column), and first order reversal curve (FORC) diagrams for representative enhanced and background prairie specimens M-1-02 and M-1-07. All FORC diagrams processed with a smoothing factor of 5 in FORCinel v3.0 using simple smooth (*Harrison and Feinberg*, 2009).

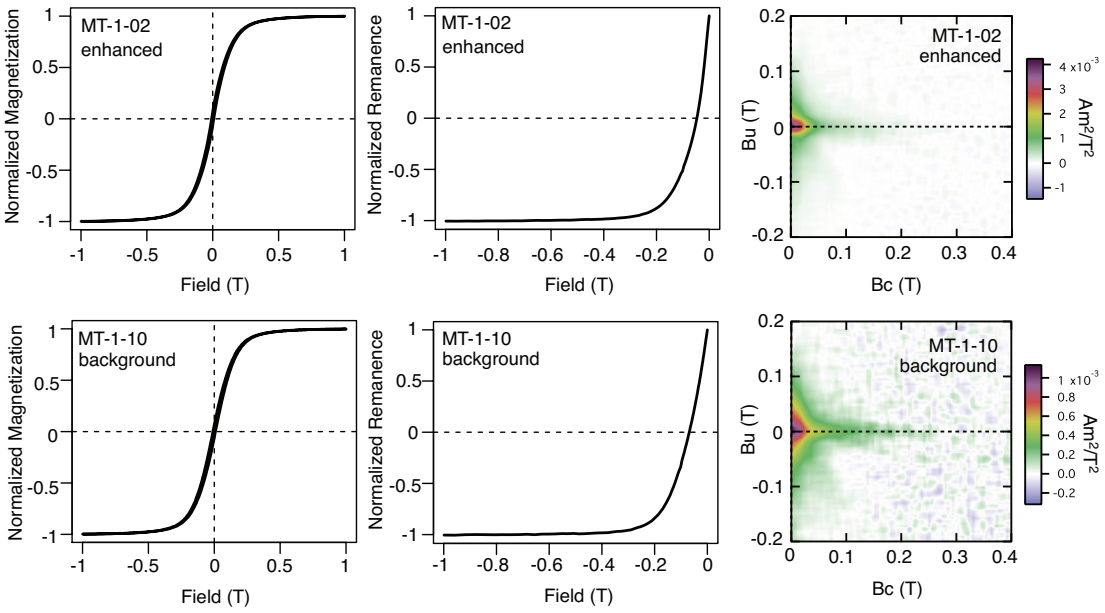

Figure A.9: Hysteresis loops (left column), backfield remanence curves (middle column), and first order reversal curve (FORC) diagrams for representative enhanced and background transitional specimens MT-1-02 and MT-1-10. All FORC diagrams processed with a smoothing factor of 5 in FORCinel v3.0 using simple smooth (*Harrison and Feinberg*, 2009).

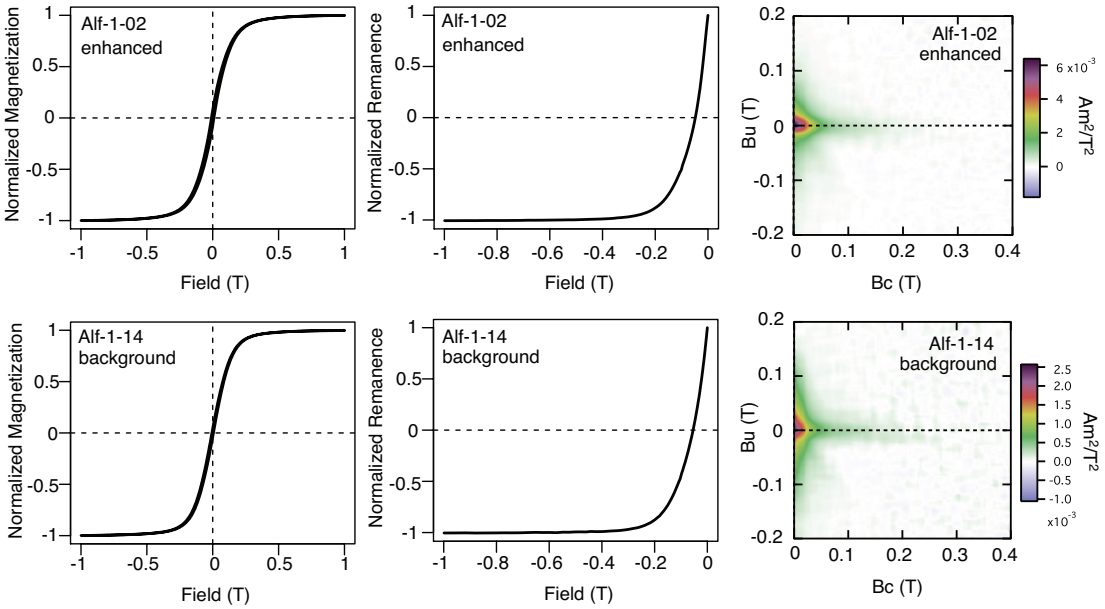

Figure A.10: Hysteresis loops (left column), backfield remanence curves (middle column), and first order reversal curve (FORC) diagrams for representative enhanced and background forest specimens Alf-1-02 and Alf-1-14. All FORC diagrams processed with a smoothing factor of 5 in FORCinel v3.0 using simple smooth (*Harrison and Feinberg*, 2009).

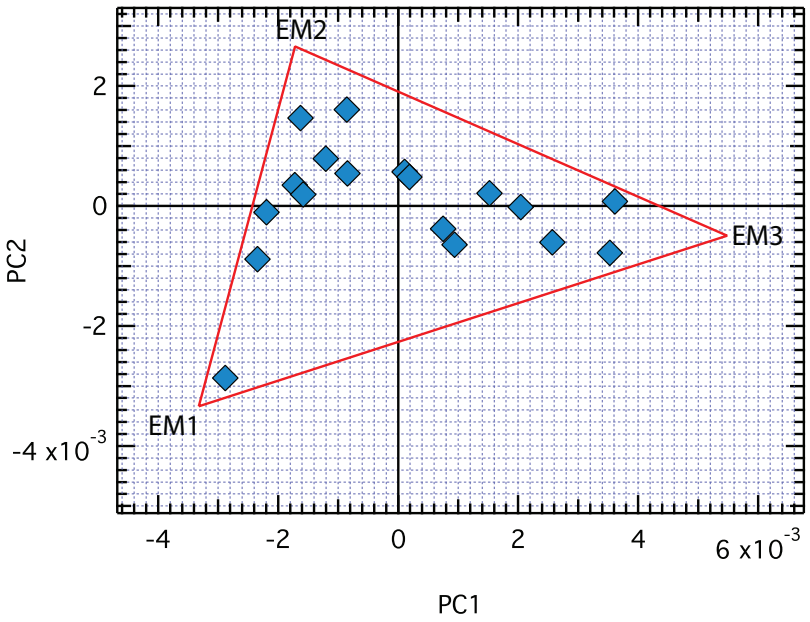

Figure A.11: Score plot results from the PCA analysis within the FORCem analytical package. End member scores are represented by the corners of the triangle and all data falls within the mixing space delineated by this triangle. See *Lascu et al.* (2015) for details.

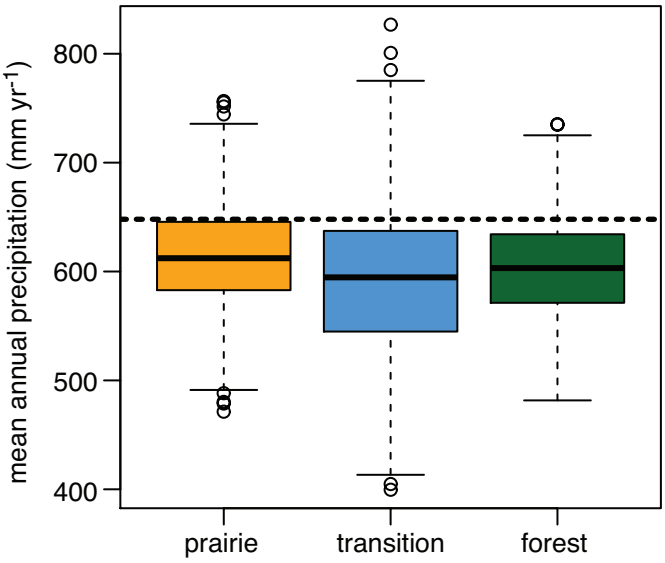

Figure A.12: Estimates of mean annual precipitation (MAP) based on the ARM/IRM proxy of *Geiss et al.* (2008). For each sampling zone, ARM/IRM for enhanced specimens was resampled 10,000 times using mean and standard deviations, assuming normality, and MAP was reconstructed from each resampled value of ARM/IRM. Box plots display median (thick center bar) 50% (colored box) and 95% (dashed vertical lines) confidence limits. Outliers beyond 95% confidence are shown as open symbols. The thick horizontal dashed line highlights the observed 30 year normal precipitation (MAP = 648 mm yr^{-1} for the transect based on PRISM data; PRISM Climate Group, Oregon State University, http://prism.oregonstate.edu, created 9 March 2016).

Appendix B

Supplement to Chapter 7

The contents of this Appendix where originally published as a supplement to Maxbauer et al. (2016b), which is reproduced in Chapter 2 of this dissertation. This work is included below in its published form with permission of all authors.

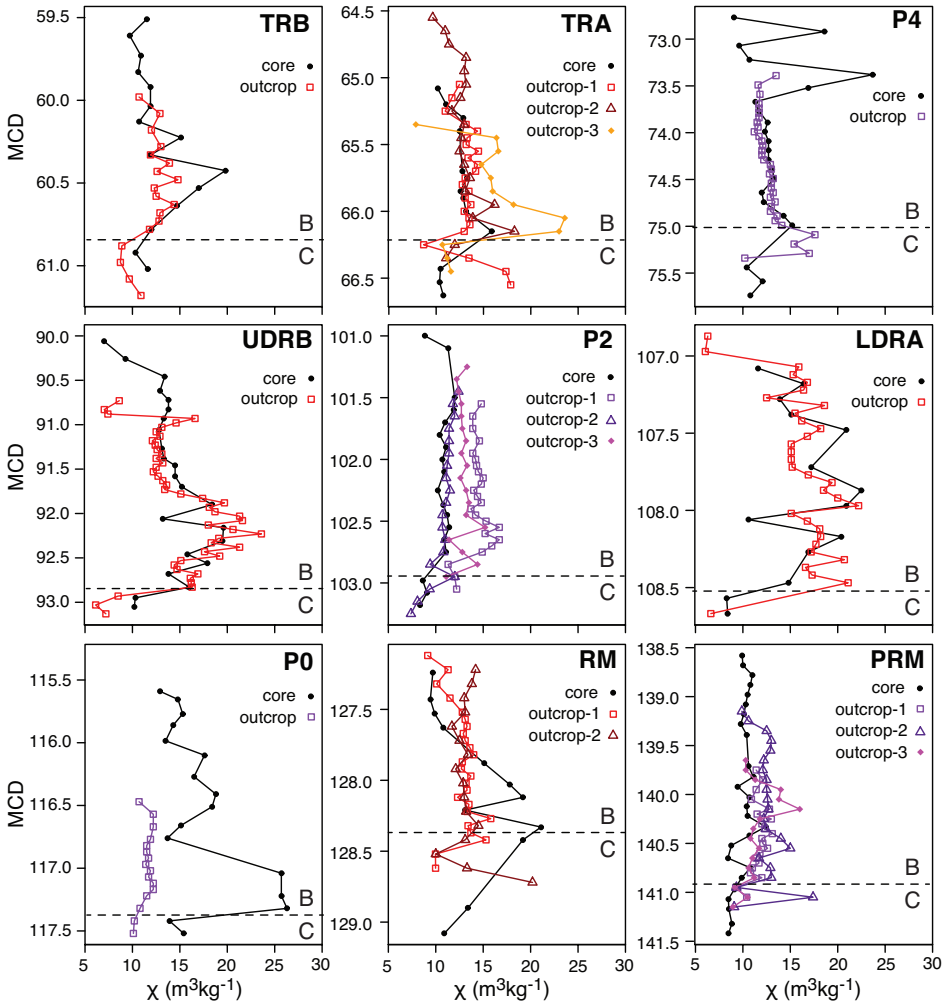

Figure B.1: Magnetic susceptibility (χ) profiles for all marker bed paleosols at Polecat Bench sampled in core (black symbols) and in outcrop (colored symbols). Paleosol name and abbreviations are provided in the upper right corner of each panel. MCD = meters composite depth. Boundary of parent material (C horizon) and B horizons are shown for each profile with dashed line.

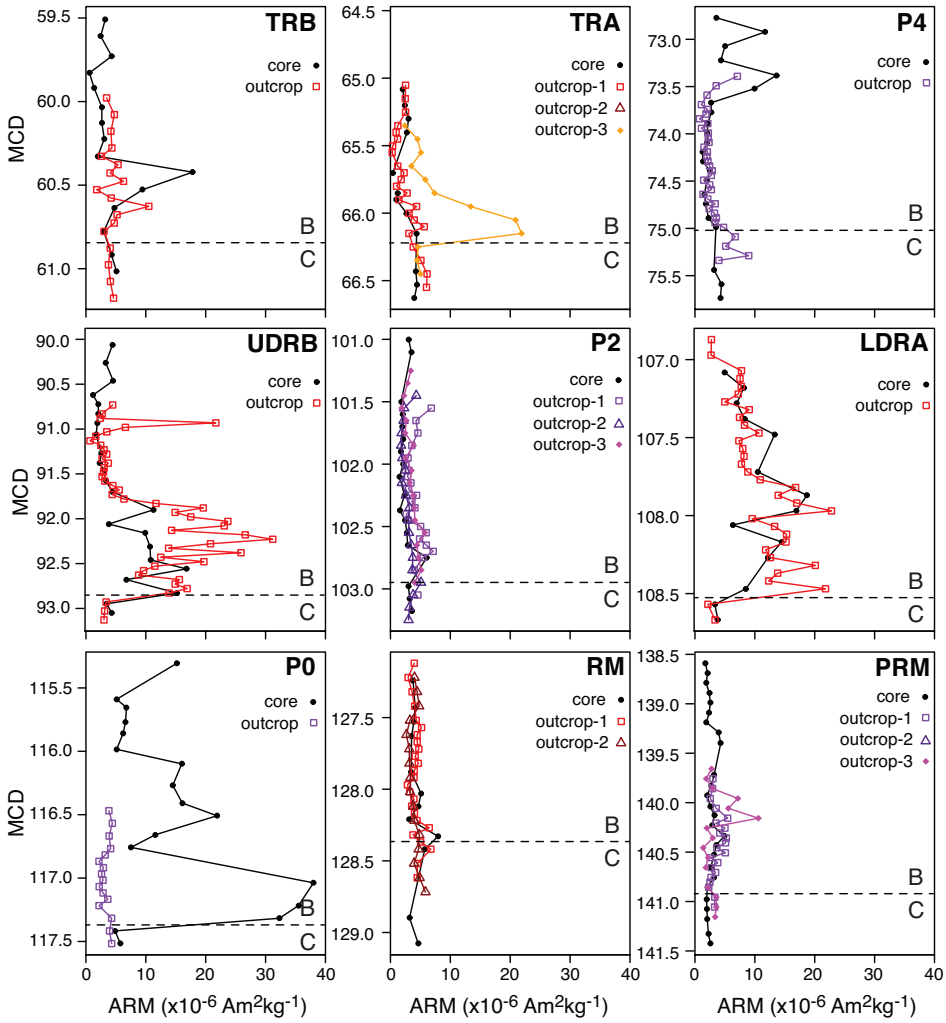

Figure B.2: Anhysteretic remanent magnetization (ARM) for all marker bed paleosols at Polecat Bench sampled in core (black symbols) and in outcrop (colored symbols). Paleosol name and abbreviations are provided in the upper right corner of each panel. MCD = meters composite depth. Boundary of parent material (C horizon) and B horizons are shown for each profile with dashed line.

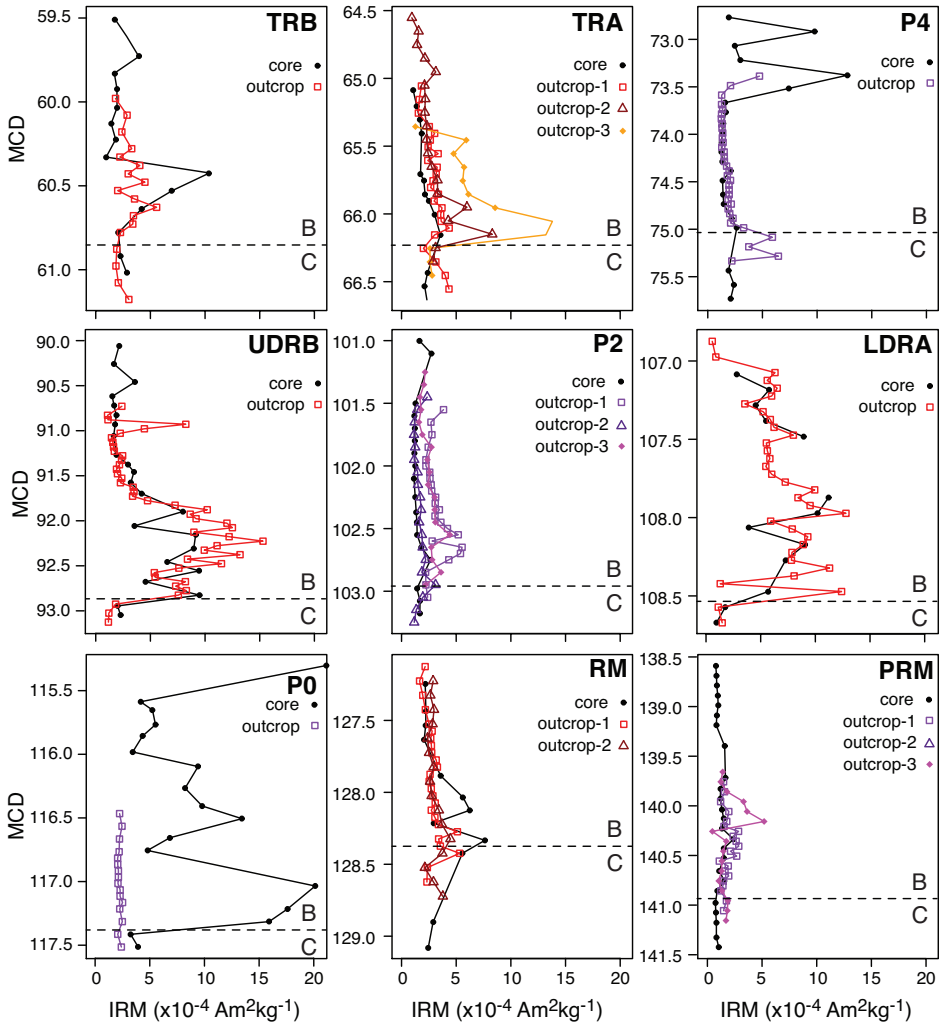

Figure B.3: Isothermal remanent magnetization (IRM) for all marker bed paleosols at Polecat Bench sampled in core (black symbols) and in outcrop (colored symbols). Paleosol name and abbreviations are provided in the upper right corner of each panel. MCD = meters composite depth. Boundary of parent material (C horizon) and B horizons are shown for each profile with dashed line.

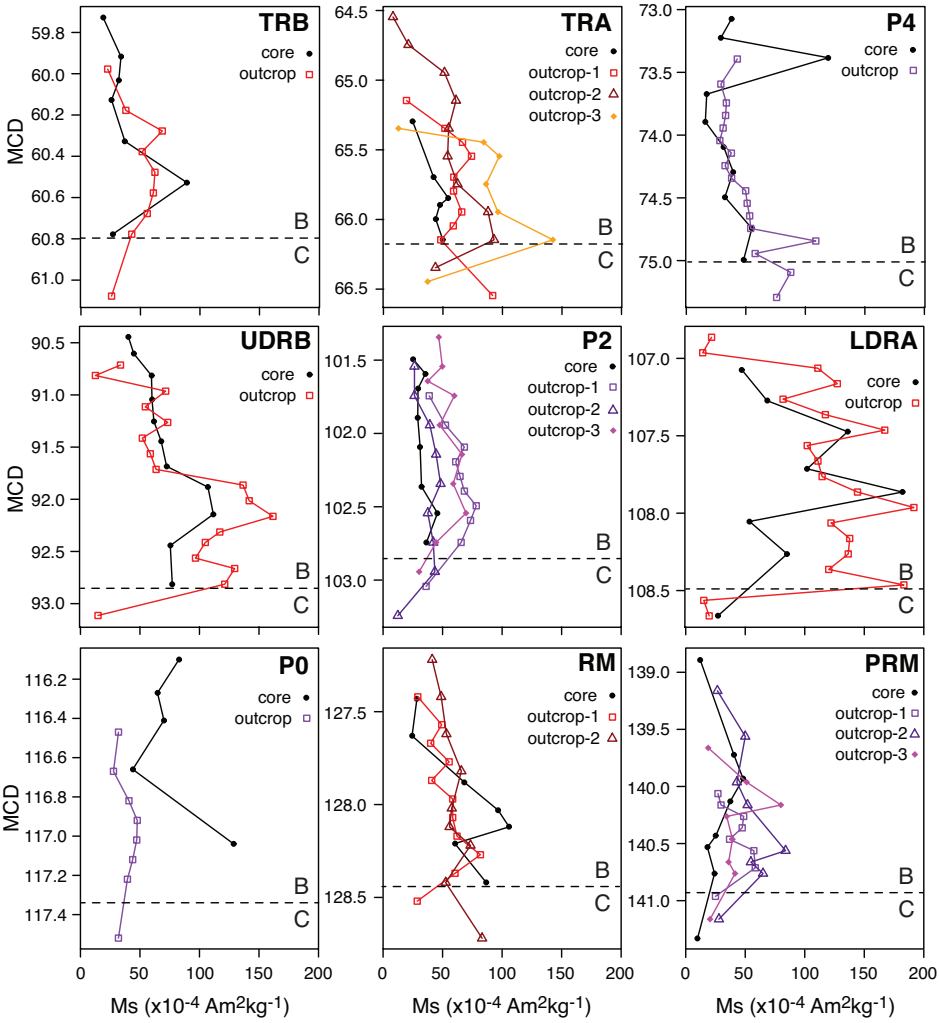

Figure B.4: Saturation magnetization (M_s) for all marker bed paleosols at Polecat Bench sampled in core (black symbols) and in outcrop (colored symbols). Paleosol name and abbreviations are provided in the upper right corner of each panel. MCD = meters composite depth. Boundary of parent material (C horizon) and B horizons are shown for each profile with dashed line.

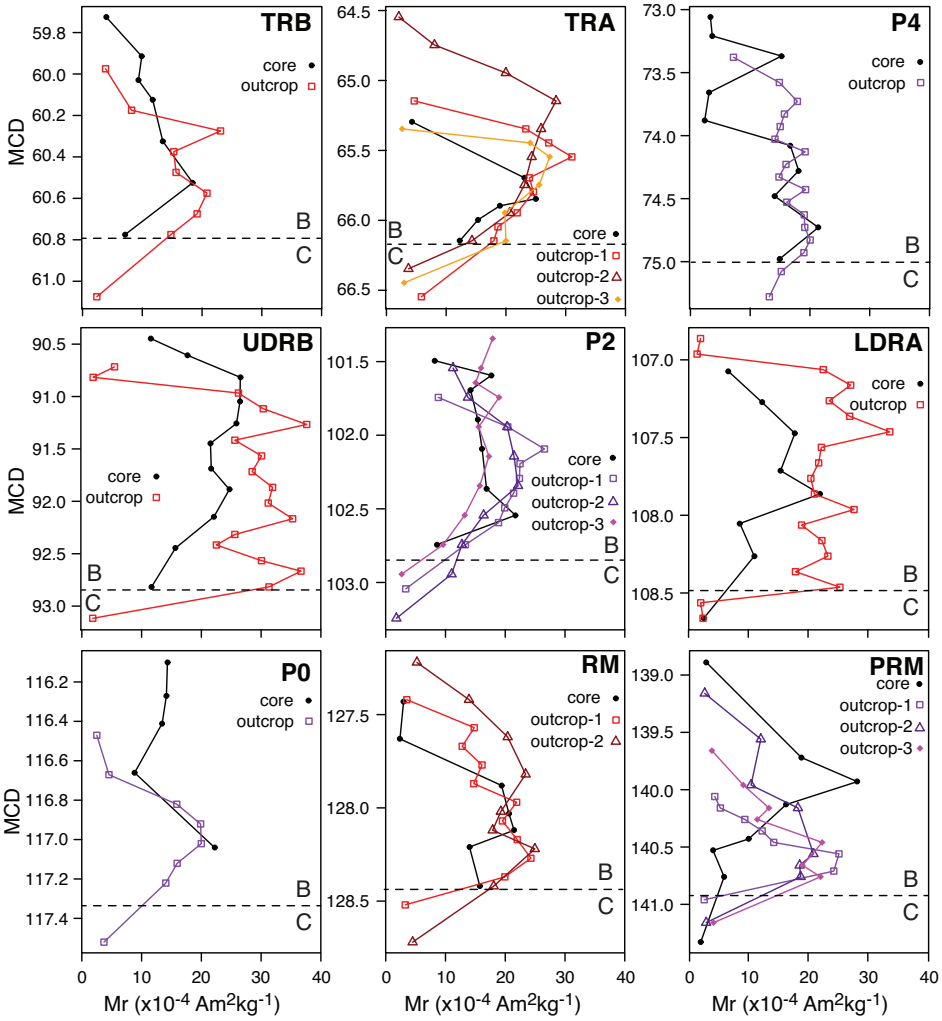

Figure B.5: Saturation remanent magnetization (M_{rs}) for all marker bed paleosols at Polecat Bench sampled in core (black symbols) and in outcrop (colored symbols). Paleosol name and abbreviations are provided in the upper right corner of each panel. MCD = meters composite depth. Boundary of parent material (C horizon) and B horizons are shown for each profile with dashed line.

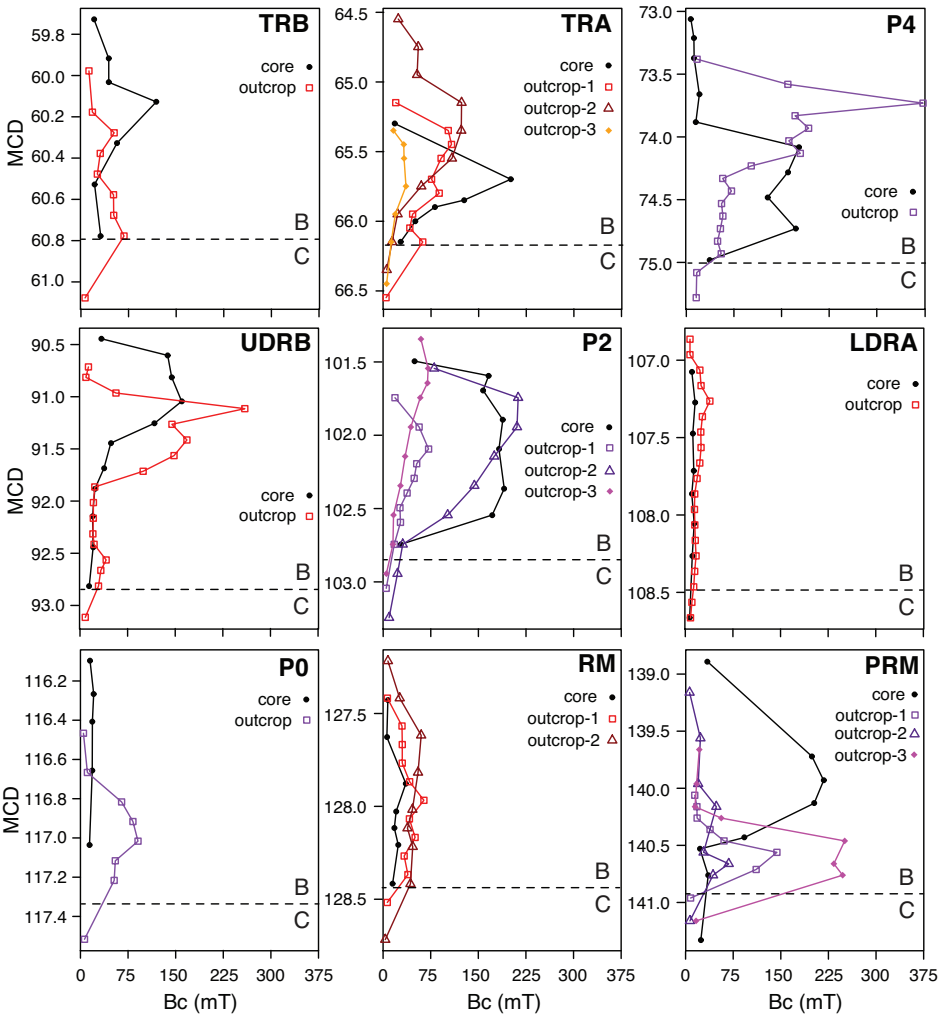

Figure B.6: Coercivity (B_c) for all marker bed paleosols at Polecat Bench sampled in core (black symbols) and in outcrop (colored symbols). Paleosol name and abbreviations are provided in the upper right corner of each panel. MCD = meters composite depth. Boundary of parent material (C horizon) and B horizons are shown for each profile with dashed line.

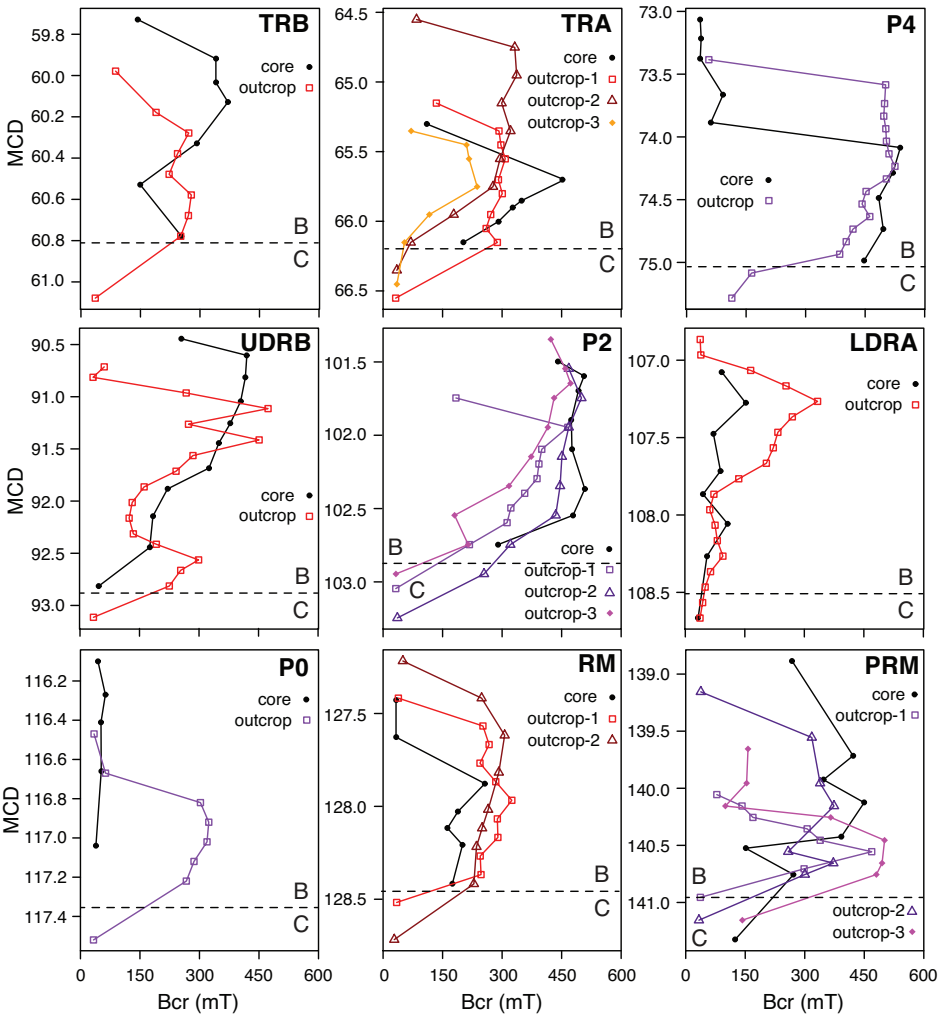

Figure B.7: Coercivity of remanence (B_{cr}) for all marker bed paleosols at Polecat Bench sampled in core (black symbols) and in outcrop (colored symbols). Paleosol name and abbreviations are provided in the upper right corner of each panel. MCD = meters composite depth. Boundary of parent material (C horizon) and B horizons are shown for each profile with dashed line.

Table B.1: Low-field magnetic properties for marker bed paleosols preserved in core. Specimen that are used for enhancement ratios are indicated in bold and italics. MCD = meters composite depth.

Paleosol	**Specimen**	**Horizon**	**MCD**	**ARM**	**IRM**	χ_{ARM}	χ
			meters	Am^2kg^{-1}	Am^2kg^{-1}	mA^{-1}	m^3kg^{-1}
LDRA	***LDRA-000***	***C1***	***108.67***	***3.84E-06***	***9.56E-05***	***9.65E-08***	***8.40E-08***
LDRA	***LDRA-010***	***C1***	***108.57***	***3.31E-06***	***1.76E-04***	***8.32E-08***	***8.29E-08***
LDRA	LDRA-020	B1	108.47	8.51E-06	5.68E-04	2.14E-07	1.48E-07
LDRA	***LDRA-040***	***B1***	***108.27***	***1.22E-05***	***7.28E-04***	***3.08E-07***	***1.69E-07***
LDRA	***LDRA-050***	***B1***	***108.17***	***1.45E-05***	***9.06E-04***	***3.64E-07***	***2.04E-07***
LDRA	***LDRA-060***	***B1***	***108.06***	***6.33E-06***	***3.90E-04***	***1.59E-07***	***1.06E-07***
LDRA	***LDRA-070***	***B1***	***107.97***	***1.69E-05***	***1.02E-03***	***4.26E-07***	***2.09E-07***
LDRA	***LDRA-080***	***B1***	***107.87***	***1.87E-05***	***1.12E-03***	***4.71E-07***	***2.25E-07***
LDRA	***LDRA-095***	***B1***	***107.72***	***1.05E-05***		***2.64E-07***	***1.72E-07***
LDRA	***LDRA-120***	***B2***	***107.48***	***1.33E-05***	***8.93E-04***	***3.34E-07***	***2.09E-07***
LDRA	LDRA-130	B2	107.38	8.29E-06	5.49E-04	2.08E-07	1.51E-07
LDRA	LDRA-140	B2	107.28	6.98E-06	4.53E-04	1.75E-07	1.39E-07
LDRA	LDRA-150	B2	107.18	8.16E-06	5.78E-04	2.05E-07	1.64E-07
LDRA	LDRA-160	C2	107.08	4.95E-06	2.80E-04	1.24E-07	1.16E-07
PRM	***PRM-000***	***C***	***141.42***	***2.58E-06***	***1.04E-04***	***6.49E-08***	***8.49E-08***
PRM	***PRM-010***	***C***	***141.32***	***2.24E-06***	***8.23E-05***	***5.63E-08***	***8.84E-08***
PRM	***PRM-025***	***C***	***141.17***	***2.06E-06***	***8.23E-05***	***5.18E-08***	***8.52E-08***
PRM	***PRM-035***	***C***	***141.07***	***2.00E-06***	***7.66E-05***	***5.03E-08***	***8.47E-08***
PRM	***PRM-045***	***C***	***140.97***	***1.94E-06***	***7.38E-05***	***4.89E-08***	***9.09E-08***
PRM	PRM-055	B1	140.85	2.09E-06	9.00E-05	5.26E-08	9.89E-08
PRM	***PRM-065***	***B1***	***140.75***	***3.18E-06***	***1.55E-04***	***8.00E-08***	***1.08E-07***
PRM	***PRM-075***	***B1***	***140.65***	***2.64E-06***	***1.09E-04***	***6.64E-08***	***8.42E-08***
PRM	***PRM-085***	***B1***	***140.52***	***3.18E-06***	***1.49E-04***	***7.99E-08***	***8.79E-08***
PRM	***PRM-095***	***B1***	***140.42***	***3.58E-06***	***1.51E-04***	***8.99E-08***	***1.07E-07***
PRM	***PRM-105***	***B1***	***140.33***	***4.92E-06***	***2.39E-04***	***1.24E-07***	***1.24E-07***
PRM	***PRM-115***	***B2***	***140.22***	***2.88E-06***	***1.35E-04***	***7.25E-08***	***1.05E-07***
PRM	***PRM-125***	***B2***	***140.12***	***3.24E-06***	***1.49E-04***	***8.14E-08***	***1.04E-07***
PRM	***PRM-135***	***B2***	***140.03***	***2.55E-06***	***1.33E-04***	***6.42E-08***	***1.07E-07***
PRM	***PRM-145***	***B2***	***139.92***	***2.02E-06***	***1.19E-04***	***5.09E-08***	***9.46E-08***
PRM	***PRM-155***	***B2***	***139.82***	***2.70E-06***	***1.20E-04***	***6.77E-08***	***1.11E-07***
PRM	***PRM-165***	***B2***	***139.71***	***3.21E-06***	***1.65E-04***	***8.08E-08***	***1.06E-07***
PRM	***PRM-185***	***B2***	***139.39***	***4.30E-06***	***1.58E-04***	***1.08E-07***	***1.04E-07***
PRM	PRM-195	B2	139.28	3.94E-06		9.90E-08	9.77E-08
PRM	PRM-205	A	139.18	1.92E-06	8.11E-05	4.81E-08	1.01E-07
PRM	PRM-215	A	139.08	2.37E-06	8.65E-05	5.96E-08	1.03E-07

PRM	PRM-225	A	138.98	2.56E-06	9.84E-05	6.44E-08	1.05E-07
PRM	PRM-235	A	138.88	2.39E-06	9.51E-05	6.01E-08	1.08E-07
PRM	PRM-245	A	138.78	1.87E-06	8.55E-05	4.70E-08	1.10E-07
PRM	PRM-255	A	138.68	2.12E-06	8.33E-05	5.34E-08	1.00E-07
PRM	PRM-265	A	138.58	1.74E-06	7.67E-05	4.36E-08	9.93E-08
P0	***P0-000***	***C***	***117.52***	***5.74E-06***	***0.000394009***	***1.44E-07***	***1.54E-07***
P0	***P0-010***	***C***	***117.42***	***4.87E-06***	***0.000324796***	***1.22E-07***	***1.39E-07***
P0	P0-020	C/B	117.32	3.23E-05	0.00159138	8.11E-07	2.63E-07
P0	P0-030	C/B	117.22	3.55E-05	0.001760371	8.92E-07	2.57E-07
P0	P0-045	B	117.04	3.80E-05	0.00201308	9.56E-07	2.57E-07
P0	P0-075	B	116.76	7.54E-06	0.000479079	1.89E-07	1.37E-07
P0	***P0-085***	***B***	***116.66***	***1.16E-05***	***0.000684296***	***2.93E-07***	***1.51E-07***
P0	***P0-100***	***B***	***116.51***	***2.19E-05***	***0.001342424***	***5.50E-07***	***1.84E-07***
P0	***P0-110***	***B***	***116.41***	***1.61E-05***	***0.00097932***	***4.05E-07***	***1.88E-07***
P0	***P0-120***	***B***	***116.27***	***1.45E-05***	***0.000822812***	***3.63E-07***	***1.65E-07***
P0	***P0-140***	***B***	***116.1***	***1.60E-05***	***0.000941768***	***4.03E-07***	***1.76E-07***
P0	P0-150	B/C	115.985	5.12E-06	0.000343738	1.29E-07	1.35E-07
P0	P0-165	B/C	115.86	6.21E-06	0.000433721	1.56E-07	1.43E-07
P0	P0-175	B/C	115.77	6.60E-06	0.000551963	1.66E-07	1.53E-07
P0	P0-185	B/C	115.655	6.78E-06	0.00052479	1.70E-07	1.48E-07
P0	P0-195	B/C	115.59	5.12E-06	0.000415785	1.29E-07	1.29E-07
P0	P0-215	C	115.305	1.52E-05	0.002112755	3.83E-07	4.63E-07
P2	***P2-000***	***C***	***103.18***	***3.58E-06***	***0.000167214***	***8.99E-08***	***8.36E-08***
P2	***P2-010***	***C***	***103.08***	***3.21E-06***	***0.000169389***	***8.07E-08***	***9.07E-08***
P2	***P2-020***	***C***	***102.98***	***3.01E-06***	***0.000140582***	***7.58E-08***	***8.63E-08***
P2	***P2-040***	***B***	***102.75***	***6.07E-06***	***0.000265463***	***1.53E-07***	***1.11E-07***
P2	***P2-050***	***B***	***102.65***	***2.87E-06***	***0.000182127***	***7.21E-08***	***1.09E-07***
P2	***P2-060***	***B***	***102.55***	***2.75E-06***	***0.000142953***	***6.92E-08***	***1.14E-07***
P2	***P2-070***	***B***	***102.45***	***2.47E-06***	***0.000140504***	***6.20E-08***	***1.12E-07***
P2	P2-080	B	102.37	1.56E-06	0.000134222	3.92E-08	1.08E-07
P2	P2-090	B	102.25	2.34E-06	0.000125065	5.89E-08	1.02E-07
P2	P2-105	B	102.1	1.53E-06	0.000113754	3.84E-08	1.09E-07
P2	P2-115	B	102	2.12E-06	0.000124491	5.33E-08	1.07E-07
P2	P2-125	B	101.9	1.77E-06	0.000117298	4.44E-08	1.11E-07
P2	P2-135	B	101.8	2.14E-06	0.000121018	5.38E-08	1.04E-07
P2	P2-145	B	101.7	1.95E-06	0.000121796	4.91E-08	1.10E-07
P2	P2-155	B	101.6	2.03E-06	0.000117741	5.10E-08	1.19E-07
P2	P2-165	A	101.5	1.79E-06	0.000127734	4.51E-08	1.20E-07
P2	P2-185	A	101.1	3.48E-06	0.000271887	8.75E-08	1.13E-07
P2	P2-195	A/C	101	3.05E-06	0.000165221	7.67E-08	8.85E-08
P4	***P4-000***	***C***	***75.74***	***4.25E-06***	***0.000209058***	***1.07E-07***	***1.08E-07***

P4	***P4-015***	***C***	***75.59***	***4.43E-06***	***0.00024033***	***1.11E-07***	***1.21E-07***
P4	***P4-030***	***C***	***75.44***	***3.18E-06***	***0.000190412***	***7.99E-08***	***1.04E-07***
P4	***P4-050***	***B***	***74.99***	***3.50E-06***	***0.000265875***	***8.80E-08***	***1.52E-07***
P4	***P4-060***	***B***	***74.89***	***2.24E-06***	***0.000216822***	***5.62E-08***	***1.43E-07***
P4	***P4-075***	***B***	***74.74***	***1.82E-06***	***0.000146645***	***4.57E-08***	***1.22E-07***
P4	***P4-085***	***B***	***74.64***	***1.59E-06***	***0.000139711***	***4.00E-08***	***1.20E-07***
P4	***P4-100***	***B***	***74.49***	***1.99E-06***	***0.000135417***	***5.01E-08***	***1.33E-07***
P4	***P4-110***	***B***	***74.39***	***2.49E-06***	***0.000210239***	***6.26E-08***	***1.31E-07***
P4	***P4-120***	***B***	***74.29***	***1.32E-06***	***0.000133432***	***3.32E-08***	***1.27E-07***
P4	***P4-130***	***B***	***74.19***	***1.30E-06***	***0.000125423***	***3.27E-08***	***1.27E-07***
P4	***P4-140***	***B***	***74.09***	***2.05E-06***	***0.00012685***	***5.15E-08***	***1.27E-07***
P4	***P4-150***	***B***	***73.99***	***2.05E-06***	***0.000133233***	***5.15E-08***	***1.23E-07***
P4	***P4-160***	***B***	***73.89***	***2.14E-06***	***0.000142194***	***5.39E-08***	***1.26E-07***
P4	***P4-170***	***B***	***73.77***	***2.72E-06***	***0.000165026***	***6.84E-08***	***1.17E-07***
P4	***P4-180***	***B***	***73.67***	***2.69E-06***	***0.00015888***	***6.76E-08***	***1.13E-07***
P4	P4-195	B	73.52	9.96E-06	0.000740292	2.50E-07	1.69E-07
P4	P4-210	B	73.38	1.36E-05	0.001277405	3.43E-07	2.37E-07
P4	P4-225	A/C	73.22	4.32E-06	0.000296431	1.09E-07	1.07E-07
P4	P4-240	A/C	73.07	5.01E-06	0.000248407	1.26E-07	9.61E-08
P4	P4-255	A/C	72.92	1.17E-05	0.000978613	2.95E-07	1.86E-07
P4	P4-270	A/C	72.77	3.61E-06	0.000194048	9.08E-08	9.07E-08
RM	***RM-000***	***C***	***129.08***	***4.64E-06***	***0.000243758***	***1.17E-07***	***1.09E-07***
RM	***RM-020***	***C***	***128.9***	***3.19E-06***	***0.000288346***	***8.01E-08***	***1.34E-07***
RM	RM-040	C	128.6				6.96E-07
RM	***RM-055***	***B***	***128.42***	***5.74E-06***	***0.000556615***	***1.44E-07***	***1.92E-07***
RM	***RM-065***	***B***	***128.33***	***7.94E-06***	***0.000762298***	***2.00E-07***	***2.11E-07***
RM	***RM-075***	***B***	***128.21***	***3.13E-06***	***0.000294199***	***7.87E-08***	***1.31E-07***
RM	RM-085	B	128.12	4.66E-06	0.000624666	1.17E-07	1.92E-07
RM	RM-095	B	128.03	5.11E-06	0.000562024	1.28E-07	1.78E-07
RM	RM-110	B	127.88	3.46E-06	0.000357474	8.70E-08	1.51E-07
RM	RM-130	A	127.63	3.53E-06	0.000207122	8.86E-08	1.08E-07
RM	RM-140	A	127.53	3.91E-06	0.000220725	9.83E-08	9.89E-08
RM	RM-150	A	127.43	4.14E-06	0.000222715	1.04E-07	9.43E-08
RM	RM-170	A	127.24	3.77E-06	0.000216847	9.48E-08	9.69E-08
TRA	***TRA-000***	***C***	***66.63***	***4.00E-06***	***0.00023206***	***1.01E-07***	***1.08E-07***
TRA	***TRA-010***	***C***	***66.53***	***4.45E-06***	***0.000211678***	***1.12E-07***	***1.04E-07***
TRA	***TRA-020***	***C***	***66.43***	***4.24E-06***	***0.000237663***	***1.07E-07***	***1.05E-07***
TRA	***TRA-035***	***B***	***66.15***	***4.37E-06***	***0.000355573***	***1.10E-07***	***1.59E-07***
TRA	***TRA-050***	***B***	***66***	***2.68E-06***	***0.000302364***	***6.73E-08***	***1.32E-07***
TRA	***TRA-060***	***B***	***65.9***	***1.01E-06***	***0.000249955***	***2.55E-08***	***1.29E-07***
TRA	***TRA-065***	***B***	***65.85***	***1.22E-06***	***0.000215255***	***3.07E-08***	***1.26E-07***

TRA	TRA-075	B	65.75		0.000204169		1.33E-07
TRA	TRA-080	B	65.7	4.03E-07	0.000173861	1.01E-08	1.28E-07
TRA	TRA-090	A/C	65.4	2.76E-06	0.000183611	6.93E-08	1.25E-07
TRA	TRA-100	A/C	65.3	3.01E-06	0.000168329	7.57E-08	1.29E-07
TRA	TRA-110	A/C	65.2	2.40E-06	0.000139812	6.04E-08	1.11E-07
TRA	TRA-120	A/C	65.08	2.06E-06	0.000106558	5.19E-08	1.02E-07
TRB	***TRB-000***	***C***	***61.02***	***5.10E-06***	***0.000282582***	***1.28E-07***	***1.16E-07***
TRB	***TRB-010***	***C***	***60.92***	***4.27E-06***	***0.000224202***	***1.07E-07***	***1.03E-07***
TRB	TRB-025	B	60.78	2.99E-06	0.000209927	7.51E-08	1.20E-07
TRB	***TRB-035***	***B***	***60.638***	***4.76E-06***	***0.000422242***	***1.20E-07***	***1.47E-07***
TRB	***TRB-045***	***B***	***60.53***	***9.46E-06***	***0.000700644***	***2.38E-07***	***1.70E-07***
TRB	***TRB-055***	***B***	***60.425***	***1.78E-05***	***0.001040407***	***4.48E-07***	***1.98E-07***
TRB	TRB-065	B	60.33	1.99E-06	9.55E-05	5.01E-08	1.19E-07
TRB	TRB-075	B	60.225	3.06E-06	0.000182215	7.70E-08	1.51E-07
TRB	TRB-085	B	60.13	2.67E-06	0.000141678	6.70E-08	1.07E-07
TRB	TRB-095	B	60.035	2.65E-06	0.000195	6.67E-08	1.19E-07
TRB	TRB-105	B/A	59.92	1.36E-06	0.00019392	3.42E-08	1.19E-07
TRB	TRB-115	A/C	59.83	5.91E-07	0.000169957	1.49E-08	1.06E-07
TRB	TRB-125	A/C	59.73	4.31E-06	0.000394514	1.08E-07	1.09E-07
TRB	TRB-135	A/C	59.61	2.46E-06	0.000283281	6.18E-08	9.72E-08
TRB	TRB-145	A/C	59.51	3.23E-06	0.000179927	8.13E-08	1.15E-07
UDRB	***UDRB-000***	***C***	***93.05***	***4.30E-06***	***0.00022667***	***1.08E-07***	***1.02E-07***
UDRB	***UDRB-010***	***C***	***92.95***	***3.46E-06***	***0.000199944***	***8.70E-08***	***1.03E-07***
UDRB	***UDRB-020***	***B1***	***92.83***	***1.52E-05***	***0.000948525***	***3.82E-07***	***1.60E-07***
UDRB	***UDRB-030***	***B1***	***92.68***	***6.74E-06***	***0.000455722***	***1.69E-07***	***1.38E-07***
UDRB	***UDRB-040***	***B1***	***92.56***	***1.68E-05***	***0.000946935***	***4.22E-07***	***1.79E-07***
UDRB	***UDRB-050***	***B1***	***92.46***	***1.08E-05***	***0.000655552***	***2.72E-07***	***1.58E-07***
UDRB	***UDRB-065***	***B1***	***92.31***	***1.07E-05***	***0.000896587***	***2.69E-07***	***1.95E-07***
UDRB	***UDRB-080***	***B1***	***92.16***	***9.86E-06***	***0.000913915***	***2.48E-07***	***1.96E-07***
UDRB	***UDRB-090***	***B1***	***92.06***	***3.80E-06***	***0.000354432***	***9.55E-08***	***1.32E-07***
UDRB	***UDRB-100***	***B1***	***91.9***	***1.13E-05***	***0.000797766***	***2.85E-07***	***1.84E-07***
UDRB	UDRB-120	B1/B2	91.7	4.47E-06	0.000419367	1.12E-07	1.52E-07
UDRB	UDRB-130	B1/B2	91.58	3.34E-06	0.000320612	8.40E-08	1.45E-07
UDRB	UDRB-140	B2	91.46	3.03E-06	0.0003498	7.60E-08	1.45E-07
UDRB	UDRB-150	B2	91.38	2.27E-06	0.000295536	5.70E-08	1.33E-07
UDRB	UDRB-160	B2	91.27	2.56E-06	0.000190544	6.44E-08	1.31E-07
UDRB	UDRB-180	B2	91.06	1.72E-06	0.000163863	4.33E-08	1.28E-07
UDRB	UDRB-190	B2	90.93	1.89E-06	0.000178386	4.76E-08	1.33E-07
UDRB	UDRB-200	B2	90.83	2.08E-06	0.000187724	5.22E-08	1.38E-07
UDRB	UDRB-210	B2	90.72	2.06E-06	0.000166863	5.16E-08	1.38E-07
UDRB	UDRB-220	B2	90.62	1.18E-06	0.000151227	2.97E-08	1.29E-07

UDRB	UDRB-235	A	90.46	4.55E-06	0.000359401	1.14E-07	1.34E-07
UDRB	UDRB-250	A	90.26	3.31E-06	0.000166467	8.33E-08	9.26E-08
UDRB	UDRB-260	C	90.06	4.43E-06	0.00021304	1.11E-07	7.01E-08

Table B.2: Hysteresis properties for marker bed paleosols preserved in core. MCD = meters composite depth.

Paleosol	Specimen	Horizon	MCD	M_s	M_r	B_c	B_{cr}	HIRM
			meters	Am^2kg^{-1}	Am^2kg^{-1}	*mT*	*mT*	Am^2kg^{-1}
LDRA	LDRA-000	C1	108.67	2.70E-03	2.54E-04	6.9	32.2	4.46E-05
LDRA	LDRA-040	B1	108.27	8.52E-03	1.10E-03	11.0	54.7	4.17E-04
LDRA	LDRA-060	B1	108.06	5.36E-03	8.59E-04	14.0	106.4	4.53E-04
LDRA	LDRA-080	B1	107.87	1.82E-02	2.20E-03	10.2	44.7	7.17E-04
LDRA	LDRA-095	B1	107.72	1.02E-02	1.54E-03	13.4	88.7	7.31E-04
LDRA	LDRA-120	B2	107.48	1.36E-02	1.78E-03	11.8	70.9	7.71E-04
LDRA	LDRA-140	B2	107.28	6.84E-03	1.23E-03	15.4	152.2	6.89E-04
LDRA	LDRA-160	C2	107.08	4.71E-03	6.65E-04	10.3	91.8	3.09E-04
PRM	PRM-010	C	141.32	9.88E-04	2.03E-04	24.0	124.4	1.02E-04
PRM	PRM-065	B1	140.75	2.42E-03	5.96E-04	35.6	271.7	3.47E-04
PRM	PRM-085	B1	140.52	1.82E-03	4.10E-04	22.7	151.0	2.03E-04
PRM	PRM-095	B1	140.42	2.53E-03	1.01E-03	92.7	391.9	7.97E-04
PRM	PRM-125	B2	140.12	3.73E-03	1.63E-03	202.6	449.8	1.37E-03
PRM	PRM-145	B2	139.92	4.82E-03	2.82E-03	217.5	347.2	2.52E-03
PRM	PRM-165	B2	139.71	4.04E-03	1.89E-03	199.1	421.8	1.62E-03
PRM	PRM-235	A	138.88	1.22E-03	2.98E-04	34.5	268.1	1.79E-04
P0	P0-045	B	117.04	1.29E-02	2.22E-03	14.3	39.0	3.65E-04
P0	P0-085	B	116.66	4.40E-03	8.84E-04	18.6	52.4	2.92E-04
P0	P0-110	B	116.41	7.02E-03	1.34E-03	18.8	51.8	4.38E-04
P0	P0-120	B	116.27	6.47E-03	1.42E-03	20.9	62.9	5.51E-04
P0	P0-140	B	116.1	8.28E-03	1.43E-03	15.1	44.2	3.95E-04
P2	P2-040	B	102.75	3.65E-03	8.56E-04	27.8	289.8	5.52E-04
P2	P2-060	B	102.55	4.57E-03	2.17E-03	171.7	478.7	1.64E-03
P2	P2-080	B	102.37	3.23E-03	1.69E-03	190.7	508.4	1.24E-03
P2	P2-105	B	102.1	3.11E-03	1.61E-03	182.3	476.0	1.12E-03
P2	P2-125	B	101.9	2.91E-03	1.54E-03	188.5	474.5	1.11E-03
P2	P2-145	B	101.7	2.94E-03	1.42E-03	157.4	492.3	1.00E-03
P2	P2-155	B	101.6	3.56E-03	1.77E-03	166.2	506.6	1.24E-03
P2	P2-165	A	101.5	2.53E-03	8.19E-04	49.2	440.6	5.36E-04
P4	P4-050	B	74.99	4.82E-03	1.49E-03	35.3	447.5	1.01E-03
P4	P4-075	B	74.74	5.51E-03	2.14E-03	170.7	495.7	1.63E-03
P4	P4-100	B	74.49	3.24E-03	1.41E-03	126.7	484.3	1.12E-03
P4	P4-120	B	74.29	3.94E-03	1.81E-03	158.5	519.9	1.27E-03
P4	P4-140	B	74.09	3.14E-03	1.67E-03	176.2	538.7	1.15E-03
P4	P4-160	B	73.89	1.60E-03	2.38E-04	13.5	61.1	8.81E-05
P4	P4-180	B	73.67	1.72E-03	3.12E-04	19.0	91.8	1.37E-04

P4	P4-210	B	73.38	1.19E-02	1.52E-03	10.8	34.4	3.02E-04
P4	P4-225	A/C	73.22	2.91E-03	3.66E-04	10.4	36.7	8.04E-05
P4	P4-240	A/C	73.07	3.80E-03	3.34E-04	5.6	34.4	8.05E-05
RM	RM-055	B	128.42	8.67E-03	1.58E-03	14.9	174.6	9.53E-04
RM	RM-075	B	128.21	6.04E-03	1.40E-03	23.9	200.2	9.54E-04
RM	RM-085	B	128.12	1.06E-02	2.15E-03	17.7	162.3	1.28E-03
RM	RM-095	B	128.03	9.66E-03	2.06E-03	20.6	188.9	1.32E-03
RM	RM-110	B	127.88	6.83E-03	1.94E-03	35.8	256.6	1.47E-03
RM	RM-130	A	127.63	2.44E-03	2.38E-04	6.0	32.6	5.20E-05
RM	RM-150	A	127.43	2.85E-03	2.99E-04	7.5	32.6	5.80E-05
TRA	TRA-035	B	66.15	4.99E-03	1.23E-03	26.9	198.7	7.88E-04
TRA	TRA-050	B	66	4.39E-03	1.53E-03	50.4	287.3	1.13E-03
TRA	TRA-060	B	65.9	4.74E-03	1.90E-03	80.8	322.8	1.51E-03
TRA	TRA-065	B	65.85	5.45E-03	2.50E-03	126.9	345.6	2.10E-03
TRA	TRA-080	B	65.7	4.21E-03	2.31E-03	200.5	453.2	1.90E-03
TRA	TRA-100	A/C	65.3	2.46E-03	4.27E-04	17.8	106.7	1.97E-04
TRB	TRB-025	B	60.78	2.68E-03	7.12E-04	31.2	251.2	4.61E-04
TRB	TRB-045	B	60.53	8.90E-03	1.84E-03	21.5	147.2	1.01E-03
TRB	TRB-065	B	60.33	3.70E-03	1.34E-03	56.8	289.5	1.02E-03
TRB	TRB-085	B	60.13	2.57E-03	1.17E-03	118.7	368.4	9.60E-04
TRB	TRB-095	B	60.035	3.18E-03	9.35E-04	43.8	337.9	7.11E-04
TRB	TRB-105	B/A	59.92	3.36E-03	9.91E-04	43.8	337.9	7.54E-04
TRB	TRB-125	A/C	59.73	1.86E-03	3.95E-04	20.6	141.0	1.99E-04
UDRB	UDRB-020	B1	92.83	7.72E-03	1.17E-03	14.6	47.5	3.50E-04
UDRB	UDRB-050	B1	92.46	7.55E-03	1.57E-03	20.7	175.8	8.99E-04
UDRB	UDRB-080	B1	92.16	1.12E-02	2.21E-03	19.8	183.8	1.27E-03
UDRB	UDRB-100	B1	91.9	1.07E-02	2.47E-03	23.4	220.6	1.52E-03
UDRB	UDRB-120	B1/B2	91.7	7.24E-03	2.17E-03	37.8	325.1	1.61E-03
UDRB	UDRB-140	B2	91.46	6.78E-03	2.15E-03	48.6	350.0	1.64E-03
UDRB	UDRB-160	B2	91.27	6.17E-03	2.59E-03	117.4	379.1	2.15E-03
UDRB	UDRB-180	B2	91.06	6.01E-03	2.65E-03	160.2	404.9	2.26E-03
UDRB	UDRB-200	B2	90.83	5.97E-03	2.65E-03	144.5	416.9	2.23E-03
UDRB	UDRB-220	B2	90.62	4.48E-03	1.77E-03	138.2	420.5	1.50E-03
UDRB	UDRB-235	A	90.46	4.03E-03	1.15E-03	33.7	255.0	7.79E-04

Table B.3: Low-field magnetic properties for marker bed paleosols in outcrop. The specimen used in the magnetic enhancement ratios are indicated in bold italics. MCD* = meters composite depth equivalent, calculated using the correlations provided by *Bowen et al.* (2015). Strat Level[1] = stratigraphic level following *Abdul Aziz et al.* (2008) stratigraphy. Strat Level[2] = stratigraphic level following *Gingerich* (2001) stratigraphy.

Paleosol	**Sample**	**Horizon**	**MCD***	**Strat Level[1]**	**Strat Level[2]**	**ARM**	**IRM**	χ_{ARM}	χ
			meters	*meters*	*meters*	Am^2kg^{-1}	Am^2kg^{-1}	mA^{-1}	m^3kg^{-1}
PCB-01-LDRA	***PCB-01-LDRA-000***	***C1***	***108.67***	***31.5***	***1511.61***	***3.35E-06***	***1.48E-04***	***8.41E-08***	***6.62E-08***
PCB-01-LDRA	***PCB-01-LDRA-010***	***C1***	***108.57***	***31.6***	***1511.71***	***2.16E-06***	***1.12E-04***	***5.43E-08***	***3.90E-08***
PCB-01-LDRA	***PCB-01-LDRA-020***	***B1***	***108.47***	***31.7***	***1511.81***	***2.18E-05***	***1.24E-03***	***5.47E-07***	***2.11E-07***
PCB-01-LDRA	***PCB-01-LDRA-025***	***B1***	***108.42***	***31.75***	***1511.86***	***1.23E-05***	***1.30E-04***	***3.08E-07***	***1.73E-07***
PCB-01-LDRA	***PCB-01-LDRA-030***	***B1***	***108.37***	***31.8***	***1511.91***	***1.38E-05***	***8.06E-04***	***3.47E-07***	***1.66E-07***
PCB-01-LDRA	***PCB-01-LDRA-035***	***B1***	***108.32***	***31.85***	***1511.96***	***2.01E-05***	***1.13E-03***	***5.05E-07***	***2.07E-07***
PCB-01-LDRA	***PCB-01-LDRA-040***	***B1***	***108.27***	***31.9***	***1512.01***	***1.26E-05***	***7.81E-04***	***3.16E-07***	***1.72E-07***
PCB-01-LDRA	***PCB-01-LDRA-045***	***B1***	***108.22***	***31.95***	***1512.06***	***1.18E-05***	***7.86E-04***	***2.98E-07***	***1.77E-07***
PCB-01-LDRA	***PCB-01-LDRA-050***	***B1***	***108.17***	***32***	***1512.11***	***1.52E-05***	***8.89E-04***	***3.83E-07***	***1.82E-07***
PCB-01-LDRA	***PCB-01-LDRA-055***	***B1***	***108.12***	***32.05***	***1512.16***	***1.53E-05***	***9.31E-04***	***3.85E-07***	***1.81E-07***
PCB-01-LDRA	***PCB-01-LDRA-060***	***B1***	***108.07***	***32.1***	***1512.21***	***1.33E-05***	***7.89E-04***	***3.33E-07***	***1.68E-07***
PCB-01-LDRA	***PCB-01-LDRA-065***	***B1***	***108.02***	***32.15***	***1512.26***	***9.56E-06***	***5.91E-04***	***2.40E-07***	***1.51E-07***
PCB-01-LDRA	***PCB-01-LDRA-070***	***B1***	***107.97***	***32.2***	***1512.31***	***2.28E-05***	***1.28E-03***	***5.73E-07***	***2.22E-07***

PCB-01-LDRA	***PCB-01-LDRA-075***	***B1***	***107.92***	***32.25***	***1512.36***	***1.70E-05***	***9.52E-04***	***4.28E-07***	***2.00E-07***
PCB-01-LDRA	***PCB-01-LDRA-080***	***B1***	***107.87***	***32.3***	***1512.41***	***1.39E-05***	***8.41E-04***	***3.48E-07***	***1.85E-07***
PCB-01-LDRA	***PCB-01-LDRA-085***	***B1***	***107.82***	***32.35***	***1512.46***	***1.68E-05***	***9.94E-04***	***4.23E-07***	***1.94E-07***
PCB-01-LDRA	PCB-01-LDRA-090	B1	107.77	32.4	1512.51	1.09E-05	7.25E-04	2.74E-07	1.69E-07
PCB-01-LDRA	PCB-01-LDRA-095	B2	107.72	32.45	1512.56	8.83E-06	6.01E-04	2.22E-07	1.52E-07
PCB-01-LDRA	PCB-01-LDRA-100	B2	107.67	32.5	1512.61	7.76E-06	5.47E-04	1.95E-07	1.51E-07
PCB-01-LDRA	PCB-01-LDRA-105	B2	107.62	32.55	1512.66	8.20E-06	5.84E-04	2.06E-07	1.51E-07
PCB-01-LDRA	PCB-01-LDRA-110	B2	107.57	32.6	1512.71	7.98E-06	5.61E-04	2.01E-07	1.51E-07
PCB-01-LDRA	PCB-01-LDRA-115	B2	107.52	32.65	1512.76	7.33E-06	5.52E-04	1.84E-07	1.68E-07
PCB-01-LDRA	PCB-01-LDRA-120	B2	107.47	32.7	1512.81	1.07E-05	7.99E-04	2.70E-07	1.82E-07
PCB-01-LDRA	PCB-01-LDRA-125	B2	107.42	32.75	1512.86	8.27E-06	6.22E-04	2.08E-07	1.62E-07
PCB-01-LDRA	PCB-01-LDRA-130	B2	107.37	32.8	1512.91	7.44E-06	5.88E-04	1.87E-07	1.55E-07
PCB-01-LDRA	PCB-01-LDRA-135	B2	107.32	32.85	1512.96	9.06E-06	5.22E-04	2.28E-07	1.86E-07
PCB-01-LDRA	PCB-01-LDRA-140	B2	107.27	32.9	1513.01	4.99E-06	3.55E-04	1.25E-07	1.25E-07
PCB-01-LDRA	PCB-01-LDRA-145	B2	107.22	32.95	1513.06	7.23E-06	6.00E-04	1.82E-07	1.64E-07
PCB-01-LDRA	PCB-01-LDRA-150	B2	107.17	33	1513.11	7.72E-06	6.51E-04	1.94E-07	1.68E-07
PCB-01-LDRA	PCB-01-LDRA-155	B2	107.12	33.05	1513.16	7.52E-06	5.60E-04	1.89E-07	1.53E-07

PCB-01-LDRA	PCB-01-LDRA-160	B2	107.07	33.1	1513.21	7.77E-06	6.31E-04	1.95E-07	1.59E-07
PCB-01-LDRA	PCB-01-LDRA-170	C2	106.97	33.2	1513.31	2.69E-06	8.98E-05	6.76E-08	6.04E-08
PCB-01-LDRA	PCB-01-LDRA-180	C2	106.87	33.3	1513.41	2.75E-06	5.71E-05	6.90E-08	6.30E-08
PCB-01-PRM	***PCB-01-PRM-000***	***C***	***141.05***	***5.3***	***1484.81***	***3.28E-06***	***1.48E-04***	***8.24E-08***	***1.04E-07***
PCB-01-PRM	***PCB-01-PRM-010***	***C***	***140.95***	***5.4***	***1484.91***	***3.31E-06***	***1.74E-04***	***8.33E-08***	***9.24E-08***
PCB-01-PRM	PCB-01-PRM-020	B1	140.85	5.5	1485.01	2.30E-06	1.23E-04	5.77E-08	1.20E-07
PCB-01-PRM	PCB-01-PRM-025	B1	140.8	5.55	1485.06	2.49E-06	1.42E-04	6.26E-08	1.08E-07
PCB-01-PRM	PCB-01-PRM-030	B1	140.75	5.6	1485.11	2.68E-06	1.45E-04	6.74E-08	1.10E-07
PCB-01-PRM	PCB-01-PRM-035	B1	140.7	5.65	1485.16	3.45E-06	1.95E-04	8.66E-08	1.17E-07
PCB-01-PRM	PCB-01-PRM-040	B1	140.65	5.7	1485.21	2.72E-06	1.61E-04	6.83E-08	1.14E-07
PCB-01-PRM	PCB-01-PRM-045	B1	140.6	5.75	1485.26	3.82E-06	1.91E-04	9.61E-08	1.18E-07
PCB-01-PRM	PCB-01-PRM-050	B1	140.55	5.8	1485.31	2.56E-06	1.09E-04	6.44E-08	1.26E-07
PCB-01-PRM	PCB-01-PRM-055	B1	140.5	5.85	1485.36	5.08E-06	2.68E-04	1.28E-07	1.21E-07
PCB-01-PRM	PCB-01-PRM-060	B1	140.45	5.9	1485.41	3.65E-06	2.12E-04	9.16E-08	1.20E-07
PCB-01-PRM	***PCB-01-PRM-065***	***B2***	***140.4***	***5.95***	***1485.46***	***5.11E-06***	***2.87E-04***	***1.28E-07***	***1.31E-07***
PCB-01-PRM	***PCB-01-PRM-070***	***B2***	***140.35***	***6***	***1485.51***	***5.24E-06***	***2.63E-04***	***1.32E-07***	***1.23E-07***
PCB-01-PRM	***PCB-01-PRM-075***	***B2***	***140.3***	***6.05***	***1485.56***	***4.15E-06***	***2.36E-04***	***1.04E-07***	***1.20E-07***

PCB-01-PRM	*PCB-01-PRM-080*	*B2*	*140.25*	*6.1*	*1485.61*	*5.01E-06*	*2.85E-04*	*1.26E-07*	*1.30E-07*
PCB-01-PRM	*PCB-01-PRM-085*	*B2*	*140.2*	*6.15*	*1485.66*	*3.49E-06*	*1.52E-04*	*8.76E-08*	*1.15E-07*
PCB-01-PRM	*PCB-01-PRM-090*	*B2*	*140.15*	*6.2*	*1485.71*	*5.47E-06*	*1.77E-04*	*1.37E-07*	*1.28E-07*
PCB-01-PRM	PCB-01-PRM-100	A	140.05	6.3	1485.81	3.56E-06	1.96E-04	8.94E-08	1.09E-07
PCB-01-PRM	PCB-01-PRM-110	A	139.95	6.4	1485.91	2.56E-06	1.21E-04	6.43E-08	1.14E-07
PCB-01-PRM	PCB-01-PRM-120	A	139.85	6.5	1486.01	2.94E-06	1.57E-04	7.39E-08	1.21E-07
PCB-01-PRM	PCB-01-PRM-130	A	139.75	6.6	1486.11	3.00E-06	1.48E-04	7.53E-08	1.14E-07
PCB-02-PRM	*PCB-02-PRM-000*	*C*	*141.15*	*5.2*	*1484.71*	*4.08E-06*	*2.22E-04*	*1.03E-07*	*9.08E-08*
PCB-02-PRM	*PCB-02-PRM-010*	*C*	*141.05*	*5.3*	*1484.81*	*1.04E-05*	*7.81E-04*	*2.61E-07*	*1.74E-07*
PCB-02-PRM	*PCB-02-PRM-020*	*C*	*140.95*	*5.4*	*1484.91*	*4.14E-06*	*1.80E-04*	*1.04E-07*	*9.32E-08*
PCB-02-PRM	*PCB-02-PRM-030*	*B1*	*140.85*	*5.5*	*1485.01*	*6.08E-06*	*3.99E-04*	*1.53E-07*	*1.30E-07*
PCB-02-PRM	*PCB-02-PRM-040*	*B1*	*140.75*	*5.6*	*1485.11*	*3.98E-06*	*3.92E-04*	*1.00E-07*	*1.29E-07*
PCB-02-PRM	*PCB-02-PRM-050*	*B1*	*140.65*	*5.7*	*1485.21*	*3.15E-06*	*2.47E-04*	*7.93E-08*	*1.17E-07*
PCB-02-PRM	*PCB-02-PRM-060*	*B1*	*140.55*	*5.8*	*1485.31*	*6.74E-06*	*5.63E-04*	*1.69E-07*	*1.50E-07*
PCB-02-PRM	*PCB-02-PRM-070*	*B1*	*140.45*	*5.9*	*1485.41*	*4.63E-06*	*3.33E-04*	*1.16E-07*	*1.40E-07*
PCB-02-PRM	*PCB-02-PRM-080*	*B1*	*140.35*	*6*	*1485.51*	*2.93E-06*	*2.36E-04*	*7.35E-08*	*1.24E-07*
PCB-02-PRM	PCB-02-PRM-090	B2	140.25	6.1	1485.61	3.32E-06	2.07E-04	8.34E-08	1.22E-07

PCB-02-PRM	PCB-02-PRM-100	B2	140.15	6.2	1485.71	4.34E-06	2.67E-04	1.09E-07	1.27E-07
PCB-02-PRM	PCB-02-PRM-110	B2	140.05	6.3	1485.81	3.81E-06	2.53E-04	9.58E-08	1.26E-07
PCB-02-PRM	PCB-02-PRM-120	B2	139.95	6.4	1485.91	4.77E-06	2.44E-04	1.20E-07	1.25E-07
PCB-02-PRM	PCB-02-PRM-130	B2	139.85	6.5	1486.01	4.15E-06	2.39E-04	1.04E-07	1.25E-07
PCB-02-PRM	PCB-02-PRM-140	B2	139.75	6.6	1486.11	4.17E-06	2.32E-04	1.05E-07	1.21E-07
PCB-02-PRM	PCB-02-PRM-150	B2	139.65	6.7	1486.21	4.20E-06	2.34E-04	1.06E-07	1.22E-07
PCB-02-PRM	PCB-02-PRM-160	B2	139.55	6.8	1486.31	4.10E-06	2.50E-04	1.03E-07	1.29E-07
PCB-02-PRM	PCB-02-PRM-170	B2	139.45	6.9	1486.41	4.33E-06	1.52E-04	1.09E-07	1.30E-07
PCB-02-PRM	PCB-02-PRM-180	B2	139.35	7	1486.51	4.00E-06	2.34E-04	1.01E-07	1.25E-07
PCB-02-PRM	PCB-02-PRM-190	A	139.25	7.1	1486.61	3.97E-06	2.08E-04	9.98E-08	1.06E-07
PCB-02-PRM	PCB-02-PRM-200	A	139.15	7.2	1486.71	3.54E-06	2.21E-04	8.90E-08	9.89E-08
PCB-03-PRM	***PCB-03-PRM-000***	***C***	***141.15***	***5.2***	***1484.71***	***3.37E-06***	***1.70E-04***	***8.47E-08***	***8.93E-08***
PCB-03-PRM	***PCB-03-PRM-010***	***C***	***141.05***	***5.3***	***1484.81***	***3.56E-06***	***1.83E-04***	***8.94E-08***	***1.05E-07***
PCB-03-PRM	***PCB-03-PRM-020***	***C***	***140.95***	***5.4***	***1484.91***	***3.56E-06***	***1.87E-04***	***8.94E-08***	***9.14E-08***
PCB-03-PRM	PCB-03-PRM-030	B1	140.85	5.5	1485.01	2.14E-06	1.33E-04	5.38E-08	1.12E-07
PCB-03-PRM	PCB-03-PRM-040	B1	140.75	5.6	1485.11		1.04E-04		1.06E-07
PCB-03-PRM	PCB-03-PRM-050	B1	140.65	5.7	1485.21	1.81E-06	1.29E-04	4.54E-08	1.10E-07

PCB-03-PRM	PCB-03-PRM-060	B1	140.55	5.8	1485.31	2.21E-06	1.33E-04	5.56E-08	1.17E-07
PCB-03-PRM	PCB-03-PRM-070	B1	140.45	5.9	1485.41	1.37E-06	1.46E-04	3.43E-08	1.08E-07
PCB-03-PRM	PCB-03-PRM-080	B1	140.35	6	1485.51	2.99E-06	1.73E-04	7.52E-08	1.11E-07
PCB-03-PRM	***PCB-03-PRM-090***	***B2***	***140.25***	***6.1***	***1485.61***	***1.98E-06***	***4.57E-05***	***4.97E-08***	***1.18E-07***
PCB-03-PRM	***PCB-03-PRM-100***	***B2***	***140.15***	***6.2***	***1485.71***	***1.06E-05***	***5.19E-04***	***2.67E-07***	***1.60E-07***
PCB-03-PRM	***PCB-03-PRM-110***	***B2***	***140.05***	***6.3***	***1485.81***	***5.57E-06***	***3.63E-04***	***1.40E-07***	***1.38E-07***
PCB-03-PRM	***PCB-03-PRM-120***	***B2***	***139.95***	***6.4***	***1485.91***	***7.17E-06***	***3.31E-04***	***1.80E-07***	***1.40E-07***
PCB-03-PRM	***PCB-03-PRM-130***	***B2***	***139.85***	***6.5***	***1486.01***	***2.96E-06***	***1.79E-04***	***7.44E-08***	***1.13E-07***
PCB-03-PRM	PCB-03-PRM-140	A	139.75	6.6	1486.11	1.88E-06	1.22E-04	4.73E-08	1.03E-07
PCB-03-PRM	PCB-03-PRM-150	A	139.65	6.7	1486.21	2.77E-06	1.40E-04	6.96E-08	1.03E-07
PCB-01-P0	***PCB-01-P0-000***	***C***	***117.52***	***22.05***	***1504.46***	***4.30E-06***	***2.40E-04***	***1.08E-07***	***1.01E-07***
PCB-01-P0	PCB-01-P0-010	C	117.42	22.15	1504.56	3.94E-06	2.07E-04	9.90E-08	1.02E-07
PCB-01-P0	PCB-01-P0-020	C	117.32	22.25	1504.66	4.29E-06	2.49E-04	1.08E-07	1.08E-07
PCB-01-P0	PCB-01-P0-025	B	117.22	22.3	1504.71	2.19E-06	2.25E-04	5.50E-08	1.15E-07
PCB-01-P0	PCB-01-P0-030	B	117.17	22.35	1504.76	3.66E-06	2.51E-04	9.20E-08	1.22E-07
PCB-01-P0	PCB-01-P0-035	B	117.12	22.4	1504.81	2.86E-06	2.28E-04	7.18E-08	1.22E-07
PCB-01-P0	PCB-01-P0-040	B	117.07	22.45	1504.86	2.21E-06	2.29E-04	5.55E-08	1.17E-07
PCB-01-P0	PCB-01-P0-045	B	117.02	22.5	1504.91	2.86E-06	2.09E-04	7.20E-08	1.19E-07
PCB-01-P0	***PCB-01-P0-050***	***B***	***116.97***	***22.55***	***1504.96***	***2.60E-06***	***2.13E-04***	***6.53E-08***	***1.14E-07***
PCB-01-P0	***PCB-01-P0-055***	***B***	***116.92***	***22.6***	***1505.01***	***2.92E-06***	***2.13E-04***	***7.35E-08***	***1.17E-07***
PCB-01-P0	***PCB-01-P0-060***	***B***	***116.87***	***22.65***	***1505.06***	***2.18E-06***	***2.07E-04***	***5.47E-08***	***1.15E-07***

PCB-01-P0	***PCB-01-P0-065***	***B***	***116.82***	***22.7***	***1505.11***	***3.22E-06***	***2.06E-04***	***8.10E-08***	***1.15E-07***
PCB-01-P0	PCB-01-P0-070	A	116.77	22.75	1505.16	4.13E-06	2.20E-04	1.04E-07	1.19E-07
PCB-01-P0	PCB-01-P0-080	A	116.67	22.85	1505.26	3.88E-06	2.23E-04	9.74E-08	1.22E-07
PCB-01-P0	PCB-01-P0-090	A	116.57	22.95	1505.36	4.41E-06	2.46E-04	1.11E-07	1.22E-07
PCB-01-P0	PCB-01-P0-100	A	116.47	23.05	1505.46	3.84E-06	2.24E-04	9.66E-08	1.07E-07
PCB-01-P2	***PCB-01-P2-000***	***C***	***103.05***	***37.6***	***1518.47***	***4.58E-06***	***2.39E-04***	***1.15E-07***	***1.22E-07***
PCB-01-P2	PCB-01-P2-010	C	102.95	37.7	1518.57		2.23E-04		1.20E-07
PCB-01-P2	***PCB-01-P2-020***	***C***	***102.85***	***37.8***	***1518.67***	***3.97E-06***	***2.20E-04***	***9.99E-08***	***1.13E-07***
PCB-01-P2	***PCB-01-P2-030***	***B1***	***102.75***	***37.9***	***1518.77***	***5.45E-06***	***4.32E-04***	***1.37E-07***	***1.49E-07***
PCB-01-P2	***PCB-01-P2-035***	***B1***	***102.7***	***37.95***	***1518.82***	***7.14E-06***	***5.39E-04***	***1.79E-07***	***1.59E-07***
PCB-01-P2	***PCB-01-P2-040***	***B1***	***102.65***	***38***	***1518.87***	***5.98E-06***	***5.54E-04***	***1.50E-07***	***1.67E-07***
PCB-01-P2	***PCB-01-P2-045***	***B1***	***102.6***	***38.05***	***1518.92***	***4.87E-06***	***2.80E-04***	***1.22E-07***	***1.52E-07***
PCB-01-P2	***PCB-01-P2-050***	***B1***	***102.55***	***38.1***	***1518.97***	***5.97E-06***	***5.19E-04***	***1.50E-07***	***1.67E-07***
PCB-01-P2	***PCB-01-P2-055***	***B1***	***102.5***	***38.15***	***1519.02***	***5.04E-06***	***4.20E-04***	***1.27E-07***	***1.53E-07***
PCB-01-P2	PCB-01-P2-060	B1	102.45	38.2	1519.07	2.97E-06	3.60E-04	7.47E-08	1.42E-07
PCB-01-P2	PCB-01-P2-065	B1	102.4	38.25	1519.12	2.64E-06	3.06E-04	6.65E-08	1.37E-07
PCB-01-P2	PCB-01-P2-070	B1	102.35	38.3	1519.17	4.09E-06	3.46E-04	1.03E-07	1.48E-07
PCB-01-P2	PCB-01-P2-075	B2	102.3	38.35	1519.22	3.58E-06	3.08E-04	8.99E-08	1.44E-07
PCB-01-P2	PCB-01-P2-080	B2	102.25	38.4	1519.27	4.37E-06	3.12E-04	1.10E-07	1.40E-07
PCB-01-P2	PCB-01-P2-085	B2	102.2	38.45	1519.32	3.03E-06	2.76E-04	7.63E-08	1.48E-07
PCB-01-P2	PCB-01-P2-090	B2	102.15	38.5	1519.37	3.42E-06	2.71E-04	8.61E-08	1.50E-07
PCB-01-P2	PCB-01-P2-095	B2	102.1	38.55	1519.42	2.87E-06	2.60E-04	7.22E-08	1.45E-07
PCB-01-P2	PCB-01-P2-100	B2	102.05	38.6	1519.47	3.06E-06	2.58E-04	7.68E-08	1.43E-07
PCB-01-P2	PCB-01-P2-105	B2	102	38.65	1519.52	2.57E-06	2.23E-04	6.46E-08	1.42E-07
PCB-01-P2	PCB-01-P2-110	B2	101.95	38.7	1519.57	2.94E-06	2.23E-04	7.38E-08	1.39E-07

PCB-01-P2	PCB-01-P2-120	A	101.85	38.8	1519.67	3.57E-06	2.44E-04	8.98E-08	1.46E-07
PCB-01-P2	PCB-01-P2-130	A	101.75	38.9	1519.77	4.58E-06	2.78E-04	1.15E-07	1.39E-07
PCB-01-P2	PCB-01-P2-140	A	101.65	39	1519.87	4.26E-06	2.69E-04	1.07E-07	1.39E-07
PCB-01-P2	PCB-01-P2-150	A	101.55	39.1	1519.97	6.81E-06	3.84E-04	1.71E-07	1.48E-07
PCB-02-P2	***PCB-02-P2-000***	***C***	***103.25***	***37.4***	***1518.27***	***3.02E-06***	***1.16E-04***	***7.59E-08***	***7.38E-08***
PCB-02-P2	***PCB-02-P2-010***	***C***	***103.15***	***37.5***	***1518.37***	***3.17E-06***	***1.35E-04***	***7.96E-08***	***8.07E-08***
PCB-02-P2	***PCB-02-P2-020***	***C***	***103.05***	***37.6***	***1518.47***	***3.79E-06***	***1.95E-04***	***9.51E-08***	***9.36E-08***
PCB-02-P2	***PCB-02-P2-030***	***C***	***102.95***	***37.7***	***1518.57***	***5.11E-06***	***3.11E-04***	***1.28E-07***	***1.20E-07***
PCB-02-P2	***PCB-02-P2-040***	***C***	***102.85***	***37.8***	***1518.67***	***3.67E-06***	***1.86E-04***	***9.22E-08***	***9.41E-08***
PCB-02-P2	***PCB-02-P2-050***	***B***	***102.75***	***37.9***	***1518.77***	***3.74E-06***	***2.21E-04***	***9.39E-08***	***1.08E-07***
PCB-02-P2	***PCB-02-P2-060***	***B***	***102.65***	***38***	***1518.87***	***3.48E-06***	***1.93E-04***	***8.76E-08***	***1.10E-07***
PCB-02-P2	***PCB-02-P2-070***	***B***	***102.55***	***38.1***	***1518.97***	***3.10E-06***	***1.86E-04***	***7.80E-08***	***1.07E-07***
PCB-02-P2	***PCB-02-P2-080***	***B***	***102.45***	***38.2***	***1519.07***	***3.03E-06***	***1.62E-04***	***7.61E-08***	***1.07E-07***
PCB-02-P2	***PCB-02-P2-090***	***B***	***102.35***	***38.3***	***1519.17***	***3.17E-06***	***1.79E-04***	***7.96E-08***	***1.11E-07***
PCB-02-P2	***PCB-02-P2-100***	***B***	***102.25***	***38.4***	***1519.27***	***2.59E-06***	***1.71E-04***	***6.50E-08***	***1.15E-07***
PCB-02-P2	***PCB-02-P2-110***	***B***	***102.15***	***38.5***	***1519.37***	***1.91E-06***	***1.50E-04***	***4.81E-08***	***1.11E-07***
PCB-02-P2	***PCB-02-P2-120***	***B***	***102.05***	***38.6***	***1519.47***	***2.52E-06***	***1.47E-04***	***6.33E-08***	***1.12E-07***
PCB-02-P2	PCB-02-P2-130	B	101.95	38.7	1519.57	1.98E-06	1.16E-04	4.98E-08	1.14E-07
PCB-02-P2	PCB-02-P2-140	B	101.85	38.8	1519.67	1.79E-06	1.25E-04	4.49E-08	1.14E-07
PCB-02-P2	PCB-02-P2-150	B	101.75	38.9	1519.77	1.86E-06	1.14E-04	4.67E-08	1.14E-07
PCB-02-P2	PCB-02-P2-160	AB	101.65	39	1519.87	2.18E-06	1.20E-04	5.49E-08	1.20E-07
PCB-02-P2	PCB-02-P2-170	AC	101.55	39.1	1519.97	2.30E-06	1.44E-04	5.79E-08	1.18E-07
PCB-02-P2	PCB-02-P2-180	AC	101.45	39.2	1520.07	4.31E-06	2.35E-04	1.08E-07	1.24E-07
PCB-02-RM	PCB-02-RM-000	C	128.72	13.95	1493.96	5.85E-06	3.78E-04	1.47E-07	2.02E-07

PCB-02-RM	*PCB-02-RM-010*	*C*	*128.62*	*14.05*	*1494.06*	*4.87E-06*	*2.92E-04*	*1.22E-07*	*1.33E-07*
PCB-02-RM	*PCB-02-RM-020*	*CB*	*128.52*	*14.15*	*1494.16*	*3.95E-06*	*2.13E-04*	*9.93E-08*	*1.00E-07*
PCB-02-RM	*PCB-02-RM-030*	*B*	*128.42*	*14.25*	*1494.26*	*4.71E-06*	*3.74E-04*	*1.18E-07*	*1.31E-07*
PCB-02-RM	*PCB-02-RM-040*	*B*	*128.32*	*14.35*	*1494.36*	*4.83E-06*	*4.47E-04*	*1.21E-07*	*1.45E-07*
PCB-02-RM	*PCB-02-RM-050*	*B*	*128.22*	*14.45*	*1494.46*	*3.99E-06*	*3.71E-04*	*1.00E-07*	*1.32E-07*
PCB-02-RM	*PCB-02-RM-060*	*B*	*128.12*	*14.55*	*1494.56*	*3.84E-06*	*3.42E-04*	*9.65E-08*	*1.30E-07*
PCB-02-RM	PCB-02-RM-070	B	128.02	14.65	1494.66	3.29E-06	2.75E-04	8.27E-08	1.29E-07
PCB-02-RM	PCB-02-RM-080	B	127.92	14.75	1494.76	3.32E-06	2.61E-04	8.34E-08	1.21E-07
PCB-02-RM	PCB-02-RM-090	B	127.82	14.85	1494.86	3.17E-06	2.93E-04	7.97E-08	1.34E-07
PCB-02-RM	PCB-02-RM-100	B	127.72	14.95	1494.96	3.15E-06	2.52E-04	7.91E-08	1.25E-07
PCB-02-RM	PCB-02-RM-110	B	127.62	15.05	1495.06	2.67E-06	2.37E-04	6.70E-08	1.17E-07
PCB-02-RM	PCB-02-RM-120	B	127.52	15.15	1495.16	3.25E-06	2.84E-04	8.17E-08	1.31E-07
PCB-02-RM	PCB-02-RM-130	AB	127.42	15.25	1495.26	4.80E-06	2.97E-04	1.21E-07	1.30E-07
PCB-02-RM	PCB-02-RM-140	A	127.32	15.35	1495.36	4.45E-06	2.64E-04	1.12E-07	1.38E-07
PCB-02-RM	PCB-02-RM-150	A	127.22	15.45	1495.46	4.02E-06	2.89E-04	1.01E-07	1.42E-07
PCB-02-TRA	*PCB-02-TRA-000*	*C*	*66.35*	*70.7*	*1548.41*	*4.57E-06*	*2.83E-04*	*1.15E-07*	*1.11E-07*
PCB-02-TRA	*PCB-02-TRA-010*	*C*	*66.25*	*70.8*	*1548.51*	*4.59E-06*	*3.05E-04*	*1.15E-07*	*1.20E-07*
PCB-02-TRA	*PCB-02-TRA-020*	*B1*	*66.15*	*70.9*	*1548.61*	*1.15E-05*	*8.24E-04*	*2.90E-07*	*1.83E-07*
PCB-02-TRA	*PCB-02-TRA-030*	*B1*	*66.05*	*71*	*1548.71*	*4.11E-06*	*4.21E-04*	*1.03E-07*	*1.39E-07*
PCB-02-TRA	*PCB-02-TRA-040*	*B1*	*65.95*	*71.1*	*1548.81*	*8.04E-06*	*5.92E-04*	*2.02E-07*	*1.62E-07*
PCB-02-TRA	PCB-02-TRA-050	B1	65.85	71.2	1548.91	2.98E-06	3.23E-04	7.49E-08	1.31E-07
PCB-02-TRA	PCB-02-TRA-060	B2	65.75	71.3	1549.01	1.90E-06	3.23E-04	4.78E-08	1.36E-07

PCB-02-TRA	PCB-02-TRA-070	B2	65.65	71.4	1549.11	1.21E-06	2.69E-04	3.04E-08	1.30E-07
PCB-02-TRA	PCB-02-TRA-080	B2	65.55	71.5	1549.21	4.15E-07	2.36E-04	1.04E-08	1.25E-07
PCB-02-TRA	PCB-02-TRA-090	B2	65.45	71.6	1549.31	8.78E-07	2.23E-04	2.21E-08	1.27E-07
PCB-02-TRA	PCB-02-TRA-100	B2	65.35	71.7	1549.41	5.38E-07	2.25E-04	1.35E-08	1.30E-07
PCB-02-TRA	PCB-02-TRA-110	B2	65.25	71.8	1549.51	2.43E-07	2.06E-04	6.10E-09	1.17E-07
PCB-02-TRA	PCB-02-TRA-120	B2	65.15	71.9	1549.61		2.11E-04		1.26E-07
PCB-02-TRA	PCB-02-TRA-130	B2	65.05	72	1549.71	3.44E-07	2.04E-04	8.63E-09	1.32E-07
PCB-02-TRA	PCB-02-TRA-140	AB	64.95	72.1	1549.81	2.87E-06	3.07E-04	7.23E-08	1.30E-07
PCB-02-TRA	PCB-02-TRA-150	AB	64.85	72.2	1549.91	2.73E-06	2.08E-04	6.87E-08	1.32E-07
PCB-02-TRA	PCB-02-TRA-160	A	64.75	72.3	1550.01	1.96E-06	1.36E-04	4.93E-08	1.14E-07
PCB-02-TRA	PCB-02-TRA-170	A	64.65	72.4	1550.11	2.88E-06	1.50E-04	7.24E-08	1.10E-07
PCB-02-TRA	PCB-02-TRA-180	A	64.55	72.5	1550.21	1.94E-06	8.82E-05	4.89E-08	9.68E-08
PCB-03-TRA	***PCB-03-TRA-000***	***C***	***66.45***	***71***	***1548.71***	***5.02E-06***	***2.80E-04***	***1.26E-07***	***1.16E-07***
PCB-03-TRA	***PCB-03-TRA-010***	***C***	***66.35***	***71.1***	***1548.81***	***4.46E-06***	***2.59E-04***	***1.12E-07***	***1.12E-07***
PCB-03-TRA	***PCB-03-TRA-020***	***C***	***66.25***	***71.2***	***1548.91***	***4.61E-06***	***2.61E-04***	***1.16E-07***	***1.07E-07***
PCB-03-TRA	***PCB-03-TRA-030***	***B***	***66.15***	***71.3***	***1549.01***	***2.19E-05***	***1.32E-03***	***5.50E-07***	***2.30E-07***
PCB-03-TRA	***PCB-03-TRA-040***	***B***	***66.05***	***71.4***	***1549.11***	***2.09E-05***	***1.38E-03***	***5.25E-07***	***2.36E-07***

PCB-03-TRA	*PCB-03-TRA-050*	*B*	*65.95*	*71.5*	*1549.21*	*1.34E-05*	*8.56E-04*	*3.36E-07*	*1.82E-07*
PCB-03-TRA	*PCB-03-TRA-060*	*B*	*65.85*	*71.6*	*1549.31*	*7.36E-06*	*6.12E-04*	*1.85E-07*	*1.60E-07*
PCB-03-TRA	*PCB-03-TRA-070*	*B*	*65.75*	*71.7*	*1549.41*	*5.82E-06*	*5.60E-04*	*1.46E-07*	*1.58E-07*
PCB-03-TRA	*PCB-03-TRA-080*	*B*	*65.65*	*71.8*	*1549.51*	*3.49E-06*	*5.72E-04*	*8.78E-08*	*1.48E-07*
PCB-03-TRA	*PCB-03-TRA-090*	*B*	*65.55*	*71.9*	*1549.61*	*5.09E-06*	*4.76E-04*	*1.28E-07*	*1.66E-07*
PCB-03-TRA	*PCB-03-TRA-100*	*B*	*65.45*	*72*	*1549.71*	*4.51E-06*	*5.92E-04*	*1.13E-07*	*1.64E-07*
PCB-03-TRA	PCB-03-TRA-110	A	65.35	72.1	1549.81	2.41E-06	1.27E-04	6.05E-08	7.90E-08
PCB-01-RM	*PCB-01-RM-000*	*C*	*128.62*	*13.95*	*1493.96*	*4.47E-06*	*2.32E-04*	*1.12E-07*	*9.98E-08*
PCB-01-RM	*PCB-01-RM-010*	*C*	*128.52*	*14.05*	*1494.06*	*4.52E-06*	*2.36E-04*	*1.14E-07*	*9.97E-08*
PCB-01-RM	*PCB-01-RM-020*	*B*	*128.42*	*14.15*	*1494.16*	*6.75E-06*	*5.31E-04*	*1.70E-07*	*1.53E-07*
PCB-01-RM	*PCB-01-RM-025*	*B*	*128.37*	*14.2*	*1494.21*	*5.04E-06*	*3.55E-04*	*1.27E-07*	*1.37E-07*
PCB-01-RM	*PCB-01-RM-030*	*B*	*128.32*	*14.25*	*1494.26*	*3.77E-06*	*3.39E-04*	*9.47E-08*	*1.34E-07*
PCB-01-RM	*PCB-01-RM-035*	*B*	*128.27*	*14.3*	*1494.31*	*6.48E-06*	*5.11E-04*	*1.63E-07*	*1.58E-07*
PCB-01-RM	*PCB-01-RM-040*	*B*	*128.22*	*14.35*	*1494.36*	*4.44E-06*	*3.37E-04*	*1.12E-07*	*1.33E-07*
PCB-01-RM	PCB-01-RM-045	B	128.17	14.4	1494.41	4.01E-06	3.05E-04	1.01E-07	1.35E-07
PCB-01-RM	PCB-01-RM-050	B	128.12	14.45	1494.46	3.54E-06	2.72E-04	8.90E-08	1.23E-07
PCB-01-RM	PCB-01-RM-055	B	128.07	14.5	1494.51	3.92E-06	3.08E-04	9.85E-08	1.33E-07
PCB-01-RM	PCB-01-RM-060	B	128.02	14.55	1494.56	3.22E-06	2.87E-04	8.09E-08	1.32E-07
PCB-01-RM	PCB-01-RM-065	B	127.97	14.6	1494.61	2.84E-06	2.72E-04	7.15E-08	1.37E-07
PCB-01-RM	PCB-01-RM-070	B	127.92	14.65	1494.66	3.93E-06	2.53E-04	9.87E-08	1.27E-07
PCB-01-RM	PCB-01-RM-075	B	127.87	14.7	1494.71	3.98E-06	2.61E-04	1.00E-07	1.28E-07
PCB-01-RM	PCB-01-RM-080	B	127.82	14.75	1494.76	4.65E-06	3.28E-04	1.17E-07	1.40E-07

PCB-01-RM	PCB-01-RM-085	B	127.77	14.8	1494.81	4.13E-06	3.17E-04	1.04E-07	1.36E-07
PCB-01-RM	PCB-01-RM-090	B	127.72	14.85	1494.86	4.74E-06	2.76E-04	1.19E-07	1.31E-07
PCB-01-RM	PCB-01-RM-095	B	127.67	14.9	1494.91	4.47E-06	2.73E-04	1.12E-07	1.29E-07
PCB-01-RM	PCB-01-RM-100	B	127.62	14.95	1494.96	4.46E-06	2.67E-04	1.12E-07	1.33E-07
PCB-01-RM	PCB-01-RM-105	B	127.57	15	1495.01	5.20E-06	2.80E-04	1.31E-07	1.31E-07
PCB-01-RM	PCB-01-RM-110	A	127.52	15.05	1495.06	4.31E-06	2.52E-04	1.08E-07	1.28E-07
PCB-01-RM	PCB-01-RM-120	A	127.42	15.15	1495.16	4.04E-06	2.18E-04	1.02E-07	1.15E-07
PCB-01-RM	PCB-01-RM-130	A	127.32	15.25	1495.26	3.61E-06	1.94E-04	9.06E-08	1.01E-07
PCB-01-RM	PCB-01-RM-140	A	127.22	15.35	1495.36	2.95E-06	1.65E-04	7.41E-08	1.13E-07
PCB-01-RM	PCB-01-RM-150	A	127.12	15.45	1495.46	3.98E-06	2.16E-04	9.99E-08	9.15E-08
PCB-03-P2	***PCB-03-P2-000***	***C***	***102.95***	***37.7***	***1518.57***	***4.05E-06***	***2.21E-04***	***1.02E-07***	***1.11E-07***
PCB-03-P2	***PCB-03-P2-010***	***C***	***102.85***	***37.8***	***1518.67***	***5.15E-06***	***3.61E-04***	***1.29E-07***	***1.44E-07***
PCB-03-P2	***PCB-03-P2-020***	***B2***	***102.75***	***37.9***	***1518.77***	***4.65E-06***	***2.80E-04***	***1.17E-07***	***1.28E-07***
PCB-03-P2	***PCB-03-P2-030***	***B2***	***102.65***	***38***	***1518.87***	***4.42E-06***	***2.72E-04***	***1.11E-07***	***1.14E-07***
PCB-03-P2	***PCB-03-P2-040***	***B2***	***102.55***	***38.1***	***1518.97***	***5.74E-06***	***4.42E-04***	***1.44E-07***	***1.52E-07***
PCB-03-P2	***PCB-03-P2-050***	***B2***	***102.45***	***38.2***	***1519.07***	***4.08E-06***	***3.09E-04***	***1.02E-07***	***1.32E-07***
PCB-03-P2	***PCB-03-P2-060***	***B2***	***102.35***	***38.3***	***1519.17***	***3.99E-06***	***3.03E-04***	***1.00E-07***	***1.35E-07***
PCB-03-P2	***PCB-03-P2-070***	***B2***	***102.25***	***38.4***	***1519.27***	***3.81E-06***	***3.03E-04***	***9.57E-08***	***1.32E-07***
PCB-03-P2	***PCB-03-P2-080***	***B2***	***102.15***	***38.5***	***1519.37***	***3.22E-06***	***2.43E-04***	***8.10E-08***	***1.26E-07***
PCB-03-P2	***PCB-03-P2-090***	***B2***	***102.05***	***38.6***	***1519.47***	***3.52E-06***	***2.56E-04***	***8.84E-08***	***1.33E-07***
PCB-03-P2	PCB-03-P2-100	B1	101.95	38.7	1519.57	2.52E-06	2.37E-04	6.33E-08	1.27E-07
PCB-03-P2	PCB-03-P2-110	B1	101.85	38.8	1519.67	3.88E-06	2.74E-04	9.76E-08	1.32E-07
PCB-03-P2	PCB-03-P2-120	B1	101.75	38.9	1519.77	2.45E-06	1.90E-04	6.15E-08	1.28E-07
PCB-03-P2	PCB-03-P2-130	B1	101.65	39	1519.87	2.65E-06	1.59E-04	6.66E-08	1.27E-07
PCB-03-P2	PCB-03-P2-140	B1	101.55	39.1	1519.97	1.87E-06	1.79E-04	4.70E-08	1.27E-07

PCB-03-P2	PCB-03-P2-150	AB	101.45	39.2	1520.07	2.26E-06	1.68E-04	5.67E-08	1.24E-07
PCB-03-P2	PCB-03-P2-160	AC	101.35	39.3	1520.17	2.86E-06	2.05E-04	7.18E-08	1.22E-07
PCB-03-P2	PCB-03-P2-170	AC	101.25	39.4	1520.27	3.39E-06	2.15E-04	8.52E-08	1.33E-07
PCB-01-P4	*PCB-01-P4-000A*	*A/B*	*75.34*	*62.45*	*1540.75*	*3.99E-06*	*2.20E-04*	*1.00E-07*	*1.02E-07*
PCB-01-P4	*PCB-01-P4-000B*	*A/B*	*75.29*	*62.5*	*1540.8*	*8.98E-06*	*6.46E-04*	*2.26E-07*	*1.70E-07*
PCB-01-P4	*PCB-01-P4-010*	*A/B*	*75.19*	*62.55*	*1540.85*	*5.13E-06*	*3.75E-04*	*1.29E-07*	*1.54E-07*
PCB-01-P4	*PCB-01-P4-020*	*A/B*	*75.09*	*62.65*	*1540.95*	*6.72E-06*	*5.91E-04*	*1.69E-07*	*1.76E-07*
PCB-01-P4	PCB-01-P4-030	B2	74.99	62.75	1541.05	4.78E-06	3.28E-04	1.20E-07	1.41E-07
PCB-01-P4	*PCB-01-P4-035*	*B2*	*74.94*	*62.8*	*1541.1*	*3.36E-06*	*2.09E-04*	*8.46E-08*	*1.34E-07*
PCB-01-P4	*PCB-01-P4-040*	*B2*	*74.89*	*62.85*	*1541.15*	*3.58E-06*	*2.31E-04*	*9.00E-08*	*1.36E-07*
PCB-01-P4	*PCB-01-P4-045*	*B2*	*74.84*	*62.9*	*1541.2*	*3.27E-06*	*2.01E-04*	*8.21E-08*	*1.29E-07*
PCB-01-P4	*PCB-01-P4-050*	*B2*	*74.79*	*62.95*	*1541.25*	*2.36E-06*	*1.86E-04*	*5.93E-08*	*1.30E-07*
PCB-01-P4	*PCB-01-P4-055*	*B2*	*74.74*	*63*	*1541.3*	*3.38E-06*	*2.15E-04*	*8.49E-08*	*1.34E-07*
PCB-01-P4	*PCB-01-P4-060*	*B2*	*74.69*	*63.05*	*1541.35*	*2.14E-06*	*1.86E-04*	*5.38E-08*	*1.29E-07*
PCB-01-P4	*PCB-01-P4-065*	*B2*	*74.64*	*63.1*	*1541.4*	*1.34E-06*	*1.96E-04*	*3.36E-08*	*1.32E-07*
PCB-01-P4	*PCB-01-P4-070*	*B2*	*74.59*	*63.15*	*1541.45*	*2.74E-06*	*1.96E-04*	*6.88E-08*	*1.30E-07*
PCB-01-P4	*PCB-01-P4-075*	*B2*	*74.54*	*63.2*	*1541.5*	*2.46E-06*	*1.94E-04*	*6.18E-08*	*1.30E-07*
PCB-01-P4	*PCB-01-P4-080*	*B2*	*74.49*	*63.25*	*1541.55*	*1.46E-06*	*2.08E-04*	*3.68E-08*	*1.32E-07*
PCB-01-P4	*PCB-01-P4-085*	*B2*	*74.44*	*63.3*	*1541.6*	*2.73E-06*	*1.79E-04*	*6.87E-08*	*1.28E-07*
PCB-01-P4	*PCB-01-P4-090*	*B2*	*74.39*	*63.35*	*1541.65*	*2.88E-06*	*1.95E-04*	*7.23E-08*	*1.30E-07*
PCB-01-P4	*PCB-01-P4-095*	*B2*	*74.34*	*63.4*	*1541.7*	*2.44E-06*	*1.72E-04*	*6.13E-08*	*1.29E-07*
PCB-01-P4	*PCB-01-P4-100*	*B1*	*74.29*	*63.45*	*1541.75*	*2.18E-06*	*1.52E-04*	*5.48E-08*	*1.22E-07*
PCB-01-P4	*PCB-01-P4-105*	*B1*	*74.24*	*63.5*	*1541.8*	*1.99E-06*	*1.51E-04*	*5.00E-08*	*1.20E-07*
PCB-01-P4	*PCB-01-P4-110*	*B1*	*74.19*	*63.55*	*1541.85*	*2.07E-06*	*1.50E-04*	*5.20E-08*	*1.20E-07*
PCB-01-P4	*PCB-01-P4-115*	*B1*	*74.14*	*63.6*	*1541.9*	*1.51E-06*	*1.28E-04*	*3.80E-08*	*1.21E-07*

PCB-01-P4	*PCB-01-P4-120*	*B1*	*74.09*	*63.65*	*1541.95*	*2.35E-06*	*1.40E-04*	*5.91E-08*	*1.20E-07*
PCB-01-P4	*PCB-01-P4-125*	*B1*	*74.04*	*63.7*	*1542*	*2.21E-06*	*1.33E-04*	*5.54E-08*	*1.17E-07*
PCB-01-P4	*PCB-01-P4-130*	*B1*	*73.99*	*63.75*	*1542.05*	*2.23E-06*	*1.37E-04*	*5.61E-08*	*1.12E-07*
PCB-01-P4	*PCB-01-P4-135*	*B1*	*73.94*	*63.8*	*1542.1*	*1.08E-06*	*1.30E-04*	*2.71E-08*	*1.16E-07*
PCB-01-P4	*PCB-01-P4-140*	*B1*	*73.89*	*63.85*	*1542.15*	*2.15E-06*	*1.31E-04*	*5.40E-08*	*1.15E-07*
PCB-01-P4	*PCB-01-P4-145*	*B1*	*73.84*	*63.9*	*1542.2*	*7.50E-07*	*1.24E-04*	*1.89E-08*	*1.17E-07*
PCB-01-P4	*PCB-01-P4-150*	*B1*	*73.79*	*63.95*	*1542.25*	*1.83E-06*	*1.26E-04*	*4.60E-08*	*1.17E-07*
PCB-01-P4	*PCB-01-P4-155*	*B1*	*73.74*	*64*	*1542.3*	*2.08E-06*	*1.36E-04*	*5.22E-08*	*1.17E-07*
PCB-01-P4	*PCB-01-P4-160*	*B1*	*73.69*	*64.05*	*1542.35*	*1.08E-06*	*1.26E-04*	*2.71E-08*	*1.17E-07*
PCB-01-P4	PCB-01-P4-170	B1	73.59	64.15	1542.45	2.02E-06	1.27E-04	5.08E-08	1.18E-07
PCB-01-P4	PCB-01-P4-180	A	73.49	64.25	1542.55	3.54E-06	2.08E-04	8.89E-08	1.16E-07
PCB-01-P4	PCB-01-P4-190	A	73.39	64.35	1542.65	7.08E-06	4.73E-04	1.78E-07	1.35E-07
PCB-01-TRA	*PCB-01-TRA-000*	*C*	*66.55*	*70.8*	*1548.51*	*6.02E-06*	*4.34E-04*	*1.51E-07*	*1.79E-07*
PCB-01-TRA	*PCB-01-TRA-010*	*C*	*66.45*	*70.9*	*1548.61*	*6.12E-06*	*4.00E-04*	*1.54E-07*	*1.74E-07*
PCB-01-TRA	*PCB-01-TRA-020*	*C*	*66.35*	*71*	*1548.71*	*5.09E-06*	*3.14E-04*	*1.28E-07*	*1.35E-07*
PCB-01-TRA	*PCB-01-TRA-030*	*BC*	*66.25*	*71.1*	*1548.81*	*3.81E-06*	*2.00E-04*	*9.58E-08*	*8.72E-08*
PCB-01-TRA	*PCB-01-TRA-040*	*B*	*66.15*	*71.2*	*1548.91*	*3.08E-06*	*3.03E-04*	*7.74E-08*	*1.30E-07*
PCB-01-TRA	*PCB-01-TRA-045*	*B*	*66.1*	*71.25*	*1548.96*	*5.65E-06*	*4.36E-04*	*1.42E-07*	*1.36E-07*
PCB-01-TRA	*PCB-01-TRA-050*	*B*	*66.05*	*71.3*	*1549.01*	*3.98E-06*	*3.63E-04*	*1.00E-07*	*1.35E-07*
PCB-01-TRA	*PCB-01-TRA-055*	*B*	*66*	*71.35*	*1549.06*	*3.12E-06*	*3.58E-04*	*7.85E-08*	*1.30E-07*
PCB-01-TRA	*PCB-01-TRA-060*	*B*	*65.95*	*71.4*	*1549.11*	*4.36E-06*	*3.70E-04*	*1.10E-07*	*1.37E-07*

PCB-01-TRA	*PCB-01-TRA-065*	*B*	*65.9*	*71.45*	*1549.16*	*1.42E-06*	*2.98E-04*	*3.58E-08*	*1.31E-07*
PCB-01-TRA	*PCB-01-TRA-070*	*B*	*65.85*	*71.5*	*1549.21*	*2.79E-06*	*3.37E-04*	*7.02E-08*	*1.35E-07*
PCB-01-TRA	*PCB-01-TRA-075*	*B*	*65.8*	*71.55*	*1549.26*	*1.02E-06*	*2.66E-04*	*2.56E-08*	*1.28E-07*
PCB-01-TRA	*PCB-01-TRA-080*	*B*	*65.75*	*71.6*	*1549.31*	*1.79E-06*	*2.88E-04*	*4.51E-08*	*1.31E-07*
PCB-01-TRA	*PCB-01-TRA-085*	*B*	*65.7*	*71.65*	*1549.36*	*2.28E-06*	*3.17E-04*	*5.72E-08*	*1.42E-07*
PCB-01-TRA	*PCB-01-TRA-090*	*B*	*65.65*	*71.7*	*1549.41*	*1.22E-06*	*3.26E-04*	*3.07E-08*	*1.44E-07*
PCB-01-TRA	*PCB-01-TRA-095*	*B*	*65.6*	*71.75*	*1549.46*		*2.40E-04*		*1.34E-07*
PCB-01-TRA	*PCB-01-TRA-100*	*B*	*65.55*	*71.8*	*1549.51*	*2.89E-07*	*3.35E-04*	*7.26E-09*	*1.45E-07*
PCB-01-TRA	*PCB-01-TRA-105*	*B*	*65.5*	*71.85*	*1549.56*	*3.61E-07*	*2.43E-04*	*9.06E-09*	*1.32E-07*
PCB-01-TRA	*PCB-01-TRA-110*	*B*	*65.45*	*71.9*	*1549.61*	*1.19E-06*	*2.63E-04*	*2.99E-08*	*1.33E-07*
PCB-01-TRA	*PCB-01-TRA-115*	*B*	*65.4*	*71.95*	*1549.66*	*9.40E-07*	*3.03E-04*	*2.36E-08*	*1.44E-07*
PCB-01-TRA	*PCB-01-TRA-120*	*B*	*65.35*	*72*	*1549.71*	*1.24E-06*	*2.54E-04*	*3.11E-08*	*1.32E-07*
PCB-01-TRA	PCB-01-TRA-130	AC	65.25	72.1	1549.81	2.53E-06	1.54E-04	6.36E-08	1.10E-07
PCB-01-TRA	PCB-01-TRA-140	AC	65.15	72.2	1549.91	2.48E-06	1.62E-04	6.24E-08	1.17E-07
PCB-01-TRA	PCB-01-TRA-150	AC	65.05	72.3	1550.01	2.53E-06	1.82E-04	6.36E-08	1.25E-07
PCB-01-TRB	*PCB-01-TRB-000*	*C*	*61.18*	*74.6*	*1554.03*	*4.61E-06*	*3.03E-04*	*1.16E-07*	*1.09E-07*
PCB-01-TRB	*PCB-01-TRB-010*	*C*	*61.08*	*74.7*	*1554.13*	*4.09E-06*	*2.07E-04*	*1.03E-07*	*9.67E-08*

PCB-01-TRB	*PCB-01-TRB-020*	*C*	*60.98*	*74.8*	*1554.23*	*3.76E-06*	*1.85E-04*	*9.45E-08*	*8.73E-08*
PCB-01-TRB	*PCB-01-TRB-030*	*C*	*60.88*	*74.9*	*1554.33*	*4.06E-06*	*1.92E-04*	*1.02E-07*	*8.88E-08*
PCB-01-TRB	PCB-01-TRB-040	B	60.78	75	1554.43	3.02E-06	2.26E-04	7.60E-08	1.18E-07
PCB-01-TRB	*PCB-01-TRB-045*	*B*	*60.73*	*75.05*	*1554.48*	*4.72E-06*	*3.39E-04*	*1.19E-07*	*1.28E-07*
PCB-01-TRB	*PCB-01-TRB-050*	*B*	*60.68*	*75.1*	*1554.53*	*5.20E-06*	*3.45E-04*	*1.31E-07*	*1.29E-07*
PCB-01-TRB	*PCB-01-TRB-055*	*B*	*60.63*	*75.15*	*1554.58*	*1.05E-05*	*5.57E-04*	*2.63E-07*	*1.44E-07*
PCB-01-TRB	*PCB-01-TRB-060*	*B*	*60.58*	*75.2*	*1554.63*	*4.22E-06*	*3.55E-04*	*1.06E-07*	*1.25E-07*
PCB-01-TRB	*PCB-01-TRB-065*	*B*	*60.53*	*75.25*	*1554.68*	*1.80E-06*	*2.01E-04*	*4.52E-08*	*1.23E-07*
PCB-01-TRB	*PCB-01-TRB-070*	*B*	*60.48*	*75.3*	*1554.73*	*6.27E-06*	*4.50E-04*	*1.58E-07*	*1.48E-07*
PCB-01-TRB	*PCB-01-TRB-075*	*B*	*60.43*	*75.35*	*1554.78*	*4.03E-06*	*2.97E-04*	*1.01E-07*	*1.26E-07*
PCB-01-TRB	*PCB-01-TRB-080*	*B*	*60.38*	*75.4*	*1554.83*	*5.37E-06*	*4.03E-04*	*1.35E-07*	*1.39E-07*
PCB-01-TRB	PCB-01-TRB-085	B	60.33	75.45	1554.88	2.59E-06	2.21E-04	6.50E-08	1.19E-07
PCB-01-TRB	PCB-01-TRB-090	B	60.28	75.5	1554.93	4.34E-06	3.29E-04	1.09E-07	1.30E-07
PCB-01-TRB	PCB-01-TRB-100	A	60.18	75.6	1555.03	4.17E-06	2.39E-04	1.05E-07	1.20E-07
PCB-01-TRB	PCB-01-TRB-110	A	60.08	75.7	1555.13	4.75E-06	2.87E-04	1.19E-07	1.29E-07
PCB-01-TRB	PCB-01-TRB-120	A	59.98	75.8	1555.23	3.45E-06	1.81E-04	8.66E-08	1.07E-07
PCB-01-UDRB	*PCB-01-UDRB-000*	*C*	*93.13*	*47.8*	*1526.77*	*3.01E-06*	*1.16E-04*	*7.56E-08*	*7.20E-08*

PCB-01-UDRB	*PCB-01-UDRB-010*	*C*	*93.03*	*47.9*	*1526.87*	*3.13E-06*	*1.20E-04*	*7.87E-08*	*6.12E-08*
PCB-01-UDRB	*PCB-01-UDRB-020*	*C*	*92.93*	*48*	*1526.97*	*3.37E-06*	*1.82E-04*	*8.47E-08*	*8.49E-08*
PCB-01-UDRB	*PCB-01-UDRB-030*	*BL*	*92.83*	*48.1*	*1527.07*	*1.39E-05*	*7.56E-04*	*3.49E-07*	*1.63E-07*
PCB-01-UDRB	*PCB-01-UDRB-035*	*BL*	*92.78*	*48.15*	*1527.12*	*1.69E-05*	*8.29E-04*	*4.23E-07*	*1.62E-07*
PCB-01-UDRB	*PCB-01-UDRB-040*	*BL*	*92.73*	*48.2*	*1527.17*	*1.49E-05*	*7.31E-04*	*3.74E-07*	*1.61E-07*
PCB-01-UDRB	*PCB-01-UDRB-045*	*BL*	*92.68*	*48.25*	*1527.22*	*1.56E-05*	*8.20E-04*	*3.91E-07*	*1.69E-07*
PCB-01-UDRB	*PCB-01-UDRB-050*	*BL*	*92.63*	*48.3*	*1527.27*	*8.80E-06*	*5.43E-04*	*2.21E-07*	*1.47E-07*
PCB-01-UDRB	*PCB-01-UDRB-055*	*BL*	*92.58*	*48.35*	*1527.32*	*9.62E-06*	*5.36E-04*	*2.42E-07*	*1.44E-07*
PCB-01-UDRB	*PCB-01-UDRB-060*	*BL*	*92.53*	*48.4*	*1527.37*	*1.15E-05*	*7.60E-04*	*2.89E-07*	*1.51E-07*
PCB-01-UDRB	*PCB-01-UDRB-065*	*BL*	*92.48*	*48.45*	*1527.42*	*1.97E-05*	*1.15E-03*	*4.96E-07*	*1.92E-07*
PCB-01-UDRB	*PCB-01-UDRB-070*	*BL*	*92.43*	*48.5*	*1527.47*	*1.25E-05*	*8.39E-04*	*3.14E-07*	*1.76E-07*
PCB-01-UDRB	*PCB-01-UDRB-075*	*BL*	*92.38*	*48.55*	*1527.52*	*2.59E-05*	*1.32E-03*	*6.52E-07*	*2.13E-07*
PCB-01-UDRB	*PCB-01-UDRB-080*	*BL*	*92.33*	*48.6*	*1527.57*	*1.38E-05*	*9.93E-04*	*3.48E-07*	*1.83E-07*
PCB-01-UDRB	*PCB-01-UDRB-085*	*BL*	*92.28*	*48.65*	*1527.62*	*2.08E-05*	*1.11E-03*	*5.22E-07*	*1.91E-07*
PCB-01-UDRB	*PCB-01-UDRB-090*	*BL*	*92.23*	*48.7*	*1527.67*	*3.12E-05*	*1.53E-03*	*7.85E-07*	*2.36E-07*
PCB-01-UDRB	*PCB-01-UDRB-095*	*B2*	*92.18*	*48.75*	*1527.72*	*2.66E-05*	*1.22E-03*	*6.67E-07*	*2.06E-07*
PCB-01-UDRB	*PCB-01-UDRB-100*	*B2*	*92.13*	*48.8*	*1527.77*	*1.43E-05*	*8.98E-04*	*3.60E-07*	*1.80E-07*

PCB-01-UDRB	*PCB-01-UDRB-105*	*B2*	*92.08*	*48.85*	*1527.82*	*2.31E-05*	*1.25E-03*	*5.80E-07*	*2.16E-07*
PCB-01-UDRB	*PCB-01-UDRB-110*	*B2*	*92.03*	*48.9*	*1527.87*	*2.37E-05*	*1.20E-03*	*5.95E-07*	*2.13E-07*
PCB-01-UDRB	*PCB-01-UDRB-115*	*B2*	*91.98*	*48.95*	*1527.92*	*1.75E-05*	*9.18E-04*	*4.41E-07*	*1.87E-07*
PCB-01-UDRB	*PCB-01-UDRB-120*	*B2*	*91.93*	*49*	*1527.97*	*1.49E-05*	*8.64E-04*	*3.76E-07*	*1.81E-07*
PCB-01-UDRB	*PCB-01-UDRB-125*	*B2*	*91.88*	*49.05*	*1528.02*	*1.96E-05*	*1.02E-03*	*4.94E-07*	*1.97E-07*
PCB-01-UDRB	*PCB-01-UDRB-130*	*B2*	*91.83*	*49.1*	*1528.07*	*1.17E-05*	*7.26E-04*	*2.95E-07*	*1.74E-07*
PCB-01-UDRB	PCB-01-UDRB-135	B2	91.78	49.15	1528.12	6.35E-06	4.74E-04	1.59E-07	1.51E-07
PCB-01-UDRB	PCB-01-UDRB-140	B2	91.73	49.2	1528.17	4.38E-06	3.37E-04	1.10E-07	1.34E-07
PCB-01-UDRB	PCB-01-UDRB-145	B2	91.68	49.25	1528.22	5.56E-06	3.50E-04	1.40E-07	1.36E-07
PCB-01-UDRB	PCB-01-UDRB-150	B2	91.63	49.3	1528.27	4.49E-06	3.42E-04	1.13E-07	1.32E-07
PCB-01-UDRB	PCB-01-UDRB-155	B1	91.58	49.35	1528.32	3.15E-06	2.26E-04	7.93E-08	1.27E-07
PCB-01-UDRB	PCB-01-UDRB-160	B1	91.53	49.4	1528.37	2.70E-06	2.38E-04	6.78E-08	1.22E-07
PCB-01-UDRB	PCB-01-UDRB-165	B1	91.48	49.45	1528.42	2.94E-06	1.99E-04	7.38E-08	1.25E-07
PCB-01-UDRB	PCB-01-UDRB-170	B1	91.43	49.5	1528.47	3.06E-06	1.90E-04	7.68E-08	1.32E-07
PCB-01-UDRB	PCB-01-UDRB-175	B1	91.38	49.55	1528.52	3.74E-06	2.17E-04	9.41E-08	1.25E-07
PCB-01-UDRB	PCB-01-UDRB-180	B1	91.33	49.6	1528.57	2.69E-06	2.36E-04	6.77E-08	1.31E-07
PCB-01-UDRB	PCB-01-UDRB-185	B1	91.28	49.65	1528.62	3.46E-06	2.46E-04	8.69E-08	1.26E-07

PCB-01-UDRB	PCB-01-UDRB-190	B1	91.23	49.7	1528.67	3.03E-06	1.70E-04	7.62E-08	1.24E-07
PCB-01-UDRB	PCB-01-UDRB-195	B1	91.18	49.75	1528.72	2.47E-06	1.63E-04	6.21E-08	1.21E-07
PCB-01-UDRB	PCB-01-UDRB-200	B1	91.13	49.8	1528.77	6.77E-07	1.57E-04	1.70E-08	1.29E-07
PCB-01-UDRB	PCB-01-UDRB-205	B1	91.08	49.85	1528.82	1.65E-06	1.44E-04	4.14E-08	1.25E-07
PCB-01-UDRB	PCB-01-UDRB-210	B1	91.03	49.9	1528.87	3.48E-06	2.24E-04	8.74E-08	1.31E-07
PCB-01-UDRB	PCB-01-UDRB-215	A	90.98	49.95	1528.92	6.59E-06	4.45E-04	1.66E-07	1.46E-07
PCB-01-UDRB	PCB-01-UDRB-220	A	90.93	50	1528.97	2.17E-05	8.24E-04	5.45E-07	1.66E-07
PCB-01-UDRB	PCB-01-UDRB-225	A	90.88	50.05	1529.02	2.38E-06	1.12E-04	5.99E-08	7.41E-08
PCB-01-UDRB	PCB-01-UDRB-230	A	90.83	50.1	1529.07	2.71E-06	1.08E-04	6.81E-08	7.03E-08
PCB-01-UDRB	PCB-01-UDRB-240	C	90.73	50.2	1529.17	4.47E-06	2.39E-04	1.12E-07	8.61E-08

Table B.4: Hysteresis properties for marker bed paleosols preserved in core. MCD* = meters composite depth equivalent.

Paleosol	**Specimen**	**Horizon**	**MCD***	$\mathbf{M_s}$	$\mathbf{M_r}$	$\mathbf{B_c}$	$\mathbf{B_{cr}}$	**HIRM**
			meters	Am^2kg^{-1}	Am^2kg^{-1}	mT	mT	Am^2kg^{-1}
PCB-01-LDRA	PCB-01-LDRA-000	C1	108.67	1.97E-03	2.42E-04	8.20	37.11	4.65E-05
PCB-01-LDRA	PCB-01-LDRA-010	C1	108.57	1.52E-03	2.03E-04	10.38	43.65	4.99E-05
PCB-01-LDRA	PCB-01-LDRA-020	B1	108.47	1.83E-02	2.53E-03	13.23	50.12	7.98E-04
PCB-01-LDRA	PCB-01-LDRA-030	B1	108.48	1.20E-02	1.79E-03	14.79	63.65	6.97E-04
PCB-01-LDRA	PCB-01-LDRA-040	B1	108.47	1.37E-02	2.33E-03	16.94	94.82	1.11E-03
PCB-01-LDRA	PCB-01-LDRA-050	B1	108.47	1.38E-02	2.23E-03	15.71	80.65	9.97E-04
PCB-01-LDRA	PCB-01-LDRA-060	B1	108.48	1.22E-02	1.89E-03	15.01	75.11	8.15E-04
PCB-01-LDRA	PCB-01-LDRA-070	B1	108.47	1.92E-02	2.77E-03	14.45	61.65	1.04E-03
PCB-01-LDRA	PCB-01-LDRA-080	B1	108.47	1.44E-02	2.11E-03	14.86	72.12	8.96E-04
PCB-01-LDRA	PCB-01-LDRA-090	B1	108.48	1.15E-02	2.05E-03	18.56	134.69	1.11E-03
PCB-01-LDRA	PCB-01-LDRA-100	B2	108.48	1.11E-02	2.18E-03	22.84	204.30	1.34E-03
PCB-01-LDRA	PCB-01-LDRA-110	B2	108.48	1.02E-02	2.22E-03	24.81	221.78	1.41E-03
PCB-01-LDRA	PCB-01-LDRA-120	B2	108.47	1.67E-02	3.37E-03	24.40	233.28	2.11E-03
PCB-01-LDRA	PCB-01-LDRA-130	B2	108.48	1.17E-02	2.70E-03	26.90	269.76	1.80E-03
PCB-01-LDRA	PCB-01-LDRA-140	B2	108.48	8.18E-03	2.36E-03	38.71	333.38	1.75E-03
PCB-01-LDRA	PCB-01-LDRA-150	B2	108.48	1.27E-02	2.71E-03	24.84	253.83	1.76E-03
PCB-01-LDRA	PCB-01-LDRA-160	B2	108.48	1.11E-02	2.25E-03	22.93	164.69	1.33E-03
PCB-01-LDRA	PCB-01-LDRA-170	C2	108.49	1.43E-03	1.43E-04	7.37	39.14	2.87E-05
PCB-01-LDRA	PCB-01-LDRA-180	C2	108.49	2.17E-03	2.01E-04	7.42	37.58	3.12E-05
PCB-01-PRM	PCB-01-PRM-010	C	140.95	2.50E-03	2.62E-04	7.89	36.86	5.57E-05
PCB-01-PRM	PCB-01-PRM-035	B1	140.84	5.85E-03	2.43E-03	111.19	298.34	2.08E-03
PCB-01-PRM	PCB-01-PRM-050	B1	140.84	5.72E-03	2.52E-03	143.90	468.71	2.06E-03
PCB-01-PRM	PCB-01-PRM-060	B1	140.85	3.68E-03	1.43E-03	60.61	338.95	1.10E-03
PCB-01-PRM	PCB-01-PRM-070	B2	140.85	4.74E-03	1.23E-03	38.54	306.05	8.99E-04
PCB-01-PRM	PCB-01-PRM-080	B2	140.85	4.87E-03	9.43E-04	18.15	169.42	5.42E-04
PCB-01-PRM	PCB-01-PRM-090	B2	140.85	2.97E-03	5.33E-04	17.89	141.90	3.01E-04
PCB-01-PRM	PCB-01-PRM-100	A	140.85	2.71E-03	4.39E-04	14.47	78.37	1.95E-04
PCB-02-PRM	PCB-02-PRM-000	C	141.15	2.79E-03	2.95E-04	6.85	33.30	5.42E-05
PCB-02-PRM	PCB-02-PRM-040	B1	140.84	6.49E-03	1.88E-03	43.27	300.21	1.30E-03
PCB-02-PRM	PCB-02-PRM-050	B1	140.84	5.47E-03	1.86E-03	67.93	372.11	1.48E-03
PCB-02-PRM	PCB-02-PRM-060	B1	140.84	8.39E-03	2.09E-03	28.34	258.33	1.36E-03
PCB-02-PRM	PCB-02-PRM-100	B2	140.84	5.19E-03	1.83E-03	48.45	373.70	1.45E-03
PCB-02-PRM	PCB-02-PRM-120	B2	140.85	4.30E-03	1.05E-03	19.83	338.69	7.34E-04
PCB-02-PRM	PCB-02-PRM-160	B2	140.84	5.00E-03	1.21E-03	23.38	317.74	8.57E-04
PCB-02-PRM	PCB-02-PRM-200	A	140.85	2.66E-03	2.71E-04	6.34	37.99	6.26E-05
PCB-03-PRM	PCB-03-PRM-000	C	141.15	2.04E-03	4.19E-04	16.51	142.70	2.32E-04

PCB-03-PRM	PCB-03-PRM-040	B1	140.85	4.14E-03	2.21E-03	247.42	480.48	1.86E-03
PCB-03-PRM	PCB-03-PRM-050	B1	140.85	3.60E-03	1.91E-03	233.54	494.84	1.57E-03
PCB-03-PRM	PCB-03-PRM-070	B1	140.85	3.93E-03	2.24E-03	250.66	501.17	1.84E-03
PCB-03-PRM	PCB-03-PRM-090	B2	140.85	3.44E-03	1.15E-03	56.23	365.45	9.05E-04
PCB-03-PRM	PCB-03-PRM-100	B2	140.84	7.99E-03	1.35E-03	14.86	99.98	6.45E-04
PCB-03-PRM	PCB-03-PRM-120	B2	140.84	5.12E-03	9.17E-04	17.37	153.48	5.07E-04
PCB-03-PRM	PCB-03-PRM-150	A	140.85	1.89E-03	3.91E-04	21.60	156.98	2.15E-04
PCB-01-P0	PCB-01-P0-000	C	117.52	3.19E-03	3.70E-04	6.39	32.88	6.79E-05
PCB-01-P0	PCB-01-P0-025	B	117.22	3.95E-03	1.41E-03	53.14	266.90	1.14E-03
PCB-01-P0	PCB-01-P0-035	B	117.22	4.39E-03	1.59E-03	54.95	286.20	1.23E-03
PCB-01-P0	PCB-01-P0-045	B	117.22	4.73E-03	2.00E-03	90.69	319.04	1.66E-03
PCB-01-P0	PCB-01-P0-055	B	117.22	4.77E-03	1.99E-03	82.66	323.41	1.64E-03
PCB-01-P0	PCB-01-P0-065	B	117.22	4.08E-03	1.59E-03	64.83	302.41	1.30E-03
PCB-01-P0	PCB-01-P0-080	A	117.22	2.77E-03	4.54E-04	10.96	63.25	1.67E-04
PCB-01-P0	PCB-01-P0-100	A	117.22	3.20E-03	2.51E-04	4.75	34.32	6.16E-05
PCB-01-P2	PCB-01-P2-000	C	103.05	3.61E-03	3.35E-04	4.80	31.95	7.65E-05
PCB-01-P2	PCB-01-P2-030	B1	102.75	6.56E-03	1.33E-03	17.49	217.62	8.80E-04
PCB-01-P2	PCB-01-P2-045	B1	102.75	7.35E-03	1.89E-03	27.27	312.56	1.37E-03
PCB-01-P2	PCB-01-P2-055	B1	102.75	7.83E-03	1.99E-03	26.47	322.06	1.46E-03
PCB-01-P2	PCB-01-P2-065	B1	102.75	6.83E-03	2.14E-03	37.72	356.89	1.69E-03
PCB-01-P2	PCB-01-P2-075	B2	102.75	6.47E-03	2.24E-03	48.84	388.01	1.79E-03
PCB-01-P2	PCB-01-P2-085	B2	102.75	6.10E-03	2.25E-03	52.84	392.77	1.83E-03
PCB-01-P2	PCB-01-P2-095	B2	102.75	6.83E-03	2.66E-03	71.54	399.93	2.18E-03
PCB-01-P2	PCB-01-P2-110	B2	102.75	5.24E-03	2.04E-03	56.64	465.63	1.55E-03
PCB-01-P2	PCB-01-P2-130	A	102.75	3.88E-03	8.81E-04	18.59	183.60	5.12E-04
PCB-02-P2	PCB-02-P2-000	C	103.25	1.24E-03	1.78E-04	9.37	36.04	3.60E-05
PCB-02-P2	PCB-02-P2-030	C	102.95	4.35E-03	1.10E-03	22.56	254.39	7.06E-04
PCB-02-P2	PCB-02-P2-050	B	102.75	4.22E-03	1.27E-03	30.81	320.80	9.08E-04
PCB-02-P2	PCB-02-P2-070	B	102.75	3.76E-03	1.64E-03	101.55	435.00	1.34E-03
PCB-02-P2	PCB-02-P2-090	B	102.75	4.83E-03	2.21E-03	143.67	446.11	1.81E-03
PCB-02-P2	PCB-02-P2-110	B	102.75	4.46E-03	2.15E-03	174.96	450.65	1.71E-03
PCB-02-P2	PCB-02-P2-130	B	102.75	3.93E-03	2.03E-03	210.83	467.96	1.64E-03
PCB-02-P2	PCB-02-P2-150	B	102.75	2.64E-03	1.38E-03	212.62	499.94	1.08E-03
PCB-02-P2	PCB-02-P2-170	AC	102.75	2.64E-03	1.13E-03	80.42	468.03	8.14E-04
PCB-02-RM	PCB-02-RM-000	C	128.72	8.32E-03	4.50E-04	3.44	28.19	9.15E-05
PCB-02-RM	PCB-02-RM-030	B	128.42	5.26E-03	1.81E-03	43.10	228.85	1.36E-03
PCB-02-RM	PCB-02-RM-050	B	128.42	7.35E-03	2.49E-03	46.69	235.40	1.91E-03
PCB-02-RM	PCB-02-RM-060	B	128.42	5.58E-03	1.79E-03	38.42	249.63	1.28E-03
PCB-02-RM	PCB-02-RM-070	B	128.42	5.77E-03	1.93E-03	46.19	264.85	1.53E-03
PCB-02-RM	PCB-02-RM-090	B	128.42	6.58E-03	2.34E-03	55.06	291.69	1.89E-03
PCB-02-RM	PCB-02-RM-110	B	128.42	5.32E-03	2.04E-03	60.00	306.42	1.69E-03

PCB-02-RM	PCB-02-RM-130	AB	128.42	4.88E-03	1.39E-03	26.20	248.34	1.05E-03
PCB-02-RM	PCB-02-RM-150	A	128.42	4.13E-03	5.22E-04	7.63	49.88	1.76E-04
PCB-02-TRA	PCB-02-TRA-000	C	66.35	4.37E-03	3.68E-04	5.21	31.26	6.76E-05
PCB-02-TRA	PCB-02-TRA-020	B1	66.15	9.29E-03	1.43E-03	13.68	66.27	5.90E-04
PCB-02-TRA	PCB-02-TRA-040	B1	66.15	8.79E-03	2.06E-03	22.31	174.60	1.26E-03
PCB-02-TRA	PCB-02-TRA-060	B2	66.15	6.23E-03	2.31E-03	59.63	273.61	1.79E-03
PCB-02-TRA	PCB-02-TRA-080	B2	66.15	5.39E-03	2.43E-03	107.99	291.32	1.96E-03
PCB-02-TRA	PCB-02-TRA-100	B2	66.15	5.48E-03	2.59E-03	122.63	317.75	2.13E-03
PCB-02-TRA	PCB-02-TRA-120	B2	66.15	6.10E-03	2.84E-03	123.09	295.36	2.33E-03
PCB-02-TRA	PCB-02-TRA-140	AB	66.15	5.13E-03	2.00E-03	53.08	333.27	1.53E-03
PCB-02-TRA	PCB-02-TRA-160	A	66.16	2.10E-03	8.04E-04	54.90	328.41	5.55E-04
PCB-02-TRA	PCB-02-TRA-180	A	66.16	8.05E-04	2.07E-04	23.40	80.84	7.93E-05
PCB-03-TRA	PCB-03-TRA-000	C	66.45	3.72E-03	2.97E-04	5.07	31.39	6.09E-05
PCB-03-TRA	PCB-03-TRA-030	B	66.15	1.42E-02	2.00E-03	12.37	50.52	6.80E-04
PCB-03-TRA	PCB-03-TRA-050	B	66.15	9.63E-03	1.98E-03	18.75	113.21	1.02E-03
PCB-03-TRA	PCB-03-TRA-070	B	66.16	8.62E-03	2.56E-03	35.52	233.69	1.80E-03
PCB-03-TRA	PCB-03-TRA-090	B	66.15	9.74E-03	2.73E-03	32.52	213.20	1.83E-03
PCB-03-TRA	PCB-03-TRA-100	B	66.16	8.43E-03	2.40E-03	32.07	206.93	1.59E-03
PCB-03-TRA	PCB-03-TRA-110	A	66.16	1.26E-03	2.63E-04	15.69	67.33	9.85E-05
PCB-01-RM	PCB-01-RM-010	C	128.52	2.87E-03	3.26E-04	6.64	34.18	7.17E-05
PCB-01-RM	PCB-01-RM-025	B	128.41	6.04E-03	1.99E-03	39.09	246.89	1.49E-03
PCB-01-RM	PCB-01-RM-035	B	128.41	8.18E-03	2.43E-03	33.24	244.79	1.76E-03
PCB-01-RM	PCB-01-RM-045	B	128.41	6.21E-03	2.20E-03	50.47	289.39	1.73E-03
PCB-01-RM	PCB-01-RM-055	B	128.41	5.85E-03	1.95E-03	41.48	288.00	1.55E-03
PCB-01-RM	PCB-01-RM-065	B	128.41	5.85E-03	2.19E-03	64.32	324.48	1.80E-03
PCB-01-RM	PCB-01-RM-075	B	128.42	4.08E-03	1.47E-03	41.86	284.01	1.18E-03
PCB-01-RM	PCB-01-RM-085	B	128.41	5.55E-03	1.61E-03	30.21	244.17	1.22E-03
PCB-01-RM	PCB-01-RM-095	B	128.42	4.00E-03	1.28E-03	30.24	267.23	9.65E-04
PCB-01-RM	PCB-01-RM-105	B	128.42	4.93E-03	1.48E-03	29.81	251.66	1.14E-03
PCB-01-RM	PCB-01-RM-120	A	128.42	2.92E-03	3.52E-04	6.82	38.52	9.06E-05
PCB-03-P2	PCB-03-P2-000	C	102.95	3.03E-03	2.67E-04	5.05	32.37	6.39E-05
PCB-03-P2	PCB-03-P2-020	B2	102.75	4.46E-03	9.61E-04	15.44	214.65	5.77E-04
PCB-03-P2	PCB-03-P2-040	B2	102.75	6.97E-03	1.32E-03	16.33	180.19	7.57E-04
PCB-03-P2	PCB-03-P2-060	B2	102.75	5.89E-03	1.57E-03	27.27	317.40	1.13E-03
PCB-03-P2	PCB-03-P2-080	B2	102.75	6.63E-03	1.73E-03	34.60	373.28	1.32E-03
PCB-03-P2	PCB-03-P2-100	B1	102.75	4.76E-03	1.56E-03	43.60	415.23	1.21E-03
PCB-03-P2	PCB-03-P2-120	B1	102.75	5.99E-03	1.90E-03	58.43	431.05	1.56E-03
PCB-03-P2	PCB-03-P2-130	B1	102.75	3.75E-03	1.50E-03	69.85	472.46	1.11E-03
PCB-03-P2	PCB-03-P2-140	B1	102.75	4.98E-03	1.59E-03	70.81	459.17	1.23E-03
PCB-03-P2	PCB-03-P2-160	AC	102.75	4.68E-03	1.79E-03	59.50	422.74	1.40E-03
PCB-01-P4	PCB-01-P4-000B	A/B	75.29	7.59E-03	1.32E-03	14.10	113.96	6.64E-04

PCB-01-P4	PCB-01-P4-020	A/B	75.09	8.77E-03	1.52E-03	14.89	163.95	8.64E-04
PCB-01-P4	PCB-01-P4-035	B2	74.98	5.78E-03	1.90E-03	53.50	385.82	1.42E-03
PCB-01-P4	PCB-01-P4-045	B2	74.98	1.09E-02	2.00E-03	47.72	402.27	1.51E-03
PCB-01-P4	PCB-01-P4-055	B2	74.98	5.41E-03	1.91E-03	52.22	419.30	1.40E-03
PCB-01-P4	PCB-01-P4-065	B2	74.98	5.32E-03	1.90E-03	56.08	461.67	1.34E-03
PCB-01-P4	PCB-01-P4-075	B2	74.98	5.11E-03	1.61E-03	53.95	442.22	1.17E-03
PCB-01-P4	PCB-01-P4-085	B2	74.99	4.99E-03	1.93E-03	69.63	452.27	1.39E-03
PCB-01-P4	PCB-01-P4-095	B2	74.99	3.81E-03	1.48E-03	55.81	503.47	1.02E-03
PCB-01-P4	PCB-01-P4-105	B1	74.99	3.25E-03	1.60E-03	100.77	525.09	1.05E-03
PCB-01-P4	PCB-01-P4-115	B1	74.99	3.79E-03	1.92E-03	178.01	510.04	1.44E-03
PCB-01-P4	PCB-01-P4-125	B1	74.99	2.82E-03	1.41E-03	159.99	503.66	1.03E-03
PCB-01-P4	PCB-01-P4-135	B1	74.99	3.09E-03	1.50E-03	191.10	502.04	1.19E-03
PCB-01-P4	PCB-01-P4-145	B1	74.99	3.30E-03	1.57E-03	169.82	496.90	1.17E-03
PCB-01-P4	PCB-01-P4-155	B1	74.99	3.37E-03	1.79E-03	371.37	498.90	1.33E-03
PCB-01-P4	PCB-01-P4-170	B1	74.99	2.90E-03	1.49E-03	158.42	501.64	1.08E-03
PCB-01-P4	PCB-01-P4-190	A	74.99	4.29E-03	7.20E-04	15.45	56.06	2.56E-04
PCB-01-TRA	PCB-01-TRA-000	C	66.55	9.18E-03	5.85E-04	4.14	28.26	9.71E-05
PCB-01-TRA	PCB-01-TRA-040	B	66.15	4.82E-03	1.80E-03	61.98	284.59	1.39E-03
PCB-01-TRA	PCB-01-TRA-050	B	66.15	5.87E-03	1.87E-03	41.58	256.28	1.41E-03
PCB-01-TRA	PCB-01-TRA-060	B	66.15	6.58E-03	2.19E-03	46.00	267.83	1.63E-03
PCB-01-TRA	PCB-01-TRA-075	B	66.15	5.89E-03	2.46E-03	87.90	297.03	1.94E-03
PCB-01-TRA	PCB-01-TRA-085	B	66.15	5.91E-03	2.39E-03	75.82	287.28	1.85E-03
PCB-01-TRA	PCB-01-TRA-100	B	66.15	7.40E-03	3.10E-03	90.80	304.50	2.49E-03
PCB-01-TRA	PCB-01-TRA-110	B	66.15	6.64E-03	2.72E-03	107.29	293.51	2.21E-03
PCB-01-TRA	PCB-01-TRA-120	B	66.15	5.16E-03	2.33E-03	102.17	288.72	1.90E-03
PCB-01-TRA	PCB-01-TRA-140	AC	66.15	1.94E-03	4.66E-04	19.37	130.90	2.39E-04
PCB-01-TRB	PCB-01-TRB-010	C	61.08	2.57E-03	2.39E-04	6.48	34.00	4.94E-05
PCB-01-TRB	PCB-01-TRB-040	B	60.78	4.27E-03	1.48E-03	67.86	249.34	1.11E-03
PCB-01-TRB	PCB-01-TRB-050	B	60.78	5.57E-03	1.92E-03	51.60	268.69	1.38E-03
PCB-01-TRB	PCB-01-TRB-060	B	60.78	6.09E-03	2.08E-03	51.31	275.98	1.52E-03
PCB-01-TRB	PCB-01-TRB-070	B	60.78	6.22E-03	1.56E-03	25.86	220.04	1.01E-03
PCB-01-TRB	PCB-01-TRB-080	B	60.78	5.15E-03	1.53E-03	30.44	241.27	1.06E-03
PCB-01-TRB	PCB-01-TRB-090	B	60.78	6.84E-03	2.31E-03	52.33	269.54	1.74E-03
PCB-01-TRB	PCB-01-TRB-100	A	60.78	3.77E-03	8.21E-04	18.10	187.15	4.68E-04
PCB-01-TRB	PCB-01-TRB-120	A	60.78	2.25E-03	3.85E-04	12.63	85.16	1.71E-04
PCB-01-UDRB	PCB-01-UDRB-000	C	93.13	1.48E-03	1.83E-04	8.33	33.87	3.66E-05
PCB-01-UDRB	PCB-01-UDRB-030	BL	92.83	1.21E-02	3.13E-03	29.16	225.13	2.04E-03
PCB-01-UDRB	PCB-01-UDRB-045	BL	92.83	1.30E-02	3.67E-03	32.80	253.76	2.44E-03
PCB-01-UDRB	PCB-01-UDRB-055	BL	92.83	9.66E-03	3.01E-03	41.24	298.92	2.23E-03
PCB-01-UDRB	PCB-01-UDRB-070	BL	92.83	1.05E-02	2.25E-03	22.21	192.44	1.34E-03
PCB-01-UDRB	PCB-01-UDRB-080	BL	92.83	1.17E-02	2.56E-03	20.32	134.47	1.43E-03

PCB-01-UDRB	PCB-01-UDRB-095	B2	92.83	1.62E-02	3.53E-03	20.96	123.85	1.91E-03
PCB-01-UDRB	PCB-01-UDRB-110	B2	92.83	1.42E-02	3.12E-03	21.15	131.57	1.73E-03
PCB-01-UDRB	PCB-01-UDRB-125	B2	92.83	1.37E-02	3.19E-03	23.32	161.69	1.91E-03
PCB-01-UDRB	PCB-01-UDRB-140	B2	92.84	6.36E-03	2.85E-03	99.51	242.11	2.30E-03
PCB-01-UDRB	PCB-01-UDRB-155	B1	92.84	5.87E-03	3.01E-03	148.11	284.74	2.55E-03
PCB-01-UDRB	PCB-01-UDRB-170	B1	92.84	5.20E-03	2.56E-03	168.44	451.45	2.16E-03
PCB-01-UDRB	PCB-01-UDRB-185	B1	92.83	7.33E-03	3.76E-03	144.81	273.42	3.22E-03
PCB-01-UDRB	PCB-01-UDRB-200	B1	92.84	5.45E-03	3.04E-03	259.62	473.96	2.59E-03
PCB-01-UDRB	PCB-01-UDRB-215	A	92.83	7.16E-03	2.62E-03	56.65	267.68	1.98E-03
PCB-01-UDRB	PCB-01-UDRB-230	A	92.84	1.26E-03	1.89E-04	9.27	32.93	2.77E-05
PCB-01-UDRB	PCB-01-UDRB-240	C	92.84	3.37E-03	5.47E-04	13.34	61.12	2.01E-04

Table B.5: Results for coercivity unmixing analysis of paleosol B horizons in core and outcrop. All parameters are displayed with standard deviations (sd) in adjacent column. MCD = meters composite depth. Units for B_h and DP are log base 10 mT. Skew factor, S, is unitless. TC = True contribution is a fraction of total remanence held by low or high coercivity component. LCC = low coecivity component. HCC = high coercivity component.

Specimen	**MCD**	**HCC**								**LCC**							
		Bh	*sd*	*DP*	*sd*	*S*	*sd*	*TC*	*sd*	*Bh*	*sd*	*DP*	*sd*	*S*	*sd*	*TC*	*sd*
TRB-025	60.78	2.77	0.03	0.41	0.02	1.00	0.06	0.68	0.07	1.50	0.05	0.46	0.02	0.74	0.05	0.32	0.06
TRB-045	60.53	2.69	0.03	0.38	0.01	1.02	0.07	0.56	0.04	1.45	0.02	0.40	0.01	0.70	0.04	0.44	0.03
TRB-065	60.33	2.67	0.02	0.33	0.01	1.04	0.06	0.74	0.11	1.58	0.08	0.50	0.03	0.66	0.06	0.26	0.10
TRB-085	60.13	2.74	0.01	0.30	0.01	1.02	0.05	0.75	0.12	1.79	0.10	0.52	0.04	0.60	0.08	0.25	0.12
TRB-095	60.035	2.75	0.02	0.30	0.01	0.98	0.05	0.70	0.07	1.64	0.07	0.56	0.03	0.67	0.07	0.30	0.08
TRB-105	59.92	2.75	0.02	0.29	0.01	0.98	0.05	0.69	0.09	1.65	0.08	0.56	0.04	0.66	0.07	0.31	0.10
PCB-01-TRB-040	60.78	2.54	0.01	0.34	0.01	1.03	0.04	0.81	0.06	1.47	0.06	0.45	0.02	0.60	0.06	0.19	0.06
PCB-01-TRB-050	60.68	2.66	0.03	0.35	0.01	1.09	0.06	0.74	0.12	1.49	0.09	0.49	0.04	0.63	0.06	0.26	0.10
PCB-01-TRB-060	60.58	2.63	0.02	0.32	0.01	1.03	0.04	0.74	0.09	1.55	0.08	0.51	0.04	0.73	0.09	0.26	0.09
PCB-01-TRB-070	60.48	2.67	0.02	0.36	0.01	1.03	0.04	0.64	0.08	1.51	0.06	0.50	0.03	0.85	0.06	0.36	0.09
PCB-01-TRB-080	60.38	2.62	0.02	0.33	0.01	1.03	0.04	0.68	0.08	1.53	0.07	0.52	0.04	0.82	0.08	0.32	0.09
PCB-01-TRB-090	60.28	2.60	0.02	0.31	0.01	1.03	0.03	0.74	0.10	1.58	0.08	0.52	0.03	0.68	0.07	0.26	0.09
TRA-035	66.15	2.56	0.02	0.31	0.01	1.11	0.04	0.65	0.10	1.51	0.06	0.45	0.03	0.70	0.06	0.35	0.09
TRA-050	66	2.64	0.02	0.31	0.01	1.02	0.05	0.74	0.10	1.57	0.08	0.51	0.04	0.65	0.06	0.26	0.09
TRA-060	65.9	2.65	0.01	0.32	0.01	0.99	0.04	0.82	0.04	1.54	0.07	0.49	0.02	0.55	0.07	0.18	0.06
TRA-065	65.85	2.66	0.01	0.29	0.01	1.01	0.04	0.82	0.10	1.74	0.12	0.49	0.05	0.58	0.11	0.18	0.10

TRA-080	65.7	2.78	0.02	0.26	0.01	1.02	0.06	0.82	0.07	1.84	0.12	0.52	0.06	0.44	0.14	0.18	0.09
PCB-01-TRA-040	66.15	2.63	0.01	0.29	0.01	1.03	0.04	0.72	0.11	1.66	0.09	0.55	0.04	0.64	0.09	0.28	0.11
PCB-01-TRA-050	66.05	2.59	0.01	0.29	0.01	1.00	0.02	0.66	0.11	1.70	0.09	0.58	0.04	0.76	0.09	0.34	0.12
PCB-01-TRA-060	65.95	2.62	0.01	0.29	0.01	1.01	0.03	0.67	0.12	1.69	0.10	0.59	0.05	0.73	0.09	0.33	0.12
PCB-01-TRA-075	65.8	2.60	0.01	0.30	0.01	1.00	0.03	0.80	0.06	1.56	0.07	0.49	0.02	0.56	0.06	0.20	0.07
PCB-01-TRA-085	65.7	2.61	0.01	0.30	0.01	1.01	0.03	0.77	0.08	1.59	0.07	0.52	0.03	0.59	0.07	0.23	0.08
PCB-01-TRA-100	65.55	2.61	0.01	0.29	0.01	1.00	0.03	0.79	0.07	1.58	0.08	0.52	0.02	0.57	0.07	0.21	0.07
PCB-01-TRA-110	65.45	2.57	0.01	0.30	0.01	0.97	0.03	0.84	0.05	1.53	0.11	0.49	0.04	0.55	0.07	0.16	0.06
PCB-01-TRA-120	65.35	2.58	0.01	0.30	0.01	0.99	0.03	0.80	0.12	1.63	0.12	0.50	0.04	0.63	0.09	0.20	0.11
PCB-02-TRA-040	65.95	2.58	0.02	0.34	0.01	1.03	0.03	0.60	0.10	1.50	0.06	0.48	0.04	0.88	0.07	0.40	0.09
PCB-02-TRA-060	65.75	2.59	0.01	0.29	0.01	0.99	0.04	0.74	0.10	1.60	0.09	0.55	0.03	0.66	0.08	0.26	0.10
PCB-02-TRA-080	65.55	2.57	0.01	0.30	0.00	0.97	0.03	0.83	0.05	1.58	0.14	0.49	0.08	0.60	0.14	0.17	0.07
PCB-02-TRA-100	65.35	2.61	0.01	0.29	0.01	0.99	0.05	0.83	0.08	1.59	0.10	0.50	0.03	0.55	0.09	0.17	0.08
PCB-02-TRA-120	65.15	2.57	0.01	0.29	0.00	0.98	0.03	0.84	0.05	1.57	0.09	0.48	0.04	0.54	0.11	0.16	0.06
PCB-03-TRA-050	65.95	2.55	0.03	0.37	0.01	1.03	0.04	0.51	0.13	1.49	0.06	0.47	0.03	0.88	0.06	0.49	0.12
PCB-03-TRA-070	65.75	2.60	0.02	0.32	0.01	0.99	0.03	0.68	0.08	1.53	0.07	0.50	0.04	0.85	0.07	0.32	0.08
PCB-03-TRA-090	65.55	2.57	0.02	0.33	0.01	1.01	0.03	0.67	0.08	1.52	0.06	0.50	0.03	0.85	0.07	0.33	0.08
PCB-03-TRA-100	65.45	2.57	0.02	0.33	0.01	1.01	0.03	0.66	0.09	1.52	0.06	0.50	0.04	0.86	0.06	0.34	0.09

P4-050	74.99	2.85	0.02	0.20	0.01	1.02	0.07	0.60	0.07	1.81	0.12	0.77	0.06	0.55	0.15	0.40	0.10
P4-075	74.74	2.82	0.03	0.21	0.01	0.93	0.09	0.74	0.11	2.04	0.19	0.52	0.07	0.43	0.13	0.26	0.14
P4-100	74.49	2.80	0.02	0.21	0.01	0.97	0.06	0.77	0.08	1.80	0.12	0.57	0.05	0.36	0.10	0.23	0.09
P4-120	74.29	2.85	0.03	0.20	0.01	0.86	0.11	0.75	0.09	1.88	0.10	0.52	0.04	0.32	0.08	0.25	0.11
P4-140	74.09	2.87	0.03	0.20	0.02	0.88	0.10	0.72	0.09	2.02	0.13	0.52	0.05	0.34	0.09	0.28	0.12
PCB-01-P4-035	74.94	2.73	0.01	0.23	0.01	0.88	0.05	0.72	0.12	1.73	0.10	0.55	0.05	0.35	0.07	0.28	0.11
PCB-01-P4-045	74.84	2.75	0.02	0.22	0.01	0.92	0.07	0.70	0.12	1.82	0.14	0.55	0.06	0.35	0.10	0.30	0.13
PCB-01-P4-055	74.74	2.80	0.02	0.24	0.01	0.95	0.07	0.68	0.12	1.86	0.17	0.60	0.07	0.48	0.17	0.32	0.14
PCB-01-P4-065	74.64	2.83	0.03	0.21	0.01	0.94	0.09	0.69	0.09	1.80	0.12	0.61	0.05	0.34	0.11	0.31	0.10
PCB-01-P4-075	74.54	2.80	0.02	0.20	0.01	0.84	0.06	0.64	0.11	1.96	0.16	0.65	0.07	0.51	0.16	0.36	0.15
PCB-01-P4-085	74.44	2.81	0.03	0.22	0.01	0.93	0.09	0.71	0.10	1.82	0.12	0.56	0.06	0.29	0.08	0.29	0.11
PCB-01-P4-095	74.34	2.85	0.02	0.20	0.01	0.98	0.07	0.69	0.06	1.75	0.10	0.68	0.06	0.34	0.11	0.31	0.08
PCB-01-P4-105	74.24	2.86	0.02	0.20	0.01	0.98	0.07	0.74	0.07	1.77	0.10	0.62	0.05	0.32	0.08	0.26	0.07
PCB-01-P4-115	74.14	2.82	0.01	0.21	0.01	0.95	0.06	0.78	0.06	1.83	0.11	0.57	0.06	0.33	0.09	0.22	0.09
PCB-01-P4-125	74.04	2.82	0.01	0.20	0.01	0.99	0.06	0.76	0.07	1.82	0.11	0.58	0.05	0.31	0.09	0.24	0.09
PCB-01-P4-135	73.94	2.81	0.02	0.20	0.01	0.95	0.07	0.78	0.07	1.80	0.13	0.58	0.06	0.34	0.11	0.22	0.09
PCB-01-P4-145	73.84	2.80	0.01	0.20	0.01	0.96	0.07	0.78	0.06	1.82	0.10	0.56	0.06	0.34	0.10	0.22	0.09
PCB-01-P4-155	73.74	2.81	0.02	0.20	0.01	0.99	0.08	0.77	0.07	1.88	0.13	0.55	0.05	0.33	0.12	0.23	0.10
PCB-01-P4-170	73.59	2.81	0.01	0.20	0.01	0.99	0.06	0.77	0.06	1.83	0.12	0.58	0.05	0.33	0.09	0.23	0.08
PCB-01-UDRB-030	92.83	2.68	0.02	0.29	0.01	0.98	0.04	0.57	0.10	1.62	0.07	0.52	0.04	0.85	0.09	0.43	0.10
PCB-01-UDRB-045	92.68	2.73	0.02	0.28	0.01	1.00	0.05	0.55	0.08	1.69	0.07	0.54	0.04	0.90	0.09	0.45	0.09
PCB-01-UDRB-055	92.58	2.69	0.01	0.28	0.00	1.01	0.03	0.65	0.05	1.71	0.08	0.58	0.05	0.92	0.10	0.35	0.08
PCB-01-UDRB-070	92.43	2.70	0.02	0.29	0.01	0.98	0.05	0.52	0.07	1.57	0.05	0.50	0.03	0.90	0.08	0.48	0.07
PCB-01-UDRB-080	92.33	2.52	0.02	0.33	0.01	1.03	0.03	0.54	0.11	1.51	0.06	0.47	0.03	0.83	0.05	0.46	0.11

PCB-01-UDRB-095	92.18	2.53	0.03	0.35	0.02	0.99	0.05	0.55	0.11	1.48	0.05	0.44	0.03	0.81	0.05	0.45	0.10
PCB-01-UDRB-110	92.03	2.53	0.02	0.32	0.01	1.07	0.03	0.53	0.09	1.52	0.05	0.46	0.03	0.86	0.06	0.47	0.08
PCB-01-UDRB-125	91.88	2.55	0.02	0.32	0.01	1.04	0.03	0.57	0.09	1.52	0.05	0.47	0.03	0.84	0.06	0.43	0.09
PCB-01-UDRB-140	91.73	2.48	0.01	0.28	0.00	1.08	0.03	0.83	0.08	1.56	0.08	0.46	0.03	0.56	0.08	0.17	0.07
PCB-01-UDRB-155	91.58	2.53	0.01	0.27	0.00	1.06	0.03	0.85	0.10	1.64	0.12	0.47	0.05	0.53	0.12	0.15	0.09
PCB-01-UDRB-170	91.43	2.78	0.02	0.24	0.01	0.95	0.06	0.79	0.08	1.75	0.12	0.57	0.06	0.34	0.11	0.21	0.09
PCB-01-UDRB-185	91.28	2.51	0.01	0.27	0.00	1.03	0.02	0.86	0.09	1.60	0.12	0.47	0.05	0.55	0.11	0.14	0.09
PCB-01-UDRB-200	91.13	2.77	0.01	0.23	0.01	0.93	0.05	0.83	0.07	1.80	0.08	0.49	0.05	0.30	0.09	0.17	0.08
UDRB-050	92.46	2.69	0.03	0.36	0.01	1.16	0.07	0.59	0.04	1.45	0.03	0.42	0.01	0.77	0.05	0.41	0.04
UDRB-080	92.16	2.67	0.02	0.32	0.01	1.09	0.06	0.57	0.04	1.46	0.03	0.42	0.02	0.79	0.06	0.43	0.04
UDRB-100	91.9	2.68	0.02	0.32	0.02	1.08	0.06	0.61	0.04	1.47	0.04	0.44	0.02	0.82	0.07	0.39	0.05
UDRB-120	91.7	2.71	0.01	0.29	0.00	1.04	0.03	0.71	0.05	1.60	0.09	0.57	0.05	0.89	0.09	0.29	0.07
UDRB-140	91.46	2.73	0.01	0.28	0.01	1.02	0.03	0.72	0.06	1.69	0.10	0.62	0.06	0.85	0.12	0.28	0.08
UDRB-160	91.27	2.69	0.01	0.26	0.00	1.03	0.03	0.83	0.06	1.65	0.08	0.52	0.04	0.39	0.06	0.17	0.07
UDRB-180	91.06	2.72	0.02	0.25	0.01	1.05	0.07	0.83	0.07	1.77	0.11	0.50	0.06	0.39	0.10	0.17	0.08
UDRB-200	90.83	2.73	0.01	0.26	0.01	1.02	0.04	0.84	0.05	1.62	0.10	0.56	0.06	0.33	0.09	0.16	0.08
UDRB-220	90.62	2.73	0.01	0.25	0.00	1.04	0.04	0.83	0.06	1.71	0.12	0.54	0.06	0.39	0.12	0.17	0.08
P2-060	102.55	2.80	0.02	0.22	0.01	0.88	0.08	0.78	0.08	1.85	0.14	0.50	0.06	0.35	0.10	0.22	0.10
P2-080	102.37	2.85	0.03	0.22	0.02	0.87	0.11	0.75	0.11	1.95	0.12	0.48	0.05	0.32	0.07	0.25	0.12
P2-105	102.1	2.86	0.05	0.22	0.02	0.82	0.11	0.69	0.18	2.06	0.15	0.44	0.05	0.34	0.09	0.31	0.18
P2-125	101.9	2.83	0.03	0.22	0.01	0.88	0.09	0.72	0.17	2.02	0.12	0.42	0.04	0.37	0.08	0.28	0.15
P2-145	101.7	2.88	0.04	0.22	0.02	0.91	0.12	0.70	0.11	2.00	0.11	0.47	0.06	0.33	0.09	0.30	0.13
P2-155	101.6	2.84	0.03	0.21	0.02	0.81	0.11	0.73	0.12	1.95	0.12	0.50	0.05	0.30	0.07	0.27	0.13
PCB-01-P2-030	102.75	2.61	0.02	0.31	0.01	1.03	0.03	0.63	0.09	1.48	0.07	0.52	0.04	0.82	0.08	0.37	0.08

PCB-01-P2-045	102.6	2.69	0.01	0.26	0.00	0.98	0.03	0.67	0.06	1.62	0.09	0.61	0.05	0.88	0.11	0.33	0.08
PCB-01-P2-055	102.5	2.70	0.01	0.26	0.00	0.97	0.04	0.67	0.06	1.62	0.08	0.61	0.05	0.91	0.10	0.33	0.08
PCB-01-P2-065	102.4	2.71	0.01	0.25	0.01	1.01	0.04	0.71	0.09	1.68	0.12	0.66	0.06	0.53	0.15	0.29	0.10
PCB-01-P2-075	102.3	2.72	0.01	0.24	0.01	1.01	0.03	0.76	0.08	1.60	0.12	0.63	0.06	0.40	0.13	0.24	0.09
PCB-01-P2-085	102.2	2.72	0.01	0.24	0.01	1.01	0.05	0.73	0.09	1.80	0.15	0.67	0.08	0.57	0.17	0.27	0.11
PCB-01-P2-095	102.1	2.72	0.03	0.25	0.02	0.97	0.07	0.79	0.06	1.63	0.17	0.59	0.09	0.37	0.14	0.21	0.08
PCB-01-P2-110	101.95	2.83	0.02	0.23	0.01	1.07	0.06	0.71	0.07	1.87	0.12	0.65	0.06	0.46	0.16	0.29	0.10
PCB-02-P2-050	102.75	2.76	0.02	0.27	0.00	1.05	0.05	0.62	0.07	1.67	0.07	0.64	0.04	0.76	0.09	0.38	0.08
PCB-02-P2-070	102.55	2.79	0.02	0.23	0.01	1.02	0.07	0.74	0.09	1.81	0.11	0.56	0.06	0.39	0.13	0.26	0.11
PCB-02-P2-090	102.35	2.79	0.02	0.23	0.01	0.97	0.07	0.75	0.11	1.89	0.14	0.49	0.05	0.36	0.11	0.25	0.13
PCB-02-P2-110	102.15	2.81	0.03	0.22	0.01	0.92	0.07	0.72	0.16	1.95	0.12	0.44	0.04	0.34	0.06	0.28	0.14
PCB-02-P2-130	102.35	2.82	0.03	0.22	0.01	0.94	0.09	0.74	0.17	2.02	0.11	0.39	0.04	0.37	0.08	0.26	0.16
PCB-02-P2-150	101.75	2.83	0.02	0.20	0.01	0.95	0.07	0.74	0.09	1.89	0.13	0.53	0.06	0.33	0.10	0.26	0.10
PCB-03-P2-020	102.75	2.74	0.03	0.43	0.01	1.12	0.07	0.66	0.04	1.36	0.03	0.48	0.01	0.67	0.04	0.34	0.04
PCB-03-P2-040	102.55	2.83	0.06	0.52	0.03	1.01	0.09	0.65	0.02	1.32	0.02	0.45	0.00	0.68	0.02	0.35	0.02
PCB-03-P2-060	102.35	2.72	0.01	0.29	0.00	1.03	0.04	0.68	0.06	1.56	0.07	0.60	0.05	0.78	0.09	0.32	0.07
PCB-03-P2-080	102.15	2.74	0.01	0.25	0.01	1.06	0.04	0.71	0.09	1.62	0.09	0.66	0.05	0.44	0.11	0.29	0.09
PCB-03-P2-100	101.95	2.77	0.02	0.23	0.01	1.00	0.05	0.69	0.09	1.80	0.13	0.69	0.06	0.56	0.14	0.31	0.12
PCB-03-P2-120	101.75	2.79	0.02	0.24	0.01	0.99	0.07	0.75	0.09	1.76	0.11	0.56	0.05	0.32	0.09	0.25	0.10
PCB-03-P2-130	101.65	2.81	0.01	0.21	0.01	0.92	0.06	0.73	0.09	1.83	0.12	0.56	0.05	0.33	0.09	0.27	0.10
PCB-03-P2-140	101.55	2.79	0.02	0.21	0.01	0.92	0.07	0.74	0.11	1.82	0.16	0.57	0.06	0.36	0.10	0.26	0.11
LDRA-040	108.27	2.58	0.05	0.56	0.02	1.04	0.07	0.49	0.05	1.30	0.01	0.41	0.00	0.63	0.01	0.51	0.05
LDRA-060	108.06	2.63	0.02	0.38	0.01	1.35	0.05	0.49	0.07	1.45	0.04	0.48	0.02	0.77	0.04	0.51	0.07
LDRA-080	107.87	2.44	0.04	0.58	0.02	0.89	0.06	0.46	0.05	1.31	0.01	0.40	0.00	0.63	0.01	0.54	0.04
LDRA-095	107.72	2.63	0.03	0.42	0.01	1.11	0.09	0.51	0.05	1.36	0.02	0.43	0.01	0.66	0.03	0.49	0.04

LDRA-120	107.48	2.62	0.04	0.46	0.01	1.07	0.08	0.50	0.05	1.33	0.02	0.42	0.01	0.65	0.02	0.50	0.04
LDRA-140	107.28	2.66	0.02	0.35	0.01	1.17	0.05	0.53	0.06	1.47	0.05	0.52	0.03	0.83	0.06	0.47	0.07
PCB-01-LDRA-040	108.27	2.65	0.04	0.42	0.02	1.32	0.07	0.46	0.10	1.51	0.05	0.45	0.02	0.81	0.04	0.54	0.13
PCB-01-LDRA-050	108.17	2.66	0.08	0.65	0.05	1.22	0.12	0.59	0.09	1.34	0.03	0.40	0.00	0.70	0.03	0.41	0.10
PCB-01-LDRA-060	108.07	2.57	0.06	0.57	0.04	1.27	0.10	0.55	0.14	1.36	0.04	0.40	0.01	0.69	0.03	0.45	0.13
PCB-01-LDRA-070	107.97	2.66	0.07	0.44	0.05	1.35	0.14	0.33	0.15	1.53	0.06	0.43	0.02	0.81	0.07	0.67	0.18
PCB-01-LDRA-080	107.87	2.61	0.05	0.41	0.03	1.20	0.08	0.42	0.12	1.48	0.04	0.44	0.02	0.80	0.04	0.58	0.14
PCB-01-LDRA-090	107.77	2.60	0.02	0.34	0.01	0.99	0.04	0.52	0.09	1.52	0.04	0.47	0.02	0.84	0.05	0.48	0.09
PCB-01-LDRA-100	107.67	2.70	0.02	0.34	0.01	1.04	0.04	0.58	0.10	1.58	0.06	0.50	0.04	0.85	0.07	0.42	0.09
PCB-01-LDRA-110	107.57	2.66	0.02	0.30	0.01	0.97	0.04	0.59	0.08	1.60	0.06	0.50	0.03	0.85	0.07	0.41	0.10
PCB-01-LDRA-120	107.47	2.69	0.02	0.27	0.01	0.89	0.04	0.56	0.06	1.63	0.05	0.52	0.03	0.93	0.06	0.44	0.07
PCB-01-LDRA-130	107.37	2.69	0.01	0.27	0.01	0.91	0.03	0.59	0.06	1.69	0.08	0.58	0.05	0.97	0.09	0.41	0.07
PCB-01-LDRA-140	107.27	2.69	0.02	0.25	0.01	0.92	0.06	0.68	0.09	1.69	0.09	0.60	0.05	0.77	0.13	0.32	0.11
PCB-01-LDRA-150	107.17	2.68	0.01	0.27	0.01	0.92	0.04	0.58	0.10	1.66	0.09	0.56	0.05	0.95	0.11	0.42	0.10
PCB-01-LDRA-160	107.07	2.53	0.03	0.36	0.01	1.08	0.07	0.65	0.11	1.44	0.05	0.42	0.02	0.69	0.04	0.35	0.09
PCB-01-P0-025	117.22	2.58	0.01	0.31	0.01	1.08	0.03	0.77	0.11	1.58	0.11	0.51	0.04	0.60	0.07	0.23	0.10
PCB-01-P0-035	117.12	2.65	0.02	0.31	0.01	1.10	0.03	0.73	0.12	1.64	0.12	0.57	0.05	0.62	0.09	0.27	0.12
PCB-01-P0-045	117.02	2.62	0.01	0.28	0.01	1.03	0.03	0.81	0.11	1.62	0.11	0.51	0.04	0.54	0.07	0.19	0.10
PCB-01-P0-055	116.92	2.64	0.01	0.28	0.00	1.03	0.04	0.77	0.13	1.73	0.14	0.55	0.06	0.63	0.12	0.23	0.12

PCB-01-P0-065	116.82	2.60	0.01	0.27	0.00	1.03	0.03	0.78	0.11	1.64	0.10	0.52	0.04	0.57	0.11	0.22	0.10
P0-085	116.66	2.96	0.08	0.70	0.10	1.08	0.18	0.39	0.09	1.48	0.01	0.34	0.01	0.66	0.01	0.61	0.13
P0-110	116.41	2.99	0.08	0.60	0.06	1.14	0.08	0.35	0.02	1.49	0.00	0.34	0.00	0.68	0.01	0.65	0.02
P0-120	116.27	2.75	0.05	0.40	0.03	0.91	0.09	0.41	0.01	1.49	0.00	0.35	0.00	0.70	0.01	0.59	0.01
P0-140	116.1	2.90	0.11	0.60	0.11	0.88	0.18	0.31	0.07	1.46	0.00	0.35	0.01	0.67	0.01	0.69	0.08
P0-165	115.86	2.82	0.07	0.57	0.05	1.00	0.09	0.47	0.04	1.42	0.01	0.38	0.00	0.64	0.01	0.53	0.03
RM-055	128.42	2.56	0.02	0.34	0.01	1.15	0.05	0.63	0.07	1.40	0.05	0.48	0.02	0.70	0.06	0.37	0.07
RM-075	128.21	2.52	0.02	0.30	0.01	1.11	0.03	0.64	0.17	1.58	0.11	0.54	0.04	0.64	0.06	0.36	0.16
RM-085	128.12	2.54	0.01	0.30	0.01	1.17	0.03	0.51	0.11	1.63	0.08	0.59	0.04	0.87	0.08	0.49	0.11
RM-095	128.03	2.53	0.02	0.31	0.01	1.11	0.04	0.63	0.11	1.51	0.07	0.53	0.04	0.76	0.07	0.37	0.11
RM-110	127.88	2.56	0.01	0.29	0.00	1.07	0.03	0.74	0.06	1.54	0.07	0.56	0.03	0.66	0.09	0.26	0.07
PCB-01-RM-025	128.37	2.57	0.01	0.30	0.01	1.07	0.03	0.72	0.09	1.58	0.07	0.53	0.03	0.65	0.07	0.28	0.09
PCB-01-RM-035	128.27	2.58	0.01	0.31	0.01	1.04	0.04	0.72	0.07	1.50	0.06	0.50	0.03	0.73	0.08	0.28	0.07
PCB-01-RM-045	128.17	2.61	0.01	0.29	0.00	1.04	0.02	0.76	0.07	1.62	0.08	0.55	0.03	0.63	0.08	0.24	0.07
PCB-01-RM-055	128.07	2.62	0.01	0.28	0.00	1.03	0.03	0.72	0.10	1.67	0.11	0.61	0.06	0.71	0.11	0.28	0.11
PCB-01-RM-065	127.97	2.64	0.01	0.27	0.01	1.03	0.03	0.78	0.12	1.64	0.13	0.57	0.06	0.55	0.10	0.22	0.10
PCB-01-RM-075	127.87	2.59	0.01	0.28	0.00	1.06	0.03	0.76	0.10	1.58	0.10	0.55	0.04	0.59	0.08	0.24	0.09
PCB-01-RM-085	127.77	2.54	0.02	0.30	0.01	1.04	0.04	0.74	0.09	1.47	0.08	0.52	0.03	0.65	0.07	0.26	0.09
PCB-01-RM-095	127.67	2.59	0.02	0.30	0.01	1.05	0.03	0.74	0.10	1.50	0.08	0.53	0.04	0.68	0.08	0.26	0.10
PCB-01-RM-105	127.57	2.56	0.01	0.30	0.01	1.05	0.03	0.76	0.08	1.46	0.07	0.51	0.03	0.63	0.06	0.24	0.08
PCB-02-RM-030	128.42	2.51	0.01	0.30	0.01	1.07	0.03	0.75	0.12	1.55	0.09	0.49	0.04	0.65	0.09	0.25	0.12
PCB-02-RM-050	128.22	2.54	0.02	0.31	0.01	1.12	0.05	0.74	0.11	1.56	0.09	0.49	0.04	0.62	0.09	0.26	0.11
PCB-02-RM-070	128.02	2.56	0.01	0.28	0.00	1.05	0.02	0.76	0.10	1.63	0.09	0.54	0.04	0.60	0.09	0.24	0.10
PCB-02-RM-090	127.82	2.59	0.01	0.27	0.00	1.03	0.02	0.76	0.12	1.64	0.14	0.57	0.06	0.60	0.10	0.24	0.10
PCB-02-RM-110	127.62	2.60	0.01	0.26	0.01	1.04	0.03	0.76	0.13	1.71	0.16	0.57	0.07	0.58	0.12	0.24	0.12
PRM-065	140.75	2.90	0.05	0.31	0.03	0.68	0.12	0.60	0.05	1.55	0.05	0.59	0.03	0.85	0.06	0.40	0.06
PRM-085	140.52	2.81	0.06	0.45	0.06	0.83	0.08	0.57	0.11	1.47	0.07	0.49	0.02	0.79	0.06	0.43	0.12
PRM-095	140.42	2.79	0.02	0.29	0.01	0.99	0.06	0.73	0.11	1.80	0.11	0.58	0.05	0.56	0.11	0.27	0.11
PRM-125	140.12	2.76	0.01	0.25	0.01	0.92	0.05	0.83	0.08	1.83	0.10	0.47	0.04	0.43	0.09	0.17	0.09

PRM-145	139.92	2.60	0.01	0.25	0.00	1.01	0.03	0.89	0.08	1.76	0.12	0.42	0.05	0.46	0.10	0.11	0.08
PRM-165	139.71	2.73	0.02	0.26	0.01	0.90	0.06	0.80	0.12	1.94	0.14	0.50	0.06	0.60	0.12	0.20	0.13
PCB-01-PRM-035	140.7	2.55	0.01	0.26	0.00	1.01	0.03	0.83	0.10	1.73	0.14	0.48	0.06	0.56	0.10	0.17	0.11
PCB-01-PRM-050	140.55	2.79	0.03	0.24	0.01	0.88	0.07	0.80	0.08	1.84	0.13	0.53	0.06	0.42	0.13	0.20	0.10
PCB-01-PRM-060	140.45	2.71	0.02	0.30	0.01	0.95	0.05	0.73	0.12	1.74	0.11	0.57	0.05	0.66	0.11	0.27	0.12
PCB-01-PRM-070	140.35	2.70	0.02	0.31	0.01	0.94	0.05	0.69	0.09	1.64	0.08	0.57	0.04	0.79	0.10	0.31	0.10
PCB-01-PRM-080	140.25	2.73	0.03	0.42	0.01	1.06	0.05	0.61	0.05	1.41	0.03	0.46	0.01	0.80	0.04	0.39	0.05
PCB-01-PRM-090	140.15	2.79	0.05	0.43	0.03	0.93	0.08	0.56	0.08	1.44	0.04	0.47	0.02	0.85	0.05	0.44	0.08
PCB-02-PRM-040	140.75	2.74	0.03	0.31	0.01	0.99	0.07	0.65	0.08	1.66	0.08	0.54	0.04	0.79	0.09	0.35	0.10
PCB-02-PRM-050	140.65	2.78	0.02	0.29	0.01	1.08	0.06	0.73	0.10	1.71	0.08	0.57	0.03	0.51	0.09	0.27	0.10
PCB-02-PRM-060	140.55	2.76	0.02	0.30	0.01	1.00	0.04	0.57	0.08	1.67	0.07	0.57	0.04	0.94	0.08	0.43	0.08
PCB-02-PRM-100	140.15	2.75	0.02	0.27	0.01	1.05	0.05	0.72	0.10	1.70	0.09	0.62	0.04	0.56	0.10	0.28	0.10
PCB-02-PRM-120	139.95	2.78	0.03	0.28	0.01	1.01	0.07	0.64	0.09	1.60	0.09	0.62	0.05	0.65	0.09	0.36	0.10
PCB-02-PRM-160	139.55	2.73	0.02	0.29	0.01	1.02	0.04	0.67	0.07	1.57	0.07	0.58	0.04	0.76	0.10	0.33	0.07
PCB-03-PRM-040	140.75	2.79	0.01	0.24	0.01	0.86	0.05	0.83	0.11	1.91	0.11	0.44	0.04	0.45	0.10	0.17	0.11
PCB-03-PRM-050	140.65	2.82	0.04	0.23	0.02	0.90	0.11	0.80	0.09	1.94	0.13	0.50	0.06	0.45	0.14	0.20	0.12
PCB-03-PRM-070	140.45	2.79	0.02	0.21	0.01	0.85	0.07	0.76	0.09	2.18	0.18	0.55	0.07	0.60	0.18	0.24	0.15
PCB-03-PRM-090	140.25	2.77	0.02	0.30	0.01	0.95	0.06	0.71	0.12	1.75	0.11	0.60	0.05	0.66	0.11	0.29	0.11

PCB-03-PRM-100	140.15	2.49	0.03	0.34	0.01	1.34	0.05	0.46	0.14	1.51	0.06	0.48	0.03	0.78	0.06	0.54	0.13			
PCB-03-PRM-120	139.95	2.74	0.04	0.45	0.02	1.01	0.07	0.60	0.06	1.40	0.03	0.44	0.01	0.77	0.04	0.40	0.06			